University of Strathclyde Engineering

Enhancement of electrochemical sensor performance through the optimisation of nucleic acid probe architecture

PhD Thesis

Paul Williamson
Department of Biomedical Engineering
University of Strathclyde
2022

This thesis is the result of the author's original research. It has been composed by the author and has not been previously submitted for examination which has led to the award of a degree.

Singed: P Williamson

Date: 16th June 2022

Abstract

A key aim in the field of diagnostics is to engineer instrumentation that fulfils three primary aims. This includes enhancing the sensitivity of a device, or improve the ability to determine minimal concentrations of analyte in a complex sample. Secondly, devices must be capable of producing a signal readout in response to the presence or absence of the target analyte in a short time window. Thirdly, manufactured devices must be feasibly deployed to a point of care setting at a low cost, often in challenging environments

Electrochemical methods can serve as the workhorse in achieving such goals, with its power in discriminating variations to a series of properties that describe a bioelectric interface. Simply, these interfaces are composed of an immobilised biomolecule upon a metal transducer surface that is capable of the capture, or detection, of a desired molecular target. In the case of nucleic acid detection, immobilised receptor nucleic acids, or DNA probes, serve as the detection element of the system. These DNA probes are engineered to share complementarity to a desired nucleic acid target, and in the presence of such a target, will capture the analyte by hybridisation through Watson-Crick base pairing laws. These hybridisation events change the interfacial properties of the transducer, and by electrochemical techniques, devices can translate such derivations in to a signal read out for the user.

Molecular self-assembly is a process whereby molecules spontaneously form organised structures, governed by the inherent interactions between the local constituents. It is this principle that drives the formation of immobilised DNA probes in a “DNA Self-Assembled Monolayer”. This technique allows for a simple method of bioelectric interface construction. Conventionally, these DNA probes are single-stranded linear elements. However, an increasing number of publications are exploring ever more complex probe geometries in biosensing applications. Despite this, there is a distinct lack of contributions to the literature detailing whether such advanced probe architectures may provide a meaningful solution to current problems facing low cost point of care devices. To this end, this thesis attempts to explore key metrics of biosensor performance with an ever-increasing bioelectric interface complexity. Here, increasing complexity is achieved by the introduction of higher order probe architectures, or by the introduction of DNA nanostructures free in solution, which may serve as signal amplifiers.

The first section of this work provides an extensive literature review. This begins with exploring the need for rapid PoC diagnostic technologies, with a particular focus on tackling antimicrobial resistance. This is followed by a detailing of current nucleic acid detection methods, the advent of DNA nanotechnology, and its recent advances and emerging applications. Thereafter, the DNA origami method is described, and its power and application in biosensor design is discussed. Finally, an account of key theoretical concepts governing electrochemical methods is provided.

Experimental chapters then follow, detailing the development and testing of a series of electrochemical biosensor designs, each with an increasing degree of probe complexity. The first of which explores a class of 1D and 2D probes. These linear and hairpin probes are thoroughly interrogated to explore potential improvements in both sensitivity, and specificity. Within this chapter, successful enhancement in sensor selectivity was observed with a hairpin probe architecture against a linear probe. Sensitivity to complementary target was deemed comparable between both probe apparatus; therefore, translation of the hairpin based bioelectric interface to a microelectrode platform was undertaken. This was successfully shown to boost sensitivity in accordance with literature reports, while maintaining the enhanced selectivity inherent to hairpin probe structures.

The second experimental chapter focuses on the introduction of tetrahedral DNA nanostructures to electrochemical biosensor apparatus. Three distinct strategies where explored. Firstly, a designed tetrahedron serves as the immobilised probe. Secondly, the same tetrahedron was modified to harbour an electroactive redox tag producing a “signal off” biosensor design. Finally, a novel approach is detailed, using free tetrahedra in solution to serve as signal amplifiers by boosting impedance following their tethering to the surface by a complementary target oligonucleotide. A valuable proof of concept is established here in the ability of nanostructures to serve as inexpensive and powerful methods of signal amplification negating the need for complex and costly chemistries common to other strategies.

The third experimental chapter builds upon the signal amplification strategy described above, with the introduction of a novel, and highly programmable DNA origami tile. In a first for the electrochemical biosensor field, this chapter reports on a series of tile nanostructure designs capable of effectively crosslinking to a linear probe DNA functionalised transducer, with the presence of a complementary target serving as the linking tether. With this approach, growth in

the impedance of the interface contributes to a significant improvement in sensor limit of detection, and importantly remains highly effective in a DNA rich complex media, proving its potential in future PoC devices.

The final section of experimental work here focuses on a novel sensing approach, with a divergence from nucleic acid detection, to the successful electrochemical interrogation of environmental conditions by a switchable DNA nanostructure. Here, a DNA origami “zipper” has been designed to be responsive to environmental stimuli, specifically pH. Such a sensing application is of need given the known alterations in local pH conditions associated with both bacterial growth, and a series of human pathologies. This zipper structure was successfully immobilised as part of mixed SAM, forming a bioelectric interface capable of discriminated local pH conditions across a broad and clinically relevant pH range.

Acknowledgements

Firstly, I would like to thank Dr Damion Corrigan for a tremendous amount of support and guidance though out this project. This has ranged from simple quick fixes to the many problems I have hit, to providing inspiration and helping me shape the direction of this research. Your input and support has been invaluable. Equally, my thanks extends out to the entirety of the advanced diagnostics group, past and present. Bringing both insight, and a good deal of fun to these years has made the PhD process a truly enjoyable one so thankyou to each and every one of you. Additionally I am grateful to the entirety of the BME department for supporting me in challenging recent years. Despite forced working from home, I always felt part of the department, even from afar.

Much of this thesis is highly collaborative. Many aspects of DNA nanotechnology, and particularly DNA origami where new to both myself, and the research group. Had it not been for the expertise of our collaborators, the output of my thesis would be far from as fruitful. Therefore, I would like to give particular thanks to Dr Veikko Leinko, Dr Heini Ijas, Dr Boxuan Shen, and Petteri Piskunen. They have undoubtedly expanded my learning in a range of nanotechnology fields, been teachers to a near novice, and shown a great deal of patience in my many questions and problems. I am enormously grateful for all of their efforts, and hope they found our collaborations as useful and beneficial as I did. I hope such close collaboration can continue in future endeavours, whatever they may be.

On a personal level, to my family and friends, thank you for all the support, willingness to hear my frustrations, and the near daily honest jibes that “I’ll need to get a real job after this“. Lastly for inspiring this past year, cheers Big Ange.

“*We never stop*”

Ange Postecoglou

Publications

Publications arising from work reported in this thesis:

Probing the Conformational States of a pH-Sensitive DNA Origami Zipper via Label-Free Electrochemical Methods

Paul Williamson, Heini Ijas, Boxuan Shen, Damion K. Corrigan, Veikko Linko

Langmuir 2021, 37, 25, 7801–7809
https://doi.org/10.1021/acs.langmuir.1c01110

Signal Amplification in Electrochemical DNA Biosensors Using Target-Capturing DNA Origami Tiles

Paul Williamson, Petteri Piskunen, Heini Ijäs, Adrian Butterworth, Veikko Linko**,** Damion K. Corrigan

ACS Sensors 2023, 8, 4, 1471-1480
https://doi.org/10.1021/acssensors.2c02469

Papers currently in peer review from work reported in this thesis:

Engineering DNA Hairpin Monolayers to Enhance Electrochemical Bio-Sensing Capabilities

Paul Williamson, Adrian Butterworth and Damion Corrigan

Submitted for peer review - RSC Analyst 2022

Contributors

This thesis represents my work as part of a fruitful collaboration with colleagues from Aalto University, Finland. Their expertise in DNA origami design, assembly, and testing has helped power much of this research project. For that, I am very grateful. As such, it is necessary to note their contributions to work presented in this thesis. These contributions can be found in Chapter 5 and 6, with aid in DNA origami nanostructure design, assembly and characterisation.

Chapter 5: DNA Origami Tile

Conceptualisation and design: Paul Williamson, Damion Corrigan, Veikko Linko, Heini Ijas

Assembly, PAGE Analysis and TEM Characterisation: Petteri Piskunen

Chapter 6: DNA Origami Zipper

Conceptualisation and design: Paul Williamson, Damion Corrigan, Veikko Linko, Heini Ijas, Boxuan Shen

Assembly, PAGE Analysis and AFM Characterisation: Heini Ijas, Boxuan Shen

Contributor Details:

Veikko Linko - https://orcid.org/0000-0003-2762-1555

Heini Ijas - https://orcid.org/0000-0001-7880-332X

Boxuan Shen - https://orcid.org/0000-0002-1107-828X

Petteri Piskunen - https://orcid.org/0000-0002-3142-3191

Damion Corrigan - https://orcid.org/0000-0002-4647-7483

Contents

Abstract i
Acknowledgements iv
Publications v
Contributors vi
Contents vii
List of Figures xii
List of Tables xv
Chapter 1 Literature Review 1
1.1 Antimicrobial Resistance 2
1.2 Nucleic Acid Detection 4
1.3 Electrochemical DNA Biosensors (e-DNA Biosensors) 9
1.3.1 Sensor Construction 9
1.3.1.1 Alkanethiol Self Assembled Monolayers 10
1.3.1.2 DNA and Alkanethiol mixed SAMs for e-DNA Biosensors 14
1.3.2 Current advances in DNA SAM construction for electrochemical Biosensors 16
1.4 Higher Order DNA Structures 27
1.4.1 DNA Nanotechnology as an Emerging Field 27
1.4.2 The DNA Tetrahedron - Development and Method of Assembly 30
1.4.3 *Advances in DNA Tetrahedra Applications; Drug Delivery and Biosensing* 32
1.4.3.1 Drug Delivery 32
1.4.3.2 Biosensing 34
1.5 DNA Origami 39
1.5.1 Emergence of a new field 39
1.5.2 Control of molecular scale positioning by DNA origami 42
1.5.3 DNA origami for macromolecular delivery 42
1.5.4 Environmentally Responsive DNA Origami 46
1.5.5 Current Application in Biosensing 50
1.6 Conclusions 53
Chapter 2 Theoretical Concepts 54
2.1 Introduction 54
2.2 The Three Electrode Cell 55

2.3 The Electrical Double Layer 57
2.4 Voltammetry 62
2.4.1 Cyclic Voltammetry 62
2.4.2 Differential Pulse Voltammetry (DPV) 65
2.4.3 Square Wave Voltammetry (SWV) 66
2.5 Electrochemical Impedance Spectroscopy (EIS) and Circuit Fitting 67
2.6 Microelectrodes 70
2.7 Statistical Methods 74
2.7.1 Box Plots 74
2.7.2 t-Tests for Determining Significant Difference 75
Chapter 3 Engineering DNA Monolayers to Enhance Electrochemical Bio-Sensing Capabilities 76
3.1 Introduction 77
3.2 Materials and Methods: 80
3.2.1 Materials 80
3.2.2 Buffers 81
3.2.3 Oligonucleotides 81
3.2.4 Electrochemical Methods 82
3.2.5 Electrode Polishing and Cleaning (PGE Preparation Method 1) 84
3.2.6 Electrode Functionalisation 84
3.2.7 Target Incubation 85
3.2.8 Sample Characterisation 85
3.3 Results and Discussion 86
3.3.1 Polycrystalline Gold Electrode Cleaning 86
3.3.2 Polycrystalline God Electrode Functionalisation 88
3.3.3 Target Sensing Performance and Specificity in Faradaic Buffer 89
3.3.4 Hairpin System using redox tag (non-faradaic buffer) 96
3.3.5 Microelectrode Cleaning and Functionalisation 99
3.3.6 Translation to a Microelectrode platform 102
3.4 Conclusions 107
Chapter 4 Investigation Higher Order DNA Nanostructures for Biosensing Applications – The DNA Tetrahedron 108
4.1 Introduction 109
4.2 Materials and Methods: 111

4.2.1 Materials 111
4.2.2 Buffers 112
4.2.3 Oligonucleotides 112
4.2.4 Electrochemical Methods 113
4.2.4 Electrode Polishing and Cleaning (PGE Preparation Method 2) 114
4.2.5 Tetrahedron Formation 115
4.2.6 Tetrahedra Polyacrylamide Electrophoresis 116
4.2.7 Electrode Functionalisation 117
4.2.8 Target Detection 118
4.2.8.1 TETv1 System: 118
4.2.8.2 TETv2 System: 118
4.2.8.3 TETv3 System: 118
4.3 Results and Discussion: 120
4.3.1 Assessment of New Cleaning Protocol 120
4.3.2 Detection of Nucleic Acid Targets – *is simple best?* 124
4.3.2.1 SAM Characterisation 124
4.3.2.2 Estimation of OXA pDNA Surface Coverage 125
4.3.2.3 Sensing of 115nt Fragment Target by OXA pDNA SAM 129
4.3.3 Confirming TDN Assembly by PAGE Analysis 133
4.3.4 TETv1 System: Electrochemical Performance 134
4.3.5 TETv2 System: Investigating the electrochemical performance of a redox-tagged tetrahedron biosensor 141
4.3.6 TETv3 System: Using DNA Tetrahedra as signal amplifiers for the electrochemical sensing of DNA hybridisation 148
4.3.7 Investigating the feasibility of system translation to a custom gold electrode array. 155
4.4 Conclusions 160
Chapter 5 Signal Amplification in Electrochemical DNA Biosensors Using Target-Capturing DNA Origami Tiles 162
5.1 Introduction 163
5.2 Materials and Methods 166
DNA Origami Tile Design and Assembly 166
5.2.1 Materials 166
5.2.2 Design, Assembly, and Purification 166
5.2.3 Agarose Gel Electrophoresis (AGE) 167

5.2.4 Transmission Electron Microscopy (TEM) 167
Sensor Construction and Electrochemistry 168
5.2.5 Materials 168
5.2.6 Buffers 169
5.2.8 Electrochemical Methods 169
5.2.9 Oligonucleotides 170
5.2.10 Electrode Preparation and Electrochemical Measurement 170
5.2.11 Electrode Functionalization 171
5.2.12 Target Detection 171
5.3 Electrode Functionalization and Detection of Free Target 172
5.4 Determining an Optimal Origami Tile Design for Signal Amplification 175
5.5 Electrochemical Performance of a DNA Origami Tile-Enhanced Biosensor 177
5.6 Confirming the Mechanism of Electrochemical Response with a Non-Complementary Target 180
5.7 Specificity of the DNA Biosensor Design 181
5.8 Conclusions 184
Chapter 6 Probing the Conformational States of a pH-Sensitive DNA Origami Zipper via Label-Free Electrochemical Methods 185
6.1 Introduction 186
6.2 Materials and Methods 188
6.2.1. DNA Origami Zipper Design and Assembly 188
6.2.1.1 Materials 188
6.2.1.2 Design, Assembly, and Purification 188
6.2.1.3 Atomic Force Microscopy (AFM) 189
6.2.1.4 Agarose Gel Electrophoresis (AGE) 189
6.2.2 Electrochemistry 190
6.2.2.1 Materials 190
6.2.2.2 Buffer Preparation 191
6.2.2.3 Electrochemical Methods 192
6.2.2.4 Electrode Polishing and Cleaning 193
6.2.2.5 Electrode Functionalisation 193
6.2.2.6 Sample Characterisation 193
6.2.2.6. Electrochemical Measurements 194
6.3 Results and Discussion 194

6.3.1 Characterisation of the DNA zipper structure 194
6.3.2 Electrode functionalisation 196
6.3.3 Investigating pH induced conformational switching of the DNA Zipper 198
6.3.4 Methylene Blue Intercalation 202
6.3.5 Live electrochemical monitoring of DNA Zipper confirmation 204
6.4. Conclusions 206
Chapter 7 Conclusions & Future Work 208
Supplementary Information 218
(B) Supplementary TEM images for Chapter 5 233
(C) SI for Chapter 6 235
References 240

List of Figures

Figure 1.1 Watson and Crick Model of Helical DNA Structure and Base Pairing 4
Figure 1.2 Overview of a typical Polymerase Chain Reaction. 6
Figure 1.3 Self-Assembled Monolayer Schematic. 10
Figure 1.4 Schematic of Decanethiol adsorbed on a gold planar surface in the “standing up” phase. 12
Figure 1.5 Simplified mechanism of action for a DNA Biosensor. 15
Figure 1.6 Fraction of e-DNA biosensor publications in the literature reporting MCH use as blocking SAMs 18
Figure 1.7 Mechanism of action for a conventional ratiometric e-DNA biosensor design 23
Figure 1.8 Combining Branched Motifs 27
Figure 1.9 Modular Assemblies of DNA Nanostructures through the linkage of distinct 2D Building Blocks 28
Figure 1.10 Modification of DNA Tetrahedra for the Targeted Delivery of Therapeutics 32
Figure 1.11 Initial workings of a tetrahedral DNA biosensor 35
Figure 1.12 Enzyme-free DNA tetrahedron e-DNA biosensors 37
Figure 1.13 Design of two-dimensional and three-dimensional DNA Origami 41
Figure 1.14 Targeted delivery of antimicrobials through a DNA origami nanocarrier 45
Figure 1.15 A reconfigurable DNA Origami nanocapsule with encapsulation and release of cargo driven through local pH control 47
Figure 1.16 Current usages of DNA origami for e-DNA biosensor designs 50
Figure 2.1 Schematic for the Gouy-Chapman-Stern (GCS) model of the electrical double layer 57
Figure 2.2 Schematic for the Gouy-Chapman-Stern (GCS) model of the electrical double layer on a SAM functionalised electrode. 60
Figure 2.3 Typical Cyclic Voltammogram for a reversible redox species 62
Figure 2.4 Schematic outlying the details of differential pulse voltammetry measurement 65
Figure 2.5 Square Wave Voltammetry waveform. 66
Figure 2.7 Analogous modelling of Real Phenomena in Electrochemical Systems, and Respective Impedance Responses 68
Figure 2.6 Example Nyquist plot detailing the electrochemical parameters that can be derived for further analysis 68

Figure 2.8 Diffusion layer profiles for both Microelectrodes (a) and Macroelectrodes (b). 71
Figure 2.9 Typical pristine microelectrode cyclic voltammogram 72
Figure 2.11 Modified Randles circuit of the fitting of EIS data from microelectrode interrogation 74
Figure 3.1 Experimental Outline 77
Figure 3.2 Analogous electrical circuits for EIS data fitting 83
Figure 3.3 Electrochemical cleaning and characterisation of gold electrodes by Cyclic Voltammetry 86
Figure 3.4 Assessment of PGE functionalisation with various OXA pDNA species by EIS..... 88
Figure 3.5 Electrochemical responses of functionalised electrodes to target incubation 89
Figure 3.6 Estimation of secondary structure for sequence HPv2 93
Figure 3.7 Schematic outlining possible hairpin secondary structures 95
Figure 3.8 Electrochemical characterisation of Ferrocene-tagged linear and hairpin probe architectures 96
Figure 3.9 Electrochemical characterisation of microelectrode cleaning and functionalisation 99
Figure 3.10 Images of Microelectrode Devices, and DPV Responses of Functionalised Electrodes to Various DNA Targets 102
Figure 3.11 Macroelectrode vs microelectrode perormance 106
Figure 4.1 Overview of DNA Tetrahedron Self-Assembly 109
Figure 4.2 Simplified Randles circuit for electrochemical circuit fitting. 114
Figure 4.3 PAGE set-up with lane map showing contents. 117
Figure 4.4 Comparison of Electrochemical Characteristics of PGE following Cleaning Methods 1 and 2 122
Figure 4.5 Electrochemical analysis of PGE following functionalisation..... 124
Figure 4.6 Anson plots of charge vs time 127
Figure 4.7 Determining sensing performance of a linear pDNA SAM against conventional targets 129
Figure 4.8 Confirmation of successful Assembly of TDN by PAGE 133
Figure 4.9 Box plot of DPV peak current for PGE post-clean, and after functionalisation with a TDN/MCP mixed SAM 135
Figure 4.10 Electrochemical characterisation of TETv1 System performance following incubation with complementary and non-complementary target. 136

Figure 4.11 Characterisation of a Ferrocene tagged Tetrahedron based biosensor by DPV and EIS interrogation. 142
Figure 4.12 TETv3 – a signal amplifying DNA biosensor design 148
Figure 4.13 Electrochemical interrogation of a novel biosensor design, employing a DNA tetrahedron signal amplifier 151
Figure 4.14 Electrochemical Cleaning of Flex Medical Array 155
Figure 4.15 Characterisation of Flex Device with combined Au CE/Ref. 157
Figure 4.16 Assessment of Flex electrode functionalisation and response to complementary and non-complementary targets 158
Figure 4.17 Device cleaning by thiol attack. 159
Figure 5.1 Design and characterization of the DNA origami tiles and their use in signal amplification in biosensors 165
Figure 5.2 Electrochemical characterization of SAM assembly, and sensing performance without DNA origami tile amplification 173
Figure 5.3 Selection of an appropriate tile design 176
Figure 5.3 Electrochemical sensor performance with DNA origami tile amplification 178
Figure 5.4 Electrochemical response to a non-complementary target. 180
Figure 5.6 Electrochemical response of sensor design to complementary and non-complementary targets in a complex media. 182
Figure 6.1 Schematics of the DNA origami zipper 187
Figure 6.2 AFM analysis of the zipper conformation in TAE buffers 195
Figure 6.3 Electrochemical assessment of zipper immobilisation on Au PGE 197
Figure 6.4 Peak current data of active pH responsive zipper and control open zipper following immobilisation on Au PGE in a closed starting confirmation. 199
Figure 6.5 Assessment of Methylene Blue intercalation by DPV interrogation. 202
Figure 6.6 Live electrochemical monitoring of DNA Zipper confirmation by repeat DPV measurements at each buffer pH point 204
Figure 7.1 A roadmap for the development of DNA nanostructured devices for biosensing applications 209
Figure 7.2 Overview of key experimental findings 217

List of Tables

Table 1.1 Detection limits for choice publications reporting isothermal nucleic acid amplifications in e-DNA biosensor designs. 25
Table 3.1 Chemicals used in this study. 80
Table 3.2 Buffers used in this study. 81
Table 3.3 Electrochemical Methods 82
Table 4.1 Chemicals used in this study. 111
Table 4.2 Buffers used in this study. 112
Table 4.3 Electrochemical Methods 113
Table 4.4 Oligonucleotide Volumes for Complete TDN Assembly. 115
Table 4.5 Materials required for the casting of polyacrylamide gels. 116
Table 4.6 Target Concentrations in TM Buffer 119
Table 4.7 Determination of Electro-active Surface Area. 121
Table 5.1 Chemicals used in this study. 168
Table 5.2 Buffers used in this study. 169
Table 5.3 Electrochemical Methods 169
Table 5.4 Tabulated electrochemical data for various DNA origami tile designs 177
Table 5.5 Tabulated electrochemical performance metrics for a conventional pDNA biosensor design and our DNA origami tile amplification strategy 179
Table 6.1 Chemicals used in this study. 190
Table 6.2 Buffers used in this study. 191
Table 6.3 Electrochemical Methods 192

Chapter 1

Literature Review

Abstract:

In order to explore how the specific architecture of a DNA probe may influence the performance of an electrochemical biosensor, one must first undertake a broad analysis of the literature across a number of disciplines. This analysis will begin by briefly addressing the need for rapid, nucleic acid detection capabilities, with a particular focus on aiding infection control, and facilitating antibiotic stewardship. Current methods of detection for target nucleic acids by central laboratories, and qualitative field-ready PoC devices will then be surmised. Thereafter, key principles for e-DNA biosensor construction are explored to reveal a number of engineering concerns that are limiting their translation to a clinical setting. From here a detailed analysis of the many varying approaches, the biosensing community have reported to tackle such challenges. Structural DNA nanotechnology is then introduced to provide the reader with an understanding of both its simplicity, elegance and power. This aims to present an argument for how DNA nanotechnology may serve as a key avenue in addressing the lasting issues of e-DNA design and manufacture hindering their potential in modern diagnostics.

Key Words:

Antimicrobial Resistance. Nucleic Acid Testing, Biosensing, Electrochemistry, Self-assembled monolayers, DNA Nanotechnology, DNA Origami

1.1 Antimicrobial Resistance

The employment of antibiotics in the defence against bacterial infections have heralded unrivalled improvements in global healthcare outcomes since their clinical introduction in the 1930's. The mechanism of action for antibiotics is variable, with multiple cellular functions serving as a target for specific classes of antibiotics. These can include the inhibition of DNA replication, prevention of protein synthesis, disruption to critical enzyme function, or the interruption to cell wall synthesis.[1] Despite the unique success of these classes of drugs, increasing concern surrounding accelerating antimicrobial resistance is powering global collaboration between governments, private industry, and public research institutions to gather novel solutions to a looming crisis. With a rapid expansion in the number of resistant strains, and limited stream of new antibiotics available, the projections for global fatalities attributed to resistant species is expected to reach upwards of 10 million deaths per year by 2050.[2]

AMR is fundamentally a genomic problem. Random mutation within the bacterial genome powers resistance to a given class of antibiotic. The ability of bacteria to exchange such advantageous characteristics though horizontal gene transfer events exacerbates selection pressure and drives the prevalence of resistant cells within a population.[3,4] Overuse and mismanagement of current antibiotic stocks in healthcare has often been an oversight. This may stem from excessive or incorrect prescription due to diagnostic uncertainty in community settings, or from prolonged and intensive usage in hospital settings for highly vulnerable immunosuppressed patients.[5] The use of antibiotics extends beyond healthcare, with their application common place in livestock farming practices. Extreme use to enhance yields contributes to a significant concentration of environmental antibiotics from animal waste and run-off. Consequently, selection pressures in local bacterial populations accelerate the proliferation of antibiotic resistance and poses a significant threat to local communities where subsequent infections may become prevalent.[6]

In 2017, the World Health Organisation published a series of critical priority pathogens to be targeted in the development of new antibiotics. However, novel therapeutics are not the only necessary solution in managing the proliferation of resistant bacterial species. Key strategies involve the enhancement of both public and professional awareness to AMR, improvements to infection prevention and control practices, responsible management of

antimicrobials in agriculture, and crucially novel PoC detection techniques for the rapid identification of infectious agents, resistance they may express, and drugs to which they may be susceptible.[7] Such diagnostic advances better facilitate the stewardship of existing antimicrobial stocks by enabling appropriate prescription, and guide global surveillance of resistant populations. Finally, at a patient level, the minimisation of lag times associated with conventional central laboratory techniques may provide an improvement in required time spent in care facilities and offer enhanced outcomes in complex infections.

Extra-intestinal *Escherichia coli* (*E.coli*) is often prevalent in clinical bloodstream infections and is the primary cause of bacteraemia, commonly presenting with multidrug resistant strains.[8] Expression of broad-spectrum β-lactamases can often contribute to alarmingly high peak resistance levels against aminopenicillin, ureidopenicillins, and cephalosporins. One such enzymatic mechanism of resistance described for *E.coli* to inhibitor penicillins is the production of OXA-1 β-lactamase.[9,10] The responsible gene *bla*OXA-1, exists in both plasmid and integron sites across a host of gram-negative species, and is often closely associated with genes encoding extended-spectrum β-lactamases (ESBLs).[11] This particular gene therefore presents as a key analytical target for helping discriminate potential resistance within a population.

To this end, AMR plasmid mimics were extracted from transformed *E.coli* DH10β cells, with the plasmid hosting a panel of key AMR genes including the *bla*OXA-1 β-lactamase gene by a colleague of mine in our research group. Recently, Dr Butterworth's work has focused on detection of Oxacillin resistance with an isothermal amplification approach on screen-printed gold electrodes, with a potential limit of detection approaching 319 cfus/ml, and sixty-minute time to result.[12] Within this publication, and a previous literature entry from 2019,[13] are details of the plasmid, and forward and reverse primers used to amplify a 116 base pair section for OXA-1. These sequences serve as the foundation to sensor designs explored in this thesis. The primer sequences designed by Dr Butterworth have been employed here as the OXA probe, and for complementary target development. Equally, the target synthetic oligonucleotide, "115nt OXA Fragment" which features heavily in this study, is based upon the 116 base pair section of the template used in his work.[12,13]

1.2 Nucleic Acid Detection

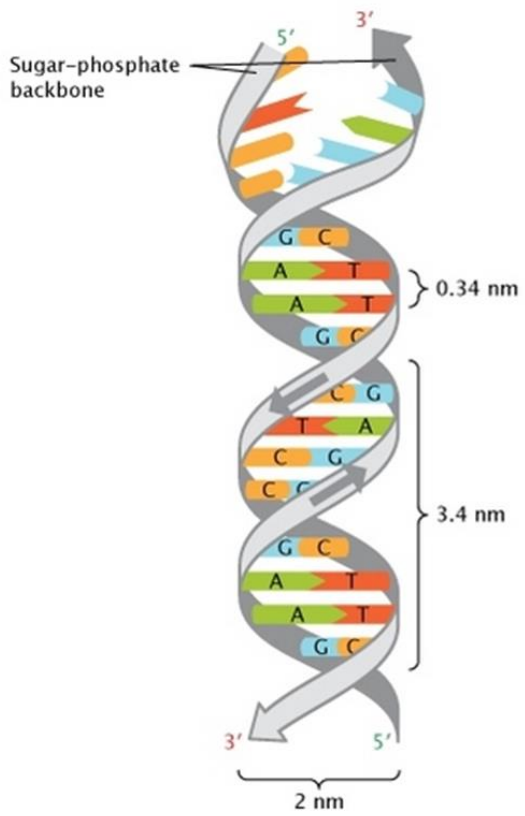

Figure 1.1 Watson and Crick Model of Helical DNA Structure and Base Pairing.

Adapted from: [15]
Pray, L. *Nature Education*. Discovery of DNA structure and function: Watson and Crick. 1(1):100 (2008)

Deoxyribonucleic Acid (DNA) is responsible for encoding the necessary information for the formation, and functioning of organisms. This definition is broadly understood throughout society, in part due to the rapid expansion of DNA science in modern diagnostics and therapeutics. The acceleration in its widespread applications since the initial works of Watson and Crick, in the modelling of DNA in 1953,[14] is perhaps unrivalled in 20th century science. Figure 1.1 displays the chemical structure of DNA in its B-form double helix, with a single nucleotide formed of a phosphate group, sugar unit, and any one of four bases, Adenine (A), Thymine (T), Cytosine (C), and Guanine (G).[15] In this double stranded (ds)DNA model, two antiparallel single-stranded (ss)DNA molecules hybridise in accordance to strict Watson-Crick base pairing laws; where A-T base pairs, and C-G base pairs form through two and three hydrogen bonds

respectively. In this confirmation, the dsDNA structure twists in a right-handed helix with 10.4-10.5 base pairs per complete helical turn (360^0), a rise of 0.34 nm per base pair, and a structural diameter of ~2 nm.[16] Further stabilising the helical structure is base stacking interactions between nucleobases, and the hydrophobic effect of non-polar nucleobases arranged in the centre of the helical structure.[17]

The elegance of DNA structural simplicity and the remarkable specificity of Watson-Crick base pairing laws, allows for the strong prediction of interactions between single stranded DNA (ssDNA) molecules. These properties power the sequencing of complete genomes into open source libraries, and allow for the determination of functionalities that can be attributed to a given sequence. These advances have heralded a new and deep understanding of particular cellular pathways, human pathologies, and identification of bacterial species.[18,19] Consequently nucleic acids can be examined as potential targets of interest in diagnostic applications.

Nucleic acid testing (NAT) is an area of diagnostics primarily concerning the identification of a given nucleic acid sequence in a particular medium. This approach is powerful, with hypersensitive detection limits, and high specificity. However, this technique currently exists in centralised laboratory settings, with complex instrumentation and skilled labour required. Often sample preparation is lengthy, with steps of cell lysis and purification necessary. NAT often assesses samples with low DNA concentrations, and amplification is required, commonly by polymerase chain reaction (PCR), summarised in Figure 1.2. Here, repeated thermal cycling of heating and cooling stages, allows a thermostable polymerase enzyme to extend a free primer sequence through the addition of free nucleotides from its 3' end. Primers are introduced with specificity to a given sequence, allowing for the amplification of a desired target from single copies in a sample to a copy number in the billions within an hour. However, the requirement for repeated heating and cooling steps by a well-controlled thermocycler maintains the high operating costs, and complex instrumentation often associated with common NAT techniques. This possess a challenge to addressing two key issues in modern diagnostics. The necessity of a rapid result, and the ability to bring testing capability to challenging environments. These two issues are critical in translating biosensing applications to a wide range of subcategories. Including, molecular disease diagnostics, bacterial pathogen detection, the enhancement of global food security, environmental monitoring, and in the detection of specific targets for defence services.[20] As such, significant resources have been devoted to the development of a sensing apparatus, with appropriate miniaturisation,

simplicity, and performance, which would enable effective point of care (PoC), and field translation. Isothermal amplification techniques of Rolling Circle Amplification, Loop Mediated Isothermal Amplification, and Recombinase Polymerase Amplification, all return numerous

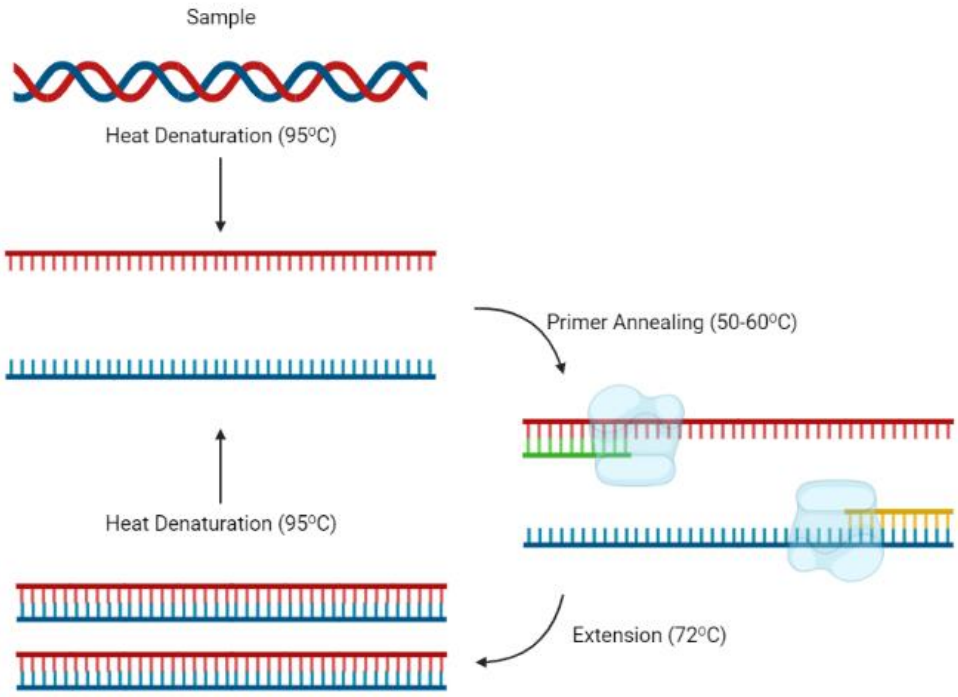

Figure 1.2 Overview of a typical Polymerase Chain Reaction.

works in literature for biosensing applications.[21–23] Rolling Circle Amplification (RCA) is an technique centred around the isothermal amplification of circular DNA templates. This method is capable of producing elongated single-stranded DNA products, providing value in the detection of specific target DNA sequences. This process is triggered by the initiation of a rolling circle mechanism, wherein the circular DNA template undergoes continuous amplification through the synthesis of new DNA strands.[21] Loop-Mediated Isothermal Amplification (LAMP) is an isothermal amplification method characterized by its use of multiple primers that recognize distinct sequences on the target DNA. This recognition leads to the formation of a distinctive loop structure, facilitating the continuous amplification of DNA. LAMP operates under constant temperature conditions, eliminating the need for a thermal cycler. Widely employed for its rapid and cost-effective DNA amplification, LAMP is particularly valuable in pathogen detection applications due to its simplicity and efficiency in point-of-care diagnostics.[22] Recombinase Polymerase Amplification (RPA) represents an isothermal amplification technique that

harnesses the synergistic activity of recombinase and DNA polymerase to selectively amplify target DNA sequences. Operating at a consistent temperature, typically around 37-42°C, RPA is renowned for its rapid amplification, high sensitivity, and suitability for point-of-care diagnostics in infectious diseases. The technique involves the formation of a recombinase complex that facilitates primer binding and strand displacement, followed by DNA polymerase-mediated amplification. The isothermal nature of RPA contributes to its practicality in resource-limited settings, making it a valuable tool in the realm of molecular diagnostics.[23] By employing polymerase enzymes capable of strand displacement; these systems avoid the need for repeated thermal cycling. As such, rapid amplification of small nucleic acid quantities can be translated to simple, and low cost devices that may prove effective in field-based settings. However, common to all of these techniques is the requirement for advanced primer design. Primers must be rigorously engineered to ensure specific targeting of a desired sequence within the DNA or RNA template. Inaccuracies in primer design heighten the risk of non-specific amplification, potentially contributing to false positives. The efficiency of primer binding is crucial for initiating and sustaining the amplification process. Minimising the risk and impact of secondary structure formations such as nucleic acid hairpins is may also require the use of a specific DNA polymerase which can navigate such structural motifs, or an initial denaturation step. Careful consideration during primer design is necessary to minimise any potential hindrance posed by these secondary structures, thereby promoting successful and reliable amplification. Each of these techniques can be considered Isothermal; however, that does not remove the requirement for close temperature control. Experimentation is often required to optimise the specific temperature at which yield and specificity is acceptable, with either extreme in temperature deviation away from optimum contributing to minimal primer annealing, or high rates of nonspecific binding. While temperature control may be provided with a small and accurate heat block, miniaturising such control to a small lab on a chip apparatus for field use may introduce a small but meaningful engineering concern. Finally, the ability to restrict sources of sample contamination is critical in these isothermal approaches, given the high sensitivity of the techniques. Low-level nucleotide contamination may introduce extraneous sequences into the reaction process contributing to false positives or inaccurate quantification and may also significantly impact in the reproducibility of these techniques,

Another approach to by passing the need for complex instrumentation associated with conventional amplification, is the direct detection of low quantity nucleic acids. This is

commonly known as DNA biosensing, and relies on the inherent specificity of base pair binding, unique to nucleic acids. With the appropriate design of a sensing, or recognition element, detection of nucleic acids is possible in clinically relevant concentrations in complex media. The premise of which is surmised in Figure 1.5 with the required recognition site consisting of a series of bases that is complementary in pairing, to a given nucleic acid of interest. Often, the recognition element is in direct spatial contact with a transducer surface, as part of a larger probe sequence, with its immobilisation driven by an interaction between a functionalised region of the probe, and the underlying substrate. Various probe confirmations exist, including single stranded DNA (ssDNA), DNA Aptamers, Peptide Nucleic Acids (PNA), and Morpholino DNA Analogues.[24–27]

This could include known nucleic acids involved in disease states, bacterial or viral infection, and water contamination.[28–30] A key benefit to the usage of DNA biosensing approaches in the above areas lies in the ability to manufacture simple and cost effective Point of Care (PoC) devices, which provide rapid determination to the presence of a target sequence. Numerous works have succeeded in employing simplified optical measurement techniques in producing sensors effective in the field.[31–33] While these approaches are promising, the signal output is often qualitative, and often lacks the sensitivity desirable in the monitoring of certain diseases.

Electrochemical methods of DNA Biosensing have been explored in recent decades, in part for the ability to detect hybridisation events at low concentrations, but also through increasing technological advances in the miniaturisation, and portability of instrumentation.[34] Electrochemical measurement techniques are numerous, with Voltammetry, Impedimetric Spectroscopy, field effect transduction, and Amperometry all reported in the scientific literature as appropriate tools for nucleic acid detection.[34] In Chapter 1.3, a detailed focus will be given to construction of electrochemical DNA biosensors, current applications, and known issues currently undergoing investigation. Possible benefits and means of signal acquisition and processing for techniques listed above that are relevant to this study are given in Chapter 2 Theoretical Concepts.

1.3 Electrochemical DNA Biosensors (e-DNA Biosensors)

e-DNA biosensors hold significant promise for the monitoring of various diseases. The potential applications are vast, with target analytes ranging from bacterial nucleic acids associated with AMR,[29,35,36] circulating tumour DNA sequences (ctDNA),[28,37] single nucleotide polymorphisms[38,39] and recently detection of clinically relevant concentrations of biomarkers for SARS COV-2 with aptasensors.[40] This method of target analyte detection has proven successful in various laboratory-based setups. Despite these advances, translation of such systems from the laboratory to a clinical environment is yet to occur, and yield the diagnostic revolution often promised.

This subchapter will cover three main areas. Firstly, a background in the chemistry that governs the formation of self-assembled monolayers for simple alkanethiols will be explored. Thereafter, detail will be provided on the incorporation of probe DNA into a mixed self-assembled monolayer, and how such a probe can serve as an electrochemical detector. Finally, recent attempts to address issues associated with SAM based e-DNA biosensors will be explored.

1.3.1 Sensor Construction

Central to the efficacy of an E-DNA sensor, is the ability to construct uniform electrode surfaces, free from contaminants or surfactants, which may hinder hybridisation events between the target of interest, and the recognition element. Through self-assembly techniques, it is possible to combine both the construction of such an anti-fouling electrode coating, and the positioning of recognition elements to form a bioelectric interface.

1.3.1.1 Alkanethiol Self Assembled Monolayers

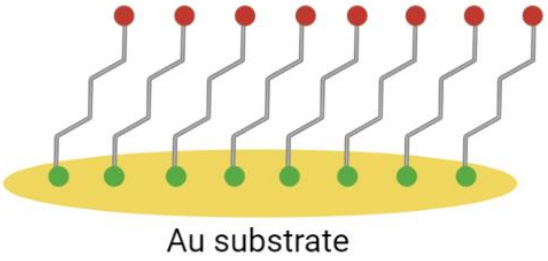

Figure 1.3 Self-Assembled Monolayer Schematic. Here a pristine metal surface (gold) is coated by with a monolayer of thiolated alkanethiols. Molecular attachment is driven by the thiol-gold interaction. Modification of an alkyl chain with a sulphur head group (green) is common practice for the immobilisation of SAMs on planar gold (i.e. Au(111). Terminal group modifications (red) can provide functionality to the monolayer. Intermolecular forces govern the orientation and density of immobilised monolayers

The deposition and adsorption of organic molecules on the surfaces of metals and metal oxides is based on the condition of atoms to seek out lower free energy states.[41] Self-assembled Monolayers provide a method of organic molecule deposition on these interfacial surfaces with adsorption from either, immediate gaseous or liquid phases. For these monolayers to form, an existing affinity must be present between a functional group of an organic compound and the substrate. Numerous bare metal and metal oxide surfaces can be functionalised by self-assembly; including gold, silver, and platinum.[42–46]

In this study, particular focus will be given to the functionalisation of gold. There are multiple advantageous properties to this noble metal that make it particularly well suited to a component of a bioelectric interface. Firstly, gold can be easily manufactured in various forms for transducer surfaces, via physical vapour deposition, sputtering or electro-deposition. Secondly, methodologies for pattering of transducer designs are well developed by multiple approaches, including photolithography, micromachining and chemical etching. Finally, the interaction of thiol and gold is sufficiently strongly to actively strip non-desirable surface adsorbed contaminants, which possess weaker affinity. Organic adsorbents alter many surface properties; including the wettability, reduction of surface atom reactivity, and formation of insulating films to electron transfer. The applications of SAMs in nanotechnology are extensive, spanning electronics manufacturing, printing technologies, and the field of molecular biology and diagnostics.[41,42,47]

Simply, self-assembled monolayers are arrangements of molecules across a solid surface, whereby intermolecular forces drive the positioning of molecules, and spontaneous formation of a layer from a liquid or gas phase. Modification of a probe sequence with an anchoring molecule allows for the immobilisation of the sequence on the underlying substrate. A common example of this throughout the literature, which will feature heavily in this study, is the addition of thiol moieties linked to an end of the probe sequence by a series of Carbon spacers. Thiols are the sulphur analogues of hydroxyl groups, with a sulphur atom in place of oxygen. The general formula for these alkanethiols is ($SH(CH_2)nR$) where (SH) denotes the thiol head group, the variable *n* accounts for the number of methylene subunits (CH_2) which compose the chain length, and R attributing to the functional tail group which terminates the molecule.

The formation of SAM based bioelectric interfaces is a multi-step process, theorised to be driven by distinct adsorption kinetics. With introduction of alkanethiols to the pre-cleaned gold planar surface, the first phenomena to be observed is physisorption. At this stage, a rapid diffusion-controlled deposition of thiolated species forms a highly disorganised system within milliseconds to minutes. The alkanethiol hydrocarbon chains exist in a lying down phase, with a low surface coverage.[48] This stage can be described by the following equation:

$$CH3CH_3(CH_2)nSH + Au \rightarrow (CH_3(CH_2)nSH)physAu \qquad \text{Equation 1.1}$$

Subsequently, covalent bonding between the Sulphur atom in the head region of the thiol and the Au(111) substrate occurs due to shared energetic characteristics:

$$(CH_3(CH_2)nSH)physAu \rightarrow CH_3(CH_2)nS\text{–}Au + \frac{1}{2}H_2 \qquad \text{Equation 1.2}$$

This chemisorption stage may take up to several minutes to occur, with transformation to a thiolate head region due to the release of the mercapto hydrogen atom. Previous research suggests that these hydrogen atoms will react to form free H_2, This was observed by Kankate et al; following scission of the thiol, S-H bond associated with thiolate formation.[49]

A reorganisation stage then follows with the reorientation of the immobilised chains into a "standing-up" phase, driven by increasing Van der Waals interactions. This produces a near vertical orientation on the chain, with a tilt of approximately 30^0 against the underlying substrate (displayed in Figure 1.4). This process is significantly longer than the initial adsorption stage, beginning after the first minutes of immobilisation, and continuing over many hours. Interactions between the immobilised SAM molecules govern the reorganisation in to a dense, continuous coating, with the specific tilt angle being a function of the SAM density.[50,51]

Finally a state of surface saturation will develop over long incubation times where the immobilised alkanethiol chains will form into a well-defined crystalline lattice with a hexagonal notation of $(\sqrt{3} \times \sqrt{3})$ $R30^0$. Each sulphur group that has bound with the Au substrate is positioned at a specific spacing of 5 Å, from its neighbouring sulphur group. This is a distance more than double the diameter of the Van der Waals interaction, and corroborates the theory of immobilised sulphur groups not interacting with one-another through disulphide bonding.[48,52]

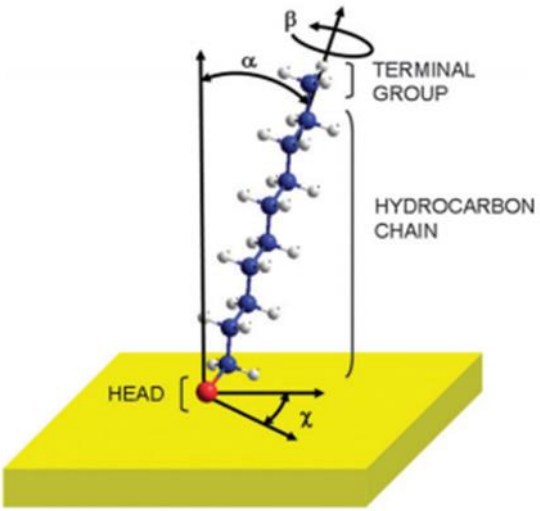

Figure 1.4 Schematic of Decanethiol adsorbed on a gold planar surface in the "standing up" phase. Associated angles include $\alpha = 30^0$, $\beta = 55^0$ and $\chi = 14^0$. Red unit represents a sulphur atom, blue represents carbon atoms and white represents hydrogen atoms.

Adapted from: [47]
Vericat et al; *Chem. Soc. Rev.* **39**, 1805-1834 (2010) doi.org/10.1039/B907301A

However, this hypothesis of secondary chemisorption serving as the dominant force in establishing ordered SAMs has been challenged. The fate of Hydrogen has been difficult to study. Recent works have highlighted the incidence of this bonding being rare between thiol moieties and planar gold Au(111). Specific conditions of high energy uncoordinated gold atoms are required, which do not exist commonly on the substrates. Researchers concluded that physiosorption is the dominant binding characteristic.[53] This interaction is still suitably strong to withstand given potentials commonly applied within electrochemical measurements, and the affinity between Gold atoms and the thiol moieties sufficient to drive migration of probes to the transducer surface for monolayer assembly.

While the specific mechanism of immobilisation (chemisorption or physiosorption) is still subject to further experimental interrogation, the resultant phases of SAM assembly are well documented. As such, it is possible to provide monolayer adsorption isotherms, to model time dependant SAM formation for all phases of assembly. In the initial "lying down" phase, there is a low adsorbent coverage with the rate of SAM growth dependent upon the proportion of available sites for covalent bonding. A derivation of the Langmuir Adsorption Model provides an approximation for detailing SAM growth:

$$\frac{d\theta}{dt} = R(1-\theta) \qquad \text{Equation 1.3}$$

Where θ represents the fraction of the gold surface occupied by an adsorbent, *R* is a rate constant and *t* is the immobilisation time. Derivation of equation 3 enables mathematical modelling of adsorption over time in a SAM:

$$\theta = 1 - e^{-Rt} \qquad \text{Equation 1.4}$$

Principle to the growth of the SAM is the increasing level of Van der Waals interactions between adsorbed alkanethiol strands. It is this principle that evokes the alteration to single molecule adsorption, with strands 'lifting' to a near perpendicular angle with the surfactant. This

phenomenon is not accounted for within the Langmuir derivation. To overcome this limitation, manipulation of the Kisliuk equation (5 and 6) with the introduction of the 'sticking coefficients' term, K_e; allowing for the incorporation of alkanethiol chain length and specific functional groups to the growth model. The term *R'* serves a coefficient documenting the effect of diffusion in SAM growth, and is proportional to the square root of the system's diffusion coefficient.[48]

$$\frac{d\theta}{dt} = R'(1-\theta)(1+K_e\theta) \qquad \text{Equation 1.5}$$

$$\theta = \frac{1-e^{-R'(1+K_e)t}}{1+K_e e^{-R'(1+K_e)t}} \qquad \text{Equation 1.6}$$

Application of the above Langmuir, and modified Kisliuk model provides an effective method of approximating surface coverage for a given SAM with respect to the immersion time employed for monolayer construction.

1.3.1.2 DNA and Alkanethiol mixed SAMs for e-DNA Biosensors

The formation of alkanethiol SAMs described above, allows for the organisation of well-structured monolayers of organic material upon a transducer surface. This composes one aspect of a bioelectric interface for sensors, with the alkanethiol coating providing an anti-fouling coating to further, non-desirable organics. The second key component of biosensor designs is the incorporation of a recognition element specific to a given target.

For electrochemical DNA biosensors (e-DNA sensors), the primary functionality is provided by the inherent and strict affinity unique to nucleic acid basepair binding. Incorporation of a probe DNA sequence, designed to host an element of complementarity to a target, within an alkanethiol SAM allows for the completion of a bioelectric interface. Taking inspiration from alkyl thiols forming spontaneous self-assemblies on gold, thiol terminated DNA probes were investigated in 1997 as part of a mixed monolayer, with the constituent probe capable of

hybridising a complementary target from solution.[24,54] This provided order to the immobilisation of DNA on surfaces, and with it the evolution of a new field.

The inherent negative charge within DNA enables charge-based repulsion of probes from inappropriate interaction and agglomeration, thus managing probe spacing in a monolayer to give a desirable density. However, in disperse DNA SAMs, ion-induced dipole binding interactions between the probe and the gold result in a "lying down" like phase.[55] The development of mixed DNA / alkanethiol monolayers minimises the incidence of such a DNA orientation by their coating of the gold substrate. Consequently, the immobilised probes adopt an orientation, perpendicular to the underlying substrate.

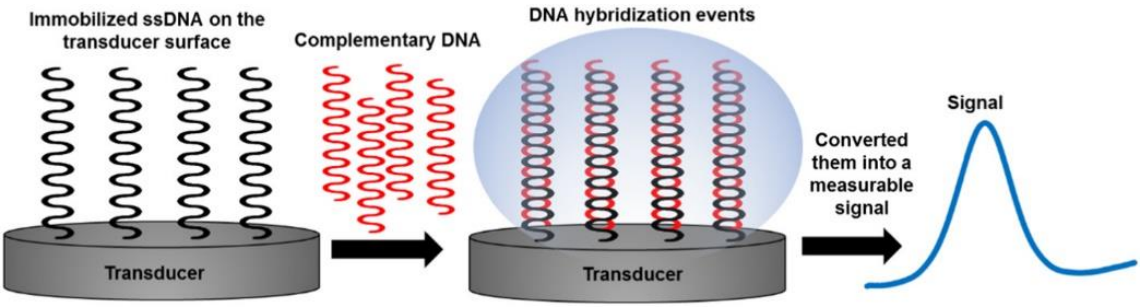

Figure 1.5 Simplified mechanism of action for a DNA Biosensor.

Adapted from: [334]
Rashid & Yusof. *Sensing and Bio-Sensing Res*. **16**, 19-31 (2017) doi.org/10.1016/j.sbsr.2017.09.001

Establishing an optimal density of immobilised DNA probes within a mixed monolayer is crucial in the manufacture of a viable biosensor. Specific attention must be given to a composition with sufficient recognition elements, such that hybridisation events would result in a detectable signal change. However, concern must also be given to determining appropriate conditions where the probe density is sufficient that, the availability of the recognition element to the target is not restricted by steric hindrance or electrostatic repulsion.

e-DNA sensors employ the above strategy of functionalised transducers, coupled with electrochemical interrogation. In a classical design, an electrode (commonly gold) is subject to functionalisation through the self-assembly of a probe DNA / alkanethiol mixed monolayer. This may occur through a co-immobilisation protocol, or through a secondary backfilling method, where the alkanethiol immobilisation occurs after probe DNA. The net result is comparable, with DNA probes interspersed within an alkanethiol passivation layer.[54,55] Modification of an

electrode with a mixed monolayer alters its interfacial properties. This directly contributes to deviations in conductance, and capacitance, both of which can be monitored through electrochemical instrumentation.

Simply, an electrode is modified to host a capture site for a given nucleic acid target by self-assembly. This functionalised electrode can be interrogated to establish a baseline electrochemical characterisation. Capture of a nucleic acid target by the immobilised probe through complementary hybridisation, further alters the interfacial properties of the sensor. This yields a subsequent deviation in electrochemical signal. For example, the hybridisation of a target oligonucleotide to its complementary sequence immobilised within a SAM may lead to the repulsion of a solution based redox mediator from the electrode surface. The schematic in Figure 1.5, outlines the basic principle of an e-DNA biosensor. The accompanying theory detailing the specific electrochemistry inherent to this biosensor design is detailed at length in the Theoretical Concepts of Chapter 2.

1.3.2 Current advances in DNA SAM construction for electrochemical Biosensors

The simple concept presented above has been investigated by numerous groups for more than two decades, with a staggering research output. However, multiple facets of e-DNA biosensor design require detailed investigation to overcome serious roadblocks to a true PoC device. In the following subchapters, distinct issues of e-DNA biosensor design are detailed, along with current solutions reported in the literature.

1. SAM Stability – current problems and proposed solutions.

Issues of varying SAM stability and degradation with time are well documented in the literature, with observations reported in as far back as 1999 by Poirier, with the metal/thiol interface undergoing rearrangement in induce holes in the metal substrate.[56] This is a function of the strength of the gold-thiol bond being sufficient to create highly mobile adatoms across the electrode, which traverse the surface and agglomerate. The consequence of which is the formation of SAM islands, and pits in the gold substrate.[57] This restructuring to regional domains of the transducer, by adatom migration contributes to deviation in electrochemical signal, and

dramatically hinders a sensors performance to monitor analyte detection events. The expectation may be that the exposed gold pits within an otherwise insulating layer, would contribute to localised regions of high conductivity. Consequently, measurements of electrochemical impedance spectroscopy may report a decaying charge transfer resistance with faradaic measurement. However, the complexity of SAM behaviour becomes apparent when literature findings are considered. For example, works by Piper et al; 2021, demonstrated a densification effect, with consecutive electrochemical impedance spectroscopy (EIS) measurements contributing to an increase in charge transfer resistance (R_{CT}) over the first 20 hours of interrogation.[58] This is at odds with conjecture surrounding SAM reorganisation with time resulting in electroactive gold pits. Importantly of concern, is the propensity for time-dependant densification reported in this study, to be misinterpreted as the detection of DNA hybridisation by a SAM based e-DNA biosensor.

Temporal instability in SAMs is not unique to the reporting of Piper and colleagues;[59–62] and is particularly well reviewed by Srisombat, Jamison and Lee, where the authors detailed at length a series of physical parameters influencing the stability of SAMs immobilised on gold. This included the impacts of oxidation, UV irradiation, local pH conditions, and heat and chemical exposure.[63] This review neatly guides the reader in considering a broader, holistic approach to SAM formation, with the development of such monolayers being a highly nuanced process significantly influenced by a range of physical conditions. However, many of the reports in the e-DNA biosensor literature often assume the mechanism of self-assembly for DNA/alkanethiol monolayers to be simple, well defined, and highly consistent, with little acknowledgement for the true transiency of these coatings. This oversight is highlighted by Shaver et al; 2020, with a literature search yielding an increasingly high proportion of research output employing only MCH SAMs for aptamer e-DNA biosensor applications, despite the issues associated with its long term stability. Figure 1.6 below details the prevalence of the assumption that a simple MCH SAM is sufficient to construct a biosensor overleaf:

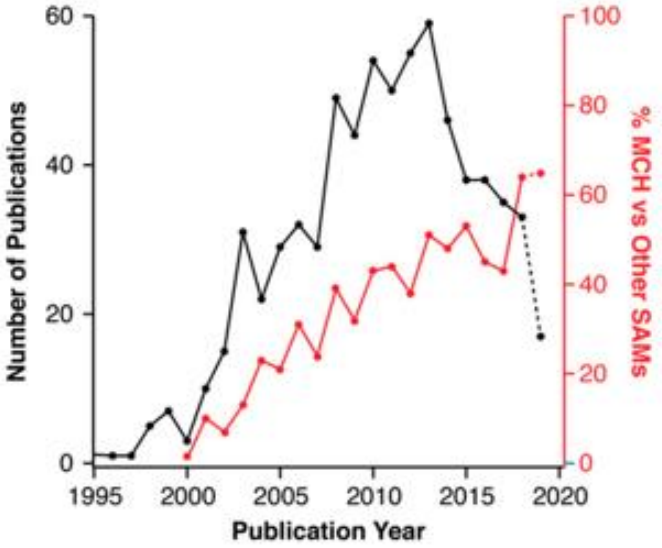

Figure 1.6 Fraction of e-DNA biosensor publications in the literature reporting MCH use as blocking SAMs.

Adapted from: [61]
Shaver et al. *ACS App. Mat. & Int*. **12**, 9, 11214-11223 (2020) 10.1021/acsami.9b22385

It is immediately apparent that the alkanethiol coating prevalent in many of the e-DNA biosensor designs is in crucial need of optimising. This is particularly pertinent as low DNA probe densities are often desirable for achieving strong target hybridisation efficiencies. This will be discussed more in the following sub-chapters of this literature review. A consequence to this is the dominance of the immobilised alkanethiol across large regions of the transducer surface.

In recent years, numerous groups have begun to revisit the importance of the alkanethiol coating of e-DNA biosensors. Specific focus has been given to head group modifications that may improve SAM stability, shelf life of a design, and progress a system towards a PoC device. This is particularly noteworthy, given seminal works by Chidsey and Loiacono in 1990, detailed the benefit of methyl-terminated alkanethiols in producing well-ordered SAMs with strong packing densities and reduced surface defects compared to carboxyl or hydroxyl terminated monolayers.[51] Following on from this observation, there is strong Neutron Reflectometry data highlighting the incidence of water penetration in hydrophilic monolayers that contributes to a time dependant stripping of the coating.[64] Inspired by such findings, Shaver and colleagues reported on a novel aptameric e-DNA biosensor design, with the immobilisation of methyl-terminated alkanethiols in a mixed monolayer, to decrease surface

solubility and wettability of the coating. Consequently, the stability of the sensor to deterioration of the bioelectric interface over long storage times in biofluids, while maintaining a high degree of sensitivity.[47] Further investigations into the optimisation of the end-group modifications of alkanethiol SAMs for e-DNA biosensors have followed. Works by Li et al; provide a comprehensive survey of alkanethiol SAMs engineered to feature non-charge, mono-charge, and zwitterionic moieties. Collating experimental data for each of these moieties allowed for the generation of radar maps, incorporating the performance in terms of wettability, antifouling, stability, and target detection sensitivity and specificity. This is of particular interest as distinct radar maps have been provided for assays in various biological fluids (sweat, urine, whole blood). Thus, a determination can be made for which alkanethiol moiety may suit a given target analyte that an e-DNA biosensor has been assigned.[65]

2. Positioning of Recognition Elements

As mentioned previously, the efficacy of an e-DNA biosensor design is highly dependent upon the availability of the recognition element for target hybridisation. Consequently, establishing an optimum density and spacing of DNA probes within the mixed monolayer is essential. Determining the appropriate functionalisation conditions has been subject to decades of work and focuses on a number of key parameters. Primarily this has related to the mechanism of SAM deposition; with multistep immobilisation (backfilling), or co-immobilisation approaches.[66–69] This has resulted in the development of widely employed electrochemical methods that can enable an estimation of the necessary probe surface coverages that yield optimal hybridisation efficiencies.[70,71] This has led to reports of a desirable probe density (> 2.5 x 10^{12} molecules/cm^2), where the electrostatic repulsion of a solution based redox mediator by the negatively charged probe/target complex is sufficient to modulate charge transfer resistance.[57] A key aspect of developing an appropriate PoC device is the stability of these probe/target hybrids for electroanalysis in varying environmental conditions, particularly in a field setting where temperature variation can be significant. A 2017 report by Macedo and colleagues, investigated the effect of probe-probe distance of the thermal stability of such hybrids by a combination of SPR and XPS measurement. The key findings of which are twofold. Firstly, the stability of the probe/target hybrid increases with either an increase in the distance between the immobilised probes, and/or the ionic strength of the buffer. An optimum profile

sharpness for hybridisation activity, and hybrid stability (melting temperature (T_m)) was noted at a probe coverage of 3.2 x 10^{12} cm^2,[72] which is broadly in accordance with the conclusions derived from electrochemical observations by Keighley et al; 2008.

The low probe coverages that are supportive of strong hybridisation efficiencies generally assume a uniform distribution of the immobilised probe across a mixed monolayer. This fits a consensus in the field, with electrostatic and steric hindrance from tightly packed probes limiting access of target to the recognition elements. However, these coverages derived electrochemical, SPR or XPS interrogation, only provide a gross overall surface density, and do not confirm the specific homo or heterogeneity of the monolayer. This previous assumption of layer uniformity is requiring further consideration, as there is growing evidence of heterogeneous probe densities in DNA/alkanethiol SAMs.[73–75] This is particularly noteworthy as a combination of high-resolution atomic force microscopy and spatial statistical analysis, revealed tightly spaced probes at distances < 10 nm, and observations of heterogeneous spatiotemporal patterns of probe/target hybridisation. Simply, target capture was clustered in regions of dense probe islands.[76]

This result of an enhancement of target binding, aided by tight probe clustering is unexpected, and goes against the current hypothesis of well-spaced probes being critical in allowing target capture. This finding strongly emphasises the complexity of SAM formation, and perhaps presents the idea of a low probe surface coverage resulting in uniform monolayers as being a significant oversimplification. Leung and colleagues have developed this notion further, by the application of parallel in situ fluorescence microscopy with square wave voltammetry to document the incidence of probe DNA cluster formation. Here, either a uniform arrangement of probes across a gold electrode, or tightly clustered probe islands could be reliably formed, depending upon a set (or range of) applied potential(s) during SAM deposition, and the specific ionic conditions of the immobilisation buffer.[77] At a high level, the primary finding is that in order to achieve either of these two conditions (uniform or clustered probe densities) reliably across multiple devices, consideration has to be given the specific deposition conditions.

This neatly introduces an emerging method for mixed alkanethiol/DNA SAMs, driven by electrodeposition.[77–80] While this method offers a degree of control surrounding the positioning of pDNA in a mixed monolayer for improving target hybridisation, a secondary key benefit is the enhancement of thermal stability for the constructed sensor.

Polycrystalline gold is inherently composed of distinct crystallographic regimes, which may serve as a potential source of initiation for thermal desorption of the monolayer. A recent report has detailed the underlying surface crystallography and the density of DNA packing is crucial in establishing thermal stability.[62] Thermally stable sensors were observed only at particularly high DNA coverages for a range of gold crystallography, which may be beyond a threshold level for allowing target hybridisation. Interestingly, potential controlled deposition methods presented by Ma & Bizzotto in 2021, (0.4 V vs Saturated Calomel Electrode (SCE) for one hour) have yielded the ability to produce low total DNA surface coverages, with a high degree of uniformity; which crucially maintain a high degree of thermal stability when compared against a standard functionalisation protocol without any potential control. These DNA SAMs possess a high degree of consistency, with probe spacing that would match the hypothesis of enhanced target hybridisation, and a thermal stability, which is crucial in building a strong shelf life, necessary for a PoC device.[80] However, these improvements were reported with the use of a single-crystal gold bead electrode, which lacks the varying crystallography present in polycrystalline gold electrodes (PGE). SAM formation on Au 111 atomic arrangements were still of poor thermal stability. This therefore presents the specific crystallography composing a working electrode for functionalisation, as a key requirement of future investigation.

Another area of investigation to control the positioning of recognition elements surrounds the use of higher order DNA nanostructures. This may include the development of thiolated-polyhedra, which host a specific series of nucleotides complementary to a given target. Or, larger DNA origami assemblies also capable of being engineered to incorporate a required recognition element. This thesis will feature these two approaches heavily. As such, a detailed review of their history, current applications, and accompanying constraints, will be provided in later in this review.

3. Improving sensitivity

In a literature search of electrochemical DNA biosensors, a researcher will immediately be provided with a great many publications; with titles including, highly sensitive, ultra-sensitive, increased, or enhanced sensitivity. Many of these conclusions are based upon a derived Limit of Detection (LoD) from experimental data analysis, the merits and issues of which is discussed in this thesis. While the sensitivity or minimum amount of analyte a sensor design can readily

discriminate in a given sample is a key design criterion to optimise, many of these research works have often failed to discuss some of the issues of instability and variability reported earlier in this chapter. However, it is undeniable that the purely analytical performance many research groups have managed to achieve, with a variety of signal boosting approaches is outstanding. Some of these approaches are detailed below.

Attempts to enhance sensitivity of e-DNA sensors through the incorporation electroactive labels within the layer itself are now commonplace. Modifications include Ferrocene,[81–84] Methylene Blue,[85–87] melamine-copper ion complex terminated probes,[88] and Tris(bipyridine)ruthenium(II) chloride ($[Ru(bpy)_3]^{2+}$) intercalation for Electrochemiluminesence.[89] Hybridisation of a target oligonucleotide to labelled probe sequences, may introduce new structural properties to the resultant complex, and either limit, or bolster availability of the label to exchange current with the electrode. This may help combat a key issue associated with redox buffer mediated sensing. In the conventional system, current is exchanged between the poised electrode and a redox couple in free solution (commonly Potassium Ferricyanide/Ferrocyanide ($Fe(CN)_6^{(-3/-4)}$). Variations in this current exchange may be induced by the changing ease of access the redox couple has to the electrode surface, via binding induced conformational changes to the immobilised layer, or by electrostatic repulsion between redox species in solution and the negatively charged DNA backbone on the probe. However, this system is complicated by layer stability issues, with transient channels often contributing to current discrepancies. This also by leads to an issue specific to the above redox couple, as recent reporting has described the incidence of CN^- formed through the partial breakdown of the redox couple with successive EIS interrogation. Consequently, free CN^- is available to attack the underlying gold electrode and etch the surface, resulting in an increase in active electrode surface area, and an accompanying signal drift.[90,91] While this a notable concern for biosensor designs with a remit, of consecutive live measurement, the impact of CN^- attack appears to be minimal for single, or low measurement repeats, where incubation times with the $Fe(CN)_6^{(-3/-4)}$ couple are minimal.

Many of the tethering redox couples detailed above exist as modifications to hairpin based DNA probes.[83,92–96] These hairpin structures also offer a key benefit of enhanced specificity, with seminal studies in 1999 by Bonnet and colleagues reporting their inherent ability to be better discriminate targets differing in only one nucleotide to a complementary, than a conventional linear probe.[97] Often a means of minimising the contribution of electrode-to-

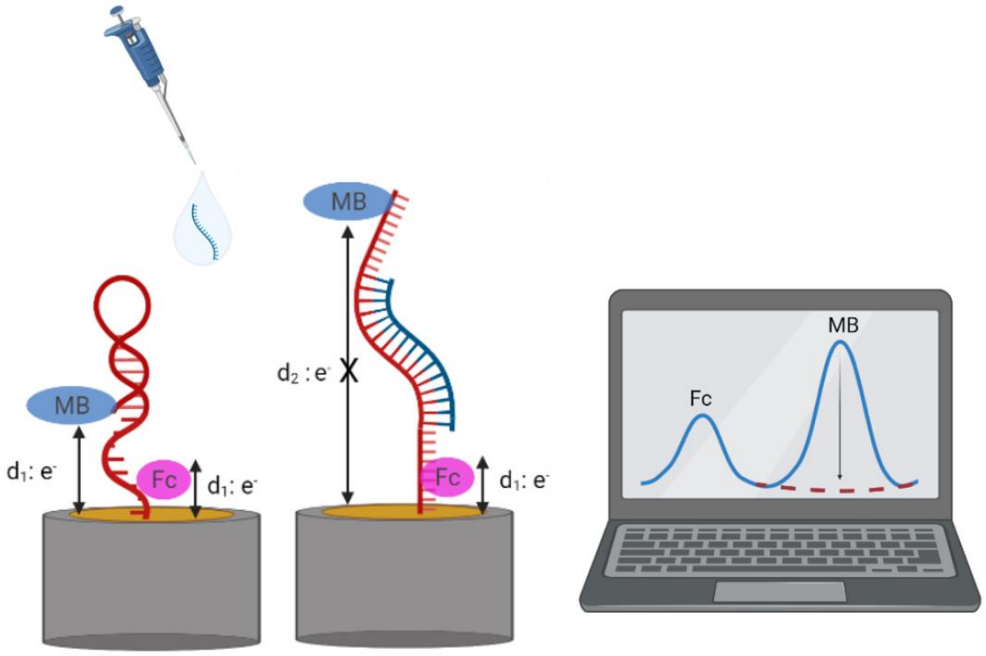

Figure 1.7 Mechanism of action for a conventional ratiometric e-DNA biosensor design. Dual tagging of a hairpin probe allows two peaks to be recorded by voltammetric methods. Addition of a complementary target induces a conformational change to the probe architecture and repositions one tag away from the transducer. This leads to a reduction in electron transfer associated with that tagged species, and a decline in one of the measured peak currents.

electrode variation is to incorporate a secondary redox mediator that provides a signal at a differing potential to the primary reporter. This secondary tag is positioned on the probe to be at a constant distance from the electrode surface, and not influenced by any hybridisation events. This allows for a ratiometric approach to sensing, adding an on device control mechanism to sensing, and enhanced confidence in signal change being attributable to target hybridisation.[85,87,98,99] A schematic for this sensing design is provided in Figure 1.7 However, there are drawbacks to this technique, with the cost of single, and dual labelled oligonucleotides significantly increasing the expenditure of manufacture. With the requirement to label an oligonucleotide with two distinct tags for this ratiometric approach, it is also necessary to consider the distinct properties of each moiety. For example, a systematic study by Kang and colleagues in 2009 reviewed the stability of probe DNA monolayers on gold with the immobilised probe tagged with either the methylene blue or Ferrocene reporter. A percentage of original signal allowed for the determination of stability for each reporter in response to repeated voltammetric scans in HEPES / sodium perchlorate buffer or fetal calf serum, or wet storage in HEPES / sodium perchlorate buffer over multiple days. While the electrochemical response to target hybridisation may be magnified by the Ferrocene moiety, it suffers from a distinct decline

in stability with the Ferrocenium ion being particularly vulnerable to nucleophilic attack, and a subsequent detachment from the probe.[100]

The mechanism of electrochemical interrogation can also influence the performance of redox moieties. This is a detail particularly pertinent to designing an efficient sensor with measurement by SWV. As signal change is derived from binding induced changes to the electron transfer rate of the reporter, the frequency of the potential pulse is critical. Importantly achieving optimal signal gain with specific redox moieties is often dependent on a distinct potential pulse frequency.[101] Therefore, a ratiometric e-DNA biosensor design requires careful consideration of the electrochemical parameters necessary to harness any potential signal enhancement. Many of the redox-label techniques detailed above rely on voltammetric methods of interrogation like SWV, which is a function of a ramping staircase square-wave potential across a specific redox reporter's potential window. While this may be appropriate for the detection of nucleic acid targets, where hybridisation events occur over longer times, other target analytes require sub second resolution of binding. This is particularly pertinent for aptameric biosensors where a given analyte could include biomarkers involved in neurotransmission events. In 2020, Downs and colleagues presented a method of faradaic impedimetric interrogation, measuring the phase shift of current response. Here, electron transfer is governed by analyte binding which induces a conformational change in the immobilised aptamer, and positions a tagged redox reporter proximal to the electrode. With this method, it was possible to observe a significant shift in phase data at a frequency of 158 Hz, in response to target binding, with a sub-second resolution.[102]

While aptameric biosensors are not specifically studied in this thesis, the requirement for optimisation of the electrochemical method specific to their target is worth noting. For any viable PoC device, the electrochemical instrumentation can ultimately contribute substantial cost. It is therefore necessary for any would be designer to consider if their sensor apparatus requires a particular measurement technique or condition which may difficult to miniaturise or engineer at a low cost.

The excellent catalytic activity, substrate specificity, and ability to facilitate increases in the prevalence of redox-active products, and therefore measureable current, positions enzymes as viable signal amplifiers. For this reason, many works have been undertaken investigating the incorporation of enzymes in biosensor designs. Common strategies for enzymatic signal

amplification involve target hybridisation events which induce opening of immobilised hairpins to free access to a probe label necessary for enzymatic action;[103–105] or, the use of restriction endonucleases to power target hybridisation cycling.[106–109] Additionally, isothermal nucleic acid amplification techniques obviate the requirement for thermal cycling to enhance target copy numbers with enzymatic support. Numerous entries in the literature note the heightened performance of e-DNA biosensors employing approaches of Rolling Circle Amplification (RCA),[110,111] Loop-Mediated Isothermal Amplification (LAMP),[112,113] and Recombinase Polymerase Amplification (RPA). [114,115] The following table surmises detection performance for choice reports referenced above:

Isothermal Amplification Technique	Detection Limit
RCA	[110] - 10 cfu/mL [111] - 0.52 aM
LAMP	[112] - 1 fM PCR fragments or 50 ng/mL LAMP products [113] - 1.76×10^{-12} mol L^{-1}
RPA	[114] - 1×10^{-15} M [115] - 1×10^{5} genomic units

Table 1.1 Detection limits for choice publications reporting isothermal nucleic acid amplifications in e-DNA biosensor designs.

While these reports listed above present excellent detection limits, there are drawbacks to these approaches. Shortcomings of high material costs, complicated storage conditions, and multi-step processing challenge their translation in to simple PoC devices for complex environments.[116]

The requirement to greater enhance sensitivity of biosensing applications also often leads to increasing surface complexities, either through functionalisation of secondary structures such as gold nanoparticles,[117–119] or more recently graphene.[120,121] These techniques primarily accomplish sensitivity gain by expanding electroactive surface areas. While these approaches are capable of reaching femtomolar detection limits, sometimes in complex media,[120] issues of large scale manufacturability, and high costs are still to be overcome. This may limit the potential of such sensors to reach the clinical setting. However, there are simpler methods for the controlled expansion of electrode surface areas. Recent developments in heat

shrinking of gold film substrates on silicon wafers provides a means of achieving this aim without the need for further costly surface modifications.[122,123] While this methodology appears promising, devices manufactured by this process are still in the early stage of development and undergoing further optimisation. Another novel method for increasing electrode surface area was presented in 2020 by Movilli and colleagues, with a micropillar-structure gold array electrode. Here, silicon substrates were fabricated by photolithography and deep reactive-ion etching, to yield hexagonal micropillar arrays with a height of 36.7 µm and diameter of 4.0 µm. These substrates where then subject to gold sputtering to complete the device, producing strong conductivity and conformity. However, these microstructures still require modification with poly-L-lysine (PLL) polymers grafted with poly(ethylene glycol) (PEG) units to facilitate a good wettability of the within the micropillar arrays, and sensing performance was only assessed with a multi-step sandwich assay.[124]

Microelectrode sensors (which have enhanced electroanalytical performance and large surface areas when arrayed) are manufactured through microfabrication techniques, allowing for reproducible components, and repeatable, low-cost production. There are indications in the literature to support increased limits of detection of targets for microelectrodes of decreasing size, or when compared against conventional macroelectrode systems.[125,126] These benefits can be further heightened with an interdigitated microelectrode design, particularly with a capacitive measurement.[127] Microelectrodes will feature briefly feature in the experimental sections of this thesis, and as such a more detailed analysis of their electrochemical responses and usages in biosensor designs is provided in the theoretical concepts of Chapter 2.

The remaining sections of this literature review will introduce the field DNA nanotechnology, from its advent through to its current applications. From here, a focus will be given to recent research exploring the use of its key principles for biological applications, including macromolecule delivery, and emerging biosensing designs.

1.4 Higher Order DNA Structures

1.4.1 DNA Nanotechnology as an Emerging Field

DNA is best understood as a biomolecule responsible for the storage and transmission of genetic information in living organisms. Its predictability and programmability is unrivalled in any other synthetic or natural molecule. These characteristics enable DNA when removed from its biological context, to serve as a useful material for the assembly of complex nanostructures. There are numerous emerging applications for assembled DNA nanostructures, including drug delivery, [128–130] biosensing,[131,132] biomimetics,[133–135] and molecular computation.[136,137]

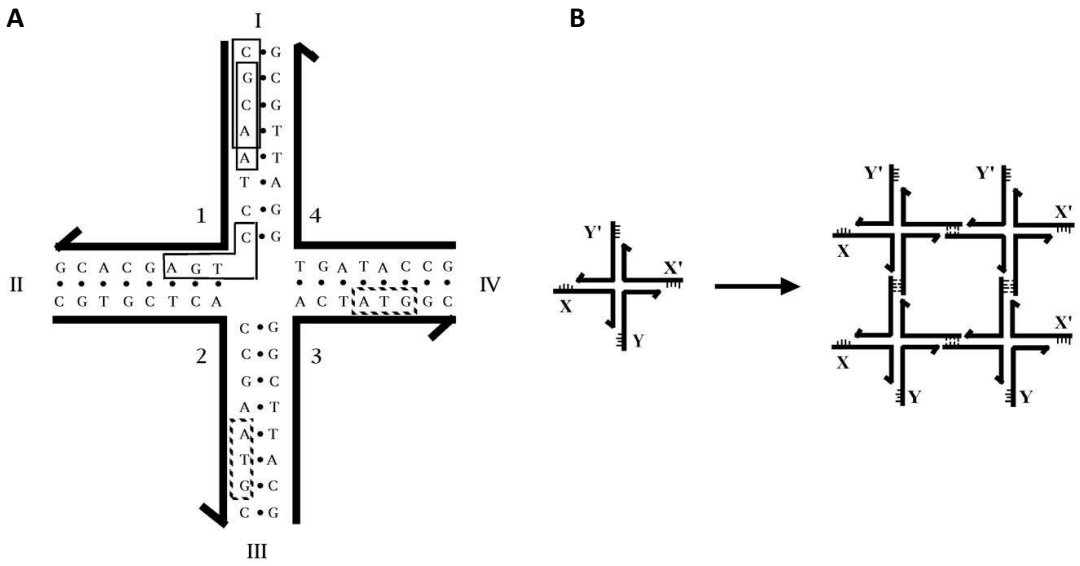

Figure 1.8 Combining Branched Motifs (**A**) Characteristic Structure of a Stable Four Strand DNA Branched Junction. (**B**) Combination of Branched Motifs by Sticky-end Ligation.

Adapted from: [138]
Seeman, N. *Methods in Mol. Bio*, **303**, 143-166 (2005) 10.1385/1-59259-901-X:143

Conventional engineering and manufacturing processes work to a "top-down" principle. Here, a structure, or device is developed, and through successive iterations, is shrunk in size. However, in moving beyond the macroscale and into the nanoscale, feasibility of such an approach becomes increasingly challenging, and costly. DNA nanotechnology makes use of an inverse method of assembly, employing the internal information unique to certain molecules,

to drive the autonomous construction of 2D and 3D geometries. This “bottom-up” method is particularly well suited for nucleic acid assemblies, due to the strictness of binding specificity, and thermodynamic stability of the molecule. [138,139]

In the early 1970s, works by Stanley N Cohen and colleagues, documented the ligation of bacterial plasmid fragments, into viable plasmids for transformation in to E.Coli.[140] This triggered the advent of genetic engineering, but also the first steps towards a new field of DNA Nanotechnology. Initially, this technique enabled lengthy, linear constructs to be formed. However, *in vivo* DNA can transiently exist in branched forms. For example, the unstable four-arm Holliday Junction is found during genetic recombination, in stages of meiotic proliferation.[141] Construction of advanced three-dimensional structures is dependent upon the ability to manufacture stable multi-arm branches.

In 1983, Dr Nadrian Seeman made this leap, in recognising the potential to manipulate DNA sequences to form immobile junctions, rather than linear duplexes. *In vivo* systems, conserved symmetry allows for migration of the junction along the strand.

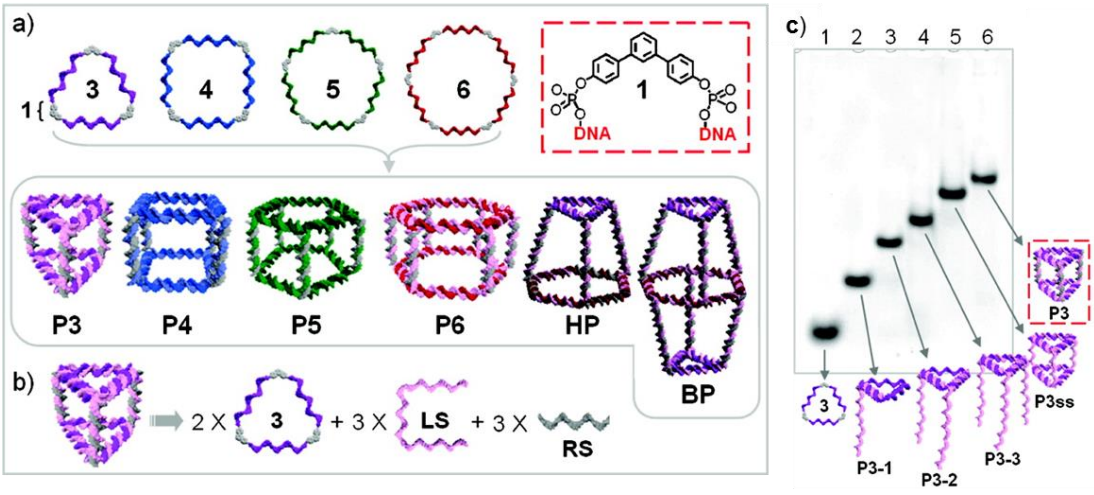

Figure 1.9 Modular Assemblies of DNA Nanostructures through the linkage of distinct 2D Building Blocks (**A**) Component building blocks, and potential 3D Nanostructures. (**B**) Specific components for the assembly of a triangular prims. (**C**) PAGE analysis of 2D triangle (Lane 1) and all intermediates through to assembled triangular prism (Lane 6).

Adapted from: [151]
Aldaye & Sleiman. *Journal of the Am. Chem Soc*, **129**, 44, 13376-13377 (2007)

Seeman noted the possibility to render holiday junctions both stable and immobile by the addition of unpaired bases at the branch points (Figure 1.8). From here, it was possible to

investigate multi arm DNA branched junctions, and determine the necessary sequence constraints to stabilise branches with up to six-way DNA junctions.[142–144] While this may appear as 2D in simplified ladder models, the true helical nature of DNA creates a 3-dimensional structure. It is the creation and addition of stable branch junctions by sticky-end cohesion that have contributed to the successful construction of a range of complex nanostructure geometries including cubic and octahedron assemblies.[145–147] This served as an early proof of concept for the ability to manufacture stable and complex geometries with DNA. However, there was an initial hurdle to overcome. The use of a high number of relatively short oligonucleotides in construction presents an issue of yield due to stoichiometric effects, therefore multiple stages of purification would be necessary.[148] A key breakthrough in the efficiency of DNA nanostructure construction was made in 2004 with *Shih et al* fabricating a nanoscale octahedron from a 1.7 Kilobase single-stranded DNA by (re)denaturation folding techniques.[149] This was followed by Goodman et al; 2005, with a series of four programmable single stranded DNA sequences forming a Tetrahedron in a one-pot assembly method.[150] Both of which offered substantial improvements in nanostructure yield. Modular techniques of assembly followed thereafter in 2007, with Aldaye & Sleiman presenting a novel method to manufacture numerous three-dimensional discrete Nanostructures. Here, a series of 2D single-stranded DNA "building blocks", including triangle, square, pentagon, and hexagon geometries, are assembled into triangular, cubic, pentameric, and hexameric prisms with accompanying linking, and rigidifying strands.[151] A further technique of assembling various polyhedra was developed in 2008, by He and colleagues, using a hierarchical method of construction. With a simple one-pot assembly, DNA binding units centred on three and five-point star motifs can form Tetrahedra, dodecahedra, and Fullerene like structures (60-carbon closed chain structures).[152] The authors had previously identified the use of three and five-point star motifs for the formation of planar 2D crystals, with neighbouring units positioned in opposite directions cancelling out the inherent curvature of DNA tiles.[153,154] The simplicity of their system revolves around two hypothesised phenomena. 1) If all tiles were orientated to face the same direction, their respective curvatures would cancel out to induce a closed structure. 2) There is a concentration-dependant kinetic effect, with high DNA concentrations favouring larger constructs like planar 2D crystals, and lower concentrations of DNA preferring smaller polyhedral assemblies. This would also induce an element of control to polyhedral size based on DNA concentration.

In 2006, a publication by Paul Rothemund, detailed a method of assembly via the use of a long, single-strand "viral scaffold", that is capable of aided folding to produce a predetermined pattern. With supporting staple strands, researchers can design sequences that induce folding into 2D structures of arbitrary complexity, including lettering, maps of the Americas, stars, and a host of other patterns.[148] This is possible with the aid of freely available software to determine necessary staple sequences; meaning almost any arbitrary design is achievable. This method titled 'DNA Origami' has experienced a rapid propulsion in possible applications, and now features in works investigating a diverse range of topics, from super resolution imaging,[155] to drug delivery.[156]

In the near four decades since Dr Nadrian Seeman's recognition of the unique ability DNA possesses to serve as a useful tool in the construction of nanostructures; the field has exploded with multiple bottom-up assembly techniques. The applications for employing DNA as a material are truly vast. In the following sections of this review, particular focus will be assigned to two particular techniques. Firstly, the self-assembly of DNA Tetrahedra (DNA-TDNs), and secondly the construction of nanostructures by a DNA Origami approach. The method of assembly for each, along with their current and possible future applications will be discussed. A particular focus will be given to their current uses in Electrochemical Biosensing.

1.4.2 The DNA Tetrahedron - Development and Method of Assembly

The construction of 3D nanostructures is dependent upon a suitably rigid material to provide necessary stability. DNA serves as an ideal candidate, thanks to its strict and programmable base pairing laws,[139] ease of synthesis, and increasing production scales continues to drive down base pair costs.[157] This specificity of binding, unique to DNA, allows for the construction of tertiary structures like Tetrahedra, with an inherently high degree of mechanical robustness and resistance to deformation.[158] This rigidity can be observed across numerous polyhedra. Polyhedral DNA structures including a cube, and an Octahedron, have previously been documented at length; though both had a requirement for enzymatic control, lengthy synthesis times, and experience issues of low yields. However, the simplicity in Tetrahedra assembly is remarkable. First reported by Goodman and colleagues in a communication in 2004, a one-pot method of assembly was devised, making use of four simple

oligonucleotides of 55 nucleotides in length in equimolar concentrations.[159] Within each oligonucleotide, lies a series of 'subsequences' that allows for the development of triangular vertices. Three regions of 17 nucleotides, designed to minimise the incidence of inappropriate interactions, hybridises with a complement to produce one of six vertices. Each of these regions are separated by a flexible two base pair 'hinge' that is not capable of hybridisation. These hinge regions are Adenine rich, and capable of facilitating an angle of 60^{o} between vertices. In the presence of TEM Buffer (10 mM Tris-HCl, 1 mM EDTA, 20 mM $MgCl_2 \cdot 6H_2O$), the reaction mix is heated via a thermal cycler to 95^{0}C for 2 minutes before being rapidly cooled to holding stage at 4^{0}C. Two possible enantiomers will form, with differing oligonucleotide sequences contributing to distinct vertices.[158] The promise surrounding the use of DNA as a material extends beyond the simplicity of self-assembly. Reports in 2009 by Keum and Bermudez, detailed the resistance of tetrahedral structures with vertices less than 50nm in length, to both specific and non-specific nuclease action.[160] Here, tetrahedra were assembled following the methodology of *Goodman et al; 2006*, with vertices of 20 nucleotides, or approximately 7 nm in length. Within which would lie a single centrally located recognition site for the Type II restriction enzyme DdeI. The assembly was incubated with the specific nuclease DdeI, and the nonspecific DNase I, and native PAGE followed. Subsequent analysis indicated a lack of tetrahedron digestion, compared to linear sequences that contained the DdeI recognition site. Repetition in a media more closely mimicking physiological conditions (10% Fetal Bovine Serum), further improved stability despite serum containing both endo and exonucleases. Assessment of band intensity in the resultant gel indicated the tetrahedron assembly had a 50-fold improvement in decay time against a linear sequence harbouring the same DdeI recognition site. The authors attribute this phenomenon to one or more of a series of possibilities. Firstly, there is the consideration of steric hindrance within this nanostructure that disrupts the effective binding of the enzyme to DNA. Initially, restriction endonucleases bind non-specifically, and with a weak affinity, prior to migration along a sequence.[161] The steric barrier suggested, from either size or geometry, may be sufficient to inhibit the endonuclease activity irrespective of its specific or non-specific mode of action. Secondly, there is evidence of restriction endonucleases distorting the helical structure of DNA prior to cleavage, and mechanically strained DNA-endonuclease complexes providing the necessary transition state intermediates for hydrolysis.[162–164] DNA has been identified as one of the stiffest known polymers with a persistence length of ~ 50 nm (150 bp) dependent upon environmental electrolyte conditions.[165,166] More recent investigations by atomic force

microscopy have detailed persistence lengths of 24 – 40 nm in range, following immobilisation on Mica substrates.[167,168] While this stiffness would be expected in both linear DNA, and assembled nanostructures, the tetrahedron may possess a collective rigidity from opposing vertices, should an enzyme bind with sufficient force to induce an arc length distortion to one of the constituent vertices.

The advantageous mechanical properties, inherent biocompatibility, and highly programmable nature of DNA nanostructure assemblies, presents a valuable tool for numerous biomedical applications. Two of which, that feature most heavily in the literature are, the use of DNA tetrahedra in drug delivery and targeted therapy, and in biosensing.

1.4.3 *Advances in DNA Tetrahedra Applications; Drug Delivery and Biosensing*

1.4.3.1 Drug Delivery

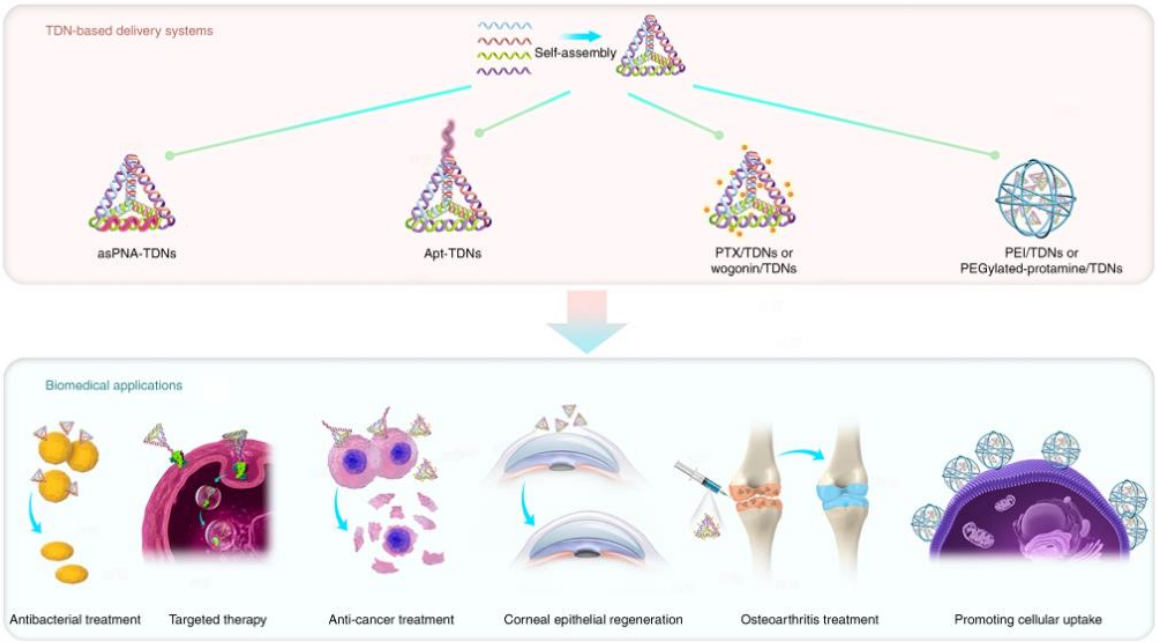

Figure 1.10 Modification of DNA Tetrahedra for the Targeted Delivery of Therapeutics. (**Top Tile**) Modifications include the introduction of antisense peptide nucleic acids (asPNA-TDNs) within a vertex, Aptamer inclusion within a vertex for target binding (Apt-TDNs), incubation with small molecular weight therapeutics i.e. Paclitaxel and Wogonin (PTX/TDNs & Wogonin TNDs), and available Tetrahedra coatings i.e. PEGylated-protamine TDNs. (**Bottom Tile**) Current applications of modified Tetrahedra.

Adapted from:[176]
Zhang et al. *Nature Protocols*. **15**, 8, 2728-2757 (2020) 10.1038/s41596-020-0355-z

Following the works of *Goodman et al*; in documenting a novel and elegant method of simple Tetrahedra Assembly in 2006, numerous researchers gained an interest in the possibility of loading such structures with therapeutics for targeted delivery. However, it was not until 2011, that the first evidence showed these assemblies could readily enter the cytoplasm of mammalian cells while marinating structural confirmation.[169] Very shortly after, Li et al; 2011, reported on the ability to append unmethylated CpG motifs to a tetrahedron nanostructure, which was capable of non-invasive entry to macrophage-like RAW264.7 cells, without requiring the use of transfection agents, and maintaining stability for ~ 8 hours. Upon entry the CpG motifs bind TLR_9 receptors and resulted in inducing production of (TNF)-α, IL-6, and IL-12.[170] In building upon this concept of readily modifying tetrahedra to accommodate various therapeutics, a range of functionalities is achieved. These include, the intercalation of Doxorubicin into such nanostructures for potential cancer therapies,[129,130,171] formation of small interfering RNA (siRNAs) overhangs for gene silencing applications,[172] and the intercalation of photosensitizers, (Methylene Blue and Pyro) to tetrahedra to serve as a transport vehicle for targeted photodynamic therapy.[173,174]

Finally, a recent report by Xue and colleagues in 2019 detailed a novel method for complexing DNA tetrahedra into a larger carrier. Here, each tetrahedron contained a single stranded tail extension from all vertices, with complementarity to specific sequences of a small interfering RNA (siRNA) which allowed for the effective cross-linking of many tetrahedra. This allowed for a mechanism of siRNA delivery and transfection into cells, with an ability to utilise RNase H for mediated cleavage of the functional siRNA within the cell. This study offered strong performance in the delivery of a functional siRNA for the knock down of target gene expression without further transfection agents where toxicity is of concern.[175]

While the above research highlights the promise simple tetrahedral constructs hold for use in targeted therapy, there are still a number of outstanding questions that require attention. The effective yield of functionalised tetrahedra following self-assembly is high; however, the long-term stability, and necessary conditions to sustain such nano-transporters has yet to be fully explored.[176] Another concern surrounds the use of an informational molecule (DNA) as a construct. Simply, will the sequences (currently generated randomly) that compose the oligonucleotides in the construct, have an effect on cellular nucleic acids? To date, there is no evidence in the literature to suggest an interaction between the scaffold DNA and genomic

DNA/RNA; however, this may require future consideration and specific design of oligonucleotide sequences to minimise this incidence. Lastly, the target tissue/site of delivery may require the further customisations to these nanostructures to ensure they are capable of passing particular barriers that may be specific to their destination. Equally, this may impact the route of administration. Currently, there are a lack of design principles to determine the appropriate nanostructure morphology necessary for various routes of administration.[128]

1.4.3.2 Biosensing

In considering the impact of surface crowding and steric hindrance associated with immobilised linear probes on electrode surfaces, Pei et al; were first to take inspiration from the seminal works of Goodman in 2005, and incorporate a DNA tetrahedron for a biosensing application. The hypothesised enhancement in sensor performance was centred around the notion of an assembled nanostructure when immobilised on an electrode, positioning a target recognition element at improved spatial intervals, and thus minimise any potential impacts of probe surface overcrowding. To investigate such a theory, the researchers designed a tetrahedron assembly comprised of three equal length sequences, each with a thiol modification to the 5', and a fourth longer sequence harbouring the recognition element. Following a thermal cycling protocol outlined by Goodman five years prior, the assembled nanostructure can then be immobilised on a gold substrate through the thiol-Au linkages at the bottom three vertices of the tetrahedron. This positions the single stranded extension from the top vertice perpendicular to electrode and allows for heightened accessibility of the recognition element for target hybridisation.[177] Electrochemical signal generation for this initial system was dependent upon enzyme-catalysed electroreduction of H_2O_2, and the sensor construction is outlined in Figure 1.11 overleaf.

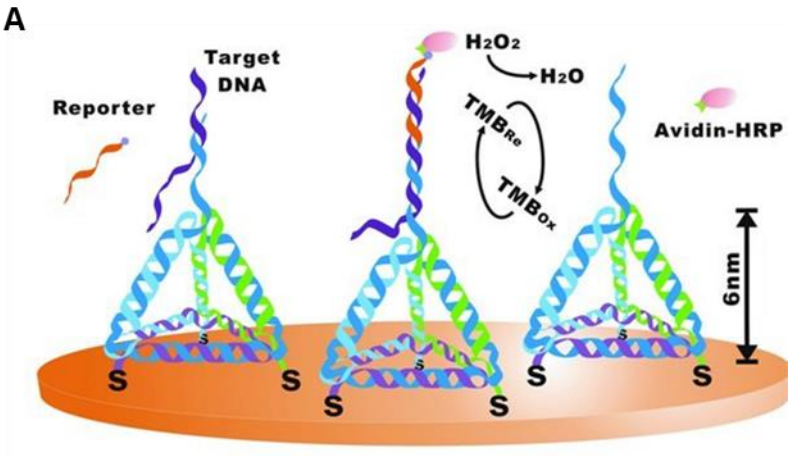

Figure 1.11 Initial workings of a tetrahedral DNA biosensor. Here, four complementary oligonucleotides at equimolar concentrations self-assemble into a three-dimensional structure. The construct is immobilised on to a gold transducer through thiol modifications to three of the constituent oligonucleotides. The top pendent extension shares complementarity to target nucleic acid. A secondary labelled reporter ssDNA oligonucleotide is then hybridised to the captured target and allow for enzymatic signal generation.

Adapted from: [131]
Pei et al. *Advanced Materials*, **22**, 42, 4754-4758 (2010) 10.1002/adma.201002767

Introduction of a biotin labelled reporter sequence binds free complementary nucleotides within the target/recognition element complex. This provides a means of capturing avidin-HRP for the resultant electro-reduction of H_2O_2 with an electroactive co-substrate TMB. This design was sufficient to discriminate single nucleotide polymorphisms through interrogation with a panel of non-complementary targets and presented a promising proof of concept for the feasibility of a DNA tetrahedron platform in nucleic acid sensing. This system was also manipulated to incorporate a free aptamer pendent specific to a host of target large analytes, where enhanced spatial intervals between the capture sites presented an improvement in molecular recognition.[177–179]

The tetrahedral biosensor design has been further optimised in the decade since its inception, with multiple entries in the literature reporting strong analytical performance. Some choice developments include the addition of hybridisation chain reaction (HCR) amplification to a tetrahedral nanostructured transducer achieving detection limits for DNA at sub-fM concentrations,[180,181] duplex-specific nuclease (DSN) assisted target recycling for signal amplification,[182] and the development of a panel of tetrahedral nanostructures for the simultaneous detection of multiple microRNA biomarkers for pancreatic carcinoma.[183]

While the quoted limits of detection, and broad working ranges of the above nucleic acid sensors is outstanding, the signal amplification processes required to achieve such performance is not simple. Enzymatic support, multi-stage chemical reactions, and often costly and unstable reagents, limits the feasibility of such designs to be readily translated to point of care diagnostics which may operate in challenging environments. For this reason, facile, and reagent-minimal sensing technologies are crucial. This does not rule out tetrahedral platforms for further experimentation in attempting to achieve this goal. Multiple research groups have investigated application of tetrahedral biosensing platforms capable of monitoring target hybridisation events at clinically relevant concentrations in complex biofluids. These approaches often employ the use of an electroactive redox tag to a particular domain in the nanostructure, which serves to electrochemical signal mediation. With target hybridisation, a conformational change to a particular domain is sufficient to enhance or supress electron transfer, by manipulating the position of the redox tag with respect to the underlying transducer. One such simple application of this labelled tetrahedron biosensing strategy is that reported by Liu and colleagues in 2015, where the top vertice single stranded extension of a tetrahedron is engineered to facilitate a hairpin confirmation. This hairpin structure is tagged with a Ferrocene label, which is held at a sufficient distance from the underlying transducer to minimise electron transfer events. Introduction of a target oligonucleotide to the sensor results in hybridisation between target and the recognition element, which is hosted in both the stem and loop regions of the hairpin. Target hybridisation is favourable against a hairpin confirmation as full complementarity exists between target and recognition element, and thus the hairpinconfirmation fails, resulting a long flexible pendant extension. This allows the Ferrocene tag to approach the transducer and facilitate electron transfer events, and “signal on” readout.[184] In 2020, Wang and colleagues reported a novel method of labelled DNA tetrahedral biosensing by harnessing the instability of partially assembled tetrahedrons as the mechanism for signal acquisition. Here, the team engineered a nanostructure where one chosen vertice would serve as the recognition element, as opposed to an extension from the top vertice. To do so, one of the four constituent oligonucleotides is of approximately half the sequence length of its neighbouring strands. This produces a nanostructure where one of the vertices remains single stranded. Incorporating principles of proximity ligation assays, a supportive probe sequence with a Ferrocene tag is supplemented along with a target nucleic acid of interest. In this situation, the tagged probe is guided into a favourable position on the vertice with its

hybridisation localising the Fc tag proximal to the transducer, and thus generating a stable and repeatable electrochemical readout. However, in the absence of the correct target, the only partial complementarity between the tagged probe and the single stranded vertice prevents the formation of favourable hybridisation, and a weak and unstable electrochemical signal.[185] These two distinct mechanisms for employing a redox label in a DNA tetrahedron biosensing system are surmised in Figure 1.12 (**A**) + (**B**)

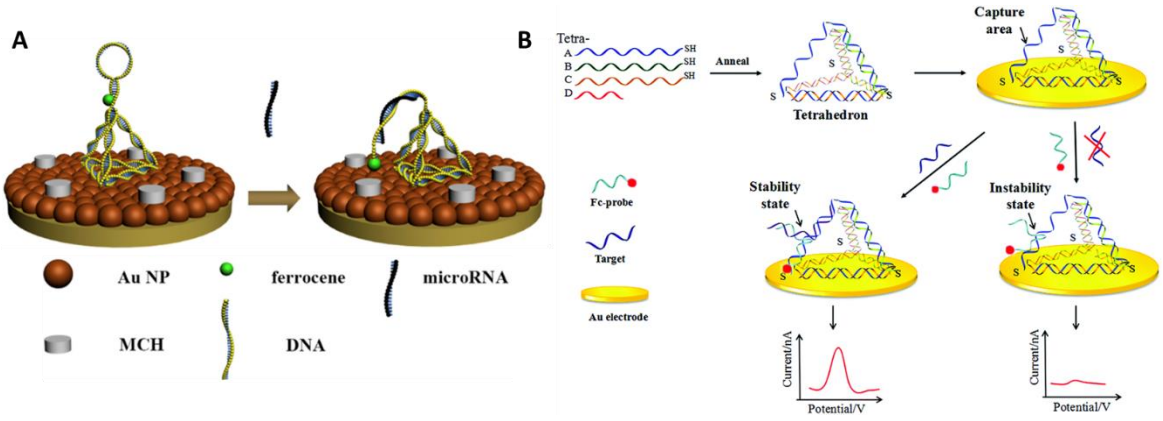

Figure 1.12 Enzyme-free DNA tetrahedron e-DNA biosensors. (**A**) DNA TDNs harbouring a top hairpin extension, labelled with a Ferrocene tag at its 3'. Hybridisation of target induces a conformational change of the hairpin to produce a linear, flexible extension. This repositions the Fc tag in close proximity to the underlying electrode to drive electrochemical signal. (**B**) Harnessing the stability of assembled tetrahedra for e-DNA biosensor assay development. Hybridisation of complementary target allows for the appropriate and stable positioning of a critical Fc-tagged probe within the assembly.

(**A**) Adapted from: [185]
Liu et al. *Biosensors & Bioelectronics*, **71**, 57-61 (2015) 10.1016/J.BIOS.2015.04.006
(**B**) Adapted from: [186]
Wang et al. *Analyst*, **145**, 1, 150-156 (2020) 10.1039/C9AN01897B

In the classical DNA biosensor system, electrochemical signal change is often associated with a deviation in the electron transfer rate of a chosen redox mediator, or through changing interfacial properties of the electrode/solution interface. Short oligonucleotide hybridisation events are sufficient to a produce a signal change that can be readily observed by electrochemical methods.

Here, the hybridisation of complementary target has been shown to be sufficient in manipulating either of the above electrochemical characteristics. In the race to further reduce the limit of detection for nucleic acids in e-DNA biosensors, an ever-increasing system

complexity is prevalent in the literature. Perhaps overlooked is the potential in using the programmability of DNA to design facile nanostructures. One can easily make the leap from an electrochemical signal change with a ~20 nt oligonucleotide hybridisation event, to the possibility of a significantly amplified signal change should a larger DNA construct be co-hybridised with a target. This could be considered analogous to the use of nanoparticle tags that manipulate electrochemical behaviour with a target hybridisation. This is a hypothesis which will feature later in the experimental Chapter 5, where DNA tetrahedrons are employed as signal amplifiers within sandwich assay design. There is little evidence in the literature of tetrahedra being employed as signal amplifiers. However, one study from 2015 does attempt this, though relies on enzymatic support to generate electrochemical signal.[186] In this particular example, a tetrahedron is first immobilised on a gold electrode though thiol modifications to three of its constituent oligonucleotides. The top ssDNA extension shares complementarity to a lengthy target oligonucleotide. The resulting target overhang can then capture a secondary avidin HRP labelled tetrahedron from solution. Such a sensor design has been demonstrated to achieve a detection limit of 1 fM with strong target sequence stringency. However the necessity for labelling and enzyme requirements, ignore the potential for harnessing the physical properties of a tetrahedral nanostructure as the mechanism for signal amplification. The hypothesis introduced above provides a simple, and cost effective potential solution to enhancing sensing power without the additional complexity of the assay detailed in [186].

1.5 DNA Origami

1.5.1 Emergence of a new field

DNA is widely understood for its biological role as an information repository, specifically for the encoding of proteins and control of their expression. The predictability of interaction between two or more single stranded DNA molecules is particularly straightforward thanks to the stringent specificity of binding unique to nucleic acids. The understanding of how DNA strands may hybridise in accordance to Watson-Crick base pairing rules was explored and investigated in great depth for the near 30-year period following the resolution of double stranded DNA structure. However, it was not until the seminal works of Dr Nadrian Seeman presented in 1982 that the leap was made to realise the potential of DNA as a highly programmable building material for the construction of nanostructures.[187] Much of the work of the following twenty-four years centred on Seeman's innovation in the employment of binding specificity, DNA junctions and lattice assemblies for the formation of DNA crystals. That is until an explosion in the field of DNA nanotechnology with the advent of a 2D DNA origami method envisioned by Dr Paul Rothemund in 2006.[188] The central aspect of this technique lies in the adoption of base pair specificity to programme a long single stranded DNA scaffold to fold into a desirable nanostructure confirmation. This is accomplished by the addition of many predefined short oligonucleotides, or staples, which help drive the formation of a given structure. Each hybridisation event between scaffold and staple, manipulates the scaffold to form a specific geometry, culminating in a fully hybridised, rigid structure secured by many repeating DNA crossovers. This method is surmised in Figure 1.13 (**a** – **c**). Aided by the simplicity and elegance of assembly, and the ability to manufacture specific oligonucleotides by modern synthesis methods with ever declining cost, the origami approach is feasible to researchers who seek to explore its potential in wide spread of applications.

A conventional method for DNA origami assembly begins with the selection of a long ssDNA scaffold. Commonly this is the genome of the bacteriophage M13mp18, or a close variant. This material at 7,249 nucleotides in length can then be folded into its desired geometry with a series of unique staple strands, with sequence design generated with the aid of specialised software.[189,190] All oligonucleotides are diluted in a folding buffer comprised of a 1× TAE and a supporting ion such as Mg^{2+} in the range of 5-20 mM, to screen the negative charges of the

phosphate backbones and prevent the incidence of electrostatic effects hindering densely packed constructs.[189] This reaction mix is then subject to a thermal annealing protocol, with a steady slow cooling occurring from a denaturing temperature (95 ^{0}C) to room temperature.

This process can be readily undertaken in laboratories working in various fields in biology, with the primary instrumentation required being a thermal cycler with a good degree of control for the slow cooling of the reaction mixture. Such a piece of instrumentation is common to many laboratories with PCR capability. The primary barrier to entry facing the DNA origami technique lies in the ability to correctly design a desired structure with the required software. Thankfully, useful guides and tutorials now exist to guide a novice in the early stage of their learning.[191,192]

The application of lattice-based DNA origami can allow for the development of two-dimensional and three-dimensional structures. The former is a method of linking dsDNA helices to form flat sheets, with a predefined pattern. 3D structures can be resolved by the arrangement of dsDNA helices into lattices with crossovers forming a structural growth to a honeycomb, square, or hexagonal geometry, and again is surmised in Figure 1.13(**d** – **g**). This has led to the development of ever-greater structural complexity, and the introduction of functionalities to these assemblies. For instance, with high programmability of resultant DNA origami structures, they can serve as key platforms for positioning and patterning at a molecular scale. For this reason, origamis have played a central role in control of chemical reactions,[193–195] formation of tuneable plasmonics systems,[196,197] and incorporation as nanorulers for super resolution imaging.[198] However, the application of DNA origami technology is not limited to positioning techniques alone. Constructs can be designed in such a way, such that in response to particular stimulus they can undertake a rotational or translational movement. These dynamic structures in effect have various confirmations that can be adopted to serve a particular functionality. The stimulus responsible for manipulating the specific confirmation of an origami structures can generally be attributed to one of three categories. Firstly, DNA-DNA interactions including, but not limited to, strand displacement.[199–201] Secondly, mediations to confirmation by molecular interactions.[202–204] Thirdly, physical stimuli including light, pH, temperature and electromagnetic fields.[205–209] Some key publications of DNA origami structures used for positioning applications, drug and enzyme delivery, stimuli responsive nanodevices, and current biosensing applications will follow.

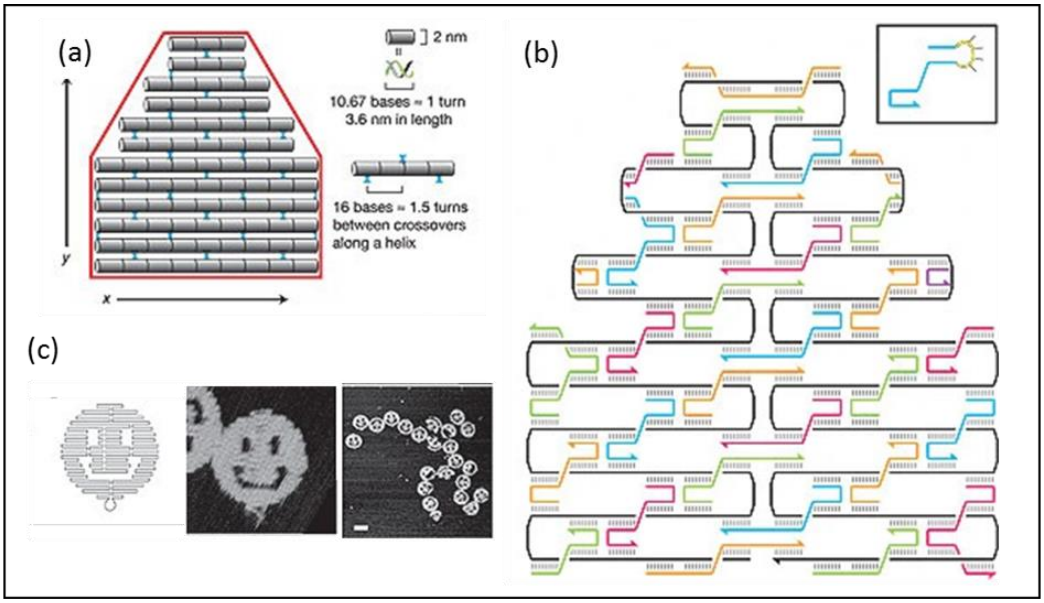

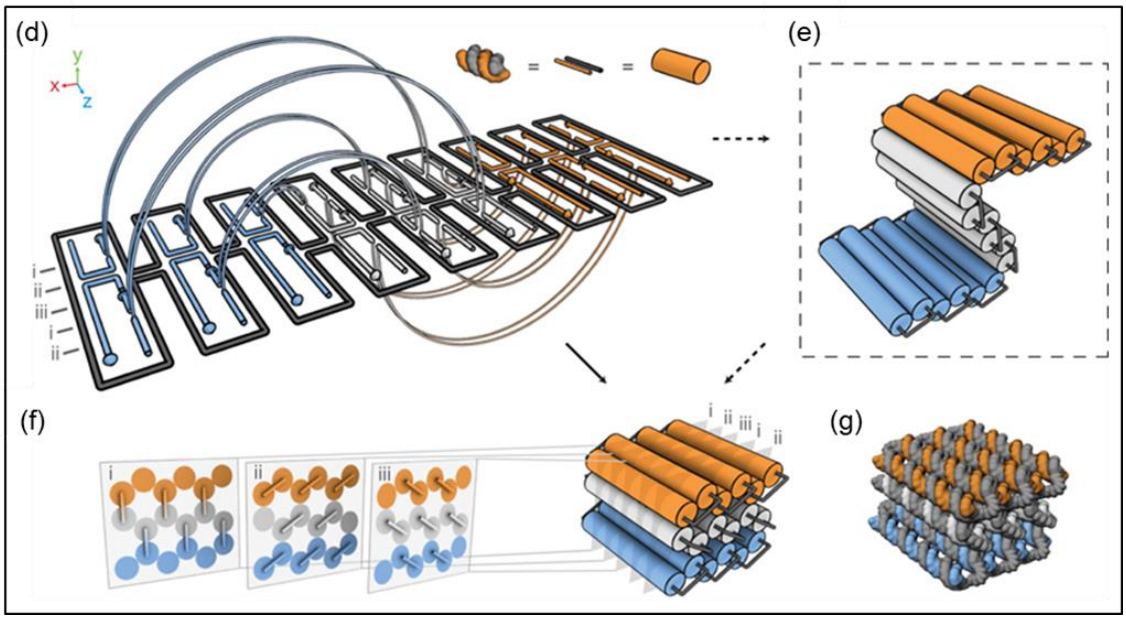

Figure 1.13 Design of two-dimensional and three-dimensional DNA Origami. (**a**) Initial design principles developed by Paul Rothemund in 2006 for the DNA origami method. Here, a desired shape is outlined by the red lines. This shape is approximated by parallel double helices which are joined by a series of periodic crossover points (blue). (**b**) The scaffold strand runs through every helix and forms desired crossovers, while a series of staple stands pull different regions of the scaffold strand to induce a desired geometry. (**c**) Folding path for a "smiley face" design and accompanying AFM images of the assembled 2D structure. White scale bar: 100 nm. (**d**) Principle of folding 2D DNA origami lattice into a 3D construct, where scaffold strand double helices and staples run in parallel to the z-axis. Phosphate linkages induce crossovers between adjacent helices, and the semicircular arcs show staple crossovers between different layers. (**e**) An intermediary cylindrical model of a "half-rolled" structure, and (**f**) the cylindrical model of the complete structure. (**g**) Atomistic model of the complete structural assembly.

(**a**-**c**) Adapted from: [148]
P Rothemund. *Nature* **440,** 297–302 (2006) doi.org/10.1038/nature04586
(**d**-**g**) Adapted from: [189]
SM Douglas et al. *Nature* **459**, 414-418 (2009) doi:10.1038/nature08016

1.5.2 Control of molecular scale positioning by DNA origami

Metallic nanostructures are key components of many advanced analytical techniques in part due to their unique optical properties. These properties form the basis of multiple analytical processes including surface plasmon resonance (SPR), surface-enhanced Raman scattering (SERS), surface enhanced infrared adsorption (SEIRA) and metal enhanced fluorescence (MEF).[210] All of which have been employed with biosensing applications. However, current methods of fabrication of metallic nanostructures limit their reach in forming the necessarily small and complex arrangements required in certain future technologies. To overcome this issue, the introduction of the programmable self-assembly of DNA origami allows for the fabrication of highly customisable structures capable of guiding the positioning of nanoparticles to produce desirable metallic nanostructures of impressive resolution.[196,211,212] The ability of DNA origami to translate its inherent spatial information for guiding the positioning of material to fit a desired purpose is not limited to metallic nanoparticles. This is of particular pertinence when one considers the necessity to understand the impact of relative positioning, stoichiometry, and chirality in protein-protein interactions. Again, the programmability of DNA origami templates and the ease in their functionalisation allows for sensitive control of distinct protein arrangements for study.[213–217]

1.5.3 DNA origami for macromolecular delivery

Published in Nature in 2009, a seminal report by Anderson in colleagues reported on the development of a 3D DNA box through an origami assembly. Crucially this addressable DNA box possesses functionality in that it can be opened through a hinged “lid” region by externally supplied DNA keys.[199] Inspired by this report, many researchers have considered the potential of such a nanostructure to carry molecular payloads for specific cell targeting. First to explore this potential was Douglas and colleagues in 2012, with the development a 3D DNA nanorobot by an origami method. This structure was designed in the form of a hexagonal barrel of 35 nm x 35 nm x 45 nm in dimensions, with two distinct domains. These two domains are covalently linked through single stranded scaffold hinges at the rear of the structure. The front of the structure contains two distinct staples that are modified with DNA aptamer-based locks. This

locking mechanism hosts a DNA aptamer, a partially complementary sequence. This lock can be destabilised, and the structure opened, by the binding of a target analyte key by the aptamer. Furthermore, this nanorobot structure was engineered to host a number of molecular payloads, including gold nanoparticles, and various Fab' antibody fragments.[218] This theory of employing DNA origami nanostructures as potential carriers for the targeted delivery of molecular payloads or therapeutic agents has been advanced significantly in the decade since the report of Douglas and colleagues.

In 2014, a key publication from Zhang et al, documented the potential for simple DNA origami constructs to accommodate the targeted delivery of Doxorubicin (DOX) to breast tumours in mice with a high rate of accumulation, strong antitumor efficacy, and an absence of observable systemic toxicity. Triangular origami nanostructures of 120 nm in length were loaded with DOX through intercalation to establish clinically relevant concentrations for intravenous tail injection. Efficacy of drug action was concluded through a reduction of fluorescence signal with associated with green fluorescence protein labelled breast tumor cells *in vivo*, and tumor volume, with the first reductions observed within 3 days. The specific localisation of doxorubicin could be monitored by its own red fluorescence emission when tumour tissue was excised. DOX was observed with a significant accumulation in the immediate tumour vasculature. The authors concluded that the DNA origami carrier benefited from enhanced permeability and retention effects which nanoparticle-based drug delivery systems experience, contributing to the passive accumulation of the structures in the immediate environment of the tumor mass. Lactic acid generation from hypoxia and acidic intracellular organelles within tumour tissue contributes to a substantial reduction in the local pH, and hindering of DOX intercalation within the structure. Consequently, the drug release appears local only to these particularly acidic regions in vivo.[219]

Advances in the development of origami driven delivery of target molecules have continued to follow. In 2014, taking inspiration from enveloped virus particles, Perrault and Shih developed a novel method of mimicking the geometry of a viral protein capsid shell with a wireframe DNA nano-octahedron by self-assembly. Here, the nanostructure was engineered to confer protection against nuclease digestion *in vivo* by PEGylated lipid bilayers, leading to an improved pharmacokinetic bioavailabity by a factor of 17, and a two order of magnitude decrease in immune activation.[220] This served as a valuable proof of concept in the ability to enhance the viability of origami nanostructures for therapeutic delivery applications, with many possible biomedical applications now opened with the integration of further functionalities.

In 2018, an entry in Nature, noted the capability of DNA nanoscale robots constructed from DNA origami methods to be further engineered for the autonomous delivery of payloads to a specific cellular target. Here, a tubular DNA construct was assembled to encase thrombin molecules for delivery to tumor-associated endothelial cells. This assembly begins with a simple rectangular origami sheet, with programmed poly-A staple sequences at predetermined domains. Thrombin molecules conjugated with poly-T oligonucleotides were then allowed to hybridise with the origami sheet. A series of nucleolin aptamer fastener strands hybridised to opposing lengths of the sheet induce a folding event along a defined seam to non-covalently close the structure. The nucleolin aptamer has two distinct roles. Firstly, it forms the targeting domain of the structure, through its binding affinity to the nucleolin protein, which is specifically expressed on the outside of tumor associated endothelial cells. Secondly, it is the molecular trigger for opening of the tubular construct and exposing the thrombin payload. In animal models, the authors were able to demonstrate the targeted delivery of thrombin to tumor associated blood vessels via the DNA nanorobot carrier, and induce significant intravascular thrombosis, cessation of tumor growth, and ultimately tumor necrosis.[221] In the years since, the continued study of DNA origami nanorobots for drug delivery has expanded to a range of therapeutics, with advances in the field well detailed by a series of strong reviews.[222,223]

Recently a publication in Angewandte Chemie reported on a novel application of DNA origami driven delivery of macromolecules. Here, Mela and colleagues developed a 2D origami tile, hosted five distinct well regions. Within each well are two single stranded staple oligonucleotide extensions, modified with biotin. This allows for the incorporation of streptavidin to each well, and the subsequent positioning of a biotinylated lysozyme within the larger tile structure. Fourteen aptamers are positioned by hybridisation with staple strands surrounding each side of the tile, and allow the attachment of the structure to a bacterial target. Specific aptamers were developed to allow the tethering of the enzyme-carrying tile to either gram-positive or gram-negative bacteria, including *B.subtilis* and *E.coli* respectively. A final modification to the design was made to incorporate four fluorophore molecules (Alexa 647) into the structure, to facilitate the detection of the nanostructures in culture. Structured illumination microscopy detailed the binding of the nanostructure to both *E.coli* and *B.subtilis*, with two distinct control experiments (no aptamer extensions from the tile, or incubation with *L.lactis*, which shares no affinity to the tile aptamers). The schematic provided in Figure 1.14 (**a**) provides an overview to the engineered antimicrobial carrier, with associated experimental growth

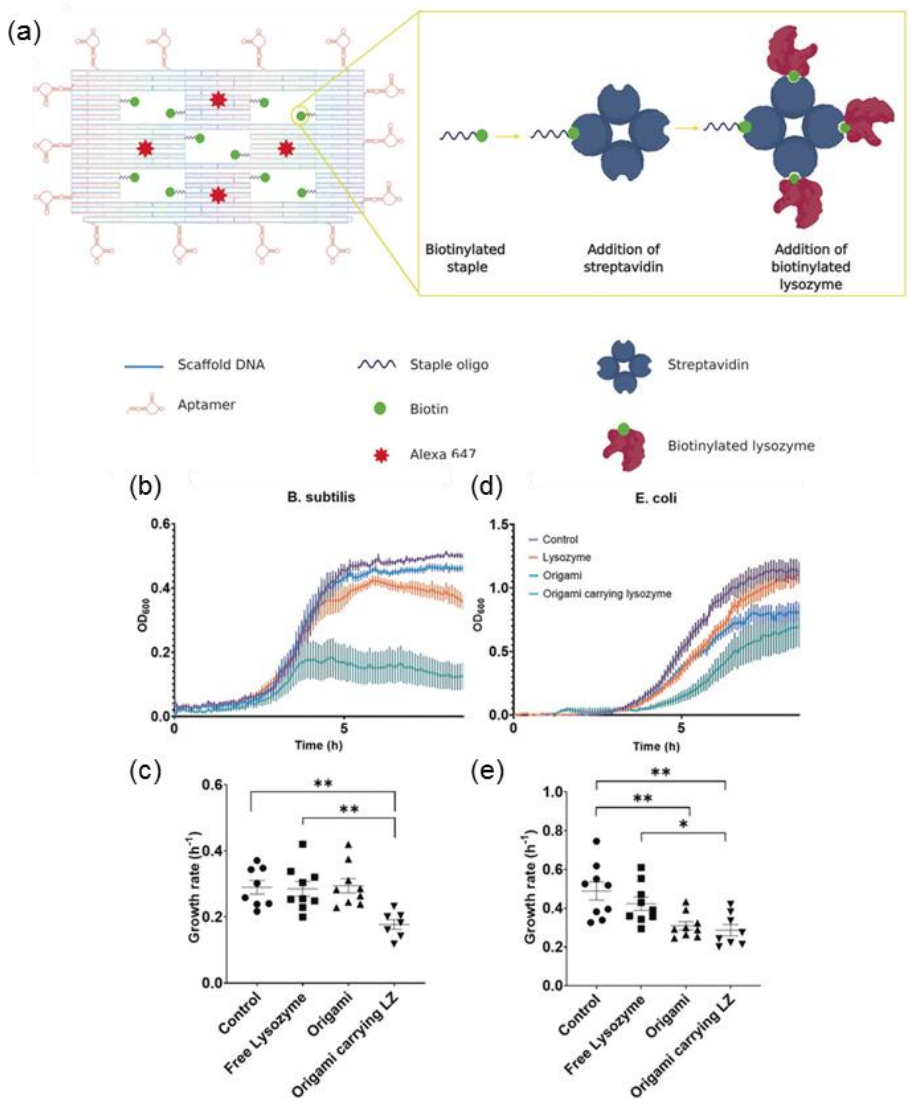

Figure 1.14 Targeted delivery of antimicrobials through a DNA origami nanocarrier. (**a**) Schematic representation of an antimicrobial DNA origami nanocarrier. Within all of the five well region is two single stranded biotinylated staples for the binding of streptavidin and subsequently the biotinylated lysozyme. Four staple extensions on each side of the structure allow for fourteen aptamers to hybridise which power the attachment of the structure to its bacterial target. Averaged growth curves (**b**) and growth rate analysis (**c**) for *B.subtilis*. Averaged growth curves (**d**) and growth rate analysis (**e**) for *E.coli.*

Adapted from: [224]
Mela et al. *Angew Chem Int Ed*, **59**, Issue 31, 12698-12702 (2020) doi:10.1002/anie.202002740

curves (**b** + **d**), and growth rate analysis (**c** + **e**). The authors noted a number of interesting conclusions from this work. Firstly, the loaded origami tiles could successfully bind both gram-positive and gram-negative bacteria (surface coverages of 22.5 % and 18.6 % respectively).

Secondly, the origami tile itself (no lysozyme loading) appears to have a significant inhibitory effect on growth for gram-negative species, suggesting that the tile binding has an interfering effect on cell division. There is however, no further benefit (as expected) no significant reduction in the growth for *E.coli* incubated with the lysozyme loaded origami tiles. Finally, for the susceptible *B.*subtilis species the reductions in growth rate is highly significant against the control, and free lysozyme, following incubation with the loaded tile. With the high programmability of DNA origami constructs, the loading of other antimicrobials to a structure for delivery of targeted payloads for gram-negative bacteria are possible. This study provides a promising and novel contribution to the origami field in detailing the potential applications of DNA origami in the fight against anti-microbial resistance.[224]

While the focus of this thesis primarily surrounds methods of improving electrochemical DNA biosensor performance with the use increasing complexity, I believe the above study by Mela et al, to be particularly pertinent. Later in this work, experimental data will be reported detailing a novel method of amplifying electrochemical signal change with a programmable DNA tile that is similar to that engineered above. More detail will be provided in Chapters 5 and 6 as to a potential development combining an origami design like that by Mela and colleagues with an electrochemical platform for bacterial susceptibility testing.

1.5.4 Environmentally Responsive DNA Origami

Multiple DNA origami nanosystems have been engineered in which an external stimulus is capable of inducing a desired structural change. These dynamic devices are responsive to a variety of stimuli including temperature and UV exposure.[206,208] Consequently, it is possible to position these devices in systems for the mediation of particular processes at the nanoscale. This includes the assembly of plasmonic antennas, Biocomputing with molecular switches, or robotic walkers for molecular sorting.[225] Perhaps most relevant to the field of biomedical engineering, and specifically the disciplines of drug delivery or biosensing, is the ability to design DNA origami constructs with a conformational trigger of environmental pH. This is particularly pertinent as varying local pH is often observed in the tumor microenvironment,[226] and a common trait in

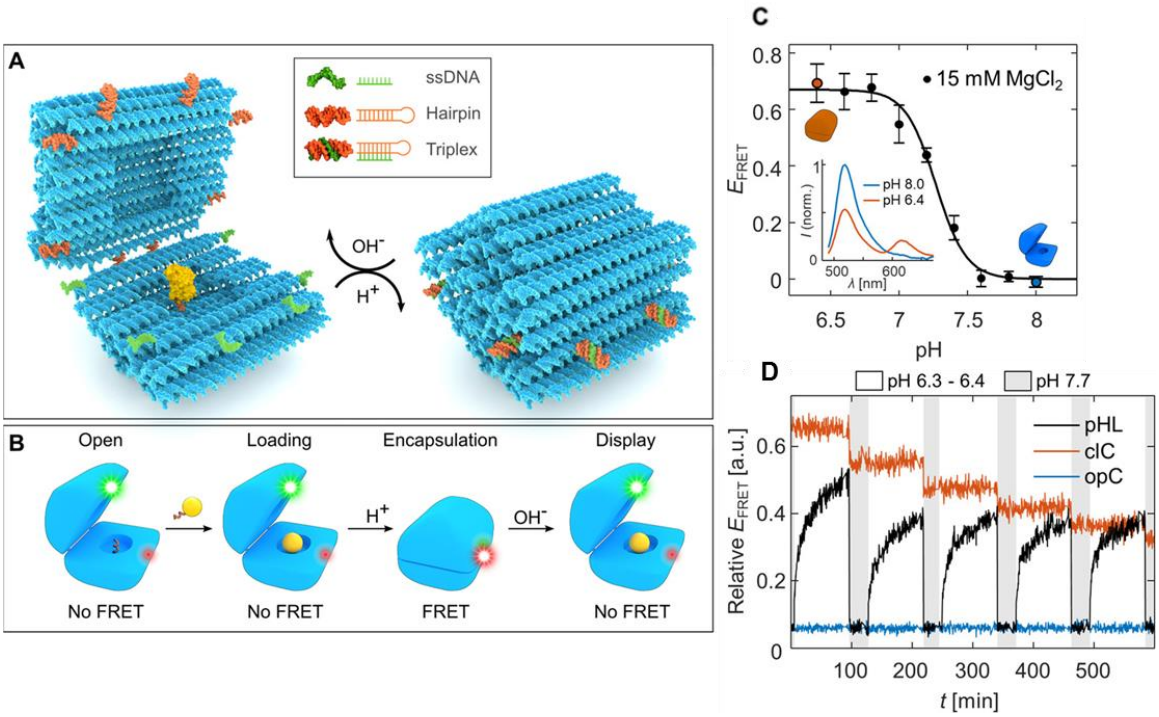

Figure 1.15 A reconfigurable DNA Origami nanocapsule with encapsulation and release of cargo driven through local pH control. (**A**) Schematic of a HRP loaded nanocapsule, where the hinged structure exists in either and open or closed confirmation aided by 8 pH-responsive Hoogsteen triplexes. (**B**) The experimental outine of labelling, loading, encapsulation , and cargo display. (**C**) FRET efficiency plotted against the solution pH for fitting by the standard Hill function. (**D**) Repetitive opening and closing cycles of the nanocapsule to establish opening/closing kinetics.

Adapted from: [232]
Ijas et al. *ACS Nano*, **13**, Issue 5, 5959-5967 (2019) doi:10.1021/acsnano.9b01857

bacterial growth with proton pumps expelling protons from the cytosol to help maintain near-neutral intracellular pH.[227] While the Watson-Crick base-pairing laws govern the overwhelming majority of DNA nucleotide interactions, it is possible to form secondary and tertiary structures via hydrogen bonding. These structural motifs are often less energetically favourable, and are pH sensitive.

One such multi-strand DNA motif is the Hoogsteen triplex, where a single stranded sequence rich in pyrimidine nucleotides binds in the minor groove of a double stranded DNA sequence. A series of sequence specific hydrogen bonds can form known as Hoogsteen bonds, with a thymine of the ssDNA molecule interacting with a T-A basepair in the dsDNA molecule. This produces a T-A·T triplet. Equally, a cytosine of the ssDNA molecule can bind in a pronated state (C^+) to a C-G basepair of the dsDNA forming a C-G·C^+ triplet.[228,229] The pronated cytosines in the Hoogsteen triplex has a mean dissociation constant (pK_a) of ~6.5, while the T-A·T triplets

become unstable as thymine is depronated and unable to form hydrogen bonds at pH beyond 10.5. With pK_a representative of the pH where 50 % of the total strand population is in a triplex state, it may be possible to design fractions of a particular triplet to manipulate the pK_a of assemblies.[230,231] In designing structures containing the necessary sequences to form Hoogsteen triplexes, it may therefore be possible to form environmentally sensitive assemblies. For example, an origami sheet could be designed to exist as a planar structure at a particular pH point, and subsequently adopt a conformational change as Hoogsteen triplexes form with a change in local pH. This design principle is analogous to the nanorobots first developed by Douglas et al, in 2012 where partially complementary aptamers and ssDNA extensions at opposing ends of the 2D structure induce a closing process, to form a resultant 3D complex.[218] In this pH responsive system, one could imagine local pH being the driving force in structure confirmation, as opposed to Watson-Crick base-pairing laws, or the presence of a complementary analyte to an aptamer.

This idea was developed by Ijas and colleagues in 2019, where a highly configurable DNA origami nanocapsule, with a reversible opening and closing cycle that can be effectively mediated across a narrow pH gradient which is comparable to local pH change in the tumor microenvironment. In this design, the opening/closing mechanism is managed by pH latches composed of a double stranded hairpin extension, and a single stranded overhang at the opposing edge of structure. The design and mechanism of action for this DNA origami nanocapsule is provided in Figure 1.15 **A** + **B**, where the local pH of the nanocapsule can induce the formation, or dissolution of a series of parallel Hoogsteen binging triplex DNA latches, and resultant closed or open confirmation. These confirmations could be viewed through tunnelling electron microscopy with a variety of opening angles. However, to confirm the specific sensitivity of a structures confirmation to pH, a donor and acceptor fluorophore where added to opposing halves of the structure. This allowed for Förster resonance energy transfer (FRET) measurement, with the FRET efficiency (E_{FRET}) dependent upon the proximity of the donor and acceptor. As the pH is increased, failure of Hoogsteen triplexes result in an increasing opening angle, and subsequent decline in E_{FRET}. This relationship is well modelled by a hill equation, shown in **C** and allows for the determination of $_pK_a$ = 7.27, which is in good accordance with the predicted $_pK_a$ based upon a Hoogsteen triplex composition of 60% T-A·T. This system was also switchable, with a pH shift in either direction capable of inducing conformational change. This is shown in **D**, with successive switches from a pH of ~6.3 to 7.7 allowing for the determination of

opening and closing kinetics. Introduction of sodium hydroxide to shift the pH to 7.7 is sufficient to induce a rapid opening mechanism noted by the immediate decline in relative FRET efficiency. However, the spiking of acetic acid to bring pH to 6.3 - 6.4 contributes to a growth in the FRET efficiency signal over a 90 minute incubation without ever reaching a stable equilibrium, highlighting a slow rate of nanocapsule closure as the Hoogsteen triplexes form. Finally, the programmable nature of the origami method allowed for a nanocapsule design that incorporates a functionalisable inner cavity with for the loading of molecular cargo. Here the authors could successfully load one of two payloads; either a gold nanoparticle for visual analysis of loading through its high contrast in TEM imaging, or horseradish peroxidase (HRP) to establish if the encapsulation method impacted cargo molecule functionality. Importantly the HRP was shown to remain highly functional after its loading within the structure, with a strong catalytic activity on ABTS oxidation to $ABTS^{\bullet+}$.[232]

This is a particularly relevant development in the application of DNA origami for drug delivery systems, though it also serves as a potential avenue for novel biosensing technologies. As mentioned previously, pH is often manipulated by pathologies or bacterial growth. Consequently, it may be possible to engineer DNA nanostructures that are responsive to a local pH change. Such a response may be a confirmation change, or the release of a given cargo molecule, either of which could serve as a contributor to a detectable signal change. This idea has formed the basis of the final experimental chapter in this thesis, where a pH responsive DNA origami zipper has been inspired, designed, and interrogated by electrochemical methods in collaboration with Ijas and colleagues.

1.5.5 Current Application in Biosensing

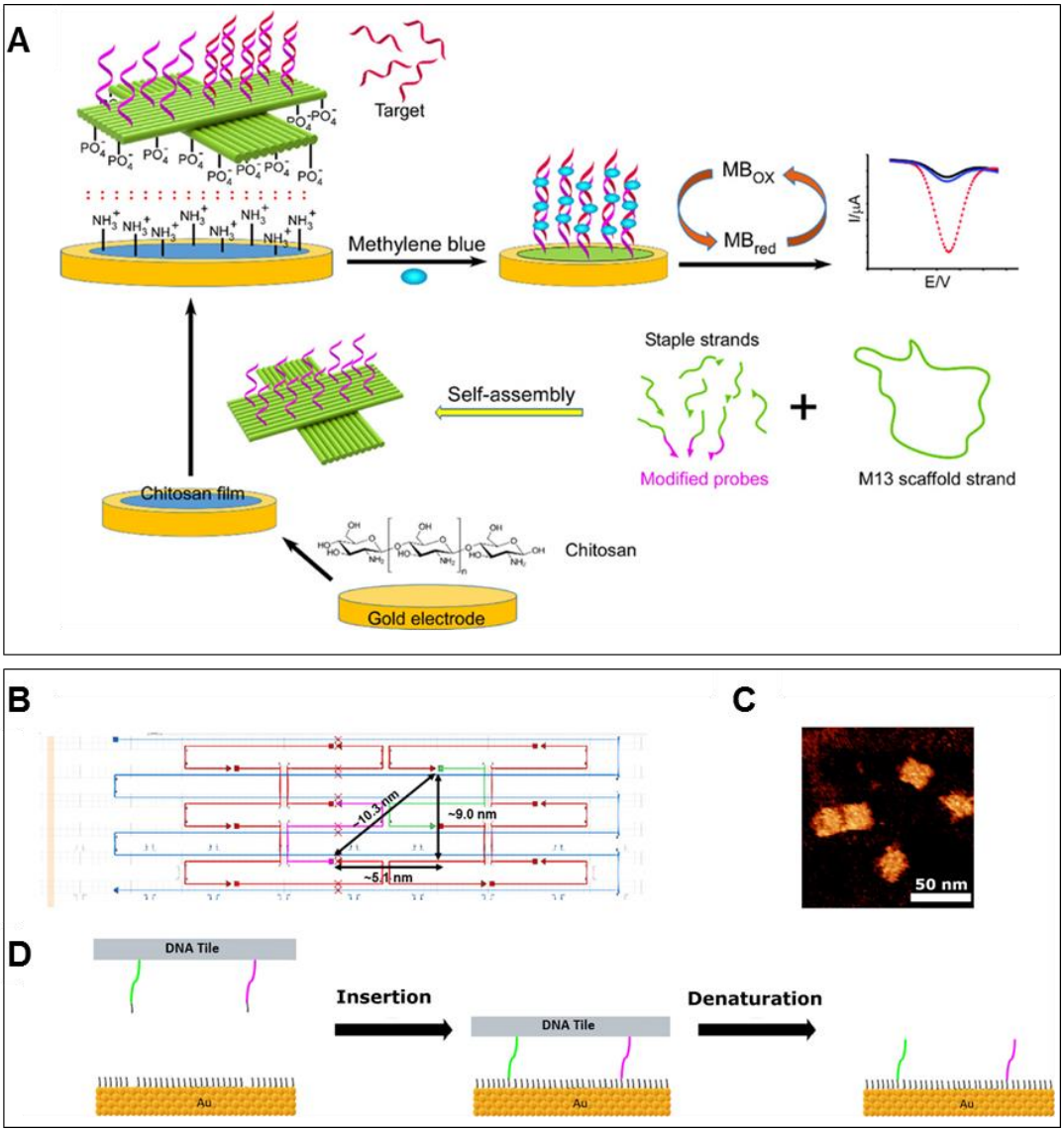

Figure 1.16 Current usages of DNA origami for e-DNA biosensor designs. (**A**) Sensor design and experimental outline of a cross-shape DNA origami nanostructure immobilised on a functionalised electrode. The origami nanostructure hosts required engineered ssDNA probes complementary to a desired target. The programmability of the DNA origami method allows for the spatial control of probe positioning and packing densities. Methylene blue intercalation within target/probe hybrids powers electrochemical signal mediation. (**B**) caDNAno schematic of a DNA origami tile for the nanoprinting of DNA probes onto a functionalised gold electrode. (**C**) AFM images of assembled DNA origami tiles for nanoprinting, and (**D**) the experimental outline of a DNA origami nanoprinting protocol.

(**A**) Adapted from: [233]
Han et al. *ACS Omega*, **4**, 6, 11025-11031 (2019) doi.org/10.1021/acsomega.9b01166
(**B**-**D**) Adapted from: [234]
Gu et al. *ACS Applied Nano Materials*. **4**, 8, 8429-8439 (2021) 10.1021/acsanm.1c01685

Central to many of the entries in the literature that highlight the use of DNA origami for biosensor applications, is the notion of employing the bottom up construction method to better resolve the positioning of capture probes for a given analyte. Two methods for achieving this aim have recently been documented in the literature, and schematics for each outlining their approach is provided in Figure 1.16. Firstly, the construct can be patterned with a rationally controlled array of single stranded DNA probes at a desired density. This entire structure can then be immobilised on to a transducer surface, and serve as a platform for the electrochemical monitoring of target hybridisation (Figure 1.16 **A**).[233] A second method of mediating capture probe positioning has been recently proposed by Gu et al in 2021. In this work, researchers designed a DNA origami with a rational controlled density of thiolated probe sequences throughout at various desired intervals. This construct was then introduced to densely coated alkanethiol SAM, and the thiolated probes allowed to compete for binding with the Au(111) surface via proposed covalent gold-thiol bond. The origami construct was then denatured via immersion in 100% formamide at room temperature, and rinsed away under Di-H_2O to produce a highly programmable probe patterned transducer with a well-defined spatial resolution of capture sites (Figure 1.16 **B - D**). This nanoprinting technique allows for AFM imaging of discrete single probe localities, and presents a means of utilising homogeneous SAM coatings for enhancing the sensitivity of electrochemical biosensors.[234]

The targeted positioning of DNA probes for SAM construction is not the only function of DNA origami in biosensor design. A key goal of future biosensor technologies is the capability to observe single biomarker entities in a patient sample without the necessity for ensemble averaging immunoassay techniques. One promising method for achieving such an aim is the use of nanopores, where a voltage is passed across its cavity, and the translocation of a single molecule target can cause momentary modulation to a steady state ion current.[235] However, the translocation of single molecules through nanopores is often rapid when the nanopores is much larger than the target molecule. Consequently, the detectable signal is low, and the signal to noise ratio is often poor. To tackle such an issue, Raveendran and colleagues set out to engineer a rationally designed DNA origami nanostructure, with an internal cavity hosting an aptamer extension into space, complementary to human C-reactive protein (CRP). The design was capable of detecting CRP to a lower limit of 3 nM, in clinically relevant biofluids. This was achieved by variation in peak shape, amplitude and dwell time distinguishing occupied and

unoccupied DNA origami channels. Consequently, a quantitative biosensing readout could be generated by a simple counting operation of occupied nanopore carriers.[236]

Noteworthy in reviewing the DNA origami biosensor literature is the absence of the nanostructures in serving as a tool for signal amplification. A brief account of such a technique is as follows. Origami techniques enable the facile assembly of highly programmable nanostructures that can be readily functionalised for hybridisation with a given analyte. It is also possible to engineer nanostructures to a meet a specific physical characteristic, including molecular weight, dimension, or geometry. As such, one could rationalise the construction of an origami assembly that is capable of being immobilised on a transducer surface through a series of linker sequences, which is tailorable in its blocking characteristics. The immobilisation of a large DNA origami assembly on a planar gold electrode may significantly alter the interfacial properties of the electrode, and consequently the electrochemical behaviour of a potential sensor. If one could design a DNA origami nanostructure that possess regions of complementarity to a given target, it is possible to consider its feasibility in a sandwich assay experiment. Simply, a transducer may be functionalised with a single stranded pDNA as part of a DNA/alkanethiol monolayer. Should a complementary target be present in solution, this target may hybridise with the immobilised probe, leaving a series of sequences as a pendent extension into solution. Consequently, an origami tile with pendent single stranded DNA extensions may then hybridise with the probe/target complex, and contribute to a dramatic alteration in the interfacial properties of the sensor. This novel hypothesis of a DNA origami construct being employed as a signal amplifier for e-DNA biosensing applications forms the basis of the experimental Chapter 5, and will be further discussed at length.

DNA origami is an ever-expanding field, with application across physical, chemical and biomedical sciences. It holds immense promise for the exploration of a revolutionary hypothesis presented by Richard Feynman more than sixty years ago; “There’s plenty of room at the bottom”. As a cornerstone of nanotechnology, DNA origami provides scientists with a method of molecular control in both positioning and functionality at the nanoscale. The potential for such control in enhancing the performance of point of care diagnostics with a DNA origami approach is outstanding.

1.6 Conclusions

In this literature review, a broad expanse of research has been detailed spanning a number of fields. The aim of which has been to develop a base of understanding for current mechanisms of e-DNA biosensing, and the potential of DNA nanotechnology to aid in overcoming some prevalent issues limiting the application of the current classes of DNA biosensors in clinical settings. In Chapter 2 a particular focus will be given to a number of key fundamentals describing electrochemistry, and its appropriateness as a measurement technique for nucleic acid detection.

Chapter 2

Theoretical Concepts

2.1 Introduction

Throughout Chapter 1, an extensive literature review has detailed numerous applications of electrochemical techniques in the development of biosensors. A range of both voltammetric and impedimetric methods have proven effective in determination of biological targets with varying success. For example, there are numerous reports of voltammetric techniques (differential pulse voltammetry and square wave voltammetry) being effective in the discrimination of nucleic acid targets, [35,37,87,96,98] and also an increasing level of reporting of the sensitivity of electrochemical impedance spectroscopy (EIS) in analyte detection.[35,37,38,40,71] These techniques will be assessed throughout this thesis, and as such, a detailed explanation to their working is necessary.

Electrochemistry can be conceptualised as the observation of charge transport across an interface, particularly between an electrode and electrolyte. The capacity to assess changes in charge transfer resulting from specific stimuli, such as an applied potential, allows for inferences about the evolving surface characteristics of this interface. Applying this perspective to electrochemical biosensors, where a bioelectric interface is established, perhaps through self-assembly on a transducer surface, gives rise to a novel working hypothesis. In this context, the successful binding of analytes to a functionalised transducer surface might be responsible for modifying crucial surface traits of the bioelectric interface leading to signal acquisition. Prior to engaging in experimentation of these sensing strategies, it is imperative to first comprehend key theoretical aspects pertaining to the functioning of electrochemical systems.

2.2 The Three Electrode Cell

The most common method of interrogating the electrochemical reactions within a given system involves the classical three-electrode cell. This is centred on a working, counter, and reference electrode, submerged in a solution containing a specific molecule (*A*) connected to a potentiostat. This allows for the application and measurement of both potential and current. A more detailed analysis of the events occurring at each of the three electrodes involved in this system.

1. Working Electrode (WE)

The working electrode serves as the interface between the electrical circuitry and solution where a given chemical reaction can be observed. The properties of this interface can be manipulated by the application of a given potential to this electrode. For example, should a reduction/oxidation (redox) species *A*, be in solution, application of a suitably high positive potential the following reaction may occur:

$$A \rightarrow A^{+} + e^{-} \qquad \text{Equation 2.1}$$

Equally, the application of a sufficiently negative potential may induce the following:

$$A + e^{-} \rightarrow A^{-} \qquad \text{Equation 2.2}$$

Simply, the application of a given potential can either oxidise or reduce the particular species in solution and give rise to the flow of electrons. The consequence of which is the potential controlled decrease in concentration of the species *A* in solution, to either its reduced or oxidised form. As a result, a concentration gradient is established between the bulk solution and the immediate electrode/solution interface. This will therefore result in the continual transfer of species *A* to the interface in attempt to replenish its decreasing concentration.

2. Reference Electrode (REF)

The potential applied to the working electrode is managed with respect to a reference potential. This is provided by a reference electrode where a stable and well-defined electrochemical reaction at equilibrium can isolated from other chemicals, which may exist in the solution in which it is immersed. A frit, commonly porous glass positioned at the end of the device, prevents interference from any chemical in solution on the stable reaction, while allowing for a degree of ionic conductivity with the electrolyte in which it is immersed (< 50 pA). This allows for the potentiostat to establish a reference potential. There are multiple reference electrodes available for electrochemical systems. This study will employ Ag/AgCl (Silver/Silver Chloride) though out.

3. Counter Electrode (CE)

Finally, the counter electrode is required to complete the cell. The material forming the CE can theoretically be any conductor. However, an inert material is preferential to prevent reactivity and contamination of the solution. Its role is two-fold. If there is current flow from the WE to solution, and the reduction of species *A*, current will re-enter the circuitry through the CE. Equally, the reverse is true should the current flow occurs in the opposite direction. The size of the CE is also of importance, with a necessity for it to be large enough to ensure it does not limit current at the WE and contribute to the resistance of the cell. In this work Platinum macroelectrode CEs are used throughout.

2.3 The Electrical Double Layer

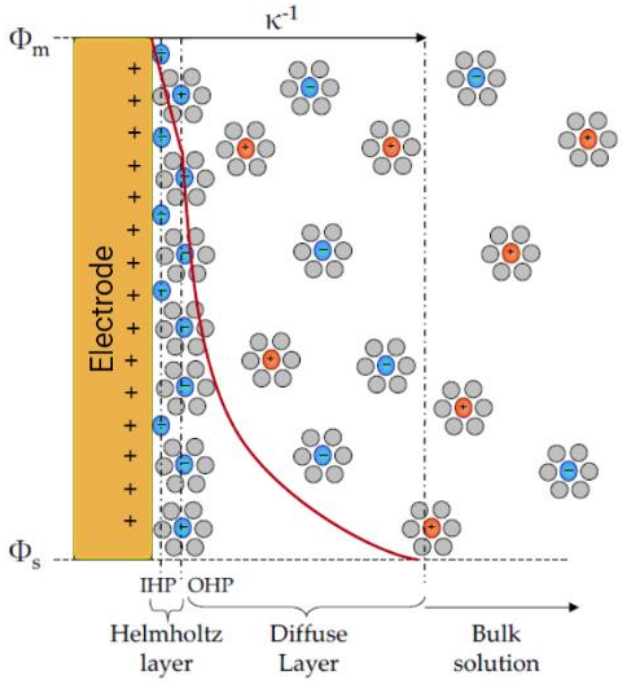

Figure 2.1 Schematic for the Gouy-Chapman-Stern (GCS) model of the electrical double layer. Here anions (blue) are specifically adsorbed at the metal surface. The grey circles represent fully solvated anions (blue) and cations (orange). $\Phi_m$and $\Phi_s$denote the respective metal electrode and solution potentials. κ^{-1}provides an approximation for the thickness of the double layer, with the potential drop across the double layer shown by the red line.

Immersion of an electrode in solution yields the formation of an electrical double layer, assuming the electrode is bare, planar, and free from adsorbed contaminants.[237] Electron availability at this metal surface generates specific charge densities, q_m. In attempt to achieve charge neutrality, ionic reorganisation within the solution, allows for an equal and opposite charged layer, q_s, to form at the metal surface. The resultant potential difference produces an electric field effect extending out into solution. This phenomenon is well documented by the Gouy-Chapman-Stern (GCS) model in figure 2.1, displaying the formation of charge layers, and the resultant potential drop.

In the Helmholtz layer, ions are positioned at a distance determined by the occupation level of the solvation shell. Solvated ions held distant from the surface form the outer Helmholtz plane (OHP). Specific adsorption of ions which are free of solvated shells, exist in the inner

Helmholtz plane (IHP). This induces a charge gradient in the solution immediate to the electrode surface, with a near lineal potential drop from the electrode surface (Φ_m) to the OHP (Φ_{OHP}). When modelled as a linear potential drop, it is possible to equate these charge layers to a parallel-plate capacitor, and derive a total capacitance for the Helmholtz layer: [238]

$$C_H = \frac{\varepsilon\, \varepsilon_0\, A}{d} \qquad \text{Equation 2.3}$$

Where ε represents the relative permittivity of material existing between the plates, ε_0 denotes the permittivity of free space, A corresponds to the electrode area, and d being the layer thickness. This however only accounts for the capacitance of one aspect of the double layer. It is necessary to account for varying charge densities present in the diffuse layer also.

The most significant concentration of electrical charge is located at the immediate metal surface, where electrostatic forces are best able to overcome thermal processes of Brownian Motion. However, at increased distance from the surface, these electrostatic forces are insufficient to maintain a high charge concentration. As such, the weakness of using a constant spacing between plates, d, for modelling the capacitance becomes clear, and an average distance of charge separation is required in the diffuse layer expression. The introduction of the Debye length, serves as a means of assessing the reach of electrostatic effects persisting into solution, and the point where thermal processes dominate ionic dispersion. We can therefore employ the Debye length as a measurement of diffuse layer thickness:[238]

$$\kappa^{-1} = \sqrt{\frac{\varepsilon_r \varepsilon_0\, \kappa_B T}{2 N_A e^2 I}} \qquad \text{Equation 2.4}$$

Where ε_r represents the relative permittivity of the solution, ε_0 denotes the permittivity of a vacuum, κ_B corresponds to the Boltzmann constant, *T* serves as the absolute temperature in Kelvin, N_A is Avogadro's number, *e* is the elementary charge, and *I* being the ionic strength of the solution.

Given ionic strength is a summation of both ionic concentration, c_i, and ionic charge, z_i, (Equation 2.3), we can therefore surmise diffuse layer thickness, and ultimately capacitance, being directly linked to the dielectric permittivity, and concentration and charge of the ionic species in solution (Equation 2.4):[238]

$$I = \frac{1}{2}\sum_{i=1}^{n}(c_i * z_i^2) \qquad \text{Equation 2.5}$$

$$C_D = (\frac{2Ie^2\varepsilon_r\varepsilon_0}{k_BT})^{1/2} \cosh(\frac{ze\Phi_0}{2k_BT}) \qquad \text{Equation 2.6}$$

Where the potential drop across the diffuse layer is given as Φ_0, and the magnitude of ion charge in a 1:1 electrolyte solution is given as z. C_D is given in μF/cm^2.

A combination theory derived by Otto Stern, proposes a model of double layer capacitance that is composed of the Helmholtz and diffuse layers:[238]

$$\frac{1}{C_{dl}} = \frac{1}{C_H} + \frac{1}{C_D} \qquad \text{Equation 2.7}$$

The summation model of double layer capacitance is useful in assessing real systems, though is not a complete reflection of electrochemical events in a system. The GCS model implies that the Helmholtz layer (C_H) is independent of potential, though this ignores phenomena such dielectric structure and saturation within the Helmholtz layer, key conditions influenced by potential. The diffuse layer (C_D) has a strong response to potential, with it varying in a V-shaped profile around the PZC, or potential of zero charge; the potential at which double layer charge exists at zero. With the double layer being an inverse expression, the smaller of the two capacitances governs the total capacitance.

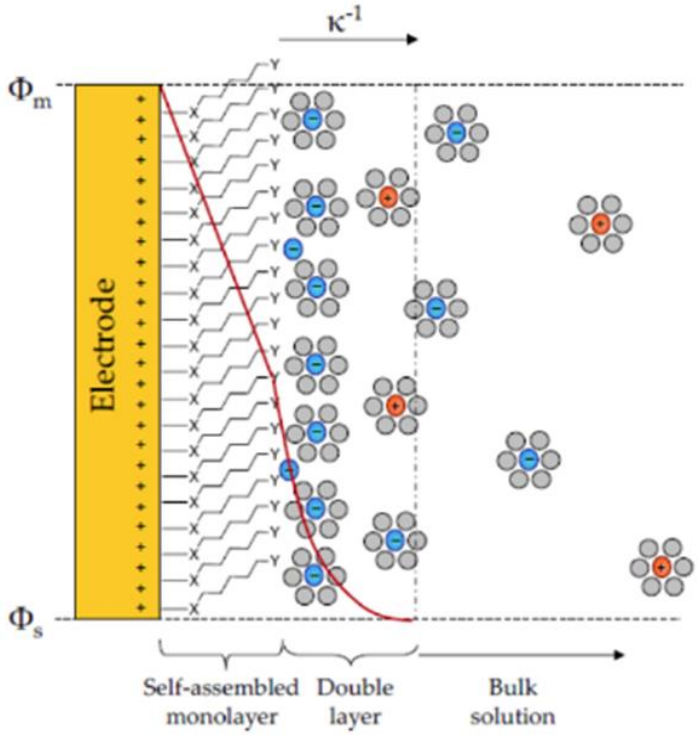

Figure 2.2 Schematic for the Gouy-Chapman-Stern (GCS) model of the electrical double layer on a SAM functionalised electrode. X describes a tail group modification allowing for the immobilisation of an alkanethiol on the metal surface. Y denotes a modifiable head group to provide the monolayer with a desired functionality. Here anions (blue) are specifically adsorbed at the SAM surface. The grey circles represent fully solvated anions (blue) and cations (orange). Φ_m and $\Phi_s$denote the respective metal electrode and solution potentials. A linear potential drop occurs across the thickness of the SAM, and is followed by a subsequent potential decay across the shifted double layer. κ^{-1}provides an approximation for the thickness of the double layer, which is now smaller than that of a cleaned electrode surface. The potential drop across the system is shown by the red line.

The presence of a well organised SAM extends the double layer away from the electrode surface. The effective thickness is dependent upon chain length, and its angle of tilt with respect to the electrode surface. The repositioning of the double layer, serves to induce a potential drop, and a capacitance (C_{SAM}) to the overall capacitance model. This is represented with an updated GCS model for a SAM functionalised electrode in Figure 2.2. Given that C_{SAM} is substantially smaller than C_H, and smaller capacitances govern total capacitance, SAM modified electrodes can have their double layer capacitance surmised by the following model:[237]

$$\frac{1}{C} = \frac{1}{C_{SAM}} + \frac{1}{C_D} \qquad \text{Equation 2.8}$$

The value of C_{SAM}, can be determined through the use of Equation 2.6, however this assumes some predetermined constants. Firstly, the SAM layer is homogeneous in its organisation, and the dielectric permittivity is not variable throughout the coating. Practically, this is a state of order that is difficult to achieve, with SAM organisation highly variable, and packing densities a function of the constituent molecules.[47,239] Equally, substrate surface roughness, and uniformity is critical in ensuring an adequate coating. Previous works have highlighted the presence of pinhole features, where electron transfer may disrupt dielectric permittivity consistency across the layer. Pinhole features primarily feature at grain boundaries, areas of a large relative roughness, and surface defects.[240] This may present as an issue in PoC diagnostics, due to the requirement to minimise material costs, simplify manufacture, and operate sensors in complex environments. Ultimately, this may require more advanced modelling methods for the true determination of double layer effects, and approximation of the total area of exposed substrate through pinholes. Tunnelling phenomena through the thickness of the layer is well documented in contributing to background current, and must be also be considered.[241] The two-capacitor model given in Equation 2.6, may appear an oversimplification for reasons listed above, but experimentally, can allow for sufficiently accurate measurements of double layer potentials in appropriate ionic strength conditions. EIS measurements in the absence of a redox mediator, suggest nanometre scale alkanethiol chains are capable of producing excellent ionic insulator layers, of a high total magnitude of impedance, and constant phase angles tending towards those of a truly insulative material at ~88-89^0.[242] Employing SAM coated electrodes in sensing based systems may rely upon terminal functional groups, for antifouling, or target capture purposes. As such, charge characteristics of the layer may change. This may be visualised as the addition of a bound layer of charge to the SAM surface, and can be modelled by the introduction of a further element to Equation 2.6:

$$\frac{1}{C} = \frac{1}{C_{SAM}} + \frac{1}{C_D + C_{cp}(\theta)} \qquad \text{Equation 2.9}$$

With $C_{cp}(\theta)$ being the capacitance of this new charged plane, as a function of ionised group (θ) fractions.

2.4 Voltammetry

2.4.1 Cyclic Voltammetry

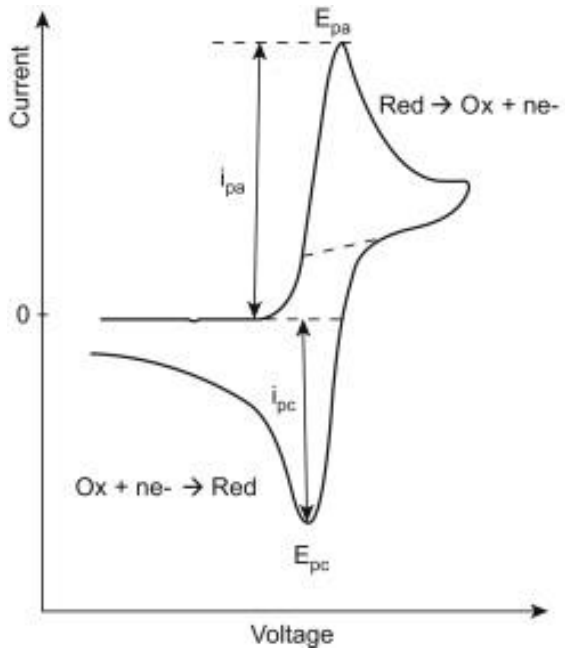

Figure 2.3 Typical Cyclic Voltammogram for a reversible redox species. i_{pc} and i_{pa} denote the peak anodic and cathodic currents, with E_{pc} and E_{pa} highlighting the applied potential at which each peak current is recorded. Adapted from: [335]

A Chagnes. *Lithium Process Chemistry.* **Chapter 2,** 41-80 (2015)
doi.org/10.1016/B978-0-12-801417-2.00002-5

Electrochemical behaviour of a system can be determined by a series of increasing step potentials form a zero potential, and the simultaneous measurement of current flow at each respective point. Potential is varied in a linear application, with time, and common sweep rates varying from 10mV/s to 1000 V/s in conventional electrodes, to rates of 10^6 V/s in Ultramicroelectrodes. Completion of current recording at a predetermined potential, completes the process of Linear Sweep Voltammetry. The Sweep Voltammetry measurement employed in this study, Cyclic Voltammetry (CV), is completed by reversing the scan direction at a given potential, E_λ. A typical cyclic voltammogram is provided in Figure 2.3. This provides a means of studying electrode potential, and the respective concentration of participants involved in a

thermodynamically or electrochemically reversible reaction, as governed by the Nernst Equation:[238]

$$E = E^{0'} + \frac{RT}{nF} In \frac{C_O}{C_R} \qquad \text{Equation 2.10}$$

Where $E^{0'}$ denotes the measured cell potential, R is the universal gas constant, T is the temperature in Kelvins, n is the total number of electron species transferred, or half-cell reaction, F is Faraday's constant, and C_O, C_R correspond to the concentrations of Oxidation and Reduction species in the reaction.

When considering a single electron reduction event, Ferrocenium (Fc^+) to Ferrocene (Fc), the term n can be set to one. This provides a powerful method of assessing how a system may respond to either applied potential, or changing redox species concentration. Assuming a measurement solution consists of Fc^+, scanning potentials out towards a negative E_λ, Fc^+ is locally reduced proximal to the electrode surface to Fc, yielding a measureable current that reaches a cathodic peak as free Fc^+ is depleted. Upon meeting $-E_\lambda$, the scan direction will switch in a positive direction, and newly accumulated Fc will be oxidised back to Fc^+, with increasingly positive applied potential. In accordance with the Nernst Equation, where $E = E_{1/2}$, (the midway potential between each peak potential) concentrations of both Fc^+ and Fc achieve an equilibrium. Separation of these peaks occurs due to diffusion events necessary to transport the particular analyte to the electrode surface.[243]

In an ideal redox event, the peak-to-peak separation (ΔE_p) between the cathodic and anodic peaks will be 59.2 mV at 25 ^{0}C.[238] In this situation, electron transfer is fast, and entirely reversible. These scenarios are commonly referred to as Nernstian. In the event of a barrier to electron transfer being created, a deviation from Nernstian behaviour may be noted, with the rate of electron transfer rate altered, an increase in ΔE_p, and a reduction in measured cathodic (anodic) peak currents.

A key experimental boundary in Cyclic Voltammetry is rate at which applied potential is scanned (scan rate). An increasing scan rate reduces the size of the diffusion layer, and contributes to greater measureable peak currents. In a readily electrochemically reversible

reaction, with freely diffusing redox species, (i.e. $Fc^+ \rightleftharpoons Fc$), the Randles-Sevcik equation (Eq 2.9) describes the linear increase of peak current (i_p) with the square root of scan rate:[238]

$$i_p = 0.446nFAC^0\left(\frac{nF\upsilon D_o}{RT}\right)^{1/2} \qquad \text{Equation 2.11}$$

Where n is the number of electrons transferred, F is Faraday's constant, A is the electrode surface area (cm^2), C^0 is the bulk concentration of the analyte, υ is the scan rate, D_o is the diffusion coefficient of the analyte, R is the universal gas constant, and T is the temperature.

In the case of a reversible electron transfer event, where the redox species may be adsorbed on to, or tethered to, the electrode surface, the current response will vary linearly with υ. Should a CV produce a deviation from linearity between i_p and $\sqrt{\upsilon}$, then we may deduce that electron transfer is occurring through an immobilised or tethered redox species. In this event, reconfiguration of the Randles-Sevcik equation, introduces the term Γ^*, to the description of current response:[238]

$$i_p = \frac{n^2F^2}{4RT}\upsilon A\,\Gamma^* \qquad \text{Equation 2.12}$$

With Γ^* providing the surface coverage of an adsorbed or tethered species in mol cm^{-2}. This may serve as useful measure of immobilisation in later chapters.

2.4.2 Differential Pulse Voltammetry (DPV)

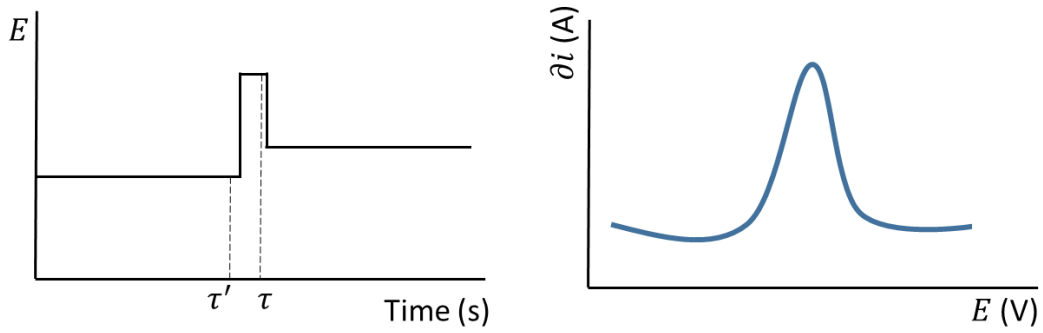

Figure 2.4 Schematic outlying the details of differential pulse voltammetry measurement. Left, overview of a single differential pulse where τ' is the first current measurement, and τ is the second current measurment. Right, typical differential pulse voltammograms where a series of pulse across a potential range allows for a multiple recordings of current. The typical bell-shaped curve is apparent, with steep aspects and a single sharp peak.

The technique of differential pulse voltammetry technique is based upon the application of potential pulses of a predefined fixed amplitude on linear ramp potential. The beginning of the measurement at a base potential where no faradaic reactions can occur. The base potential is then increased by pulses of equal increments, with a current measurement immediately prior to the pulse τ', and at a time τ after the pulse. The difference between these two measurements can then be plotted against a linear range of potential. In including a wait time within pulse application and measurement, the charging current is allowed to decay and better detail the true redox activity of the couple in solution. As the baseline potential approaches the formal potential of the redox couple E^0, oxidation reactions can occur to a concentration of the species that is in close proximity to the electrode surface. Successive pulses drive a reduction in the concentration of the species as it is oxidised, and forces an enhanced flux to the electrode surface from the bulk solution, thus contributing to an increase in faradaic current. Passing the formal potential of the redox couple, contributes to a reduction in the transfer of the species to an electrode, and a decline in the measured current. This technique is summarised in Figure 2.4.

2.4.3 Square Wave Voltammetry (SWV)

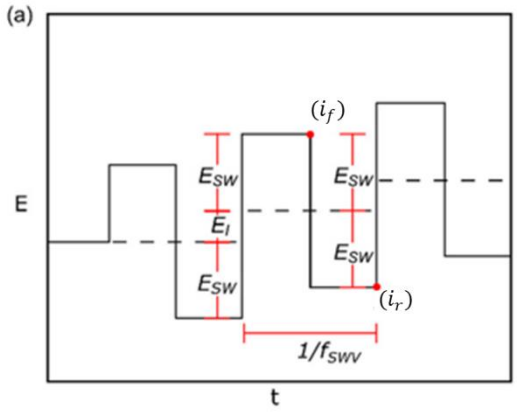

Figure 2.5 Square Wave Voltammetry waveform. Detailing the staircase pulse (E_I), and overlaid SWV pulses (E_{SW}). Current recording points at (i_f) *and* (i_r).
Adapted from: [336]

Cobb & MacPherson. *Anal. Chem*. **91**, 12, 7935–7942 (2019) doi.org/10.1021/acs.analchem.9b01857

SWV is a particularly effective technique for the interrogation of an electrochemical cell. It involves the application of a series of potential pulses from a predetermined potential staircase (E_I). This is overlaid upon a square wave pulse (E_{SW}), containing both the forward and reverse pulse on each step of the staircase. This is best understood through Figure 2.5, where the applied potential is plotted against time, allowing for the effect of both staircase, and square wave pulse to be observed. A forward scan current is measured after the first pulse (i_f), and with a reverse of the scan direction, the reverse scan current (i_r) is measured at the end of the second pulse. This therefore produces two distinct voltammograms, as it pulses around the baseline in both a forward and reverse direction. However, the SWV voltammograms presented in this thesis will be presented with a single trace of current against time. This is possible as the difference between both the recorded currents of the forward and reverse scans:

$$\Delta_i = (i_f) - (i_r) \qquad \text{Equation 2.13}$$

The potential window can be varied to observe a particular electron transfer event associated with a given redox agent. Equally, it is possible to vary the frequency of the potential

steps (>100 Hz) to allow for the monitoring of fundamentally fast electron transfer events. This allows for optimisation of electrochemical parameters to fit a given experimental constraint. This has been well documented by Dauphin-Ducharme & Plaxco in 2016, where potential step and frequency parameters were optimised to generate maximum signal gain for a series of redox species common to e-DNA biosensors.[101] Thus highlighting the importance of understanding the fundamental redox theory specific to particular redox couple in designing an appropriate sensing platform.

2.5 Electrochemical Impedance Spectroscopy (EIS) and Circuit Fitting

Electrical impedance denotes the obstruction to the flow of charge in an electrical circuit, following an applied potential. Its determination is analogous to that of resistance, though the application of an alternating current (AC) potential, generates a frequency dependent impedance response. With both a magnitude, and phase component, impedance is given as $Z(f)$ andcan be determined by:[244]

$$Z(f) = \frac{E_t}{i_t} = \frac{E_0 \sin(2\pi f)}{i_0 \sin(2\pi f + \phi)} \qquad \text{Equation 2.14}$$

With f being the oscillation frequency in Hz, E_0 the potential amplitude, i_0 the current amplitude, and φ representing the phase shift between potential and current. With total impedance being a composite of both a real component (Z_{real} or Z') and an imaginary component ($Z_{imaginary}$ or Z''), it can be noted as:

$$|Z| = Z' - jZ'' \qquad \text{Equation 2.15}$$

This allows impedance to be represented as a vector in a Z' versus $-Z''$ graph, known as a Nyquist plot, which is shown in Figure 2.6.

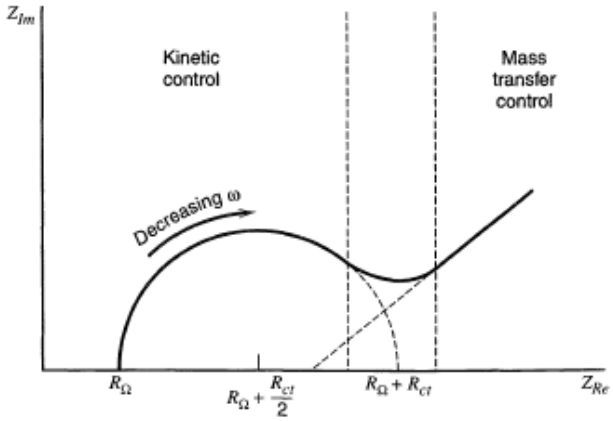

Figure 2.6 Example Nyquist plot detailing the electrochemical parameters that can be derived for further analysis. Here R_S and R_{CT} exist as real impedance factors and can be derived from the x-axis, and the double layer capacitance, C_{dl}, being the imaginary impedance from the y-axis. Combining both real and imaginary impedance produces the semi-circle response common to Nyquist plots, with mass transfer events dominating the system at low frequencies.

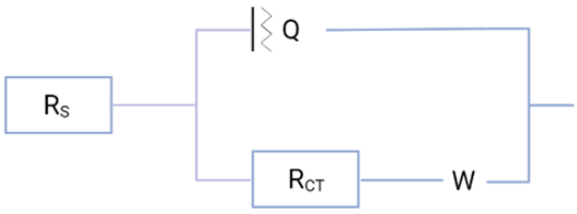

Figure 2.7 Analogous modelling of Real Phenomena in Electrochemical Systems, and Respective Impedance Responses. Solution Resistance (R_s), Double Layer Capacitance (Q), Charge Transfer Resistance (R_{ct}) and Warburg Impedance (W).

Data gathered from EIS, is often assessed by fitting to an analogous electrical circuit. Circuit complexity is increased in order to best fit the data, while ensuring all elements, accurately represent real physical events occurring within the system. In the conventional three-electrode cell, capacitive, resistive, and impedance responses, all require modelling.

With electrons following the path of least resistance, electrons will flow through the capacitor at high frequencies preferentially, charging the element in the model circuit. Charging effects of the double layer are near a pure capacitance, and can be well described by a single capacitor C_{dl}. This is often exchanged for a constant phase element (Q) to better model surfaces functionalised with an organic film. Organic coatings will often fail to form ideal, homogeneous films across the entirety of a surface, with either variations in monolayer thickness or density

inducing local conductivity discrepancies. The impedance of the constant phase element is given by:[245]

$$Z_{CPE} = \frac{1}{Y_0(j2\pi f)^n} \qquad \text{Equation 2.16}$$

Where Y_0 is the CPE-constant and n the CPE-exponent. The value of n provides an indication to the behaviour of the system with a value of 1, indicative of pure capacitive behaviour. Reduction in this value provides a method for assessing contributions of resistive behaviour, and is associated with a depression in the semi-circle region of impedance spectra. As the frequency reduces, the capacitor approaches being fully charged and the electron flow will switch to follow the pathway of the parallel resistor. This resistor (R_{CT}) effectively models the charge transfer resistance, i.e. the ability of the cell to exchange current to and from a solution-based redox species and electrode surface. This circuit element therefore serves as a vital analytical tool in electrochemical interrogation of an e-DNA sensor. The composition of a modified electrode surface, including the density, molecular make-up, and thickness of a self-assembled monolayer will fundamentally influence the value of R_{CT}, and as such provide crucial information to changing interfacial properties. For example, the functionalisation of an electrode surface may provide both a physical or electrostatic hindrance to the availability of a redox couple to reach the surface. Considering DNA films on electrode surfaces, hybridisation of a nucleic acid target may further influence the resistive behaviour of the surface, which may serve as a method of deriving an electrochemical signal change. C_{dl} modelled by either a single capacitor, or constant phase element may also provide a key analytical parameter, as the charging characteristics of a surface are fundamentally dependent upon the molecular composition of surface-adsorbed species. This is a particularly pertinent analytical tool in non-Faradaic sensing approaches, however this methodology which is not adopted in this thesis. Progressing to the low frequency domain, a mass-transport controlled regime becomes dominant in the system described by a typical angled straight-line tail in the EIS spectra. This is effectively modelled by the Warburg element, though little analytical insight will be gathered from this region of the Nyquist plot in this study.

Despite the use of supporting electrolyte in solution, enabling electron transfer and closing of the circuit, a solution resistance, R_s is present. This is analogous to wire resistance within an electrical circuit, and modelled by a resistor in series, with the capacitance element. This shifts both the parallel charge transfer resistance and double layer charging behaviours along the x-axis of the Nyquist plot. To minimise any meaningful contributions from the solution resistance, an excess of background electrolyte is commonly employed, for example 100 mM KCl.

Increasing deployment of EIS in biosensing applications is based in its potential for label free assay development. Throughout this thesis, discussions and data are provided for various electrochemical labels that drive signal acquisition. However, EIS possess the power to directly monitor biomolecule binding events through deviations of electrical signals that can be attributed to biochemical interactions on the electrode interface. This removes the requirements for potentially costly chemical modifications to a bio-interface, and offers an opportunity to eliminate further processing, accelerating potential time to result.

2.6 Microelectrodes

With any e-DNA biosensor design, a key criterion is to have an optimal electrode design that allows for the maximisation of signal transduction. In much of this thesis, experimental protocols employ polycrystalline gold macro electrodes, with macro electrode generally a descriptor for a device with a critical dimension exceeding 25 µm. Many of the sensing approaches undertaken in this study are exploratory, and PGE serve as a useful tool for data acquisition for proof of concept studies. However, there will be a brief experimental reference to the translation of one of the sensing mechanisms reported, to a microelectrode platform. As such, it is necessary to consider some of the key theoretical concepts that govern the electrochemical activity of microelectrode devices.

The rationale behind microelectrode selection becomes apparent when the benefits of such a device are considered. This include enhanced signal to noise ratios, the rapid development of steady-state faradaic processes from rapid mass transport, minimal charging currents resulting from small electrode areas, lesser incidence of ohmic drop, and the ability to

work with small sample volumes thanks to the constraints of small device dimensions.[125,126,238,246–248] A brief theoretical background follows for these characteristics specific to microelectrodes.

Application of a step potential from a point where faradaic events can occur, leads to a reduction in ion concentration immediate to the electrode, as the species is reduced/oxidised and depleted. Consequently, a concentration gradient can form, from the bulk solution to the electrode, forcing the migration of ions via diffusion. This diffusion layer grows with time, as distant ions in solution are driven to the environment immediate to the electrode to replenish these depleted species. The diffusion behaviour of system is governed by the ratio of the electroactive surface area, and the solution volume, with a significant alteration in diffusion governed by a decreasing area. This is particularly pertinent to this study, as disk microelectrodes are employed for the electrochemical interrogation of a faradaic DNA sensing system. Here, diffusion occurs in two dimensions as opposed to the planar diffusion profile with increasing time of a macroelectrode. There is a radial diffusion profile with respect to the axis of symmetry (*z*-axis in Fig 2.8 (**a**)) and diffusion profile normal to the plane of the electrode (*r* axis in Fig 2.8(**a**)). Consequently, a hemispherical diffusion profile arises as the more efficient diffusion of bulk species to the edge of the electrode dominates. This will occur if the critical dimension is lesser than the thickness of the diffusion layer, a trait unique to the microelectrode.

Hemispherical diffusion is a higher efficiency process than planar diffusion, and therefore is the dominant process controlling mass transport to the electrode surface. As such the contribution from convection is minimal and the electrochemical reactions will settle in a time-independent steady state, or limiting current (i_L).

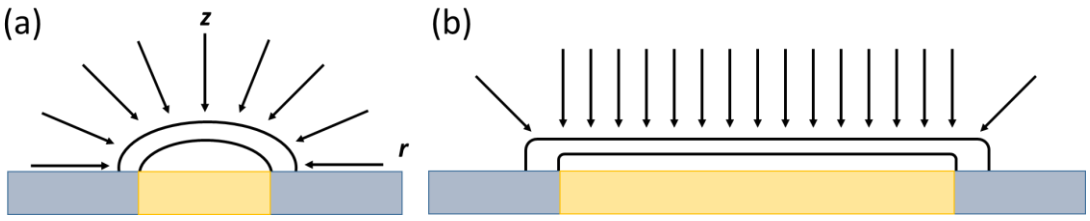

Figure 2.8 Diffusion layer profiles for both Microelectrodes (a) and Macroelectrodes (b). Here the arrows denote the direction of the diffusion from solution.

The faradaic current for a microelectrode disk (as employed in this thesis) under the influence of a diffusion-controlled regime can be neatly described as follows:

$$i_L = 4nFDcr \qquad \text{Equation. 2.15}$$

Where, n is the number of electrons transferred in a given reaction, F is Faradays constant, D is the diffusion coefficient of the specific redox species, c is the concentration of such species, and r is the radius of the electrode. Note in the Cottrell equation governing microelectrode limiting current, the dependence of electrode dimension r (radius) is apparent, and not A (area). This therefore allows for microelectrodes to experience a greater faradaic current to charging current ratio, in comparison to a conventional macroelectrode i.e. PGE.

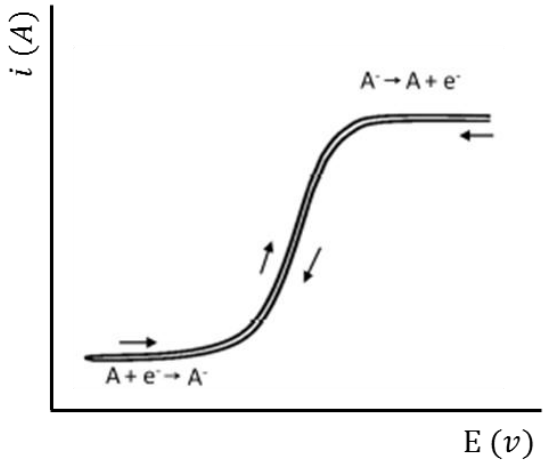

Figure 2.9 Typical pristine microelectrode cyclic voltammogram with characteristic "wave-like" sigmoidal profile. Here three distinct regions are present. Firstly, an anodic steady state head region with a limiting current. Secondly a non-steady state region in the centre of the voltammogram. Thirdly, a cathodic steady state region with a limiting current.

In response to a faradaic redox reaction, a microelectrode can be typically characterised by a diffusion controlled steady state, or time independent limiting current. In Figure 2.9 an exemplar cyclic voltammogram is provided, to display a positive potential sweep where a given redox species (*A*) is reduced prior to establishing a limiting current. Thereafter, a potential sweep is reversed to observe the corresponding oxidation of the mediator. Note the steady state

regions (anodic at the head, and cathodic at the tail of the voltammogram), and the tightness between the forward and reverse scan. This exemplar voltammogram assumes a perfect microelectrode, which is a surface of pure gold and free from surface adsorbed contaminants. It is therefore possible to generate a qualitative measure of electrode cleanliness from a cyclic voltammogram, as adsorbents can influence electroactive area of the surface. As such, a reduction of limiting currents may be observed. Equally, modification of a microelectrode through alkanethiol film formation, or mixed alkanethiol/DNA SAM immobilisation may also result in a reduction in limiting currents and provide a measure to the success of surface functionalisation.[249] This effect is represented in Figure 2.10 below, with the impact of MCP SAM formation on the voltammogram of a pristine gold microelectrode.

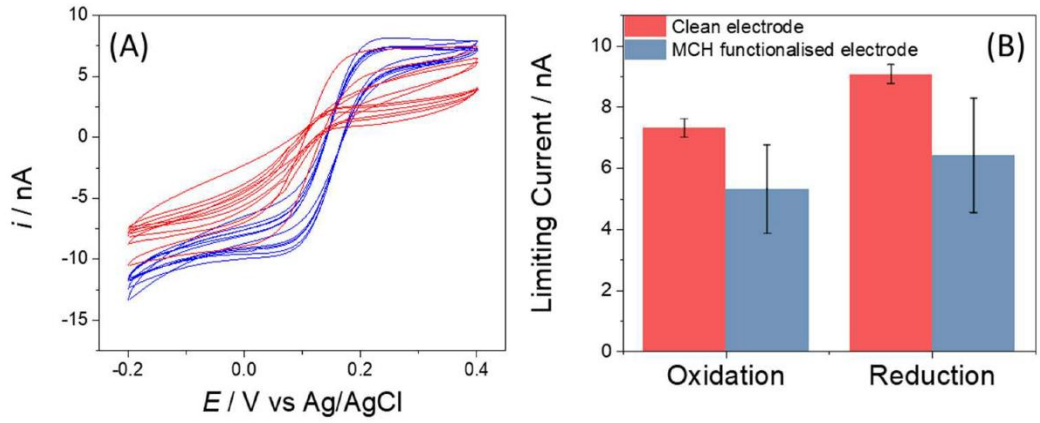

Figure 2.10 (**A**) Cyclic voltammogram of pristine gold microelectrode (blue) and after formation of a MCP SAM (red). (**B**) Respective limiting currents of both oxidation and reduction. N = 6, with SD as the error bars.
Adapted from: [16]
Corrigan et al. *Sensors*. ***18***, 6, *1891* (*2018*) doi.org/10.3390/s18061891

Finally, in response to impedimetric measurements microelectrodes may also produce a Nyquist plot distinct from that of a macroelectrode. This often contains a characteristic second semi-circle region occurring in the low frequency range. This is representative of the hemispherical diffusion profile associated with a true microelectrode and therefore requires a modification to the traditional simplified Randles circuit used for the fitting of macroelectrode EIS data, and is shown below:

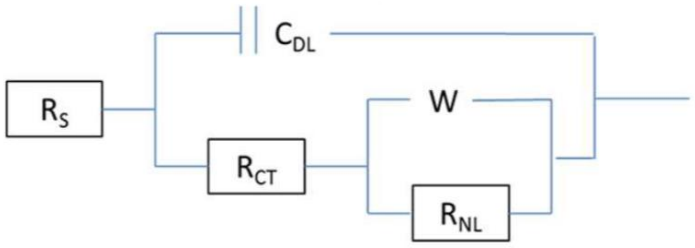

Figure 2.11 Modified Randles circuit of the fitting of EIS data from microelectrode interrogation.
Adapted from: [16]
Corrigan et al. *Sensors*. ***18***, 6, *1891* (*2018*) doi.org/10.3390/s18061891

The previous circuit features a non-linear resistance in parallel with the Warburg element to account for the hemispherical diffusion events in the system. EIS measurement of microelectrodes will be briefly investigated later in this thesis. The above circuit will be employed for electrochemical circuit fitting functions if the Nyquist plot evidences the characteristic response of a microelectrode. A distinction will be made for the appropriate circuit used to model the data.

2.7 Statistical Methods

2.7.1 Box Plots

Box Plots feature extensively in this thesis for the presentation and analysis of electrochemical data. They allow for a simple visualisation of a whole data set with a simple pictograph. The box plots used in this work detail a mean and median of the data set, with a box and whisker defining the range of all gathered data. Data is arranged in quartile ranges, with the minimum value of the whisker to the bottom of the box (lower quartile) corresponding to 25% of all the data set. The length of the box from the bottom to the top, lower to upper quartile, represents 50% of the data set. This range is classed as the interquartile range, or IQR (upper quartile – lower quartile). From the whisker to the top of the upper quartile details 75% of the data set. Often in electrochemical measurements, data points will be gathered that exist far removed from the range of the box and whisker. Establishing criteria for their exclusion from further analysis is necessary. In this work, an outlier is classified as a data point that exists out with 1.5 × IQR. Box plots also provide a simple method for assessing the distribution of the data

set. For example, if the data is normally distributed, one would expect both the median and mean to fall near the centre of the box. Equally, both a negative or positively skewed data set can be readily observed by the position of the mean with respect to the median.

Finally, it is possible to employ box plots as a useful method of comparing data sets, with the position of the median and IQR providing a visual representation of the difference between two distinct groups. If the median of one data set exists out with the IQR of another data set, it is likely that the two distinct groups are different. However, to determine the significance of such a difference further analysis is required.

2.7.2 t-Tests for Determining Significant Difference

In order to establish if two data sets can be classed as significantly different, the means of each group require direct comparison. In this thesis, either paired or unpaired t-tests are used for this purpose. Levels of significance are determined upon the output of the hypothesis testing functions in OriginPro, with the following criteria for significance deployed; *ns* $p > 0.05$, * $p \leq 0.05$, ** $p \leq 0.01$, *** $p \leq 0.001$.

Chapter 3

Engineering DNA Monolayers to Enhance Electrochemical Bio-Sensing Capabilities

Abstract:

DNA biosensing represents a key technology in the early diagnosis, and monitoring of human disease. This chapter documents the development, and performance of a hairpin based electrochemical system that does not rely on Faradaic signal through a redox label for detection of target oligonucleotides and which can operate down to the low pM sensitivity range. Self-assembly of modified hairpin oligonucleotides into a monolayer structure on polycrystalline gold electrodes, co-immobilised with 3-Mercapto-1-propanol, yields a functionalised transducer surface with a biorecongition element, specific to the capture of a target oligonucleotide from solution. Electrochemical investigations by Differential Pulse Voltammetry (DPV) and Electrochemical Impedance Spectroscopy (EIS), assess the performance of the sensor in response to various concentrations of complementary and non-complementary target; in Faradaic and non-Faradaic conditions. Faradaic conditions are found to be the most sensitive and reliable and the resulting assay is reported to be sensitive to incubation with a target sequence at sub nanomolar concentrations, more specific than the linear DNA probe strand format, with a large dynamic range; in the presence of the Ferri/Ferro cyanide redox couple. This system was successfully translated onto a microelectrode platform, with enhanced

sensitivity, while crucially maintaining a high degree of selectivity to appropriate targets. This non-labelled approach, for the direct measurement of hybridisation, excludes the requirement for the costly and complex tethering of redox active species to DNA hairpin probes. Thus, better establishes a system with improved ease of manufacturability, for translation to a point of care device.

3.1 Introduction

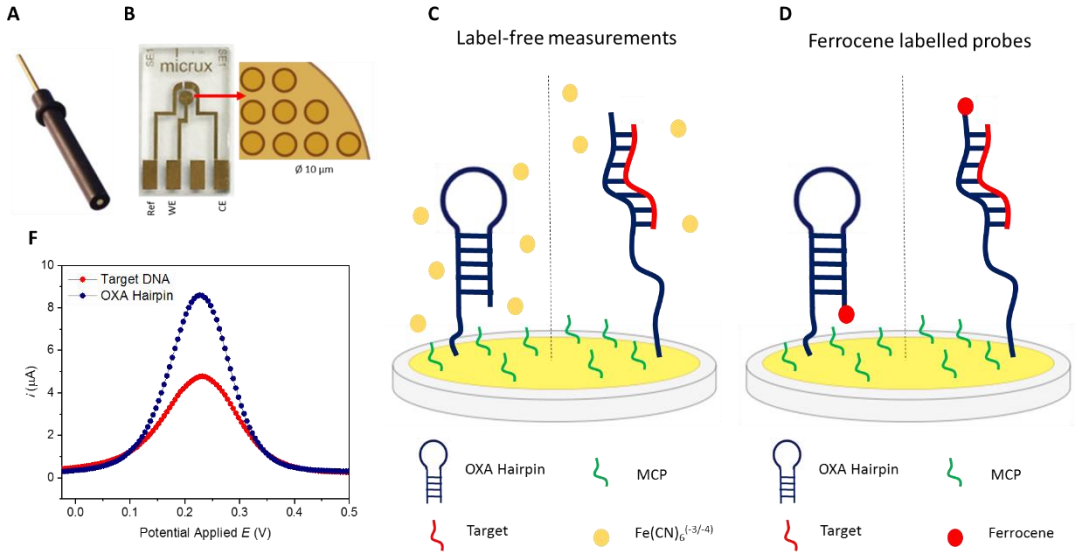

Figure 3.1 Experimental Outline. Images of (**A**) polycrystalline gold electrode (PGE) and (**B**) Micrux microelectrode with schematic of zoomed in working electrode array. Representation of functionalised electrodes and response to complementary target for a label-free (**C**), and Ferrocene labelled (**D**) measurements. (**F**) Exemplar Differential Pulse Voltammetry (DPV) data following target incubation, with a redox buffer of 2 mM $Fe(CN)_6^{(-3/-4)}$ in 100 mM KCl.

Continuous efforts to enhance both sensitivity and specificity of DNA biosensing devices has resulted in novel surface modifications, of increasing complexity. By the immobilisation of single stranded oligonucleotides into a layer through self-assembly, on a transducer (commonly planar gold or carbon electrodes), capture and detection of a complementary target sequences in solution may be possible. The potential applications are vast, with target analytes varying from bacterial nucleic acids associated with AMR,[13,29,35] circulating tumor DNA sequences (ctDNA),[28,37] and single nucleotide polymorphisms.[38,39]

Impedimetric electrochemical DNA biosensing makes use of this approach, typically employing the support of background electrolyte and redox species in solution to measure variations in current flow and impedance, associated with DNA binding events across an electrode surface. This method of target analyte detection has proven successful in various laboratory-based setups. Despite this, translation of these systems from the laboratory to a clinical environment is yet to occur, and yield the diagnostic revolution often promised. There are numerous issues yet to be resolved, associated with DNA biosensing at the fundamental level. Much of this stems from the inherent variability in the manufacture of uniform DNA layers, issues of layer instability over time, optimisation of receptor molecule packing densities, availability of binding sites for target hybridisation, and the determination of appropriate electrochemical parameters for maximum signal gain.[75,101,250–254]

One method of correcting for some of these issues, and enhancing signal gain of DNA biosensors, is the use of electroactive labels incorporated within the layer itself. Modifications include Ferrocene,[14,83] Methylene Blue,[255–257] melamine-copper ion complex terminated probes,[88] and Tris(bipyridine)ruthenium(II) chloride ($[Ru(bpy)_3]^{2+}$) intercalation for electrochemiluminesence.[89] Hybridisation of a target oligonucleotide to labelled probe sequences, may introduce new structural properties to the resultant complex, and either limit, or bolster availability of the label to exchange current with the electrode. This may help combat a key issue associated with redox buffer mediated sensing. In the conventional system, current is exchanged between the poised electrode and a redox couple in free solution (commonly Potassium Ferricyanide/Ferrocyanide ($Fe(CN)_6^{(-3/-4)}$). Variations in this current exchange may be induced by the changing ease of access the redox couple has to the electrode surface, via binding induced conformational changes to the immobilised layer, or by electrostatic repulsion between redox species in solution and the negatively charged DNA backbone on the probe. However, this system is complicated by layer stability issues, with transient channels often contributing to current discrepancies.[9] Many of the tethered redox couples detailed above exist as modifications to hairpin based DNA probes.[10-14,16,17] Often a means of minimising the contribution of electrode-to-electrode variation is to incorporate a secondary redox mediator that provides a signal at a differing potential to the primary reporter. This secondary tag is positioned on the probe to be at a constant distance from the electrode surface, and not influenced by any hybridisation events. This allows for a ratiometric approach to sensing, adding an on device control mechanism to sensing.[17,85,87,99] The requirement to greater enhance

sensitivity of biosensing applications also often leads to increasing surface complexities, either through functionalisation of secondary structures such as gold nanoparticles,[117–119] or more recently graphene.[120,121] While these approaches are capable of reaching femtomolar detection limits, sometimes in complex media,[27] issues of large-scale manufacturability, and high costs exist. This may limit the potential of such sensors to reach the clinical setting.

Another target for enhancing sensor performance is amplifying electrode surface area. Recent developments in heat shrinking of gold film substrates on silicon wafers provides a means of achieving this aim without the need for further costly surface modifications.[122,123] While this methodology appears promising, devices manufactured by this process have yet achieve uniformity, and reach high-throughput manufacturability. Microelectrode sensors (which have enhanced electroanalytical performance and large surface areas when arrayed) are manufactured through microfabrication techniques, allowing for reproducible components, and repeatable, low-cost production. There are indications in the literature to support increased limits of detection of targets for microelectrodes of decreasing size or when compared against conventional macroelectrode systems. [125,126] A solution based redox mediator was used to explore SAM formation, sensitivity and selectivity, of each probe for target hybridisation. It is shown that high sensitivity is achieved without the use of a redox tag which dramatically simplifies the system. Thereafter, we seek to characterise sensor development and performance on a microelectrode platform, with the aim of enhancing sensitivity and selectivity without the requirement for complex structural modifications to the sensor surface. Taking such an approach, i.e. employing a hairpin structure without a Faradaic label, has two major advantages. (1) Opens up bulk scale oligonucleotide synthesis where for example, kg quantities of thiolated DNA probes can be produced because of the lack of a redox tag. (2) It allows the relatively straightforward and sensitive EIS measurement of the hairpin probe to be carried out in the closed (unbound) configuration and open (bound configuration).

This study investigates the feasibility of employing both linear, and hairpin probes for detection of the OXA-1 beta-lactamase (OXA) gene, a known marker associated with drug resistant gram-negative infections. Here, immobilised probes, and capture arms are primer sequences for the amplification of a region of an artificial plasmid attributing to the *bla*OXA-1 β-lactamase gene; encoding extended-spectrum β-lactamases (ESBLs) and resistance to Oxacillin, across a host of gram-negative species. This *bla*OXA-1 β-lactamase gene sequence serves as the complementary target sequence in this study. While improvements in antibiotic stewardship are

essential in the management of bacterial resistance; rapid detection of resistant infections is critical in both clinical and long-term care settings. Point of care (PoC) biosensors serve as a key tool in tailoring effective antibiotic usage to enhance patient outcomes, while minimising community transmission of highly resistive species.

3.2 Materials and Methods:

3.2.1 Materials

All measurements were undertaken using an Autolab PGSTAT128N potentiostat with the additional FRA32M electrochemical impedance spectroscopy module, by scripts written in the Nova 2.1 software package (Metrohm Autolab) or a PalmSens 4 potentiostat (PalmSens, Houten, Netherlands). Polycrystalline Gold Electrodes (PGEs) of a 2 mm diameter were purchased from IJ Cambria Scientific Ltd (Llanelli, UK). An external platinum counter electrode (Metrohm, Runcorn, UK) and Ag/AgCl 3M KCl^- reference electrode (Cole-Parmer, UK) complete the electrochemical cell. Microelectrode devices were purchased from Micrux Technologies (Asturias, Spain), with the thin-film gold single electrode device encompassing a gold counter, and reference electrode (ED-SE1-Au) chosen for this study. Oligonucleotides for this work were sourced from Sigma Aldrich (Dorset, UK). 3-Mercapto-1-propanol (MCP) was obtained from Sigma Aldrich (Dorset, UK). All other chemicals required in this study are detailed in Table 3.1.

Chemical	Abbreviation	Supplier
De-ionised Water (resistivity ≥ 18 MΩcm)	Di	Sigma Aldrich (Dorset, UK)
Ethanol	EtOH	Sigma Aldrich (Dorset, UK)
Hydrogen Peroxide	H_2O_2	Sigma Aldrich (Dorset, UK)
Sulphuric Acid	H_2SO_4	Sigma Aldrich (Dorset, UK)
Potassium Chloride	KCl	Sigma Aldrich (Dorset, UK)
Potassium Ferricyanide	$K_3[Fe(CN)_6]$	Sigma Aldrich (Dorset, UK)
Potassium Ferrocyanide	$K_4[Fe(CN)_6]$	Sigma Aldrich (Dorset, UK)
Tris(hydroxymethyl)aminomethane	Tris Base	Sigma Aldrich (Dorset, UK)
Hydrochloric Acid	HCl	Sigma Aldrich (Dorset, UK)
Magnesium Chloride Hexahydrate	$MgCl_2 \cdot 6H_2O$	Sigma Aldrich (Dorset, UK)
Phosphate Buffered Saline Tablets	PBS	Sigma Aldrich (Dorset, UK)

Table 3.1 Chemicals used in this study.

3.2.2 Buffers

De-ionised water was used as the solvent for making all aqueous solutions in this study. Details are given below in table 5.2.

Buffer	Composition
Piranha Solution	18 M H_2SO_4 + 30 % H_2O_2 at a 3:1 (v/v) ratio
Functionalisation Buffer	1× PBS
TM Buffer (pH 8) + TCEP	50 µM TCEP in 10 × Tris-HCl (10 mM) + 50 mM $MgCl_2 \cdot 6H_2O$
Redox Buffer	2 mM Potassium Ferricyanide / Potassium Ferrocyanide in 100 mM KCl
Rinse Buffer	1× PBS

Table 3.2 Buffers used in this study.

3.2.3 Oligonucleotides

1× PBS + TCEP (at a concentration ×5 that of the probe) was used for the dilution of thiolated oligonucleotides. Specific sequences are provided in Supplementary Information Table S1.

3.2.4 Electrochemical Methods

Two electrochemical scripts were required in this work, which encompassed numerous techniques necessary to achieve the goals of the study. Details are provided below:

Cleaning CV 1	**Measurement Script 1**
For the stripping of contaminants from PGE	*Performance characterisation*
<u>Cyclic Voltammetry</u> **Potential Window:** -0.1 V to 1.6 V **Scan Rate:** 0.1 V/s **N^{O} of scans:** ≤ 15	**Hold:** 600 seconds
	<u>DPV</u> **Potential Window:** -0.1 V to 0.65 V **Step:** 0.005 V
	<u>SWV</u> **Potential Window:** -0.1 V to 0.5 V **Step:** 0.005 V **Frequency (Hz):** 25 or 50
	<u>OCP Determination</u> **Duration:** 20 seconds
	<u>EIS</u> **Applied Potential:** 0 V vs OCP **Frequency Range (Hz):** 10k – 0.1 **N^{O} of Frequencies / decade:** 10

Table 3.3 Electrochemical Methods

Electrochemical circuit fitting of Nyquist Data from EIS measurements is required to extract analytical parameters of solution resistance (R_s), Charge Transfer Resistance (R_{CT}), and Capacitance (C). Two equivalent electrical circuits were chosen to determine these parameters:

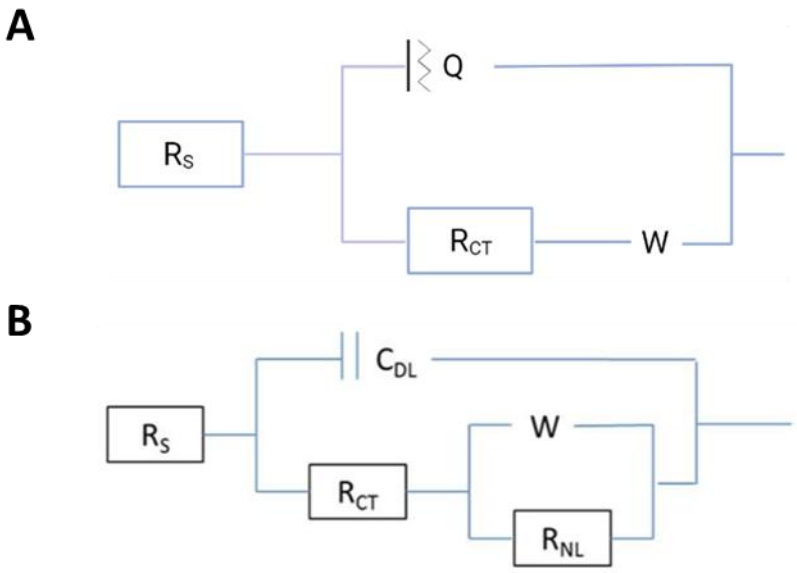

Figure 3.2 Analogous electrical circuits for EIS data fitting. (**A**) Circuit for Polycrystalline Gold macroelectrodes (PGE) and (**B**) for Micrux microelectrodes.

3.2.5 Electrode Polishing and Cleaning (PGE Preparation Method 1)

Appropriate cleaning is required to achieve conformity in PGE surfaces, and the removal of immobilised organics and contaminants. Mechanical polishing was first undertaken produce a near mirror finish via a series of decreasing alumina slurry diameters from 1 µm to 0.03 µm, on microcloths of varying roughness, with sonication in IPA for 2 minutes between each polishing step. Polishing occurred in a figure of eight motion for a duration of two minutes per electrode. Stripping of organics was attained by immersion of the gold surfaces in hot piranha (H_2SO_4 and H_2O_2 3:1 (v/v)) for 15 minutes. Electrochemical cleaning was undertaken by repeated cyclic voltammetry in 0.1M H_2SO_4 at 0.1 V/s, with a potential window of -0.1 to 1.6 V until a stable reduction peak was observed in the voltammogram (< 15 scans). It was necessary to confirm the effectiveness of the cleaning protocol with subsequent electrochemical interrogation of the each PGE by Faradaic methods. Measurement Script 1 was used to determine if key analytical tools of Peak Current (A) from DPV and SWV, and R_{CT} (Ω) from EIS, lie within a consistent range for PGE immersed in Redox Buffer. For microelectrode systems, a 70-second immersion in room temperature piranha solution was sufficient to produce clean surfaces and cyclic voltammograms near the ideal response for a pristine microelectrode.

3.2.6 Electrode Functionalisation

After cleaning, electrodes were immersed in Ethanol for 3 minutes, rinsed in Di-H2O, and then dried under a steady Argon stream. Electrodes were functionalised by overnight incubation (18 hours) at 37^0C, in a solution of 1 µM Probe DNA, and 10 µM MCP, in excess 50 µM TCEP (Tris(2-carboxyethyl)phosphine hydrochloride). Following this step, electrodes are named as Functionalised Electrodes. All oligonucleotides employed in this study are tabulated in Table S1 of Supplementary Information. Electrodes were washed in Di H_2O after 18 hours, prior to use.

3.2.7 Target Incubation

A serial dilution of targets down to 100 pM was undertaken in 1× PBS. A 20-minute incubation period of target and functionalised electrodes was deemed sufficient for hybridisation events to occur. Temperature was controlled at 37^0C throughout.

3.2.8 Sample Characterisation

Electrochemical measurements were undertaken in a conventional three-electrode cell (Gold Working PGE, Platinum Counter, and Saturated Ag/AgCl Reference). An Autolab PGSTAT302N potentiostat (Metrohm-Autolab, Utrecht, Netherlands), was employed to run all PGE measurements. Microelectrode devices were measured with the aid of a PalmSens 4 (PalmSens, Houten, Netherlands). Measurement Script 1 was employed to interrogate devices. For EIS the associated spectra was fitted to an equivalent circuit (Figure 3.2 (**A** or **B**)); with the χ^2 value determining the goodness of fit. Redox Buffer was chosen for the faradaic measurements of devices. When investigating the performance of Ferrocene tagged probes, 1× PBS was used as the measurement buffer.

3.3 Results and Discussion

3.3.1 Polycrystalline Gold Electrode Cleaning

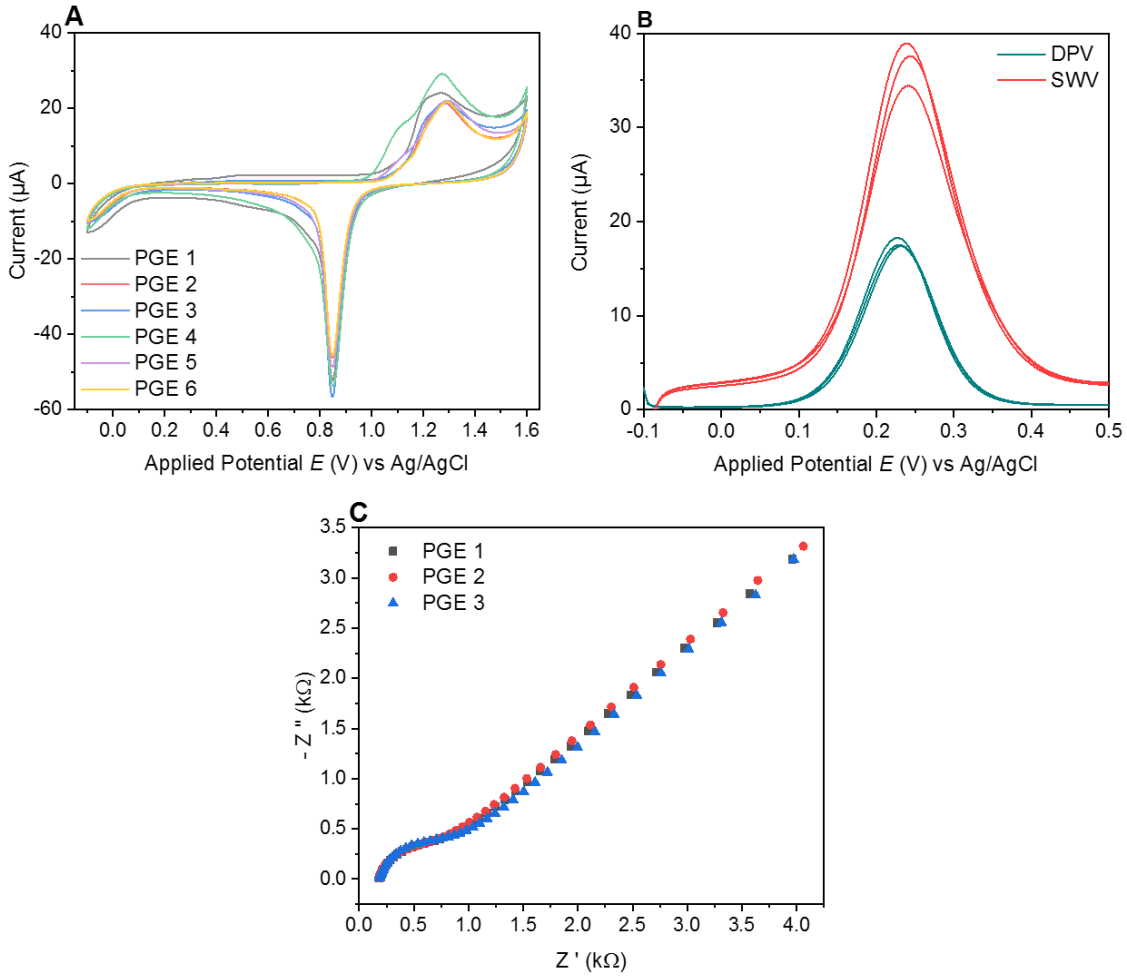

Figure 3.3 Electrochemical cleaning and characterisation of gold electrodes by Cyclic Voltammetry. (**A**) Polycrystalline gold electrodes (PGE) cycled in 0.1M H_2SO_4, at 100 mV/s. *E* (V) vs $Ag/AgCl^-$. (**B**) Typical DPV and SWV responses, and (**C**) typical Nyquist plot for PGE following cleaning protocol. (**B** + **C**) undertaken in 2 mM $Fe(CN)_6^{(-3/-4)}$ in 100 mM KCl, with *n* = 3 PGE.

Electrochemical cleaning of gold electrodes by cyclic in dilute Sulphuric Acid is a commonplace, and well described technique.[243,258] There are two key benefits to this approach. Firstly, there is an ability to determine an estimate of the electrode surface area through the integration of the area under the oxide reduction peak. The graphical area is proportional to the electrode area, assuming that one complete atomic layer of gold oxide is produced.[259] Secondly,

the establishment of a stable reductive peak is analogous to a constant electrode area, and thereby a surface stripped of surface contaminants. In (**A**), voltammograms for six independent PGE after 30 scans are shown. While there is variation in the magnitude of the reduction peak across the data set, evolution of this peak has ceased in all devices by ~10-15 scans. The variation in the reductive peak current can therefore be attributed to micron scale variation in the surface roughness, which can significantly influence electroactive area. Polishing of devices is sufficient to achieve a "mirror-like" shine, when regenerating these surfaces; however, this is purely a visual representation of surface topography. Once such devices are interrogated by faradaic measurements of DPV, SWV, and EIS, area associated inter-device variation is carried forward. However, the key analytical parameters of peak current and charge transfer resistance generally fall in to an acceptable range where devices can be considered "clean" and applicable for further measurement. Development of an acceptable range for determining the success of a cleaning protocol requires a large sample size, which has currently not been generated at this stage of the research. However, such a data set does exist in this thesis for PGE cleaned with an additional O_2 plasma stage. Details to follow in Chapter 4. In the work of this current chapter, cleanliness has been assumed where DPV peak currents and SWV peak currents are tending towards 20 μA and 40 μA respectively, as shown in (**B**), and R_{CT} can be estimated at ~500 Ω (**C**).

3.3.2 Polycrystalline God Electrode Functionalisation

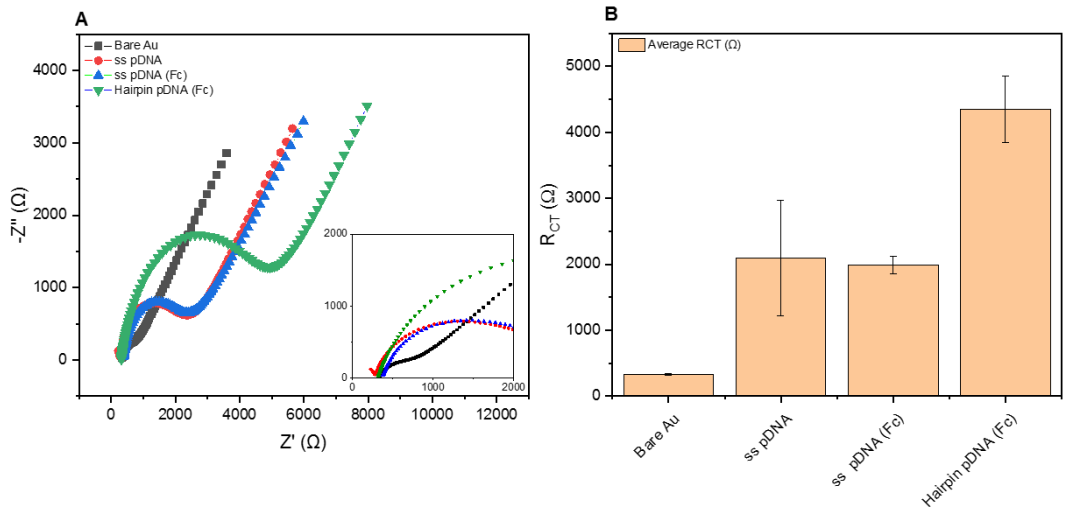

Figure 3.4 Assessment of PGE functionalisation with various OXA pDNA species by EIS. (**A**) Nyquist plot of various electrode modifications. (*Inset* – Close up of high frequency range impedance spectra). (**B**) Averaged R_{CT} (Ω) (*n=3*) for each electrode condition, with error bars displaying standard deviation. Impedance measurements undertaken in 2mM $Fe(CN)_6^{(3-/4-)}$ in 100mM KCl^-.

Electrode polishing and cleaning protocols employed in this study, have previously been identified as successful methods of removing contaminants from gold surfaces; with cyclic voltammetry in the presence of the $Fe(CN)_6^{(-3/-4)}$ redox couple yielding peak separations of 73 mV, near the ideal of 59 mV predicted by the Nernst Equation. This is further supported here with the low rate of electron transfer presented in the Nyquist Plot in Figure 3.4 (**A**), and minimal associated variation in the bare gold measurements. As also shown in Figure 3.4 (**B**), the increase in R_{CT} is dramatic following the functionalization of the electrode via self-assembly of ss probe DNA, ss Fc labelled probe DNA and the hairpin structure into monolayers; shifting from 325 Ω in a cleaned state, to 2094 Ω, 1990 Ω, and 4353 Ω for each respective functionalised condition. Interestingly, variation within electrodes functionalised with a conventional linear probe appears largest. The large R_{CT} associated with Hairpin Probe functionalisation, may be a function of the increased mass of immobilised DNA, creating both a physical, and/or negative charge barrier between the redox mediator in solution, and underlying gold substrate. As expected, variations in measurement parameters derived from EIS within each electrode condition are high. Inconsistency in initial electrode area, sporadic layer reorganisation, and the high sensitivity of the technique may all contribute to discrepancies in R_{CT}, which are prevalent

throughout the literature. Therefore, a relative signal change for each electrode will be determined following successive target incubations.

3.3.3 Target Sensing Performance and Specificity in Faradaic Buffer

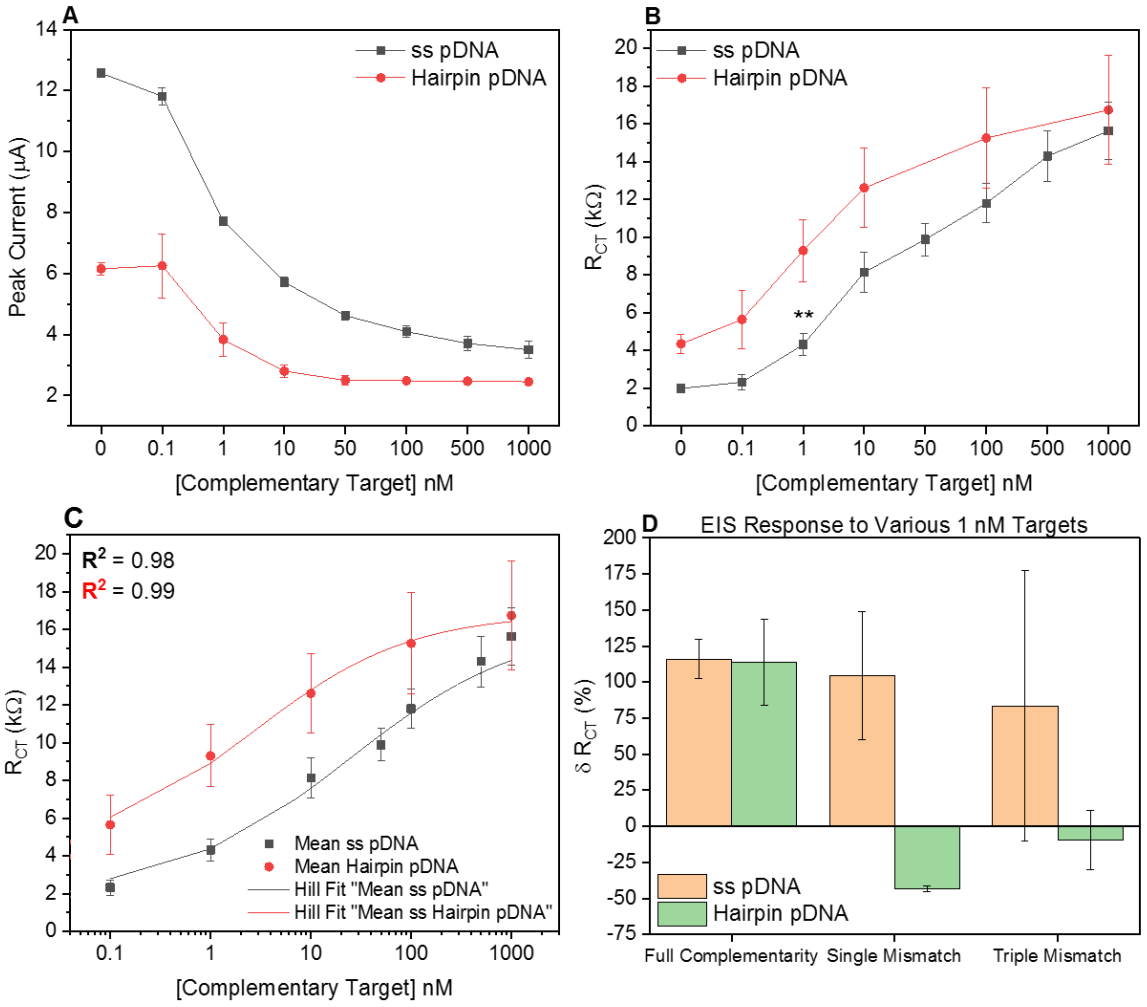

Figure 3.5 Electrochemical responses of functionalised electrodes to target incubation. (**A**) Mean DPV Peak Current (µA), and (**B**) Averaged R_{CT} (Ω) in response to a range of complementary target concentrations. (**C**) Hill function fitting of target response assay EIS data for both ss pDNA, and Hairpin pDNA functionalised PGE. (**D**) Mean % change of R_{CT} in response to various degrees of target complementarity. *N* = 3 PGE for each condition. Levels of significance given as ns $p > 0.05$, * $p \leq 0.05$, ** $p \leq 0.01$, *** $p \leq 0.001$.

Prior to target incubation, averaged peak currents are noted in Figure 3.5(**A**) at approximately 6 µA, and 12.5 µA, for the linear probe and hairpin probe respectively. Equally, in Figure 3.5 (**B**) the averages of measured R_{CT} data at 1990 Ω, and 4353 Ω, support the hypothesis of a larger probe architecture manipulating the rate of electron transfer, possibly through an enhanced electrostatic repulsion of the solution based redox mediator. Successive target incubations produce a dose response for both DPV and EIS measurements; with 1 nM of complementary target sufficient to induce a statistically significant difference in measured signal. This provides a promising start, with confirmation of effective SAM formation for both linear and hairpin probes, and the ability to detect a low nanomolar concentration of complementary target. In (**A**), the mean peak current appears to stabilise for the Hairpin probe FEs following incubation with 50 nM of complementary target. This may be evidence of sensor saturation. The ss pDNA architecture however does not share the same saturation point, with a small continuing loss of detected peak current following successive target incubations. Estimations of sensor performance are often presented by a limit of detection, and a working range. The former is attributable to the minimum analyte concentration that could be detected, though not specifically quantified, where an instrumental signal change is significant against the blank or background signal. This can be estimated the following equation:[260]

$$Y_{LoD} = y_B + 3SD \qquad \text{Equation 3.1}$$

Where, Y_{LoD} is the limit of detection, y_B is the mean of the blank signal (FE condition for this study), and SD is the standard deviation of this mean. Use of this estimation requires a number of repeats of the blank condition to generate an effective measure of discerning analyte binding signal from background noise. Gathering a large data set for the blank condition is time-consuming, particularly with EIS measurements; and evidence reported in the literature for signal drift associated with repetitive EIS measurements may make this an undesirable method for performance analysis. Thereafter, a calibration curve would then be required to derive a X_{LoD}, which would then be attributable to a target concentration which exceeds the noise threshold. Many studies employing this method of analysis, often derive an estimation of the Y_{LoD} through linear regression analysis of the experimental calibration curve (see Equation 3.4),[261] to bypass the requirement of multiple blank repeat measurements. However, this

method requires a truly linear response to target analyte binding that is not often observed. In this particular study, response to target generates a sigmoidal response, often with minimal signal change at low concentrations, a slope region where the response is near linear, and a final stage tending towards sensor saturation.

The R_{CT} data provided in (**B**) exists as a sigmoidal growth trend, enabling its appropriate fitting by a Hill function. This is shown in (**C**) for both systems, exhibiting strong correlation coefficients.

$$Y = V_{max} \frac{x^n}{k^n + x^n} \qquad \text{Equation 3.2}$$

Where, V_{max} is maximum binding obtained, x is the concentration of the target, k is the dissociation coefficient and n is the Hill slope describing cooperativity. Successful fitting allows for an estimation of sensor LoD by the application of the following equation:[26]

$$LoD = \frac{3\sigma}{slope} \qquad \text{Equation 3.3}$$

Where σ is the standard deviation of the blank (FE condition) and $slope$ the parameter n from the Hill fitting. It is therefore possible to provide an estimation of sensor LoD of detection for both probe architectures, with the linear ss pDNA system at 836 pM, and the hairpin system at 2.71 nM.

Finally, an indicative working range of the sensor can be determined by the boundaries of a linear region in the data set. The lower limit of which has been set in this thesis as the first target concentration where incubation produces a significant difference in mean signal. In the DPV plot given in (**A**) linear fitting does not produce a strong correlation coefficient indicative of a linear response for any region of the data set. For the Nyquist plot of (**B**), linear regions are only observed from the ss pDNA system, beginning at 1 nM and extending towards the final experimental concentrations. Its upper boundary is not yet established, which may be indicative

of either of two outcomes; that a series of immobilised probes remain free of hybridisation, or that electrochemical signal is suffering from a near linear drift which may be contributed to by SAM reorganisation, and or degradation.

It was necessary to assess the selectivity of each sensor design by introducing varying degrees of mismatched targets (single mismatch and triple mismatch, with respect to a complementary target oligonucleotide). For this assessment, EIS was selected due to heightened measurement sensitivity of the technique, in the aim of better electrochemically observing hybridisation. Following single mismatch target incubation shown in Figure 3.5 (**D**), the linear probe elicited a response similar to that of a complementary hybridisation event with a near 100% increase in mean R_{CT}. Note, there is an increased variation in this signal change. This may be a function of a decreased occupancy rate of the recognition elements across the sensor surface due to mismatches, and a higher influence of non-specific binding events on signal. Progressing on to the hairpin based system; the single mismatch target induces a decline in measured R_{CT}. The expected result would be for a small increase in mean R_{CT}, as we hypothesise there would be a degree of non-specific interaction between the target and hairpin based monolayer. The observed decline in mean R_{CT} is not suggestive of a hybridisation event and may be an artefact of layer re-organisation associated with washing, or target injection steps.

With a triple mismatch target, there is the suggestion of a lesser number of successful hybridisation events in the linear probe, as indicated by the declining mean R_{CT} and high standard deviation (see Figure 3.5(**D**)). Again, this increased standard deviation may represent a combination of factors; non-specific interactions between target and the functionalised electrode, and varying levels of hybridisation across electrodes. Conversely, the hairpin-based system appears largely unresponsive to such a target, with minimal signal change against the baseline measurement being indicative of negligible hybridisation. From this, we can surmise the enhanced specificity of a hairpin probe against a conventional short linear probe. The biorecognition element within the hairpin probe exists in the loop, where a region of self-complementarity exists between as few as six base pairs in the stem of the structure (see figure 3.6). We hypothesise that complementary target oligonucleotides at 20 nt in length can sufficiently out compete this phenomena, and open the hairpin into a long single strand extruding into solution.[262,263] However, the introduction of successive basepair mismatches between target and the recognition element, limits the hybridisation efficiency, and thus resultant signal change.

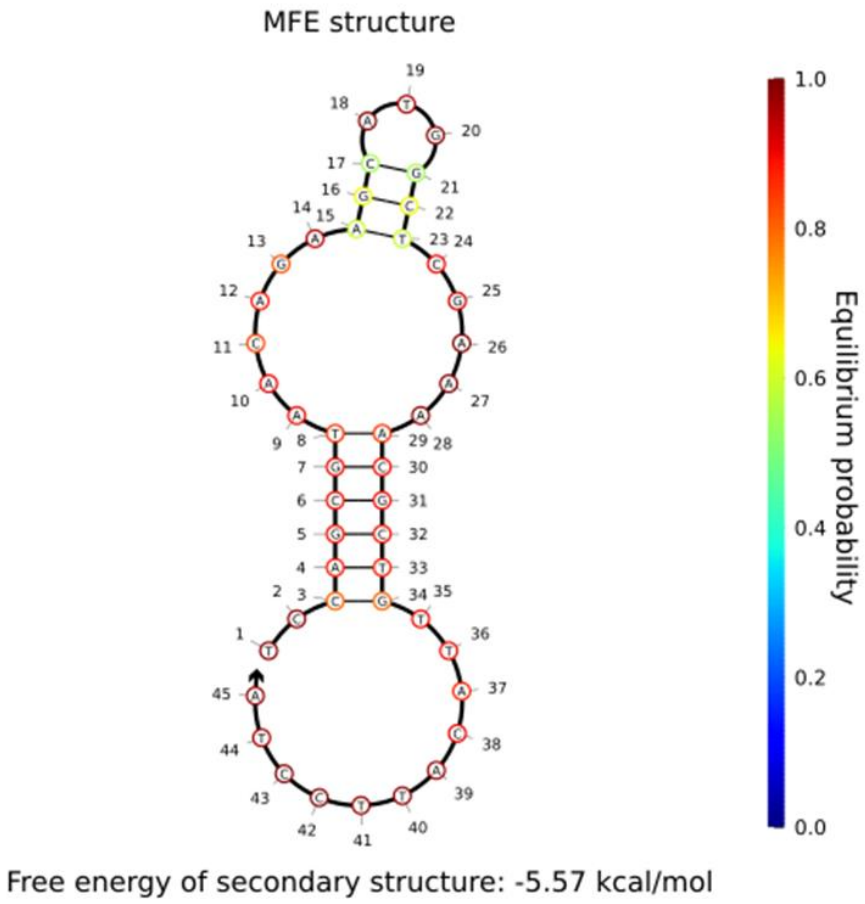

Figure 3.6 Estimation of secondary structure for sequence HPv2. Fc tag at the 3' of the sequence (following nt 45). The OXA (target) recognition element exists within nt 8 – 28. The secondary stem-loop region within the recognition element is perhaps not optimal, though specificity trials in Figure 3.5 suggest this not to be a significant hindrance to sensor design. Figure generated from NUPACK (nupack.org)

The quenching of R_{CT} signal change associated with base pair mismatches between the target oligonucleotide, and the recognition element of the hairpin is promising. While other works have been reliant upon tagged redox molecules to the probe to be the mediators of a ratiometric signal, this simple method allows for label-free electrochemical observations of target binding events in the presence of a solution based redox mediator alone.

Noteworthy here, is the minimal variation in mean peak current and charge transfer resistance as shown by the tight standard deviation of the mean shown throughout all data points. While this is for a small sample size (n = 3), such consistency in key electrochemical parameters is not common throughout this thesis. While this data set is promising, and does generally fit choice data reported in the literature where sample sizes are small and error bars

often minimal, it is imperative to note prior and subsequent repeats of this experiment (full data not shown here), have yielded highly variable FE mean peak currents. These have ranged from ~ 1 μA – 20 μA, despite similar methodologies for electrode preparation and functionalisation.

An initial aim of this study was to investigate the appropriateness of the Ferrocene tag to serve as the redox mediator, in a non–faradaic buffer. As mentioned in the introduction to this chapter, Ferrocene tags have been reported to present strong electrochemical signals with appropriate positioning in respect to the underlying transducer. Works by Fan and colleagues noted electron transfer events with Ferrocene tags at similar hairpin concentrations yielding mean DPV peak currents in the nA range.[264] Prior to the undertaken of this work, an estimation of the specific confirmation of the chosen probes for this study with NUPACK analysis.[265] The linear probe at 20nt in length has an insignificantly small likelihood of a confirmation other than linear given the ionic conditions of the buffer; structural condensation is unlikely in a 1× PBS measurement buffer.[266] Estimations of secondary structure for the hairpin-designed sequence were as desired, with high likelihood of a hairpin confirmation. Consequently, it was hypothesised that there would be two distinct observations for the chosen probes for sensor development.

Firstly, the linear single stranded probe should be of sufficient flexibility to facilitate electron transfer events by positioning the Ferrocene tag at a necessary distance to the underlying electrode.[82,267] This was assumed, dependant specifically on the SAM conditions. For example, the probe monolayer must be somewhat homogeneous, and not exist as dense clusters where electrostatic repulsion between neighbouring strands forces a perpendicular strand orientation to the surface.

Secondly, should a desired hairpin confirmation exist, the Ferrocene tag should in theory be near the electrode surface, and capable of undergoing oxidation at an approximate applied potential of 400 mV. However, redox activity attributable to the Ferrocene tag is not confirmatory of the probe confirmation. This may be as a result of lengthier hairpin probe sequence than required. For example, if a sequence length of approximately 34 -36 nt be chosen, the Ferrocene tag would be positioned at the end of the stem region (3’). Here, the long single stranded tail may result in poor tag positioning. This would be a logical place to open future investigations on labelled hairpin probes.

Consideration should also be given to the specific locale for stem and loop formation. When evaluated, a specific secondary structure was deemed likely. However, the specific hairpin confirmation when immobilised as part of a mixed SAM may be variable. This is described by the following schematic, with a representation of how three distinct hairpin outcomes may influence Ferrocene tag availability aid in electron transfer.

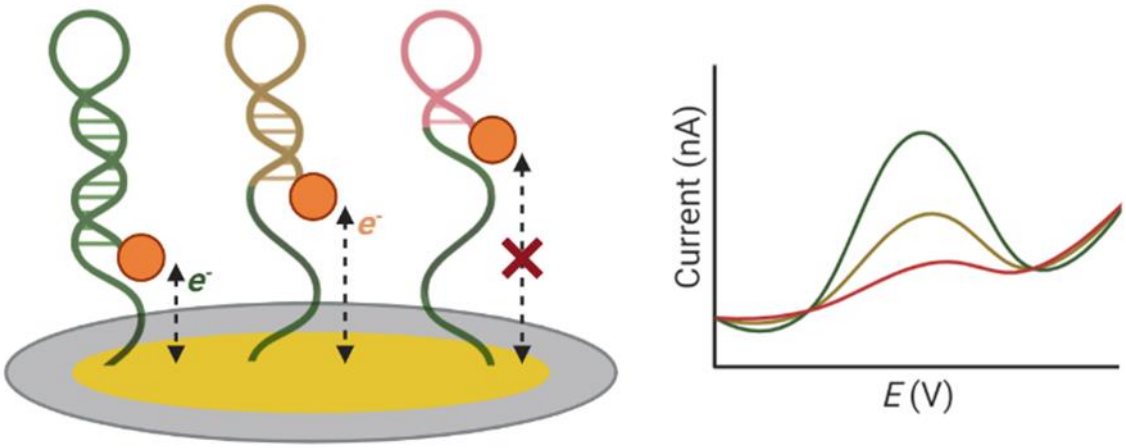

Figure 3.7 Schematic outlining possible hairpin secondary structures, and the hypothesised impact variable Ferrocene tag surface proximity may have on electrochemical signal.

Numerous experiments were attempted to characterise the feasibility of a Ferrocene labelled mediation of signal transduction through various electrochemical methods. In the absence of a solution based redox mediator and supportive electrolyte, total impedance of the cell is high and traditional circuit fitting techniques for analysis were not possible. DPV and SWV were therefore elected as the primary measurement tools for the assessment of sensor systems in the absence of the $Fe(CN)_6^{(-3/-4)}$ redox couple.

3.3.4 Hairpin System using redox tag (non-faradaic buffer)

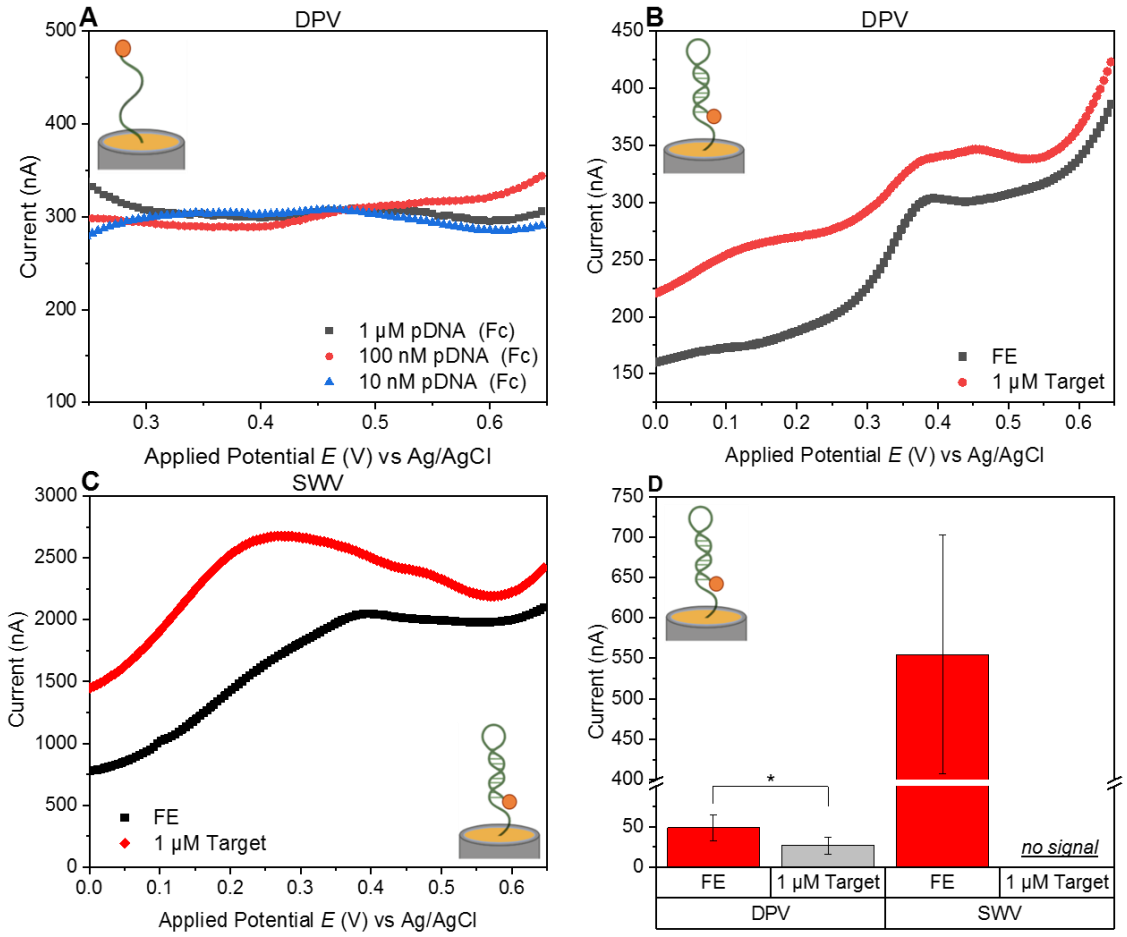

Figure 3.8 Electrochemical characterisation of Ferrocene-tagged linear and hairpin probe architectures. (**A**) Typical DPV traces for 3 PGE each functionalised with a distinct linear probe concentration (1:10 probe:MCP ratio). Typical DPV (**B**), and SWV (**C**) traces for a hairpin probe tagged with Ferrocene, prior to and after target incubation. (**D**) Recorded mean peak current for pre, and post-target DPV and SWV measurement with hairpin probe. Error bars = SD. Levels of significance given as ns $p > 0.05$, * $p \leq 0.05$, ** $p \leq 0.01$, *** $p \leq 0.001$.

Mean DPV voltammogram traces are presented in Figure 3.8 (**A**) with various concentrations of the Fc-tagged single stranded pDNA OXA probe. Common to all is consistency in the ratio of probe to MCP (1:10) for electrode functionalisation by the coimmobilisation. Each trace is the averaged signal for two functionalised PGE. It is apparent that there is no defined peak that could be attributed to Ferrocene oxidation. However, with significant data smoothing and baseline subtraction in OriginPro 2018, a peak did emerge for one of the six FE interrogated. Note, this peak was small (< 10 nA), particularly broad in its aspects, and smeared across a wide

potential range. It is mentioned here, as it cannot currently be definitively discounted as Ferrocene oxidation, though it is more likely a noise artefact. With a hairpin confirmation at a concentration of 1 µM, there is evidence of a small, though defined peak near the formal potential of 400 mV (**B**). Peak analysis was possible in over 80% of DPV interrogated devices (5 out of 6). With target incubation the mean profile of the DPV trace changes, with a depression in peak amplitude, and a loss of sharpness and definition. With the SWV measurement (**C**), a peak was apparent of a substantially larger magnitude across all devices; however, it again was smeared across a large potential range and was poorly defined. Incubation with target dramatically alters the profile of the mean SWV trace, quenching any peak which could be attributable to Fc oxidation. The magnitude of each peak currents for fc tagged hairpin probes is compared in (**D**) following both DPV and SWV interrogation. The red columns denote mean recordable peak current for the functionalised devices, with the error bars attributable to the standard deviation of the mean. Following DPV, a mean peak current of 48.9 nA is recorded, though the standard deviation of this data set is large at ± 15.9 nA. It is possible for this to be a function of the condition of the underlying electrode, i.e. surface roughness/electroactive area. However, as emphasised previously the availability of the Ferrocene tag to drive electron transfer is conditioned on its proximity to the electrode surface. This is therefore dependent upon the specific confirmation a probe species may adopt when immobilised. Estimations of secondary structure cannot guarantee the nature of such a hairpin confirmation once immobilised, where neighbouring probes and incidence of SAM heterogeneity can influence probe densities and orientations.[74] The schematic given in Figure 3.7 detailing possible hairpin outcomes may provide a contribution to signal variance though the magnitude of such a contribution is not yet clear. Complementary target incubation at 1 µM is sufficient to induce a significant decline in mean peak current (p = 0.047). The column for mean peak current of FE interrogated by SWV is greater than an order of magnitude larger at 554.84 nA, with a large standard deviation of ± 120.4 nA. SWV interrogation following complementary target incubation period yields voltammograms for all devices, absent of a defined peak that one can attribute to Ferrocene oxidation. As such, no recordable mean peak current can be employed for a derivation of hybridisation induced signal change. In this study, SWV was undertaken at a frequency of either 25 or 50 Hz, with the data surmised so far at 50 Hz. Subsequent analysis of literature entries for redox tagged DNA probes highlight the delicate interplay between the probe structure, the electron transfer kinetics of the redox reporter, and the frequency of the

square wave pulse chosen to interrogate the system. Dauphin-Ducharme and Plaxco launched a systematic investigation into the specific electrochemical parameters required to monitor and best maximise redox tag signal for a series of electroactive species. Notable, was the inability to observe a "signal on" phenomena at any employed SWV pulse frequency for a Ferrocene reporter. The authors attributed this to the rapid electron transfer rate of the species, and estimated "signal on" behaviour only to be observable at frequencies greater than 25 kHz.[14] In their sensor design, the aptamer probe is immobilised in a confirmation that limits access of the Ferrocene tag to the underlying electrode. Target analyte binding would induce a conformational change in the probe and reposition the tag proximal to the surface. The hairpin design in this study is theorised to function in by an opposite process, with target hybridisation opening the secondary structure and reducing tag/electrode proximity. While this method would be described as a "signal off" approach, the electron transfer kinetics of the Ferrocene tag are still a critical consideration in developing a successful assay. As such, a detailed investigation would be required for establishing appropriate SWV parameters to best optimise this electrochemical method for Ferrocene tags. At the time of undertaking the experimental work in this chapter, failing to consider the subtleties of SWV pulse frequency and the electron transfer kinetics of the tagged species was an oversight. It may also be apparent to the reader the emission of any cyclic voltammetry data displaying the reversibility of Ferrocene redox, which would be beneficial in confirming the availability of the tag to the electrode. In retrospect, this was an important experiment to have undertaken in establishing a base characterisation for Ferrocene tagged pDNA SAMs.

Introduction of a redox tag to the two distinct probe architectures was proposed as a means of enhancing sensitivity. However, the recorded peak currents for this Ferrocene redox mediated system are small, variable, and often transient. As such, it was theorised that translation of the system to a microelectrode platform may offer the improved sensitivity desired for device development without electroactive labelling, or enzymatic support. Microelectrodes offer a multitude of electroanalytical advantages, and therefore serve as a promising technology for biosensing applications. Reduced *iR* drop, enhancement of the signal to noise ratio, and lack of sensitivity to convection improve the feasibility of complex measurements.[29] As such, microelectrodes have been employed across a range of disciplines, due to their ability to outperform macroelectrodes in chemical,[268] industrial,[247,248] and biomedical applications.[32]

3.3.5 Microelectrode Cleaning and Functionalisation

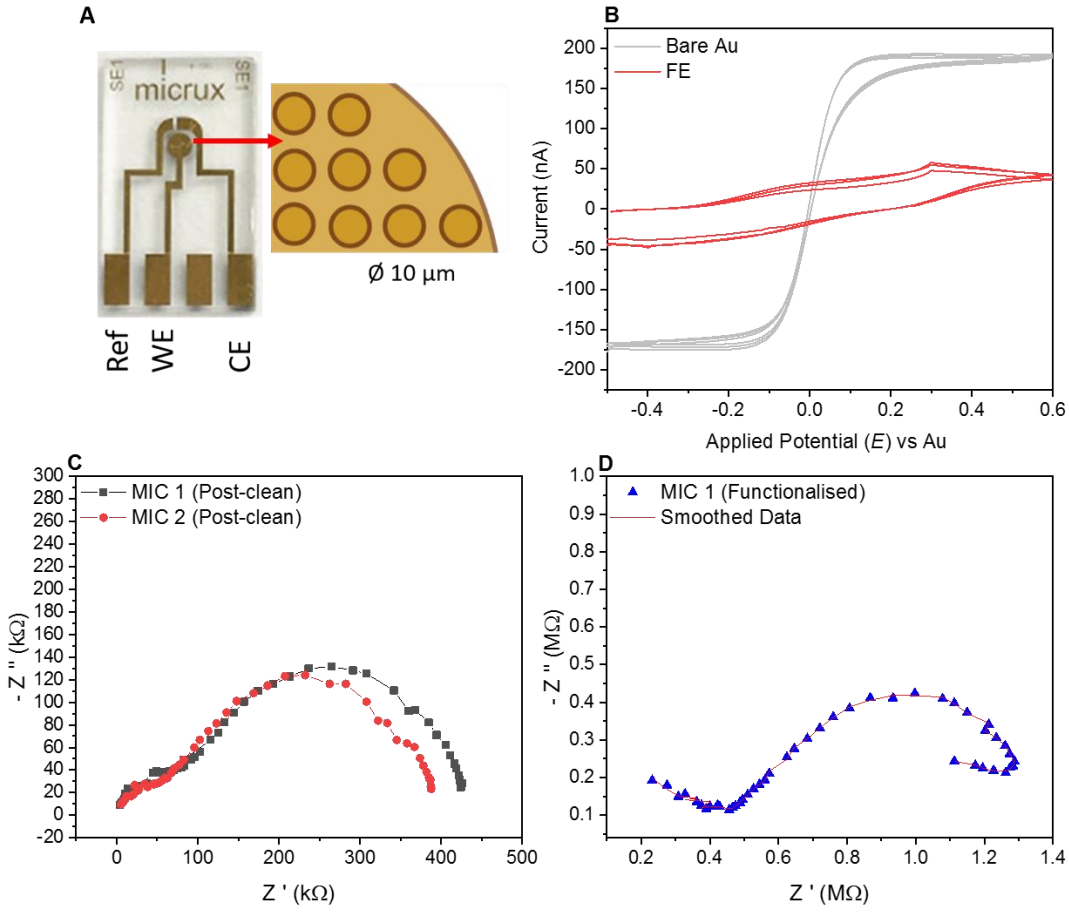

Figure 3.9 Electrochemical characterisation of microelectrode cleaning and functionalisation. (**A**) Schematic of Micrux Microelectrode Device with zoomed in region showing array of 10 µm diameter working electrodes. (**B**) Cyclic voltammogram of a typical Micrux device following piranha immersion (grey traces) and after functionalisation with 1 µM Hairpin pDNA + 10 µM MCP (18 hours) (red traces). 3 scans for each condition. (**C**) Nyquist plot for two independent devices, with interrogation post-clean. (**D**) Nyquist plot for a single device after functionalisation. Measurements undertaken in 2 mM $Fe(CN)_6^{(-3/-4)}$ in 100 mM KCl.

A schematic of the Micrux devices used (ED-SE1-Au) is provided in Figure 3.9 (**A**), detailing the device comprising the working electrode with EPON SU8 providing the insulation and patterning. Accompanying the WE, is an on chip Au reference and counter electrode. This approximate cell size is of 2 mm diameter allowing for small sample volumes of between 1-5 µL. According to the manufacturer, cyclic voltammetry is required for the cleaning of devices, with a minimum of 10 scans in 0.1 M H_2SO_4 at a rate of 0.1 V/s. This was attempted in the research

group, though the claim of enhanced performance was not observed. As such, a chemical cleaning stage was investigated, with various immersion times in concentrated piranha to ensure the appropriate removal of surface bound organics. An immersion time of 70 seconds appeared sufficient to provide cyclic voltammograms displaying typical traits of a microelectrode, as evidenced in (**B**) with the "wave-like" voltammogram.[249] Here, the grey traces denoting three scans for a single Micrux device with diffusion limiting current for the oxidation of potassium ferrocyanide to ferricyanide at ~190 nA at and above an applied potential of 200 mV. The limiting current for the reduction of potassium ferricyanide to ferrocyanide flows in the reverse scans at ~172 nA beyond -200 mV. Following functionalisation with a hairpin pDNA / MCP monolayer (red traces) the voltammogram displays clear evidence of reduced limiting currents within the system. This is primarily a function of changing interfacial properties, as the mixed monolayer hinders access of the solution based redox species to mediate electron transfer. The previously "wave-like" profile of the voltammogram is quenched to faintly sigmoidal profile. This is reflected by a limiting current for oxidation of < 50 nA, and a the reduction reaction > -50 nA. Quantifying a true limiting current for both reactions is challenging for this device given the lack of stability in the voltammogram. Progressing on to interrogation by EIS, (**C**) provides a Nyquist plot for two cleaned devices. Note, a number of data points across the impedance spectra have been removed for clarity. Noise is a particular issue at the high frequency range (kHz) on all measured devices. The two traces provided are choice responses, from a series of devices. Commonly noise limits the availability to record any meaningful data sets for analysis. There are two possible explanations for this. Firstly, the experimental set-up is subject to interference from a high degree of electrical noise. Many of these repeats where undertaken on the bench-top, and likely poorly isolated from environmental noise. Secondly, the data gathered in this chapter with microelectrode devices was undertaken using the PalmSens 4 potentiostat. While this instrument has capability of running EIS at a broad frequency range (μ-MHz), laboratory experience has suggested its propensity to suffer the effects of electrical noise to a greater degree than the Autolab PGSTAT302N potentiostat. Within (**C**), each EIS spectrum does display some interesting behaviour, which is in accordance with previous reports in literature. At the high frequency range, there is an indication of a small charging loop that may be analogous to charge transfer resistance.[269] Thereafter, the expectation would be for a flattened loop region encompassing the remaining frequency range that is supportive of the hemispherical diffusion profile. There is a hint of such a profile apparent

in both traces of (**C**); however, there is a greater rise and fall in these traces than in those observed by Sheffer et al, and Corrigan et al.[46,47] Following overnight functionalisation, the profile of the Nyquist plot is dramatically changed. As seen in (**D**), the small initial charging loop at the high frequency is no longer apparent. It may be possible that this has failed to be captured by the upper frequency limit; extension to 20 kHz may have allowed this to be documented. At the low frequency range there is evidence of inductive behaviour. This is a phenomena observed previously by Sheffer et al, where they theorised such a response to be indicative of a porous electrode, covered by an imperfect SAM. Equally the gathered impedance spectra now is better viewed with a MΩ scale, further indicative of the immobilised hairpin / MCP monolayer hindering the incidence of electron transfer. Again, it is imperative to emphasise the Nyquist plots of (**C**) and (**D**) are comprised of two independent devices. Numerous devices were selected for electrochemical interrogation, however the quality of data generated from EIS interrogation was mainly very poor. From the data set provided in (**C**) and (**D**), analogous electrical circuit fitting was attempted using the circuit of Figure 3.2 (**B**). Despite trial and error to better model the impedance spectra, generating a $\chi^2 < 1$ was not possible, indicating the poor quality of fitting.

While EIS was a useful measurement tool for the probing of functionalised macroelectrodes previously in this chapter; its use in the microelectrode set up is complicated by numerous factors. These include its high susceptibility to noise, poor quality electrochemical circuit fitting, inability to multiplex sequential measurements of different devices in a single protocol, and long-time requirement (~ 20 minutes / device) for the gathering of a full frequency spectra. As such, rapid measurement techniques such as DPV were deemed better suited for the assessing the translation of a DNA hairpin SAM to a microelectrode platform.

3.3.6 Translation to a Microelectrode platform

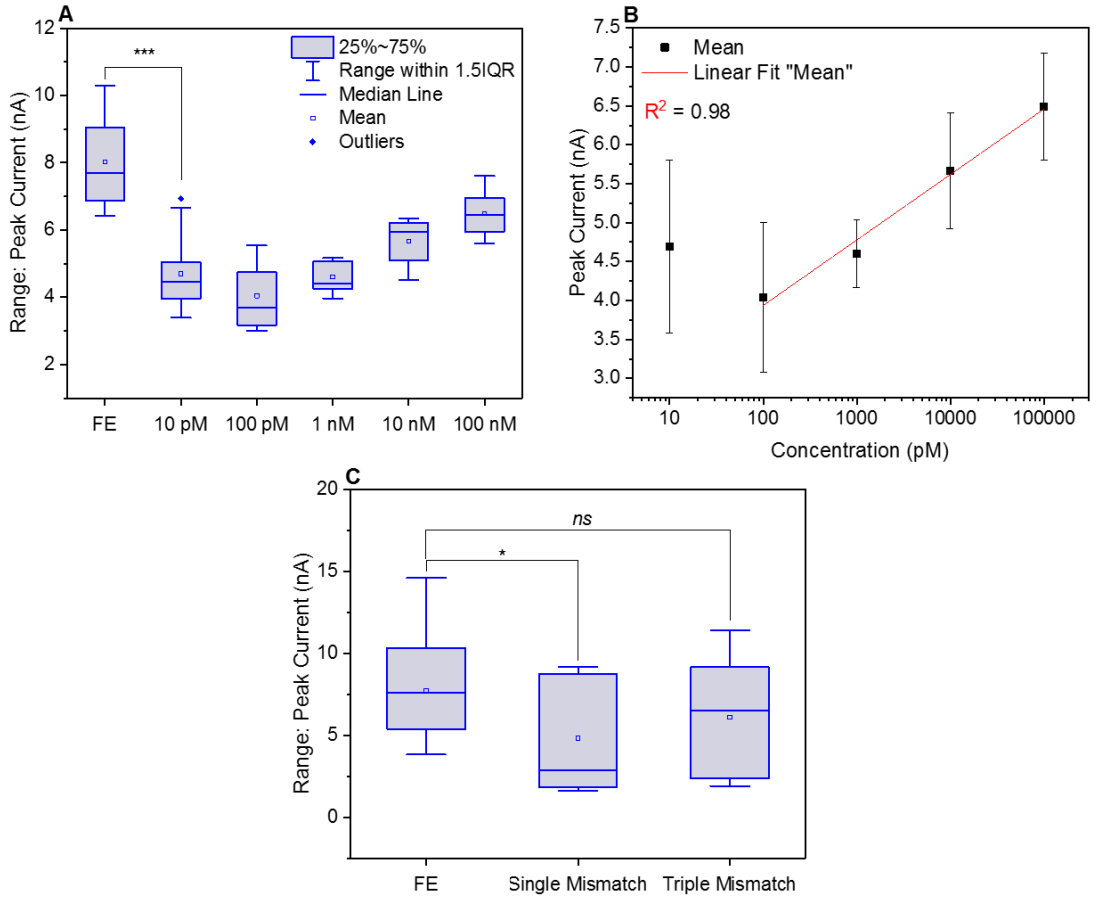

Figure 3.10 DPV Responses of Functionalised Electrodes to Various DNA Targets. (**A**) Incubation with increasing concentrations of a complementary target oligonucleotide . (**B**) Linear fit of Mean Peak Current (nA). (**C**) Peak Current following incubation with a 10 pM concentration of target with either a single, or triple basepair mismatch. Levels of significance given as ns $p > 0.05$, * $p \leq 0.05$, ** $p \leq 0.01$, *** $p \leq 0.001$.

In Figure 3.10 (**A**), incubation with a 10 pM concentration of complementary target yields a significant decline in mean peak current ($p = 0.0007$), at ~39 %. This signal change is achieved from a target concentration two orders of magnitude smaller than the minimum target concentration used in the PGE study. This is promising in working towards a heightened sensitivity from a microelectrode platform. A further reduction in mean peak current is then noted with 100 pM target incubation. However, subsequent increasing concentrations of target incubation yields an increasing mean peak current beyond. The expectation for an increasing mass of target bound to the surface would be an increasing negative charge density, the subsequent repulsion of redox species in solution, and a resultant decline in mean peak current.

The observation is at odds with this expectation, but is reflected in numerous investigations yet unpublished from our group. Equally, this behaviour has been reported in the literature. In 2015, Miodek et al; commented on an observation of increasing shifts in R_{CT} with low concentrations of complementary target, only to note a negative shift in R_{CT} with incubation of a high concentration. This was suggested to be a function of non-specific interactions dominant at low concentrations, and specific target binding at high concentrations. Important to note is the specifics of their investigated system, with an aptameric probe immobilised to capture a large thrombin molecule of an approximate molecular weight of 72 kDa.[270] As such the influence capturing such a large molecule may have on global SAM behaviour may not be directly analogous to the system explored in this work.

In (**B**), the mean peak currents are plotted against target concentration to allow for further analytical assessments. Many e-DNA biosensor designs in the literature will report a sensor limit of detection (LoD), or working range. The inflection point in mean peak current following incubation with a 100 pM target concentration, leads to a linear response with increasing concentration (Adj. R-Square = 0.98). Such a linear region is often selected for estimations of sensor LoD by the following equation: [37]

$$Y_{LoD} = Y_{int} + 3SD_{int} \qquad \text{Equation 3.4}$$

This leads to an estimated limit of detection at 7.63 pM. This is an important point for consideration. Here, four data points have been selected all of which exist at concentrations equal to or greater than the inflection point. Had the experimental window not stretched to 10 pM, this point would have been missed, and the LoD calculated from equation 1 would have been used to estimate the performance of the sensor. With a percentage change of ~39%, a highly significant decrease of mean peak current (p = 0.0007) following a 10 pM incubation was experimentally observed. This would suggest the true LoD is perhaps markedly lower than the quoted value of 7.63 pM. Further work is required to validate this suggestion, and determine if a primary linear response is observed for target concentrations < 10 pM. Simply, the experimental data set requires significant expansion below target concentrations of 10 pM, in order to determine if a saturation point is met with 10-100 pM incubations, and if the following

inflection is perhaps through global layer organisation. This serves as an important reminder in having a broad experimental window. Relying on a small number of target concentrations to assess sensor performance may hide changes in trend direction, like those observed here, and in other works in literature.[48]

While this system has yet to determine a LoD that is competitive with those noted in literature, this initial work has presented a data set those does show a feasibility for microelectrode based sensitivity enhancement. It was next necessary to discern if the strong specificity for target sequences with a hairpin probe architecture that was evidenced earlier in this chapter is maintained upon translation to a microelectrode device. In Figure 3.10 (**C**), mean peak data is provided to highlight that the selectivity of this system is sufficient to differentiate between a single, and triple basepair mismatch, of target to recognition element in the hairpin. Following incubation with a single basepair mismatched target, a significant decrease in peak current is observed ($p = 0.0232$), attributable to ~40 %. However when a triple mismatch target introduced to this system, no significantly relevant decrease in mean peak current is identifiable ($p = 0.2129$). Again, we attribute that to the hairpin design, and location of recognition element within the region of self-complementarity inherent to the hairpin. While the incubation of a single mismatch target still contributes to a significant reduction in mean peak current, there is potential for minimising any nonspecific interactions contributing to this signal loss, which may be occurring between target and hairpin, with more stringent washing steps.

Experimental variation in this system is notably large for the functionalised electrode condition using Micrux devices. While the data presented previously in this chapter indicated hairpin based SAM consistency to be high with a microelectrode ($n = 3$), this is not a common observation in the many other experiments undertaken prior to and after that particular study. The conclusion to which is SAM formation variance is high, irrespective of the underlying electrode platform employed. While surface roughness and electroactive area is undoubtedly a contributing factor to this, previous assumptions of SAM homogeneity and simplicity in manufacture is likely a substantial oversight. This was discussed previously in review of SAM literature, though it was worth re-emphasising the need to better understand the specific mechanisms for SAM assembly, and the dynamism present in the layers with time.[9,10,11,12,58]

One possible explanation to this variance is in the impact of pin-hole formation within the monolayers. Literature entries have previously reported an increased incidence of pin hole

formation for SAM-functionalised devices.[47] Given the peak currents observed in this system exist in the low nano amp range, smeared DPV traces are a more common occurrence than typical bell shaped curves. While certain data points may exist far from the mean peak current, we cannot readily identify them as true outliers and must therefore be included within any statistical analysis. However, we are aware of certain areas of optimisation that can be explored to minimise the impact of know issues within this system. Firstly, repeated handling of these small components does increase the risk of damage to the thin tracks connecting contact pads with counter, reference, and working electrodes, which are often difficult to visually identify, and can contribute to erroneous data. Secondly, in dealing with micro volumes, issues surrounding evaporation, and or the migration of fluid across the device its self can also lead to fluctuations in generated signal. By the incorporation of a microfluidic device to control, electrode functionalisation, washing, and target incubation, we believe that we will be able to better differentiate true target binding events, and further increase sensitivity of the sensor, with the aim of working towards a viable PoC device. Finally, currents recorded with a microelectrode device are commonly in the single nA range, which poses a challenge to their application in complex settings, where electrical shielding and powerful potentiostatic instrumentation may not be appropriate for fulfilling the design criteria of a low cost, portable system. However, there are possibilities for circumventing such shortcomings. For example, signal multiplication is possible through the introduction of microelectrode arrays, which can be readily manufactured and already have been demonstrated in biosensor applications.[271]

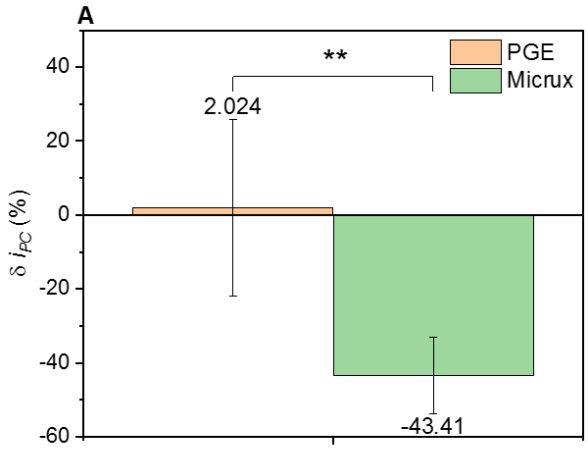

Figure 3.11 Macroelectrode vs microelectrode perormance (A) Percentage change of mean DPV peak current in response to 10 pM complementary target incubation for both PGE and Micrux, Hairpin pDNA functionalised devices. n = 3 devices per group. Error bars = SD Levels of significance given as ns $p > 0.05$, * $p \leq 0.05$, ** $p \leq 0.01$, *** $p \leq 0.001$.

Despite the lack of optimisation works currently undertaken on this platform, and an accepted need to address a number of concerns in the fundamentals of SAM assembly; there is early promise in the use of microelectrodes for sensitivity gains. This is evidenced when a comparison in mean percentage signal change is drawn between functionalised PGE and Micrux devices in response to complementary target. This is shown in Figure 3.11 (**A**), where the comparative percentage signal change in mean peak current (A) in response to 10 pM of complementary target is shown. The given signal changes are as +2.024 % (± 23.854), and –43.41 % (± 10.406) for the PGE and Micrux systems respectively, with both data sets highly significantly different (p = 0.0012). This improvement in performance with a microelectrode system against a conventional macroelectrode system, is in keeping with previous observations in the literature, [32,36] and serves as a promising indication to the future ability of microelectrode devices to provide an appropriate platform for point of care diagnostic applications.

3.4 Conclusions

This chapter introduces a simple DNA hairpin probe, self-assembled monolayer, which is capable of identifying clinically relevant concentrations of a target oligonucleotide of interest down to ~2.7 nM. While a conventional linear, single-stranded DNA probe offered a lower limit of detection to a complementary 20nt target oligonucleotide at ~836 pM; the hairpin motif allowed for an improved specificity in discerning single and triple nucleotide substitutions to the target. This probe architecture was engineered to facilitate with a strong incidence, the positioning of the target recognition element within the loop region of the hairpin oligonucleotide. Consequently, target hybridisation is dependent upon the ability to outcompete the favourability of the sequence to adopt a secondary structural confirmation.

A comparative investigation exploring the feasibility of incorporating a Ferrocene tag into both linear, and hairpin architectures was undertaken. This was launched to discern if a sensitivity boost could be generated through a “signal off” biosensing design. While multiple reports in the literature support the theory of Ferrocene tagged probes, yielding low detection limits, notes of its instability are well supported here by transient signal observations and minimal current.

With evidence of sensor specificity strengthened by a hairpin design, it was next necessary to explore alternative methods of sensitivity gain, which meet the remit of a low cost PoC device. Therefore commercial gold microelectrode devices were employed in attempt to harness the favourable electrochemical characteristics observed in a series of chemical and biological sensing applications. Again, simple label-free electrochemical interrogations, which minimise costly and complex labelling chemistries, proved sufficient observe the strong specificity hairpin architectures offer in e-DNA biosensor designs. Additionally, the incidence of significant change in mean peak current was reported with 10 pM of complementary target, two orders of magnitude lower than that achieved with a polycrystalline macro gold platform.

Chapter 4

Investigation Higher Order DNA Nanostructures for Biosensing Applications – The DNA Tetrahedron

ABSTRACT:

DNA polyhedra such as the tetrahedron have been proposed for a range of biomedical applications. The ability to rationally design these nanostructures, to incorporate specific nucleic acid recognition sites, and encompass a cargo molecule for targeted drug delivery, positions them as useful tools in sense and release strategies. In this chapter, three distinct DNA tetrahedron (TDN) biosensor designs are reported following their electrochemical interrogation with both complementary and non-complementary targets. Small, though meaningful enhancements in sensing performance are noted for immobilised TDN (TETv1 system) when contrasted to linear single stranded pDNA SAMs. Additionally, a proof of concept is noted for a novel TDN biosensor design, where solution-based TDNs are employed as signal amplifiers in a label-free sandwich assay through a growth in charge transfer resistance (R_{CT}) following their target-linked tethering to a functionalised gold electrode.

4.1 Introduction

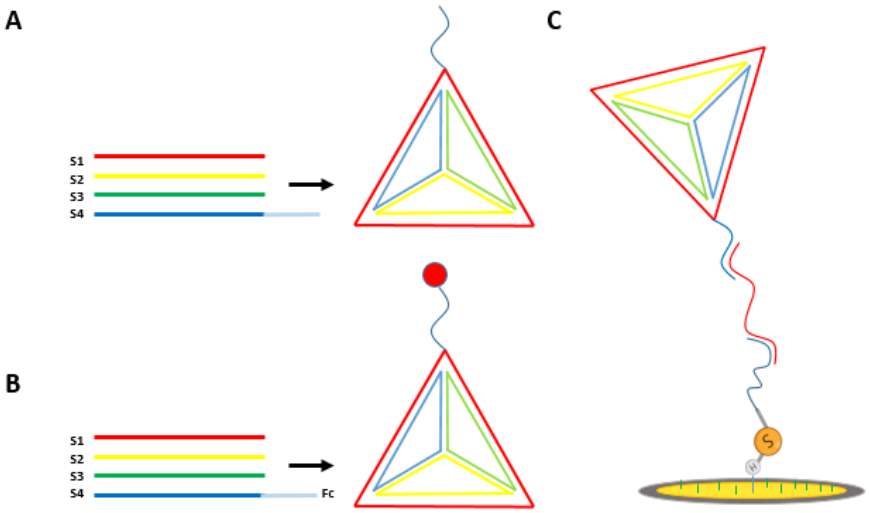

Figure 4.1 Overview of DNA Tetrahedron Self-Assembly. (**A**) TETv1 (**B**) TETv2 and (**C**) TETv3 Systems. (**A**) Immobilised TDN on PGE through thiol linkages, with a single stranded capture arm extending out from the top vertice for target hybridisation. Signal transduction achieved through the use of a Faradaic measurement buffer. (**B**) As for A, though top capture stand is labelled with a Ferrocene tag for signal transduction. (**C**) Target dependant tethering of solution based TDNs, which serve as signal amplifiers by increasing R_{CT} through enhanced repulsion of solution based redox mediator.

The DNA Tetrahedron serves a promising tool across a broad range of biosensor applications in part due to its advantageous mechanical properties, and in its ability to better order the recognition sites of probe DNA for the detection of solution based nucleic acid targets. From the initial reports detailing its construction in 2005 by Goodman et al,[150] the structure has been assessed for multiple sensing applications.

This chapter makes use of electrochemical methods of DPV, SWV, and EIS to interrogate the appropriateness of Tetrahedra in various forms, to discern the presence of a synthetic oligonucleotide target. This target is analogous to a base pair sequence for the OXA-1 gene, from AMR plasmid mimics (115nt OXA Fragment). Tetrahedra methodologies of sensing are varied, with the most prevalent mechanism in the literature being through the direct immobilisation of the structure to a transducer surface, commonly through thiol linkages.[177,178,184] This leaves a free single stranded extension from the top vertice which may serve as a recognition element to a given target.

Here, we seek to explore the performance of such sensor designs, primarily as a learning tool to better understand Tetrahedra design and manufacture ((**A**) of Figure 4.1). Thereafter the feasibility of incorporating a redox tag to the extended recognition element was explored ((**B**) of Figure 4.1). This would build upon a key question of Chapter 3, as to whether a tagged redox label is preferential for sensing performance compared to a solution-based mediator. Finally, a novel system was explored which examined the application of Tetrahedra as signal amplifiers in response to target hybridisation with a PGE functionalised with linear probe DNA ((**C**) of Figure 4.1). Common to all of these approaches, is the specific engineering of constituent oligonucleotides to synthesise Tetrahedra, where the extension of top vertice adopts a linear single stranded confirmation. In Chapter 3, strong evidence was provided to advance the notion of achieving heightened specificity of sensor designs through the adoption of a hairpin apparatus. The combinatory design of a tetrahedron and single-stranded hairpin complex, was considered to determine if such a construct may improve both sensitivity and specificity. However, such an assembly was challenging to design, with structural confirmation analysis by NUPACK highlighting the propensity for a lengthy extension harbouring the recognition element to form a pseudoknot like structure. For this reason, a simple linear extension was deemed appropriate at this stage.

This Chapter further explores the hypothesis considered throughout this thesis, whether is a significant benefit to engineering structurally complex monolayers for biosensing applications. This progresses SAM design out from 2D geometries and into three dimensions.

4.2 Materials and Methods:

4.2.1 Materials

All measurements were undertaken using an Autolab PGSTAT128N potentiostat with the additional FRA32M electrochemical impedance spectroscopy module, by scripts written in the Nova 2.1 software package (Metrohm Autolab). Polycrystalline Gold Electrodes (PGEs) of a 2 mm diameter were purchased from IJ Cambria Scientific Ltd (Llanelli, UK). An external platinum counter electrode (Metrohm, Runcorn, UK) and Ag/AgCl reference electrode (Cole-Parmer, UK) complete the electrochemical cell. Multi-electrode devices were provided by Flex Medical Ltd (Stirling, Scotland). Oligonucleotides for this work were sourced from Sigma Aldrich (Dorset, UK). 3-Mercapto-1-propanol (MCP) was obtained from Sigma Aldrich (Dorset, UK). All other chemicals required in this study are detailed in Table 4.1.

Chemical	Abbreviation	Supplier
De-ionised Water (resistivity ≥ 18 MΩcm)	Di	Sigma Aldrich (Dorset, UK)
Ethanol	EtOH	Sigma Aldrich (Dorset, UK)
Hydrogen Peroxide	H_2O_2	Sigma Aldrich (Dorset, UK)
Sulphuric Acid	H_2SO_4	Sigma Aldrich (Dorset, UK)
Potassium Chloride	KCl	Sigma Aldrich (Dorset, UK)
Potassium Ferricyanide	$K_3[Fe(CN)_6]$	Sigma Aldrich (Dorset, UK)
Potassium Ferrocyanide	$K_4[Fe(CN)_6]$	Sigma Aldrich (Dorset, UK)
Tris(hydroxymethyl)aminomethane	Tris Base	Sigma Aldrich (Dorset, UK)
Hydrochloric Acid	HCl	Sigma Aldrich (Dorset, UK)
Magnesium Chloride Hexahydrate	$MgCl_2 \cdot 6H_2O$	Sigma Aldrich (Dorset, UK)
Phosphate Buffered Saline Tablets	PBS	Sigma Aldrich (Dorset, UK)
40 % Acrylamide/bis-Acrylamide	-	Sigma Aldrich (Dorset, UK)
10× TBE	-	Invitrogen
Ammonium persulphate	APS	Sigma Aldrich (Dorset, UK)
N,N,N',N'-Tetramethyl-ethylenediamine	TEMED	Sigma Aldrich (Dorset, UK)
Hyperladder 25bp	-	Meridian Bioscience
5× Loading Buffer, Blue	-	Meridian Bioscience
Ethidium Bromide	EtBr	Sigma Aldrich (Dorset, UK)

Table 4.1 Chemicals used in this study.

4.2.2 Buffers

De-ionised water was used as the solvent for making all aqueous solutions in this study. Details are given below in table 4.2.

Buffer	Composition
Piranha Solution	18 M H_2SO_4 + 30 % H_2O_2 at a 3:1 (v/v) ratio
TM Buffer (pH 8)	1× Tris-HCl (1M) + 50 mM $MgCl_2{\cdot}6H_2O$
TM Buffer (pH 8) + TCEP	50 µM TCEP in 10 × Tris-HCl (10 mM) + 50 mM $MgCl_2{\cdot}6H_2O$
Redox Buffer	2 mM Potassium Ferricyanide / Potassium Ferrocyanide in 1× PBS
Rinse Buffer	1× PBS

Table 4.2 Buffers used in this study.

4.2.3 Oligonucleotides

TM Buffer (pH 8) + TCEP was used for the dilution of thiolated oligonucleotides. TM buffer (pH 8) was employed for the dilution of oligonucleotides with no thiol modifications. Specific sequences are provided in Supplementary Information Table S1.

4.2.4 Electrochemical Methods

Cleaning CV 1	**Measurement Script 1**	**Measurement Script 2**
For the stripping of contaminants from PGE	*Performance characterisation*	*Determining surface coverage*
<u>Cyclic Voltammetry</u> **Potential Window:** -0.1 V to 1.6 V **Scan Rate:** 0.1 V/s **N^{O} of scans:** 10	**<u>DPV</u>** **Potential Window:** -0.1 V to 0.5 V **Step:** 0.005 V **<u>SWV</u>** **Potential Window:** -0.1 V to 0.5 V **Step:** 0.005 V **Frequency (Hz):** 25 **<u>OCP Determination</u>** **Duration:** 20 seconds **<u>EIS</u>** **Applied Potential:** 0 V vs OCP **Frequency Range (Hz):** 10k – 0.1 **N^{O} of Frequencies / decade:** 10	**<u>Chrono Colometry</u> (**Δt > 1 ms) **Apply Potential:** 0 V ***Record Signal:*** **Duration:** 1 s **Interval Time:** 0.0025 s **Apply Potential:** 0.15 V ***Record Signal:*** **Duration:** 1 s **Interval Time:** 0.0025 s ***Apply Potential:*** *-0.35 V* ***Record Signal:*** **Duration:** 2 s **Interval Time:** 0.0025 s

Table 4.3 Electrochemical Methods

Electrochemical circuit fitting of Nyquist Data from EIS measurements is required to extract analytical parameters of solution resistance (R_s), Charge Transfer Resistance (R_{CT}), and Capacitance (C). An equivalent electrical circuit was chosen to determine these parameters, shown overleaf.

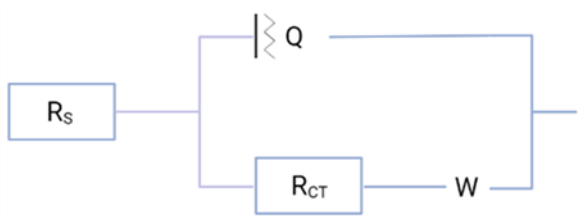

Figure 4.2 Simplified Randles circuit for electrochemical circuit fitting.

4.2.4 Electrode Polishing and Cleaning (PGE Preparation Method 2)

Appropriate cleaning is required to achieve conformity in PGE surfaces, and the removal of immobilised organics and contaminants. Mechanical polishing was first undertaken produce a near mirror finish via a series of decreasing alumina slurry diameters from 1 µm to 0.03 µm, on microcloths of varying roughness, with sonication in IPA for 2 minutes between each polishing step. Polishing occurred in a figure of eight motion for a duration of two minutes per electrode. Stripping of organics was attained by immersion of the gold surfaces in hot piranha (H_2SO_4 and H_2O_2 3:1 (v/v)) for 15 minutes. To ensure the removal of any remaining sulphur species from the electrode surfaces, a Diener Electronic Zepto (Model 8 Base Unit) generated an O2 plasma. The O_2 process gas was applied as a permanent stream, regulated by the integrated inlet valve and adjusted to a range of approximately 0.3 - 0.4 mbar. The processing stage was repeated twice, for a total time of two minutes. Finally, electrochemical cleaning was undertaken by repeated cyclic voltammetry in 0.1M H_2SO_4 at 0.1 V/s, with a potential window of -0.1 to 1.6 V until a stable reduction peak was observed in the voltammogram (< 10 scans). It was necessary to confirm the effectiveness of the cleaning protocol with subsequent electrochemical interrogation of the each PGE by Faradaic methods. Measurement Script 1 was used to determine if key analytical tools of Peak Current (A) from DPV and SWV, and R_{CT} (Ω) from EIS, lie within a consistent range for PGE immersed in Redox Buffer. PGE that record mean signals for any one of the above that exist out with 1.5 IQR, were discounted and not carried forward for further experimental work.

4.2.5 Tetrahedron Formation

TDNs were synthesised in accordance with a well-defined methodology of self-assembly.[176] Specific modifications to this protocol specific are required for each system employed:

(i) **TETv1 system**: Equimolar concentrations of each oligonucleotide are combined with a ×10 concentration of TCEP (Tris (2-carboxyethyl) phosphine hydrochloride) in TM buffer to a total volume of 100 µL.

(ii) **TETv2 system**: Equimolar concentrations of each oligonucleotide are combined with a ×10 concentration of TCEP (Tris (2-carboxyethyl) phosphine hydrochloride) in TM buffer to a total volume of 100 µL.

(iii) **TETv3 system**: Equimolar concentrations of each oligonucleotide are combined with TM buffer to a total volume of 100 µL.

The required volumes and concentrations are dictated by the application of the TDNs. Details are provided in the Table 4.4 below:

	PAGE		**Electrochemistry**	
Oligonucleotide	Volume from stock (µL)	Final Concentration (µM)	Volume from stock (µL)	Final Concentration (µM)
S1	3.5	7	1	2
S2	3.5	7	1	2
S3	3.5	7	1	2
S4	3.5	7	1	2

Table 4.4 Oligonucleotide Volumes for Complete TDN Assembly.

Various combinations of each oligonucleotide are required for the assessment of appropriate TDN formation by PAGE. The equimolar combinations are listed as follows; [S1,S2,S3], [S1,S2,S4], [S1,S3,S4], [S2,S3,S4] and TET [S1,S2,S3,S4]. Each of these combinations was heated to 95^0C for 10 minutes, before being rapidly cooled to 4^0C in a SimpliAmp Thermal Cycler (Applied Biosciences by Thermo Fisher Scientific). Mixtures were held at 4^0C until required.

4.2.6 Tetrahedra Polyacrylamide Electrophoresis

Polyacrylamide gels at 8% (wt/vol) were cast as follows:

	Volume Required
diH_2O	7.8 mL
40 % (wt/vol) acrylamide/bis-acrylamide	3 mL
10x TBE	1.2 mL
10 % (wt/vol) APS (ammonium persulphate)	100 uL
TEMED	10 uL

Table 4.5 Materials required for the casting of polyacrylamide gels. Sufficient volume for two gels given in this table.

Care was taken to ensure the above mixture was well mixed prior to pouring in to the gel cassette of the BioRad Mini-PROTEAN Tetra Cell (BioRad, California US). 10-well combs were inserted in to the top of each gel, and allowed to set for ~ 30 minutes. 1 µL of 6× Loading Buffer and 5 µL of ssDNA, partially assembled DNA combinations, and TDNs respectively were mixed. 5 µL of each sample was then added to its predesignated well. 2 µL of Hyperladder was added to well number 5. Electrophoresis was then ran at 80V for > 80 minutes (until the blue coloured bands of loading buffer were approaching the end of the gel) in 1× TBE. Upon completion of electrophoresis, gels were stored in 1× TBE, prior to rinsing and staining in EtBr.

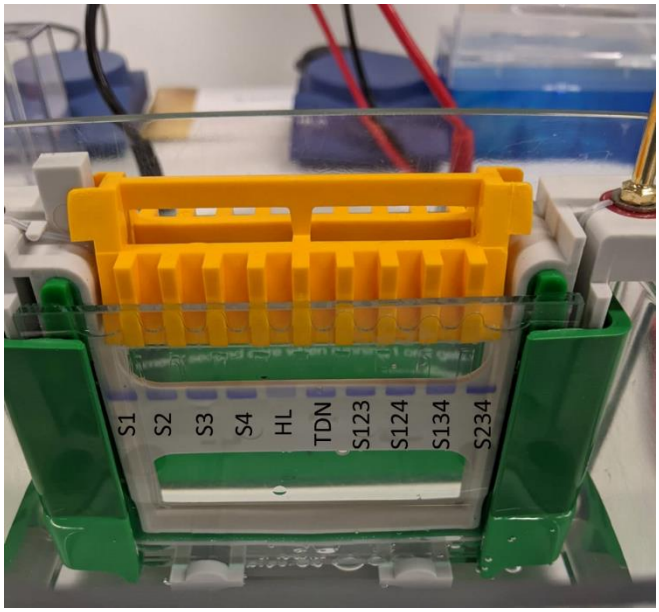

Figure 4.3 PAGE set-up with lane map showing contents. Combinations of oligonucleotides are at equimolar concentration.

4.2.7 Electrode Functionalisation

After cleaning, electrodes were immersed in Ethanol for 3 minutes, rinsed in Di-H_2O, and then dried under a steady Argon stream. Two functionalisation protocols for the TETv1 and TETv2 systems, and the TETv3 system respectively were required:

(i) **TETv1** and **TETv2 Systems**: A mixed SAM of TDN and MCP was formed by overnight incubation (18 hours) at 37^0C, with electrodes immersed in a solution of 2 µM TDN : 20 µM MCP, in excess 100 µM TCEP (Tris (2-carboxyethyl)phosphine hydrochloride). The primary solvent throughout was TM Buffer at pH 8 (1× Tris-HCl (1M) + 50 mM $MgCl_2{\cdot}6H_2O$). Following this step, electrodes are named as Functionalised Electrodes (FEv1). With the completion of the functionalisation protocol, all electrodes were rinsed in a gentle flow of Di water for 10 seconds to remove non-specifically adsorbed oligonucleotides from the sensor surface. FE were then dried under a steady stream of argon.

(ii) **TETv3 System**: A mixed SMA of OXA pDNA (v2) and MCP was formed by overnight incubation (18 hours) at 37^0C, with electrodes immersed in a solution of 1 µM probe : 10 µM MCP, in excess 50 µM TCEP (Tris (2-carboxyethyl)phosphine hydrochloride). The primary solvent

throughout was TM Buffer at pH 8 (1× Tris-HCl (1M) + 50 mM $MgCl_2 \cdot 6H_2O$). Following this step, electrodes are named as Functionalised Electrodes (FEv2). With the completion of the functionalisation protocol, all electrodes were rinsed in a gentle flow of Di water for 10 seconds to remove non-specifically adsorbed oligonucleotides from the sensor surface. FE were then dried under a steady stream of argon.

For all systems, it was necessary to assess the performance of the functionalisation protocols. FE were subject to electrochemical interrogation in Redox Buffer, following Measurement Script 1. Again, any data point existing out with 1.5IQR was noted as evidence of abnormal functionalisation and this electrode was discounted for further study.

4.2.8 Target Detection

4.2.8.1 TETv1 System:

The detection method of this approach is the direct hybridisation of a solution-based target by the recognition element of the immobilised Tetrahedron. As such, a target diluted in TM buffer could be directly incubated on FEv1. The 115nt OXA Fragment was diluted in TM Buffer to complete the required concentration range. This target is common to all TET systems. Each concentration was gently vortexed prior to incubation on the FEv1 surface for 30 minutes at 37 ^{0}C in a sealed Eppendorf tube to prevent evaporation. A non-complementary "junk" sequence of 115nt was used as a control, and treated in the same way. This non-complementary sequence is used in all TET systems. The electrode was then rinsed in 1× PBS for 10 seconds, to remove non-specifically absorbed target from the sensor. Following which PGE were immersed in Redox Buffer, ready for electrochemical interrogation. Target concentrations for the TETv1 system are listed below in Table 4.6.

4.2.8.2 TETv2 System:

Target detection for this system employs the same methodology given in 4.2.8.1, with one modification. All measurements were carried out in 1× PBS, and not Redox Buffer. Target concentrations for the TETv2 system are listed below in Table 4.6.

4.2.8.3 TETv3 System:

The detection method of this approach is centred around a capture of a Tetrahedron/Target complex from solution, by an immobilised probe on the electrode surface.

As such, it was first necessary to incubate a solution of both Tetrahedra and target to allow this complex to form. In this study the Tetrahedra was held at an assumed concentration of 500 nM, based upon a yield of 100% from the assembly process against a varying target concentration. This complex was allowed to form by a 30 minute incubation at 37 ^{0}C. After which, FEv2 were incubated directly in this solution for a further 30 minutes at 37 ^{0}C. Target concentrations for the TETv3 system are listed below in Table 4.6.

Following all Target incubations, electrodes were rinsed in 1× PBS for 10 seconds, and gently dried under a steady stream of Argon gas. They were then immersed in Redox Buffer or 1× PBS for the electrochemical characterisation of sensing performance using Measurement Script 1.

TETv1 System + TETv2 Systems		**TETv3 System**	
Complementary	Non-complementary	**Complementary**	Non-complementary
1 pM	1 pM	**5 pM**	500 nM
10 pM	10 pM	**50 pM**	-
100 pM	100 pM	**500 pM**	-
1 nM	1 nM	**5 nM**	-
10 nM	10 nM	**50 nM**	-
100 nM	100 nM	**-**	-
1 uM	1 uM	**-**	-

Table 4.6 Target Concentrations in TM Buffer.

4.3 Results and Discussion:

4.3.1 Assessment of New Cleaning Protocol

With re-useable macro electrodes in this work, it is essential that any surface bound contaminants are removed, and all possible sources of electrode fouling is minimised prior to functionalisation. Throughout the literature, there is reference to a multitude of methods proving sufficient to achieve this aim. These range from simple chemical baths, to more involved electrochemical techniques, and combinations of both.[243,258] While increasing the complexity, expense, and time involved in electrode cleaning moves a potential biosensing system further from the ideal PoC device, it is necessary to ensure that a consistent base electrode is in place for determining the promise this novel approach to sensing may have. The introduction of an O_2 Plasma cleaning stage enables the successful removal of surface physisorbed sulphur from thiol groups, which a piranha clean may not be able to achieve, and the formation of Au_2O_3.[272,273] Figure 4.4 (**A**) shows characteristic voltammograms recorded for PGE in 0.1M H_2SO_4, following Cleaning Method 1, and 2 respectively (with vs without O_2 plasma treatment). A visual estimation of electrode cleanliness can obtained from position and sharpness of peaks in the voltammogram. For each recorded trace, there is a single, sharp reduction peak with a comparable cathodic peak current. However, common to many PGE treated with a plasma cleaning stage, voltammograms exhibit a series of small oxidation peaks at potentials ≥ 1V. This suggests a greater surface oxide formation, which may be proportional to the conditions of the plasma cleaning stage. There is some initial evidence to suggest greater chamber pressure, and/or increased number of cleaning repeats contributes to this phenomenon, though more study is required to confirm this.

It is possible to generate both a quantitative assessment of electrode cleanliness, and estimate surface area and roughness by the manipulation of cyclic voltammogram data. This is achieved by the integration of curve area, for the reduction peak of PGE cycled in 0.1M H_2SO_4. Here, CV data was replotted as current against time, and the subsequent integration yields an electrode charge (Q_{Red}) (μC). The real electrode area (A_{Real}) (cm^2) can then be estimated as follows:

$$A_{Real} = \frac{Q_{Red}\ (\mu C)}{482\ (\mu C/cm^2)}$$ Equation 4.1

Where 482 µC/cm^2 represents the charge of a monolayer of Oxygen on polycrystalline gold.[274] With an estimation of real electrode area made, it was then possible to calculate a surface roughness factor by:

$$RF = \frac{A_{Real}}{A_{geom}}$$ Equation 4.2

Table 4.7 below summarises the real area and roughness factor for PGE following Cleaning Methods 1 and 2 respectively:

	Method 1	**Method 2**
A_{geom} (cm^2)	0.0314	0.0314
Q_{Red} (µC)	72.62 ± 19.08	62.85 ± 5.5
A_{Real} (cm^2)	0.151 ± 0.04	0.130 ± 0.01
RF	4.80 ± 1.26	4.15 ± 0.36

Table 4.7 Determination of Electro-active Surface Area.

The geometrical area, from πr^2, is smaller than that of the real area for PGE treated with both cleaning methods. This is to be expected, as the surfaces of these electrodes are not strictly 2D. Each surface is rich in peaks and valleys at the atomic level, and mechanical polishing will still allow for variation in the depth and frequency of these microscale features. Despite attempting to achieve a “mirror like” surface with successive polishing steps, eradication of such features is not possible. This is shown by the variation present in all parameters calculated using Equations 4.1 and 4.2.

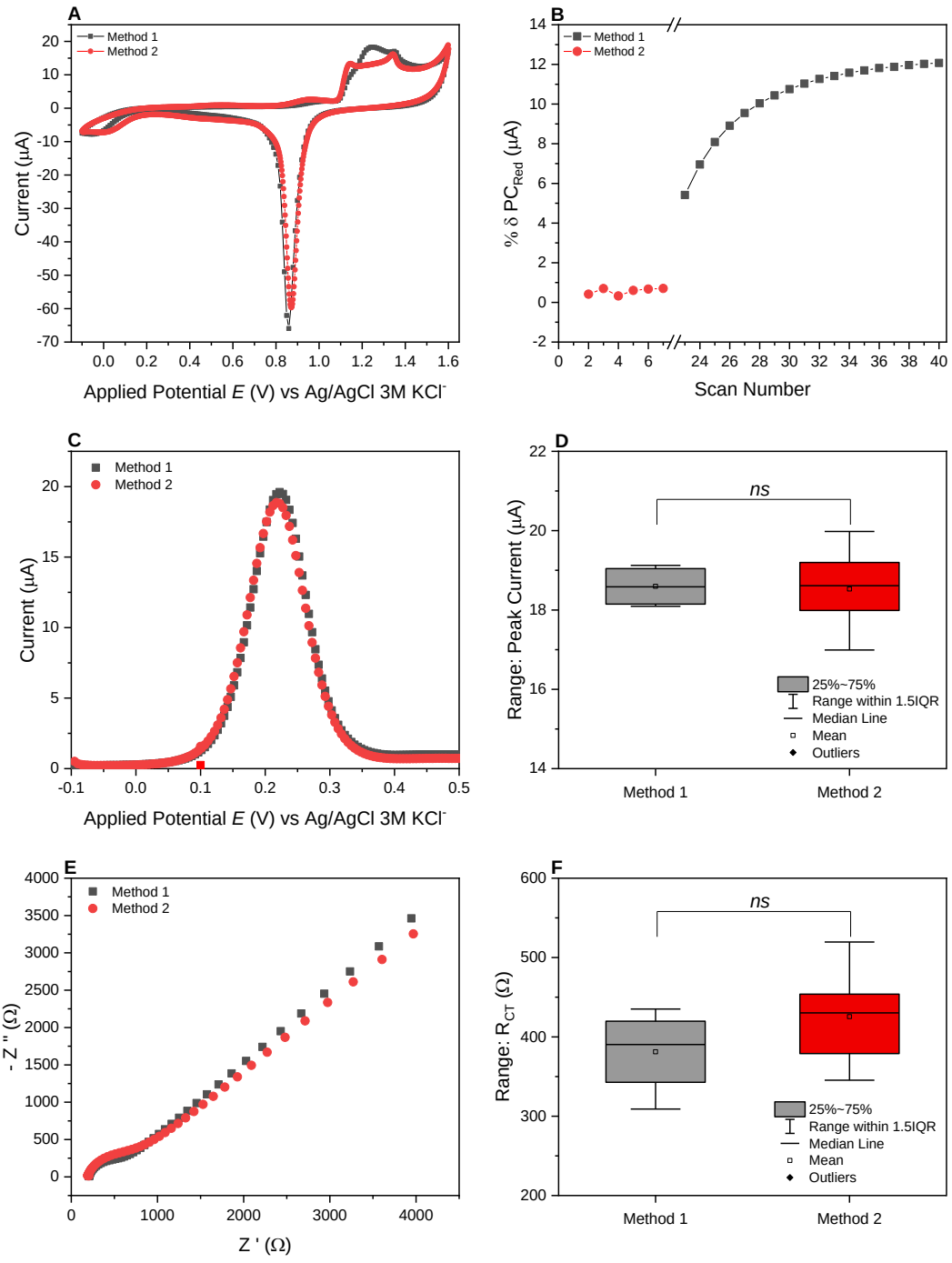

Figure 4.4 Comparison of Electrochemical Characteristics of PGE following Cleaning Methods 1 and 2.(**A**) Typical voltammograms for PGE following cleaning cyclic voltammetry. (**B**) % change of mean reductive peak current with increasing scan number. (**C**) Typical DPV trace for PGE cleaned by Method 1 and 2. (**D**) Box plot comparison of DPV peak current for both cleaning methods. (**E**) Typical Nyquist plots for PGE cleaned by Methods 1 and 2. (**F**) Box plot comparison of R_{CT} for both cleaning methods. n ≥ 5 PGE for (**D** + **F**). Measurement Buffer 1 used for faradaic measurements.

A key benefit to the introduction of a plasma cleaning stage is lesser number of CV scans required to achieve a stable reduction peak in the voltammogram when compared to PGE

Cleaning Method 1 (no plasma cleaning stage). This is shown in Figure 4.4 (**B**) where ΔPC_{red} is minimal within five scans. However, it can often require 40 scans to reach a stable reduction peak following Cleaning Method 1.

The plasma cleaning stage is complete within ~3 minutes (dependant on the time to pull a complete vacuum), and the instrument can accommodate upwards of 16 PGE in a single run. This provides a significant advantage in maximising the number of electrodes available for functionalisation per day. For both Cleaning Method 1, and 2, the CV data provides a good indication of PGE cleanliness. However, it is important to characterise the Faradaic performance of such surfaces prior to any functionalisation protocols. As such, PGE were interrogated electrochemically following each cleaning method by DPV and EIS in the presence of Redox Buffer (2 mM $Fe(CN)_6^{(-3/-4)}$ in 100 mM KCl). The results of which are shown in Figure 4.4 (**C** – **F**). Voltammograms of typical responses for PGE cleaned by Method 1, and Method 2 respectively are given in 4.4 (**C**), and present the expected characteristics of well defined, sharp bell-shaped curves, with peak positions at approximately 210 mV. The box plot 4.4 (**D**), presents the corresponding peak current (μA) for each group of PGE, with no significant difference between either mean current ($p > 0.05$). The Nyquist plot of 4.4 (**E**) again display characteristic features of a well-defined semi-circle region in the high frequency range, with diffusion processes dominating the low frequency range. Again, no significant difference between Mean R_{CT} (Ω) exists for either PGE group. As such, an initial conclusion can be drawn that both Cleaning Methods produce comparable surfaces, with little variation in baseline metrics of cleanliness. While literature suggests there is an advantage in using Plasma cleaning to strip stubborn sulphur atoms from gold surfaces,[272] there is no evidence provided in the above data set to suggest that contributes to an observable difference in electrochemical characterisation. However, the time to cleanliness (required number of cleaning CV scans in 0.1M H_2SO_4) is reduced with the use of an O_2 plasma stage. As such, Cleaning Method 2 was selected for future use.

4.3.2 Detection of Nucleic Acid Targets – *is simple best?*

4.3.2.1 SAM Characterisation

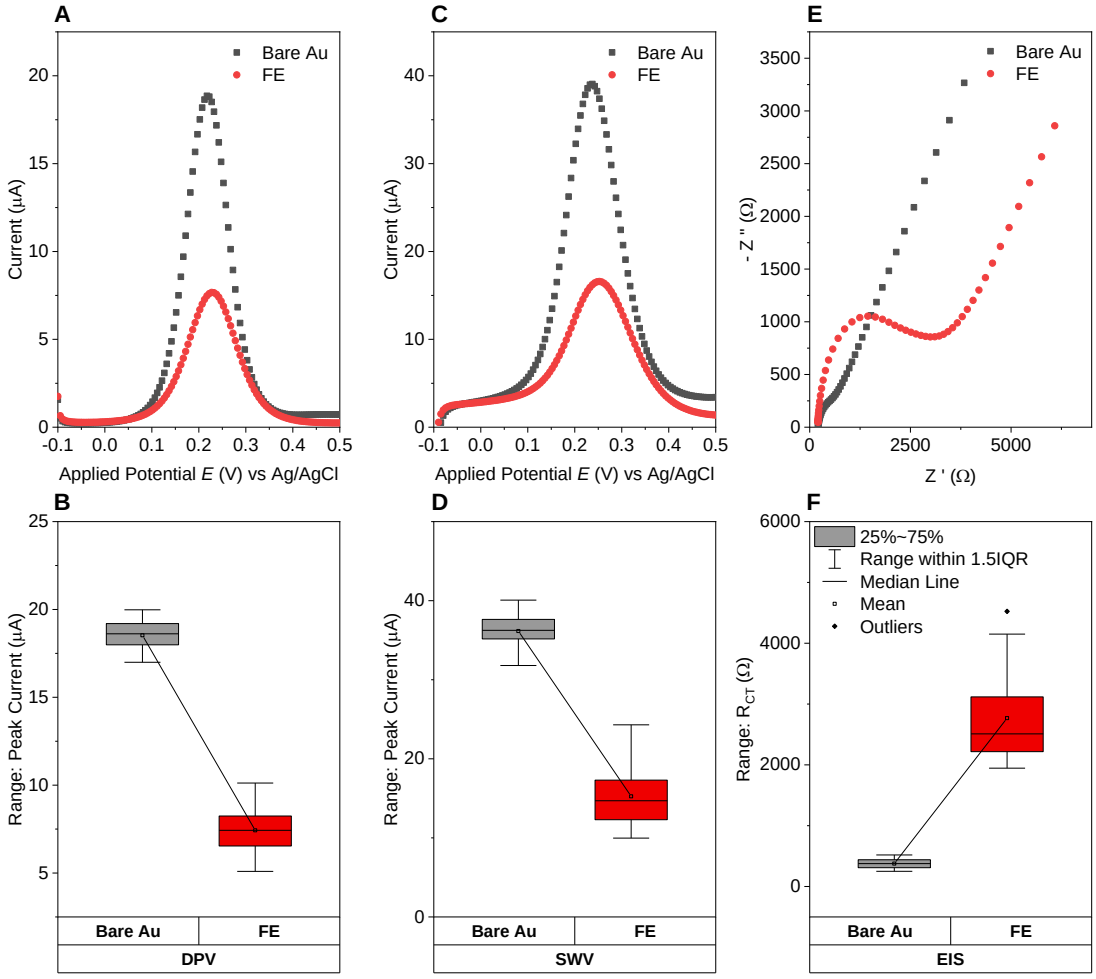

Figure 4.5 Electrochemical analysis of PGE following functionalisation. Average DPV (**A**), SWV (**C**) and Nyquist (**E**) plots, for PGE post-clean (Bare Au) and after functionalisation (FE). (**B**,**D**,**F**)Box plot comparison of DPV peak current, SWV peak current, and R_{CT} respectively. Error bars = SD. $n \geq 6$ PGE. Measurement Buffer 1 used for characterisation.

Prior to the introduction of DNA Tetrahedron structures, it was first necessary to determine the performance of a simple, linear probe based assay for the detection of the synthetic 115nt OXA Fragment. The methodology employed was carried forward from earlier works documented in this study and centres around the co-immobilisation of a DNA Probe along with the alkanethiol MCP, at a 1:10 ratio. Importantly, the pDNA sequence is lengthier than that immobilised in prior chapters to help aid the capture of the 115nt target (OXA Probe v 2). Specific

sequences are again provided in Supplementary Information Table S1. Modifications to the primary solvent used as probe diluent (TM Buffer instead of 1× PBS), and PGE surfaces that have been cleaned with an additional O_2 plasma-cleaning step, establish a need for documenting the behaviour of this functionalisation protocol.

In Figure 4.5, PGE cleaned by Method 2, are functionalised overnight by a simple protocol of co-immobilisation (TETv2 System), with probe DNA and MCP at a 1:10 ratio. Their electrochemical interrogation is complete through Measurement Script 1. In tiles (**A**), (**C**) and (**E**), average recorded traces are displayed for DPV, SWV and EIS. Common to all are clear changes in signal traces, with reduction in peak current amplitude, and growth of the semi-circle region of the Nyquist plot. A quantitative assessment of analytical parameters; Peak Current (μA), and R_{CT} (Ω), is given in Box Plots (**B**), (**D**) and (**F**). Again, common to all is a highly significant change in mean signal following functionalisation (**** $p \lessgtr 0.0001$, $20 \geq n \leq 28$ PGE). Significant reductions in mean peak current following functionalisation is expected. DPV and SWV interrogations are limited by both physical and charge based repulsion of the solution based redox mediator from the transducer surface. This is suggestive of well-ordered, mixed monolayers of probe and MCP. The FE group for (**B**) and (**E**) display a tightness of the data set clustered around the mean peak current, and an absence of any data point existing out with 1.5IQR. Mean R_{CT} behaves as expected in response to PGE functionalisation, with a significant increase following functionalisation. Analysis of data within the FE group of (**F**) shows a single outlier of one PGE. This electrode was not carried forward for any subsequent incubations. At a functionalisation concentration of 1 μM pDNA, the electrochemical data suggests an ability to form reproducible and consistent sensors. However, a detailed assessment of surface coverage is required to ensure the appropriateness of this method for a sensing application.

4.3.2.2 Estimation of OXA pDNA Surface Coverage

It was possible to estimate the surface density of pDNA on FE, by employing the electrostatic attraction between a redox cation and the negatively charged phosphate backbone of the anchored probe. FE are incubated in a low ionic strength buffer, containing a given concentration of the cationic redox marker, Hexaammineruthenium(III) Chloride ($Ru(NH_3)_6^{3+}$). The redox cation exchanges for native counterions associated with the probe backbone and

saturate within the layer. At this point, the surface density of the probe can be determined chronocoulometry. Well-described protocols of Steel et al; 1998, and Keighley et al; 2008,[70,71] were followed to generate mean OXA pDNA surface densities for the 1:10 coimmobilisation of probe : MCP.

FE were first incubated for 5 minutes in a low ionic strength buffer, 10 mM Tris-HCl pH 7.4, which had been purged with Argon for 30 minutes prior to use. The potential was then stepped from 0.15V to -0.35V for 1000 ms, and the resultant charge flow recorded. FE were then transferred to an Argon purged solution of 100 µM ($Ru(NH_3)_6^{3+}$) in Tris-HCl pH 7.4 for a further 5 minutes. The potential was then again stepped, and charge flow recorded as above (more detail provided in Table 5.3 – *Measurement Script 2*). While FE incubate in the low ionic strength buffer, trivalent $Ru(NH_3)_6^{3+}$ exchanges preferentially with monovalent counterions, and associates with the negatively charged phosphate groups of the probe backbone at 1:3 ratio. The resultant charge *Q* as a function of time *t*, is a summation of the reduction of $Ru(NH_3)_6^{3+}$ diffusing from the bulk solution, the double-layer charge, the charge from the reduction of surface entrapped $Ru(NH_3)_6^{3+}$. *Q* is given by the Cottrell equation:

$$Q = \frac{2nFAD_O^{1/2}C_O^*}{\pi^{1/2}}t^{1/2} + Q_{dl} + nFA\Gamma_O \qquad \text{Equation 4.3}$$

Where *n* is the number of electrons per molecule for reduction, *F* the Faraday constant (C/mol), *A* the electrode area (cm^2), D_0 the diffusion coefficient (cm^2/s), C_0^* the bulk concentration of $Ru(NH_3)_6^{3+}$ (mol/cm^3), Q_{dl} the capacitive charge (C), and $nFA\Gamma_0$ the charge from the reduction of Γ_0, the amount of surface confined redox marker (mol/cm^2). And the pDNA surface coverage is given by:

$$\Gamma_{DNA} = \Gamma_0(\frac{z}{m})(N_A) \qquad \text{Equation 4.4}$$

Where; Γ_0 is the surface density of $Ru(NH_3)_6^{3+}$ (mol / cm^2), Γ_{DNA} is the surface density of DNA (mol / cm^2), *m* is the number of phosphate groups on the pDNA, *z* is the charge of the redox

molecule, and N_A is Avogadro's number. Q is the charge which can be obtained either by calculating the chronocoulometric intercept at t = 0.

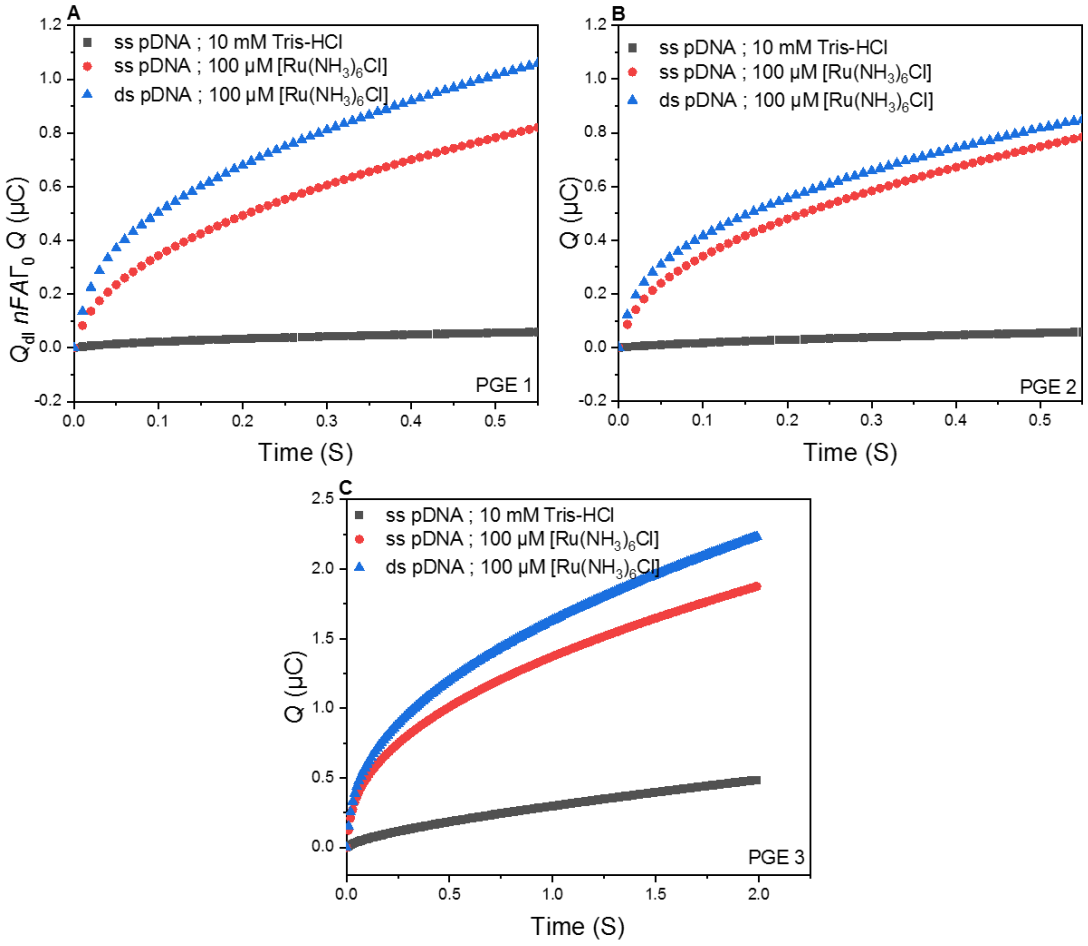

Figure 4.6 Anson plots of charge vs time. Least squares fit to linear region of each trace allows for an estimation of Q_{dl} and $nFA\Gamma_O$ (Y-intercept).

By the extrapolation of the linear region of each trace to the Y-intercept, at t = 0, it is possible to estimate a number of parameters required by the Cottrell Equation. Firstly, extrapolation of the black trace (FE in the absence of $Ru(NH_3)_6^{3+}$) yields a Y-intercept equivalent to the Q_{dl}. Extrapolation of the red trace provides $Q_{dl} + nFA\Gamma_O$, with the difference of these Y-intercepts providing $nFA\Gamma_O$. This gives an estimation of surface density at 4.62 ± 2.28 x10^{12} molecules/cm^2. This is broadly in accordance with original material in the literature,[12] where an expected linear relationship between the mole ratio (probe : total thiol (MCH)) and probe density is shown for a range of (1.3-9.1) x10^{12} probes/cm^2. In the Keighley et al study, R_{CT} growth following tager hybridisation was shown to be occur at probe densities ≥ 2.5 x10^{12}

molecules/cm^2, and optimum at 5.4 $x10^{12}$ molecules/cm^2. While the estimated figure of probe density is not too distant from the optimum quoted by Keighely at al; the variation is high. This is attributable to the earlier determination of mean A_{real}, with seemingly small discreations in the true macroscopic area of PGE contrinuting significanltly to the outcome of coverage. This analysis of surface probe density is an important consideration if a better understanding of SAM charactersitcs is to be formed. Note, in this study the sample size was limited to three PGE, with time constraints on this project. However, there is still value in this analysis in effectively showing the ability to form appropriate mixed monolayers of OXA pDNA and MCP. Ideally, this method of analysis would be applied to large number of PGE, all of which having had a unique estimation of A_{real} determined prior to interogation by the Keighley protocol. This would provide an enhanced insight into how reproducible the cleaning, and functionalisation systems are in forming such monolayers.

4.3.2.3 Sensing of 115nt Fragment Target by OXA pDNA SAM

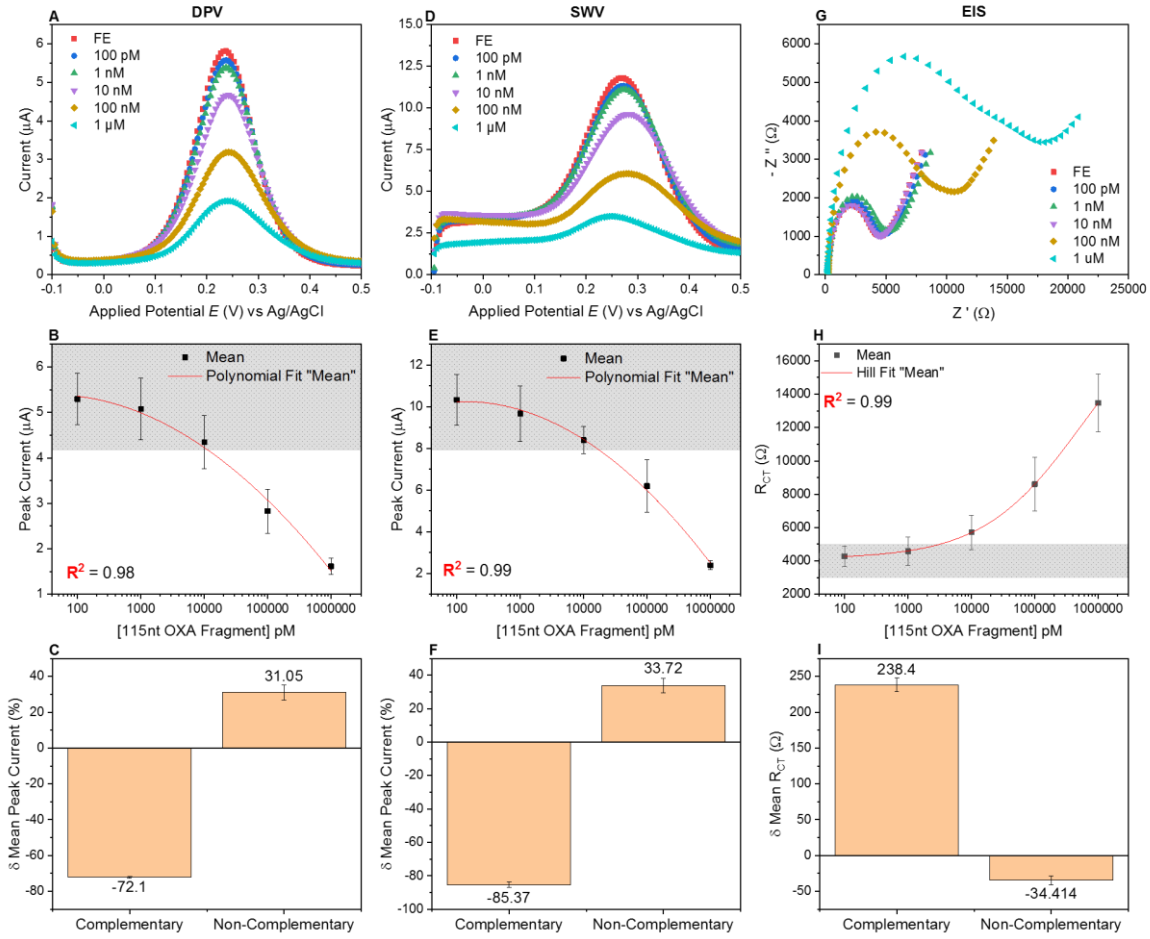

Figure 4.7 Determining sensing performance of a linear pDNA SAM against conventional targets. Mean signal trace of electrochemical measurements following incubation with 115nt OXA Fragment across various concentrations (**A**) DPV, (**D**) SWV, (**G**) EIS. Fitting of data to allow for estimation of Limit of Detection for 115nt OXA Fragment by (**B**) DPV, (**E**) SWV and (**H**) EIS. Comparison of SAM specificity, with % Signal Change given in response to 1µM Complementary (115nt OXA Fragment), and Non-Complementary (115nt Junk Fragment) sequences. Responses shown for (**C**) DPV, (**F**) SWV and (**I**) respectively. Error bars = SD. *n* = 4 PGE per condition.

With a detailed assessment of SAM formation, it was next necessary to determine the sensing capability of such functionalised PGE. The mean recorded signals behave as expected for all electrochemical measurements. For the Voltammetric methods (DPV and SWV), sharply formed peaks decay in amplitude and broaden with successive target concentration incubations. In the case of the SWV traces (**D**) the smearing of peaks with high concentrations of target is

dramatic. This is an early indication of interaction between target and the functionalised transducer surface, with the increasing mass, and/or the strengthening negative charge associated with phosphate groups of the target hindering charge transfer between transducer and the solution based redox mediator. Equally, the Nyquist plot (**G**) generated from EIS supports this observation with increasing target concentration broadening the semi-circle region of the plotted impedance data, corresponding to the charge transfer resistance (Ω). Quantitative assessments for the impact of target on FE is displayed in the second and third rows of Figure 4.6. In the second row, tiles (**B**) + (**E**) display mean peak current (μA), and (**H**) gives R_{CT} (Ω) plotted against target concentration. Within each of these tiles, the shaded region corresponds to the mean peak current or R_{CT} ± 3*SD of FE. This shaded region is shown to provide a data range where any subsequent data point could be considered as lying within the variation associated with functionalised PGE. To quantify a LoD, the following equation could be used:

$$Y_{LoD} = Y_{int} + 3^{*}SD \qquad \text{Equation 4.5}$$

From which, the LoD (*X*) could be found in the Fitting Analysis tab of OriginPro. This method of fitting a data set, is based upon the extrapolation of a linear to intercept the Y-axis, and further has previously been critiqued in Chapter 3.3.6. Again, this method of analysis is not applicable here, as the experimental data does not express a strong linear region. There does however appear to be a strong correlation between the increasing target concentration and peak current (μA), with polynomial fitting producing correlation coefficients of 0.98, 0.99 for DPV and SWV data (**B** + **C**). Given the shaded band can be considered analogous to background noise, it is possible to assign an indicative LoD at target concentrations exceeding 10 nM. Interestingly the concentration range extends to 1 μM, however there is no evidence of sensor saturation noted in this data set. Expansion of the target concentration range may complete a sigmoidal profile, which would be supportive of full recognition element occupancy rates. In (**H**) the mean R_{CT} plotted against target concentration allows for the successful fitting by the standard Hill function. This allows for estimation of the sensors LoD for the 115nt OXA fragment at 2.53 nM. Extrapolating a straight line from this concentration on the x-axis, gives a point of intersection with the fitting line which falls just outside the 3*SD region attributed to

background noise. Previously in Chapter 3.3.3 the LoD for the same immobilised probe was estimated at 836 pM. However, the target employed in that particular work was a simple 20nt oligonucleotide. It is possible that the short fragment is perhaps easier to capture by the immobilised probe than the 115nt OXA fragment. While dilutions of the fragment are made in TM buffer + $MgCl{\cdot}6H_2O$ to screen the negative charges of the phosphate backbone, there is still the potential for steric hindrance effecting the efficiency of hybridisation, when a lengthy oligonucleotide is the target. There is corroborating reports in the literature documenting related findings. For example Corrigan et al, noted in 2014 an optimised EIS signal change in response to short targets with overhangs of 15 nt, with an increasing overhang length limiting the ability of the target to be successfully inserted within the monolayer.[275] Their work involved the immobilisation of charge neutral PNA probes, where steric hindrance from the lengthy targets was the predominant influence in reducing hybridisation efficiency.

The third row of Figure 4.6 details the specificity of the immobilised probe to hybridise a complementary target. The signal change is given as the mean percentage difference in recorded signal of FE, and PGE incubated with either a complementary (115nt OXA Fragment) or non-complementary (115nt Junk Sequence) target at a concentration of 1 µM. Tiles (**C**) and (**F**) display the Voltammetric data sets, with complementary target incubation yielding a mean peak current decrease of 72.1% and 85.3% for the DPV and SWV measurements respectively. In both columns, the response to complementary target produces minimal variation in mean signal decrease, with a SD of ± 0.56 and ± 1.63 for DPV and SWV measurements. However, the incubation of a non-complementary sequence also at 115nt produces a positive signal change in mean peak current of 31.05 % ± 4.19, and 33.72 % ± 4.29 with DPV and SWV interrogation. Finally, the probing of sensitivity by EIS in (**I**) documents a large increase in mean peak current at 238.4 ± 9.45 when the sensor is incubated with a complementary target, and a % decrease of 34.41 ± 6.31 in response to the non-complementary target. This allows for a number of possible conclusions to be drawn surrounding the sensitivity of this simple SAM in target detection. Firstly, the highly significant signal changes in response to complementary targets across all measurement techniques ($p < 0.0001$), is suggestive of a common influence that the target is having on the electrochemical behaviour of all PGE. This is further validated by the small SD for each electrode in the data set, and points towards hybridisation events on the transducer surface. This hypothesis is further bolstered by the opposite response observed with non-complementary target incubation. Here, the randomly generated 115nt oligonucleotide does

not contain the 20nt region with complementarity to the recognition element of the probe. Any interaction of this junk sequence with FE should be non-specific, and have a low binding efficiency. In effect, the non-complementary sequence is poorly adsorbed to the transducer surface by one of two possible means. Firstly, there is the possibility of single basepair interactions with the immobilised probe. Stringent washing steps with low ionic strength solutions should be sufficient to minimise the incidence of this, and optimising of washing steps is required. Secondly, there is a possibility for non-complementary sequences to interact directly with exposed regions of the gold transducer surface through ion-induced dipole dispersive interactions, whereby the negatively charged phosphate groups induce dipoles in the polarisable gold particles.[55] The later mechanism of inappropriate adsorption may account for the apparent increase in mean peak current / decrease in mean R_{CT}. The poor orientation of the sequence interacting with the gold transducer may induce transient reorganisation of the dominant MCP regions of the mixed SAM. As such, pinhole defects in the continuity of the layer may grow and contribute to local increases in redox events.

It is clear that the newly established protocol for co-immobilisation of pDNA with MCP at a 1:10 ratio in TM buffer is proficient in forming well-ordered and consistent mixed monolayers. While there is still a variation in the electrochemical characteristics of such layers, the sufficiently large data set of PGE treated in such way allows for the creation of limits to an acceptable range of such characteristics. PGE that exist within the limits can be classed as FE, and employed in future analysis. Equally, PGE with particularly high (or low) mean peak currents (μA) / R_{CT} (Ω) can be discounted. These layers appear sensitive to target concentrations in the low pM range, while being specific to complementary target. This gives confidence to their appropriateness for future usage. The premise of this chapter was to investigate the use of higher order structures that could be incorporated either directly within, or hybridised to a mixed SAM, and assess the potential gain in sensing efficacy this may bring. As such, further optimisation work on linear probe based detection of targets was not required, and an exploration into the potential of such tertiary structures undertaken.

4.3.3 Confirming TDN Assembly by PAGE Analysis

PAGE was used to characterise the physical properties of molecular weights for the ssDNA, partially assembled combinations, and complete tetrahedra, and ultimately judge the success of TDN construction.

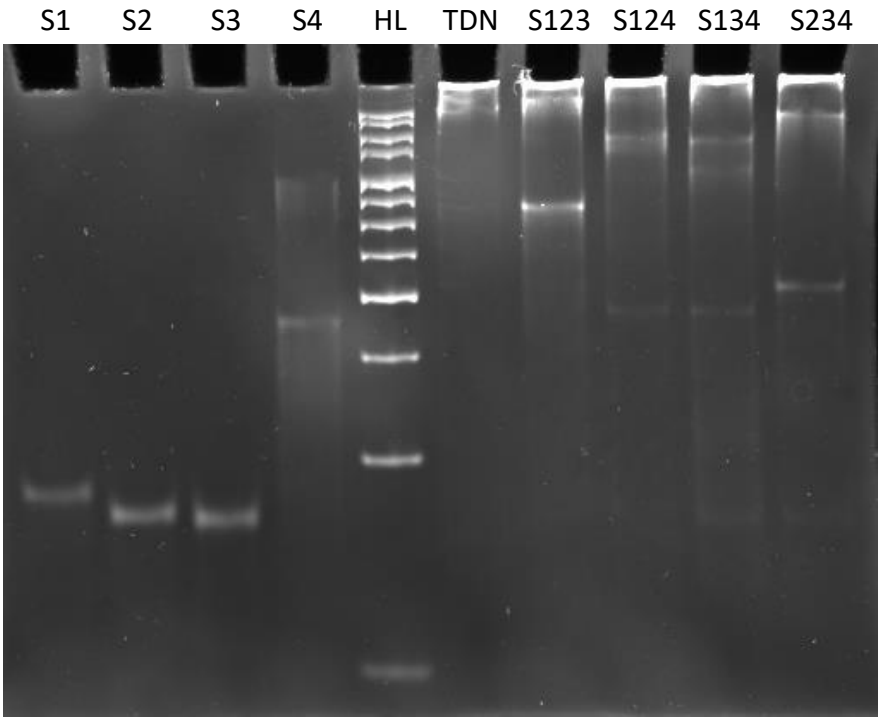

Figure 4.8 Confirmation of successful Assembly of TDN by PAGE. 8% polyacrylamide gel ((wt/vol), electrophoresis at 80V for > 80 minutes in 1x TBE. Gel was stained after electrophoresis in running buffer with EtBr (0.5 mg/mL) for 30 minutes prior to imaging. Lane map above gel denotes contents of each lane.

The gel image in Figure 4.8 provides confirmation of TDN assembly in lane 6, with the absence of any clear band within the lane. This is suggestive of a large molecular weight structure that cannot successfully migrate through the gel. The absence of a band in this particular lane has been used as confirmation in numerous works in the literature, as all partially assembled combinations (lanes 7-10) show multiple bands at various distances. This is suggestive of complexes forming between either two or three of the constituent oligonucleotides, with migration dependent upon the total number of base pairs in the complex. Lane 6 shows an absence of any band present in Lanes 7-10, only a particularly bright region proximal to the well. This is suggestive of all oligonucleotides in the well of Lane 6 forming a larger complex, and leaving no constituent oligonucleotide free at a meaningful concentration

that can be observed by imaging. Note the oligonucleotides used in this analysis feature no thiol modification to the 5' end (TETv3 system). As such, there is no incidence of potential oligonucleotide dimers contributing to the brightness of any bands in this image. In this work, both TETv1 and TETv2 systems, use thiol modifications to immobilise these structures on to the transducer surface, through TCEP reduction steps are employed to prevent dimerisation of constituent oligonucleotides. In the literature, detailed PAGE analysis shows the incidence of dimers forming for thiolated sequences in the absence of TCEP. However, a reduction step like that used in this study was sufficient to prevent this from occurring, and is highlighted by the loss of the band attributed to the formed dimer.[185]

4.3.4 TETv1 System: Electrochemical Performance

The first of three tetrahedral biosensing designs investigated in this study was based upon the immobilisation of the structure as a constituent in a mixed monolayer. Building upon the well-documented electrode functionalisation protocol described earlier in this chapter, the conventional OXA pDNA was exchanged for an assumed matched concentration of the assembled tetrahedron. The theory in literature reports an enhancement in hybridisation efficiency correlated to the better positioning and spacing of the recognition elements, encompassed in the pendant extension of a tetrahedron.[131] Chronocoulometric methods developed by Steel et al, and Keighley et al, could have been employed here to assess the surface coverages following incorporation of tetrahedron assemblies. Time constraints prevented such an analysis contrasting linear probe coverage against tetrahedron coverage, to determine if it was possible to validate improved spatial position of the recognition sites.

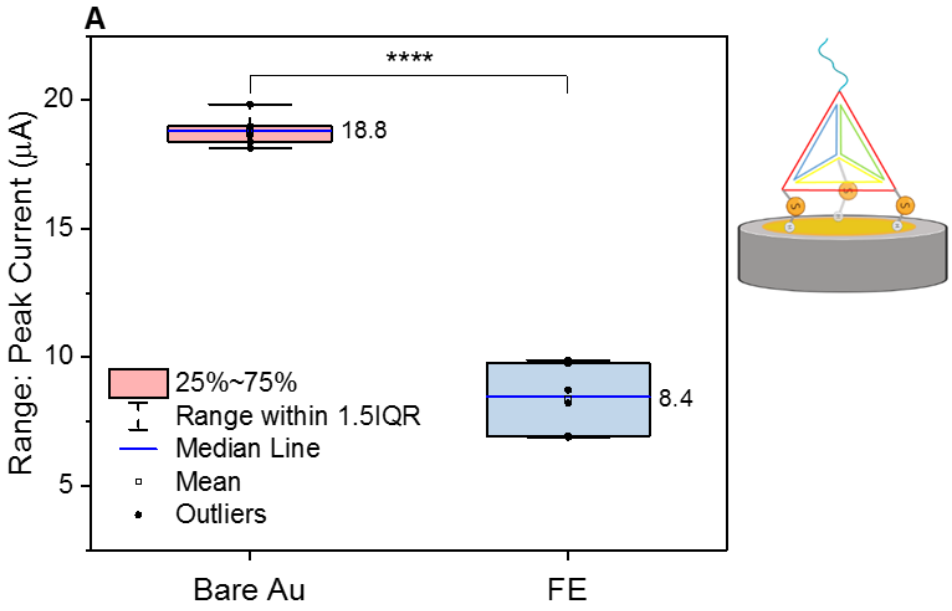

Figure 4.9 Box plot of DPV peak current for PGE post-clean, and after functionalisation with a TDN/MCP mixed SAM. *n* = 6 PGE. Accompanying schematic for TETv1 system, where the immobilised structure has a top extension hosting the recognition element. Electron transfer mediated by 2 mM $Fe(CN)_6^{(-3/-4)}$ solution.

Initial observations report general consistency in peak currents (µA) and R_{CT} (Ω) with those associated with linear probe DNA SAMs. This is shown in Figure 4.9 (**A**) where a highly significant decline in peak current follows overnight incubation in a solution of 2 µM TDN : 20 µM MCP, in excess 100 µM TCEP. After which mean peak current for such FE is recorded as 8.4 ± 1.3 µA. This is comparable to the range in which the FE protocol is deemed successful for the co-immobilisation of a linear pDNA / MCP SAM. A figure collating high sample size of PGE functionalised with linear probes using this method is provided later in this thesis (see Chapter 5.3) Electron tunnelling is well evidenced for immobilised alkanethiols, with tunnelling current strongly dependent on chain length.[241] With consistency in peak current, it is possible to suggest the currently unknown total number, or surface coverage of the tetrahedra has not significantly influenced the electrochemical characteristics of the functionalised electrode condition. However, the primary benefit of such a sensor design lies in the improvement of recognition site availability, with a lesser impact of electrostatic and steric hindrance from a proposed greater spacing between adjacent recognition elements. This would be evidenced by a magnified electrochemical signal change in response to lesser target concentrations than a conventional linear probe system.

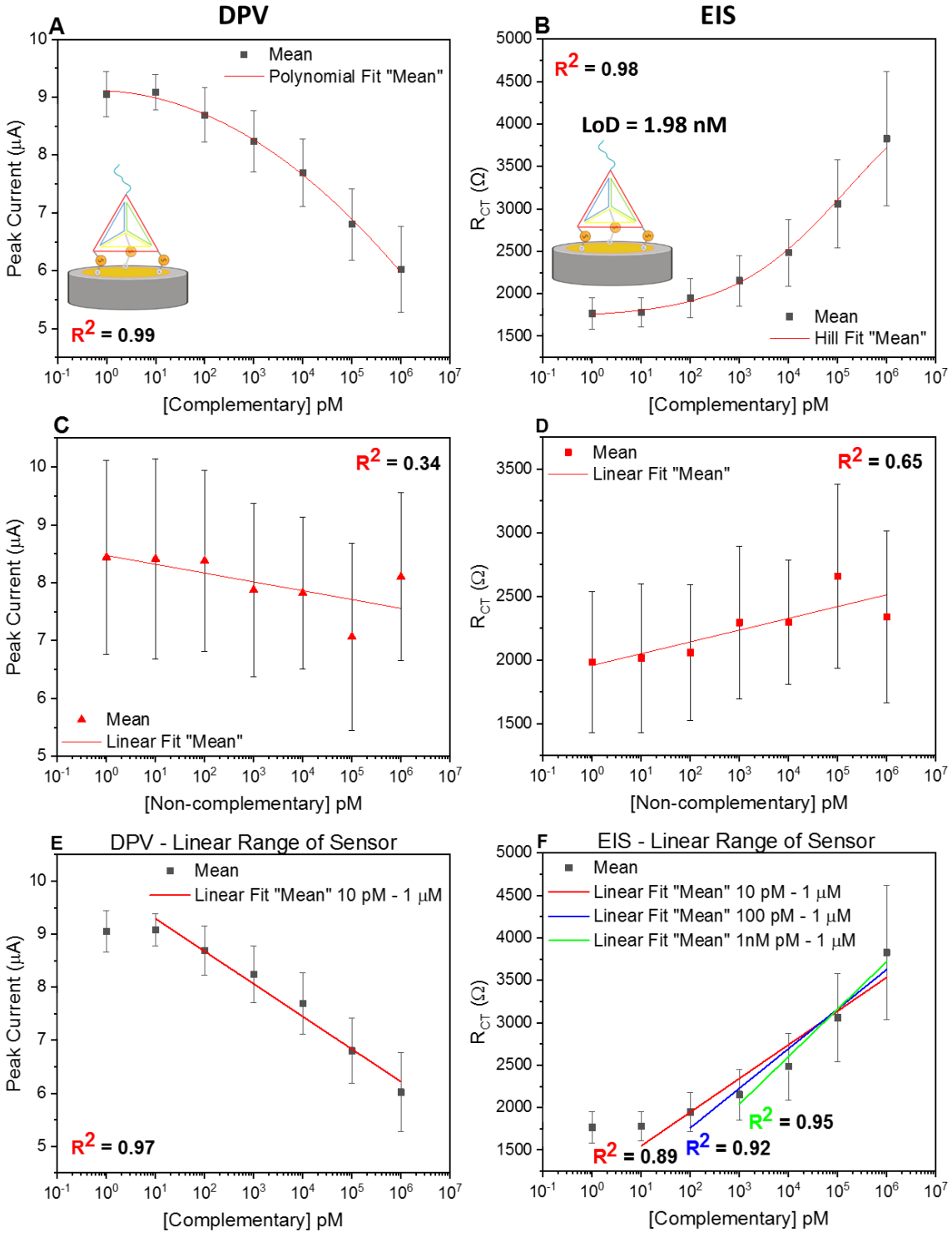

Figure 4.10 Electrochemical characterisation of TETv1 System performance following incubation with complementary and non-complementary target. (**A**) Peak current with increasing complementary target. (**B**) R_{CT} against complementary target. (**C**) Peak current with increasing non-complementary target concentrations. (**D**) R_{CT} against non-complementary target. Estimation of linear range of sensor with DPV interrogation (**E**) and EIS (**F**). Complementary target = 115nt OXA Fragment, Non-complementary = 115nt Junk Fragment. *n* = 3 PGE for all tiles this figure. Error bars = SD

In Figure 4.10, the tetrahedra functionalised electrode has been exposed to increasing concentrations of complementary target, at a range of 1 pM to 1 µM. The plotting of DPV derived peak current (µA), and charge transfer resistance (R_{CT} (Ω)) from EIS, against the varying target concentration is provided in Figure 4.10 (**A**) and (**B**) respectively. The DPV data set is well fitted by a polynomial function with a strong correlation coefficient of > 0.99. Given the sigmoidal growth trend for R_{CT} in response to increasing target concentrations, fitting with a Hill function was deemed appropriate. Subject to low concentrations of complementary target, both peak current and R_{CT} induce minimal deviations from the mean of the functionalised condition. Thereafter, a linear region can develop which is hypothesised to be a resultant from increasing target capture incidence. The data set does not expand out beyond a target concentration of 1 µM, therefore there is no experimental observations of sensor saturation here. However, the expectation would be for an expanded target concentration range the dataset would develop into a sigmoidal, dose response curve. The fitting of data in (**B**) by the hill function allows for an estimation of sensor LoD at 1.98 nM. This is advance on the LoD estimated for an immobilised linear probe in the sensing of the 115nt OXA fragment.

With known issues of sensor drift associated with time dependent SAM reorganisation,[58–60] it was necessary to assess the stability of the sensor construction to repeated incubations, rinsing stages, and varying temperatures with a non-complementary target. Recent data gathered by Piper et al, reports the incidence of drift in charge transfer resistance for short chain alkanethiol SAMs formed on noble metals. Repeat EIS measurements present a near linear response with significant increases in R_{CT} (Ω) over the first 10 hours, before a steady state is reached.[18] It is therefore vital to determine if any such sporadic reorganisation that may occur throughout the ~ 7 hour experimental procedure, is contributing to the signal change previously associated with target hybridisation.

In (**C**) and (**D**), mean peak current (µA), and R_{CT} (Ω) is again provided in response to a changing concentration of a non-complementary target. All other experimental parameters mirror those employed in (**A**) and (**B**). The data is then fitted with a linear regression to contrast directly with the data gathered from the complementary target study. For both data sets, no linear relationship is observed which could be associated with SAM reorganisation, or from the direct impact of strong nonspecific binding events. This is reflected in the poor correlation coefficients of 0.34 and 0.65 for DPV and EIS interrogation. Also of note is the high variation in the data for each non-complementary target concentration, which is not present where a

complementary target is used. The conclusion of which, is that nonspecific interactions are poorly defined, and highly variable in their impact. This confirms the signal changes reported in (**A**) and (**B**) are a function of target hybridisation, however it does not confirm the stringency of sensor selectivity. This could be achieved by the incorporation of a series of basepair-mismatched targets, and contrasting of any resultant signal changes with those associated with the complementary target. Finally, this control assay provides some confidence surrounding a potential area of concern for tetrahedron feasibility. In a recent publication by Carter et al, a thorough investigation into tetrahedron stability was carried out, detailing melting temperatures (T_m) of the tetrahedron by UV and fluorescence melting experiments. At a temperature of ~46 ^{0}C, global melting of the entire structure was observed. The DNA melting curves reported in this work display typical profiles analogous to exponential growth curves. At a temperature of ~37 ^{0}C, the melting curves are at the junction between a lag phase and exponential growth phase.[276] This is noteworthy, as all tetrahedron systems employed throughout this chapter are subject to incubation temperatures held at 37 ^{0}C. This is tending towards a threshold temperature where structural deterioration may be a significant concern. The electrochemical data gathered for the complementary and non-complementary studies do not share consistency in any particular trend. Should repeated incubations at 37 ^{0}C induce dissolution of the assembled tetrahedron, this would be expected to induce a common observation in the electrochemical data across both experiments.

Finally, a limit of detection can be successfully estimated for the TETv1 system, when EIS interrogation produces a sigmoidal growth curve of R_{CT} vs complementary target concentration. However, LoDs are quoted ubiquitously in the literature for electrochemical DNA biosensors, from data of various trends. There is often a large variation in the chosen method of derivation, and as discussed previously while documenting the performance of a linear pDNA mixed SAM, the use of a linear regression analysis and Equation 4.5, raises issues over the validity of its determination. Specifically when experimental data is modelled as a linear calibration curve, or when pre-target (blank) measurement of functionalised electrodes encompasses a large standard deviation. As such, (**E**) and (**F**) revisit the complementary target data set for both DPV and EIS measurements. Here a particular focus is given to fitting a linear range of the data set, where an estimation of sensor working range can be established. The working range is modelled specifically from real recorded data. In (**E**) peak current plotted against complementary target concentration gives a strong linear response in the target range

of 10 pM to 1 µM with a correlation coefficient of 0.967. With this voltammetric technique, the sensor design can therefore be concluded to have a working detection range of 10 pM ≥ 1 µM. Note, sensor saturation has not yet been observed with this data set so it is feasible the range is greater than that quoted here. However, when contrasted with the working range given for the conventional pDNA biosensor design, the lower limit is shifted from 1 nM to 10 pM, offering an improvement of two orders of magnitude in target concentration. This is a promising result for gaining enhanced signal performance from the incorporation of structural complexity to the functionalised electrode. Interestingly, the improvement in a working sensing range is not shared with impedimetric interrogation. In (**F**), R_{CT} growth can be fitted at with a linear regression across one of three possible ranges (red, blue and green lines). The correlation coefficients strengthen with an increase in the lower limit of fitting. This is noteworthy for while there is consensus in a stronger R^2 being beneficial in establishing the veracity of a fitting operation in electrochemical biosensors, there is no commonly observed threshold in the literature that an R^2 value must exceed. This presents two immediate issues. First in the use of linear regressions for the derivation of a sensor LoD, and secondly for working range. For the former, if no common standard is observed for this method of analysis, it becomes a significant challenge to establish truly comparable LoDs from linear regression that can be attributable to the performance of a given sensor design. With regard to the working range, two orders of magnitude exist between the lowest and highest lower limit of range. It is therefore critical to establish an appropriate boundary for determining which data points can be included in the regression.

In plotting these three ranges with a “least squares” linear fit it is clear that there is not a strong linear relationship across all concentrations of complementary target and R_{CT} for both the red and blue traces. This does not challenge the hypothesis that an increasing target concentration is contributing to hybridisation, and a subsequent derivation in electrochemical signal, only that the relationship is not strictly linear, specifically in the pM range.

In such a situation, it was therefore appropriate to subject R_{CT} data to t-tests to establish the point of significance in signal change, which could therefore be assigned as the lower limit of the linear working range.[261] Significant change in mean R_{CT} is first observed following incubation with 1 nM of complementary target (p = 0.0484). This allows for the establishment of a working range of 1 nM ≥ 1 µM, with fitting of this data set (green trace) giving the strongest R^2 value of 0.95. This is surprising as the expectation for EIS is to boost sensitivity, compared to

voltammetric methods, with target hybridisation hindering the charge transfer rate of the solution based redox mediator.[244]

As mentioned at the beginning of Chapter 4, the incorporation of the TETv1 system was primarily to serve as learning tool, for developing techniques of structure design, construction and analysis by PAGE. However, there are still promising electrochemical results generated with the use of a tetrahedron : MCP SAM based biosensor design. Additionally there are further investigations that could follow on from these preliminary findings. For example, the size of the tetrahedra may be worth consideration. In 2015, a report by Lin et al; noted that the fine tuning of tetrahedron size by manipulating the length of sequences composing each edge of the structure, gave rise to a changed surface density, spacing between capture sites, and ultimately target hybridisation efficiency. Here, the authors noted a trade-off between large tetrahedra providing an optimum hybridisation efficiency as capture sites are well distanced from one another, with a then weakened LoD as the number of available capture sites decreases with larger structures coating a finite electrode area. Consequently, the strongest sensing performance was observed in TDN with edges of 26 base pairs in length. With a reduction in edge length to 17 base pairs, the LoD was two orders of magnitude higher.[277] The TDNs used in this chapter are composed from sequences recommended in a well-referenced protocol from Zhang et al; 2020,[176] and produce structures with edge lengths of 20 base pairs. It can therefore be theorised that further performance gains may be readily achievable with the rational design of various TND geometries.

The faradaic method of signal generation was primarily driven by the solution based redox mediator $Fe(CN)_6^{(-3/-4)}$. In the literature, much of the tetrahedron applications incorporate a tagged redox species within the structure, commonly located in the pendant ssDNA extension of the top vertice. With much of the sensitivity of such designs derived from target hybridisation impacting the electron transfer rate of the tagged species, it was next necessary to incorporate such a tag into the tetrahedron design reported in this subchapter.

4.3.5 TETv2 System: Investigating the electrochemical performance of a redox-tagged tetrahedron biosensor

Earlier in Chapter 3, this study explored the potential for Ferrocene tagged oligonucleotides to enhance the sensing capabilities of a mixed SAM monolayer. The premise for this investigation was centred on a growing consensus in the literature surrounding a tethered redox mediator yielding meaningful advances in the limit of detection for a nucleic acid target.[85,93,255,278] While the most recent developments focused on a ratiometric approach, the requirement for a secondary modification to the probe oligonucleotide contributes to a significant increase in cost, and further removes a potential biosensor design from a low-cost PoC device.

In both the linear and Hairpin probe systems documented in Chapter 3, a number of common issues were prevalent. However, perhaps most curiously, redox signal appeared transient between measurements. Measureable peak currents derived from DPV interrogation would frequently decrease to be undetectable against background noise, only to re-appear upon further measurement. Equally, the magnitude of peak current was highly variable between PGE functionalised with Ferrocene tagged oligonucleotides. A possible explanation for this was previously provided with the density of immobilised probe limiting the propensity of redox events to occur. Should the probe density of been too high, the large electrostatic repulsion between neighbouring probes may prohibit the necessary orientation required to bring the redox tag proximal to the transducer surface.

Tetrahedra have previously been promoted as viable structures to immobilise on gold electrodes as they contribute directly to a lesser but more efficient packing density. Electrostatic effects and steric hindrance minimise the incidence of close quarters between immobilised structures. As such, the ability of target to reach a recognition element is enhanced. By expanding upon this finding, it was hypothesised that the better spacing of tetrahedra may help minimise previous issues with recording reliable electrochemical signals from a Ferrocene tagged probe. Modification of custom oligonucleotides with a secondary redox is costly. It is hoped that the tethering of a single redox tag to a tetrahedral nanostructure may address the same issues tackled by the dual-tag ratiometric approach in literature,[99] while minimising the financial burden of sensor design. Electrochemical data is presented overleaf in Figure 4.11.

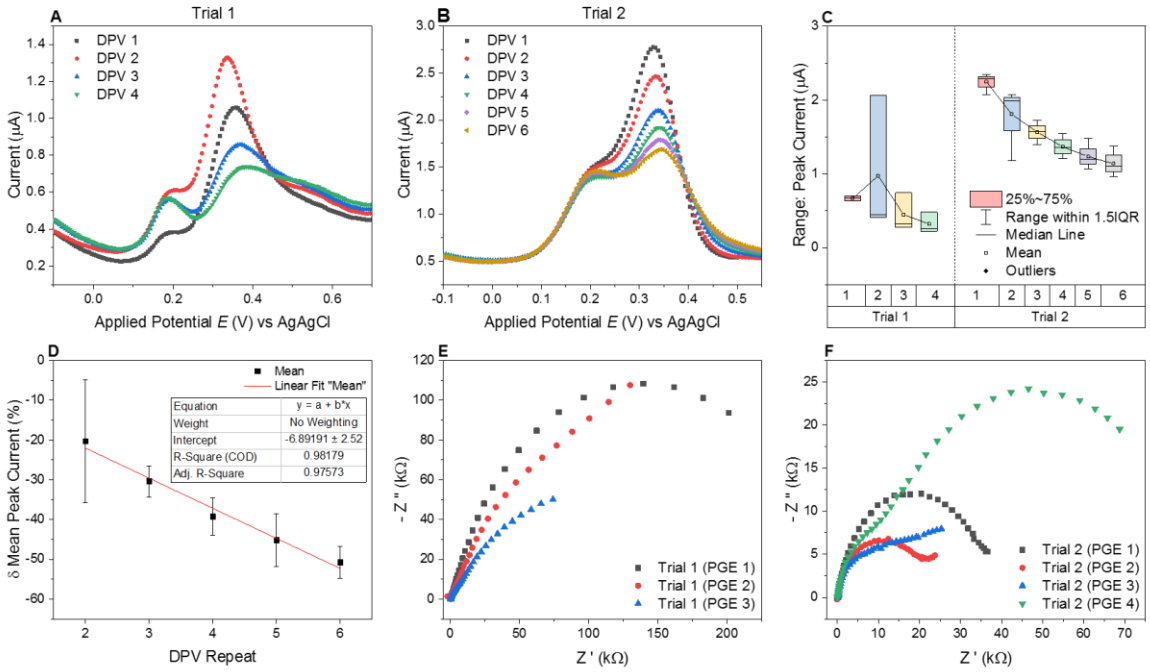

Figure 4.11 Characterisation of a Ferrocene tagged Tetrahedron based biosensor by DPV and EIS interrogation. (**A** + **B**) Averaged Voltammograms of functionalised electrodes in response to repeat DPV interrogation. (**C**) Box plot of DPV peak currents attributable to Ferrocene oxidation from Trial 1 and 2. (**D**) Scatter plot of percentage change in mean peak current. (**E** + **F**) Nyquist plots from EIS measurements of Trail 1 and 2. Trial 1; *n* =3 PGE, Trail 2; *n* = 4 PGE.

In tiles (A) + (B) the averaged responses for DPV interrogation of FE are given. Here the stability of such systems is explored with repeated to measurements. Trial 1 and trial 2 describe two distinct attempts to characterise such a sensor design each with an n = 3, and an n = 4 PGE respectively. The first measurement (DPV 1) yields a mean discernible peak current of 1.15 ± 0.45 µA, upon an applied potential of 0.343 ± 0.017 V with all PGE collated across both trials. The magnitude of this peak variation is high, and the potential of this dominant peak following a single DPV measurement is short of the formal oxidation potential of Ferrocene (II) vs Ag/AgCl, of ~approximately 400 mV.279 Interestingly, the profile of the DPV trace is not a typical single peak curve. In Trial 1, a minor peak centred on ~180 mV, evolves with successive measurement from the left shoulder of the major peak; both in amplitude, and in definition. Though common to both trials, the clarity of this peak is strongest in Trial 1, with its growth to 166.21 nA by DPV 4.

Note, the red trace of Trial 1 (DPV 2) opposes this trend. In the previous measurement, a connection failure in the measurement cell rendered a short for the channel hosting PGE 2.

DPV 2 was the first real measurement of PGE 2, and the mean current trace for DPV 2 is duly influenced by the inclusion of this electrode.

The occurrence of this minor peak has previously been observed in earlier in Chapter 3, and again the cause of this electrochemical event is not yet confirmed. Of all the DNA bases, guanine oxidation occurs at the lowest potential (~700 – 800 mV for both Au and Carbon electrodes).[280,281] This therefore removes the possibility of base oxidation from being a contributing factor to this peak growth. By contrasting the growth of this minor peak, with the greater oxidation peak of Ferrocene centred on ~ 340 mV, it is possible to derive an explanation to what is occurring in this system.

While this Fc/Fc^+ redox couple is readily reversible through cyclic voltammetry, the use of DPV as the primary measurement technique limits the quantity of available Fc species present on the electrode surface. In effect, repeated pulses of increasing potential leads to further oxidation, a decrease in the concentration of Fc, and an increase in the concentration of Fc^+. The net result of which would be a decline in the oxidative peak current, common to both Trial 1 and 2 of Figure 4.11. In an ideal system, cyclic voltammetry of the Fc/Fc^+ redox couple produces a ΔE_ptending towards to canonical value of 59 mV.[26] The $\Delta E_p$for this system is expected to be significantly larger than this. Initial works by Fan et al; into the use of a Ferrocene, tagged stem-loop DNA biosensor gave $\Delta E_p \approx$ 100 mV.[264] This is of relevance as the SAM designed in their work was developed from a 1 µM probe DNA incubation, subsequently backfilled with excess 2-mercaptoethanol at 1 mM. This is comparable to the Ferrocene tagged probes explored in Chapter 3. The expectation for ΔE_p of a tetrahedral biosensor would be that it is greater than that detailed by Fan et al. The minor and major peaks of the DPV traces for Trial 1 in Figure 4.11 (**A**) are at difference in potential of ~ 175 mV. It is possible that evolution of the minor peak is the reduction of a number of now Ferrocenium tags back to Ferrocene. Unfortunately, CV data has not been gathered to confirm this theory.

This method of repeated DPV aims to address an issue associated with the validity of future target sensing measurements. Hybridisation of target has been shown throughout this thesis to be associated with a decline in peak current. Gathering such data requires repeated measurements at each concentration point in the assay. Were a voltammetric method such as DPV or SWV to be employed as the measurement tool for a Ferrocene tagged system, it is essential to understand the impact of Fc oxidation, and the resultant decline in available Fc

species for subsequent measurements. The total concentration of the Fc tags is finite, and governed by the number of immobilised structures on each PGE. In faradaic buffers (i.e. $Fe(CN)_6^{(-3/-4)}$) both species of the redox couple are ubiquitous in solution, and repeated DPV/SWV measurement contributes to no meaningful decline in the oxidative peak.

Without a potential sweep back in the negative direction, the frequency of Fc tags would decrease with each successive measurement. The result of which is shown in Figure 4.11 (**D**), with the % change in peak oxidative current given against measurement number. The fitting of the data exhibits a linear response, (adjusted R-square = 0.97573), with a decrease of peak current at 50.75 ± 4.03 %, by the sixth and final DPV measurement. This is a noteworthy trend, as this decline in the oxidative peak current is attributable to a drifting baseline. Ultimately, this drift would contribute to any signal loss associated with successive target incubations, and must be understood, quantified, and subtracted from data gathered in a subsequent assay.

The Fc-tagged tetrahedral system described above can be considered as a "signal off" biosensor design. The functionalised electrodes in both trials present peak currents at potentials supportive of Fc oxidation. This is indicative of the tagged extension from the top vertice positioning the tag close to the transducer surface. In theory, the hybridisation of target to the tagged extension of the top vertice may induce a change in persistence length,[168] and a reduction in flexibility of the extension necessary to bring the tag close to the transducer surface. This would contribute to "signal off" effect. This would be comparable to previous works with Ferrocene tagged DNA hairpin probes in the literature.[88,98] As discussed above, a consideration into the impact of drift associated with successive DPV/SWV measurements would be necessary in establishing validity in such a sensing apparatus.

However, it is worth emphasising again that one aim of this investigation was to develop a "signal on" sensor design. For this particular aim, the sequence design of S4 was modified to fulfil two distinct requirements. Firstly, the appropriate assembly of a tetrahedral structure. Secondly, to produce a top extension in a hairpin confirmation. This has been reported previously in the literature, where the hybridisation of target at a toehold site on hairpin would induce a conformational change. The opening of which was directly associated with signal gain.[184] An attempt to replicate such a sensing strategy as reported by Lui et al; 2015 was made with modification to the S4 sequence which would incorporate the target recognition site for

the OXA targets used in this study. However, as mentioned previously, the design of such a sequence proved challenging, and further consideration is required.

As evidenced throughout Figure 4.11 (**A**-**D**), oxidative peak currents in the absence of target, suggests the single stranded extension from the tetrahedron is adopting a linear confirmation, though there is a large degree of variation for the positioning of the tag with respect to the transducer.

It is useful to consider this point further. While signal transduction through the Ferrocene tag of the Hairpin probe analysed earlier in Chapter 3 suffers from transiency between functionalised electrodes, a signal attributable to Ferrocene redox is noted in approximately 83 % of FE. The sequence engineered to adopt this secondary structure is relatively short, and passivation of the gold substrate by MCP between neighbouring structures should accomplish two valuable criteria. Firstly, if the sequence were to exist only in a linear confirmation (i.e. fail to form the designed hairpin), the relative short sequence length would maintain a degree of rigidity in the strand and result in an orientation perpendicular to the electrode. This would distance the Ferrocene tag from the surface and minimise signal transduction. Secondly, the MCP film ubiquitous across the electrode would minimise the incidence of DNA immobilising in a "lying down phase",[47] again restricting the feasibility of Ferrocene tag accessing the electrode. Combined, these two considerations provide a degree of confidence that the sequence design of Chapter 3, can adopt a hairpin confirmation. However, confirming the exact state of the linear extension of the tetrahedron is challenging by assessing the electrochemical activity of the tag alone. The angle at which the capture pendant sequence extends from the nanostructure governs the tag position with respect to the underlying transducer surface. This variable extension angle may be a factor in variation of electrochemical signal. Optimisation of pendant sequence length may improve the consistency of extension angle, and therefore signal acquisition.

Finally, the Nyquist plots of tiles (**E**) and (**F**) further detail the variability inherent to this assembly. Electrochemical circuit fitting of data present in these tiles is challenging. The simplified Randles circuit used successfully in previous chapters' breaks down as an effective model of events in the electrochemical cell. Consequently, the necessary complexity of circuit design to appropriately model surface effects in challenging, and further limits the feasibility of this Fc-tagged system to serve as an appropriate candidate for a viable biosensor design.

In subchapters 4.3.4 and 4.3.5, two distinct methods of using immobilised tetrahedra as part of a mixed SAM have been explored. Firstly, a solution based redox mediator was used to drive signal transduction (TETv1 System). In the second method, a Ferrocene tag incorporated to one of the constituent oligonucleotides was chosen as the redox signal mediator (TETv2 System). The potential benefits, and current difficulties have been discussed at length, however for clarity it is worth providing a brief summary of the high-level findings of this study.

- TETv1 System:
    - Tetrahedron based SAMs appear consistent in initial characterisation to those of a conventional pDNA based biosensor
    - No observable electrochemical response to potential thermal melting of the structure
    - Enhancement to the estimated LoD
    - Improved sensor working range with a tetrahedron based mixed SAM
    - Ability to discriminate between complementary and non-complementary targets
    - Further work necessary to discern the true selectivity of the sensor design
- TETv2 System:
    - The linear extension may position the tag at varying distances from the underlying electrode as evidenced by the transient and highly variable DPV peak current associated with Ferrocene oxidation.
    - Complex signal output (poorly defined peaks for analysis)
    - High variability of recorded voltammetric signals (peak currents)
    - High variability in the profile of Nyquist plots contributing to complex circuit fitting requirements

The brief summary above generated a question of direction for how best to explore the potential of tetrahedral biosensors. The TETv1 system shows promise, though its novelty is poor and to improve current advances in the literature would require significant investment. This may include more complex chemistries, such as enzyme-based signal amplification,[178] or Hybridisation Chain Reaction Amplification to boost sensitivity.[180] Investigating such techniques may be beneficial as a learning tool, though would likely lack any meaningful and novel contributions to the biosensing field.

While searching the literature for inspiration, reports of signal amplifiers aiding detection limits for nucleic acid biosensors are commonplace. Many of which rely on enzymatic amplification, or nanoparticles to enhance performance. A clear emission in the field emerged, with no reporting of DNA nanostructures as signal amplifiers. Self-assembly methods are capable forming well-defined geometries, of predetermined size and confirmation. These assemblies can be tailored to produce a desired characteristic of size, and specific charge. This is comparable to the advantageous properties of nanoparticles used in other biosensor designs. This chapter has already documented an ability to form tetrahedra, with a pendant sequence of DNA capable of hybridising a target. Therefore, a hypothesis was formed to develop an assay where by a simple linear DNA probe functionalised electrode would attempt to detect a larger complex of the desired target DNA, coupled to a Tetrahedron in solution. The schematic of Figure 4.12 overleaf gives an overview of this process. Simply, a linear probe was designed to house a recognition element specific to a region of synthetic target, analogous to the OXA-1 gene derived from AMR plasmid mimics. At the opposing end of this target exits a serious of bases to which the pendant extension of a tetrahedron shared complementarity. Incubation of a target rich solution with a given concentration of tetrahedra at 37 ^{0}C, allows for the hybridisation forming a larger complex. The resultant complex would then be introduced to a pDNA-functionalised surface, for electrochemical interrogation.

4.3.6 TETv3 System: Using DNA Tetrahedra as signal amplifiers for the electrochemical sensing of DNA hybridisation

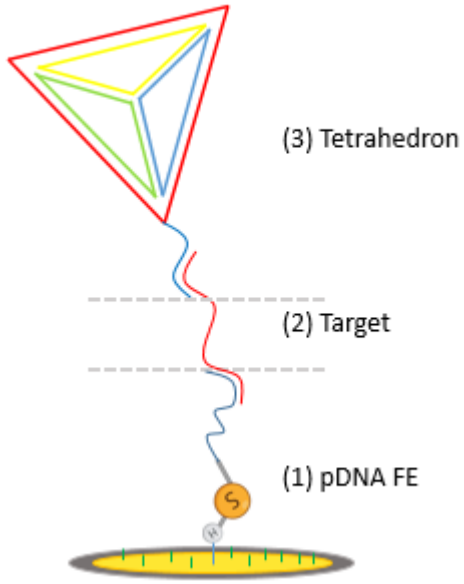

Figure 4.12 TETv3 – a signal amplifying DNA biosensor design

The above sensor design investigated in this subchapter is composed of three central constituents. Firstly, a functionalised transducer with a short probe DNA / MCP monolayer. Second is a target oligonucleotide, with a series of nucleotides positioned at its 3' and 5' domains. Each of which serve as unique recognition sites. Thirdly is a DNA tetrahedron, with a single stranded pendant extending from its top to vertice. The target oligonucleotide links the tetrahedron with the probe-functionalised electrode. In the absence of this target oligonucleotide, the Tetrahedron cannot appropriately tether itself to the functionalised electrode without the presence of the linking target. The working principle of this sensor design is centred on enhancing both charge, and steric hindrance of a redox mediator from accessing transducer surface. Thus, impedance is theorised to increase. The specificity of such an approach is dependent upon the ability, and presence of a target oligonucleotide to be sensed by the functionalised transducer surface, and capture the larger tetrahedra. In absence of the correct target sequence, incorporation of these nanostructures into the bioelectric interface may not be possible. This design can be considered analogous to signal amplification strategies incorporating redox tags, which are commonplace in literature. However, in place of harnessing

the electrochemical activity of such tags for signal transduction, charge based repulsion and steric hindrance serve as the tools for mediating electrochemical signal.

Throughout Chapter 4, the primary target of interest has been a 20nt synthetic oligonucleotide (OXA). This sequence is analogous to a gene present in the plasmid of many gram-negative bacteria encoding antimicrobial resistance (OXA-1 beta-lactamase). The subchapter to follow is an exploratory attempt at understanding how DNA nanostructures may aid in future designs of PoC electrochemical biosensors. As such, DNA sequences used for the Tetrahedron assembly, and sensing apparatus have been optimised to assess the feasibility of such a sensor design. It is beneficial to consider the nucleic acids employed in this work as purely materials at this stage, and not biological information molecules.

The "target" chosen for this work is a synthetic oligonucleotide of 115nt. It has a basis in biology, being derived from the amplicon of the above OXA gene,[36] though it has been engineered to remove any overhangs at its 5' or 3'. Consequently, this leaves two key distinct recognition sites free for hybridisation, allowing it to serve as the key in linking the tetrahedron to the functionalised electrode. The constituent oligonucleotides of the tetrahedron design are consistent with those used previously for the TETv1 and TETv2 systems.

For clarification, the terms "Target" and "Complementary Target" in this subchapter specifically denote the 115nt OXA fragment. This will be subject to a varying concentration as the primary analyte of interest in this assay. "Non-Complementary Target" is specific to the randomly generated 115nt Junk Fragment. The tetrahedron will be held at a fixed concentration throughout at 500 nM (again assuming a production yield of 100%). The independent variable "target concentration" will be used interchangeably in the analysis that follows in the following format. "xM of target" and "xM:500nM". Both describe an assumed complex forming between a varying concentration of the analyte and a fixed concentration of the tetrahedron.

The experimental protocol for this system has previously been detailed in *4.2.8.3;* however, a brief recap may be beneficial to both author and reader:

1. Functionalisation of Au PGE
    a. pDNA + MCP (18 hrs at 37^0C)
2. Incubation of target oligonucleotide and assembled tetrahedron
    a. XM : 500 nM (30 minutes at 37^0C)

3. Incubation of FE with target/tetrahedron complex
    a. Further 30 minutes at 37^0C
4. Electrochemical measurement
    a. DPV,SWV,EIS

The resultant electrochemical data from the above outline is provided overleaf in Figure 4.13.

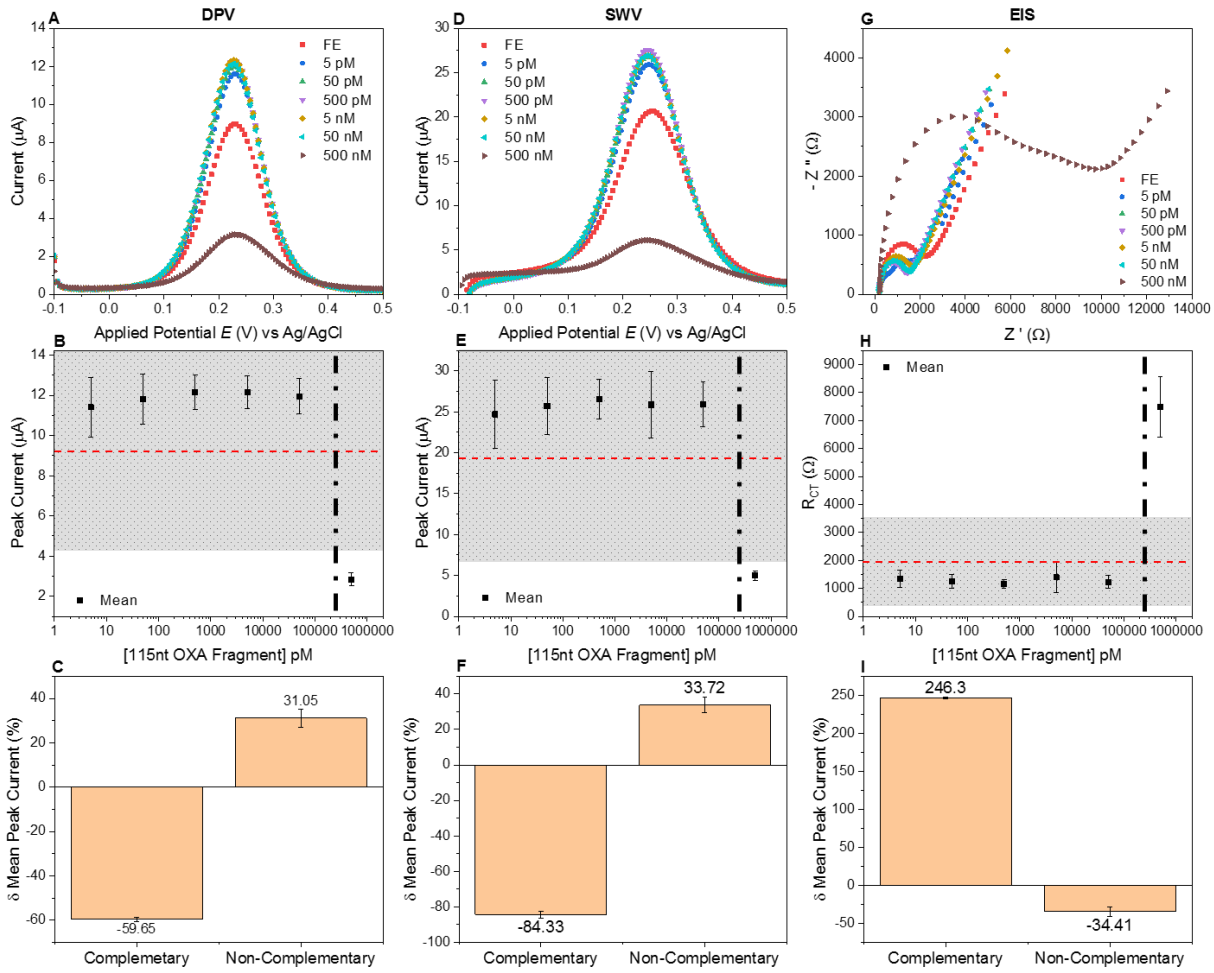

Figure 4.13 Electrochemical interrogation of a novel biosensor design, employing a DNA tetrahedron signal amplifier. Top row; electrochemical data from complementary target assay following DPV (**A**), SWV (**D**) and EIS (**G**) measurements. Middle row; mean peak current from DPV and SWV (**B** + **E**), and R_{CT} from EIS (**H**) in response to varying complementary target concentrations. Red dashed line is the mean FE signal, and grey band denotes 3*SD of the mean FE signal. Black dashed line marks the division of two distinct trials. Bottom row; mean % signal change for DPV and SWV peak current (**C** + **F**) and EIS derived R_{CT} (**I**). *n* = 6 PGE per condition (and Trial).

In the top row of Figure 4.13, recorded signals for voltammetric methods of DPV (**A**), and SWV (**D**), and electrochemical impedance spectroscopy (**G**) are provided. The corresponding peak current and R_{CT} in response to given target concentrations compose the row (**B**), (**E**) and (**H**). Common to all is a change in signal magnitude that is unexpected. Specifically, the incubation of the complex at a ratio of 5 pM:500 nM contributes to a small gain of peak current in the DPV and SWV measurements, and a decline in R_{CT} for EIS interrogation. This deviation from the pre-target condition is consistent across all target concentrations through to data point 5 (50nM:500nM). However, no individual data point of peak current or R_{CT} is significantly

different from the mean of FE. ($p > 0.05$) up to data and including data point 5. The mean of FE peak current/R_{CT} is displayed as the red dashed trace, as a visual aid for detailing a shift in either peak current/R_{CT} with target incubations.

There are a number of interesting questions raised by the second row of Figure 4.X. Firstly; the tetrahedron possesses only one region of complementarity to the target, located in the single stranded DNA pendant extending from its top vertex (oligo S4). Consequently, hybridisation should only be supported by those specific sequences. At the lowest target concentration of 5 pM, the accompanying Tetrahedron is present at a concentration x100, 000 greater. All constituent oligonucleotides forming the tetrahedron are present at an equimolar concentration during assembly, therefore the concentration of the oligo S4 is 500 nM, and exists in the assay either as free single stranded sequence, or as part of the assembled Tetrahedron. Given that solution-phase DNA hybridisation is a high efficiency process,[282,283] it is highly probable that at its lowest concentrations (data points 1-5 of the second row of Figure 4.13) the target has hybridised with the recognition site of S4, either as part of an assembled tetrahedron, or a linear double stranded complex. PAGE analysis may provide a useful insight to the specific mechanism, with specific band presence in a lane containing assembled tetrahedra and target denoting mechanism of hybridisation.

The electrochemical data would suggest that target, either free in solution, or hybridised to the tetrahedron pendant, has poor availability to be captured by the immobilised probe, and cannot be directly monitored. Previous investigations in this study have identified significant changes in peak currents and R_{CT} associated with the capture of single stranded DNA targets by immobilised probes, down to the low pM range. This suggests that the design of the target to serve as a tether between probe and tetrahedron may have failed at this objective.

However, the final data point (500 nM : 500 nM) across the second row of Figure 4.13 yields a significant change in peak current and R_{CT} with minimal variance between PGE. This data point is from a separate prior trial (n = 6 PGE, with duplicate measurement) investigating the specificity of this sensing apparatus. This is worth inclusion along with the assay data, as it highlights the requirement for additional work to enhance the repeatability of this sensor design, while also hinting at its potential. Evidently there is a meaningful signal change associated with this distinct data set (500 nM : 500 nM), however the responsible mechanism for this is not yet clear. While the target concentration is larger (10x greater than the largest

target concentration in the assay), it is still matched with that of S4 (tetrahedron). It is therefore unlikely to be solely contributed to free target hybridising with the probe DNA, and not a combinatory function of free target, and target/tetrahedron complexes. Nor should the signal change associated with that data set be dominated by non-specific adsorption, causing perturbations in the underlying mixed monolayer, and an increasing current leakage. This is evidenced in (**C**), (**F**) and (**I**) of Figure 4.13 where the mean peak current significantly declines by 59.65% and 84.43% for respective DPV and SWV measurements, and mean R_{CT} significantly increases by 246.3% with complementary target ($p \leq 0.0001$ for all quoted signal changes). Note these signal changes are larger than those observed in Figure 4.7 during the performance assessment of the underlying SAM in sensing a single stranded target oligonucleotide that was at a x2 larger concentration in TM buffer alone.

At a high level, this suggests there is potential in this method of sensing. However, variation between distinct experiments is large (highly significant signal change in trial 1, no significant signal change for any target concentration in the assay trial 2). However, this is a preliminary and exploratory study into the feasibility of such a sensing apparatus. It is worth stressing the numerous avenues of optimisation that could aid in potentially eliminating some of the quoted issues to date. Firstly, the hybridisation temperatures and incubation times for the formation of target/tetrahedron complexes are yet to be fully investigated. These were chosen based on previous works with conventional linear probe DNA SAMS, and short single stranded targets.[126] It is not entirely clear how this incubation stage may influence the confirmation of the tetrahedra, and contribute to a structural failure, though 37 ^{0}C should be insufficient to induce global structure melting.[19] This optimisation will require multiple studies across a wide temperature gradient comparing electrochemical signal change, with PAGE analysis. Should this higher temperature incubation be contributing to structural breakdown this may be reflected in the appearance of multiple bands. A strong hybridisation efficiency of the target and capture site of the tetrahedron would be indicated by the presence of a sole band in the gel, with a migratory distance equal to that of a similar molecular weight band in the Hyperladder.

Secondly, the concentration of the Tetrahedron used in this particular system has been fixed at an assumed concentration of 500 nM. This is dependent upon an effective yield of 100% for the assembly stage. The assembly protocol follows closely that of the 2021 Nature Protocols paper of Zhang et al,[176] where a detailed methodology is provided for assembly verification by

PAGE analysis, size and morphology characterisation by AFM, and particle size and zeta potential measurement by Dynamic Light Scattering (DLS). The latter two characterisation methods of AFM and DLS where unfortunately beyond the remit of this study due to time constraints. However, the tetrahedron design (specifically the complementary sequences that force self-assembly), buffer conditions, and annealing and cooling stages mirror those recommended in the protocol of Zhang et al. The only discrepancy is the modification of S4 to incorporate the specific recognition element of the chosen target. This region contains no complementarity to any other constituent oligonucleotides that would otherwise effect final structure confirmation. In only being able to review the performance of assembly by PAGE analysis, there was no method of reliably estimating the effective yield of tetrahedra assembly. An assumed yield was given at 100%, and resultant working concentration of 500 nM could be studied. This however raises the issue of how an undefined yield may by influencing the working tetrahedron concentration used in this study. This may account for the inter-experimental variation between the electrochemical data of Trail 1 and 2, in Figure 4.13. A yield determination would be highly beneficial in establishing true working concentrations of tetrahedra for future assays. This would allow for an optimisation study of the required tetrahedra concentration to elicit the strongest sensing performance. This would be beneficial to all tetrahedra systems detailed throughout Chapter 4, where all structures have been assessed at an assumed concentration. Finally, one of the three key components of the TETv3 system is the immobilised DNA probe/MCP mixed monolayer. The design of which to date been based upon the ability of such a layer to detect the hybridisation of a linear target alone (see Figure 4.7). The packing density of this probe may require modification to ensure that the capture of a larger target : tetrahedron complex may not be limited by steric hindrance of crowded surfaces.

To conclude, the TETv3 system presented here is a novel approach, and this study surmises some preliminary and exploratory investigations in to its feasibility as a biosensing apparatus. Numerous aspects of this design require multiple optimisation trials. However, there is electrochemical data to support the potential of this methodology (specifically Trial 1 data). With further experimentation and system interrogation, it is possible to finely tune tetrahedron concentrations to maximise the signal change of a successful target detection by the immobilised probe. This could be achieved without the high costings of additional metallo-nanoparticles, or enzymatic cascades that are conventionally employed in signal amplifying biosensor designs.

4.3.7 Investigating the feasibility of system translation to a custom gold electrode array.

With initial experimentation undertaken for all three of the DNA tetrahedral designs, and some promising electrochemical data gathered, focus was shifted to exploring increasing experimental throughput with the use of a custom multi-electrode array from Flex Medical Ltd. Initially, the devices were interrogated with a conventional cleaning methodology, with CV in 0.1M H_2SO_4 only, followed by characterisation in Measurement Buffer 1 (2 mM $Fe(CN)_6^{(-3/-4)}$ in 100 mM KCl.

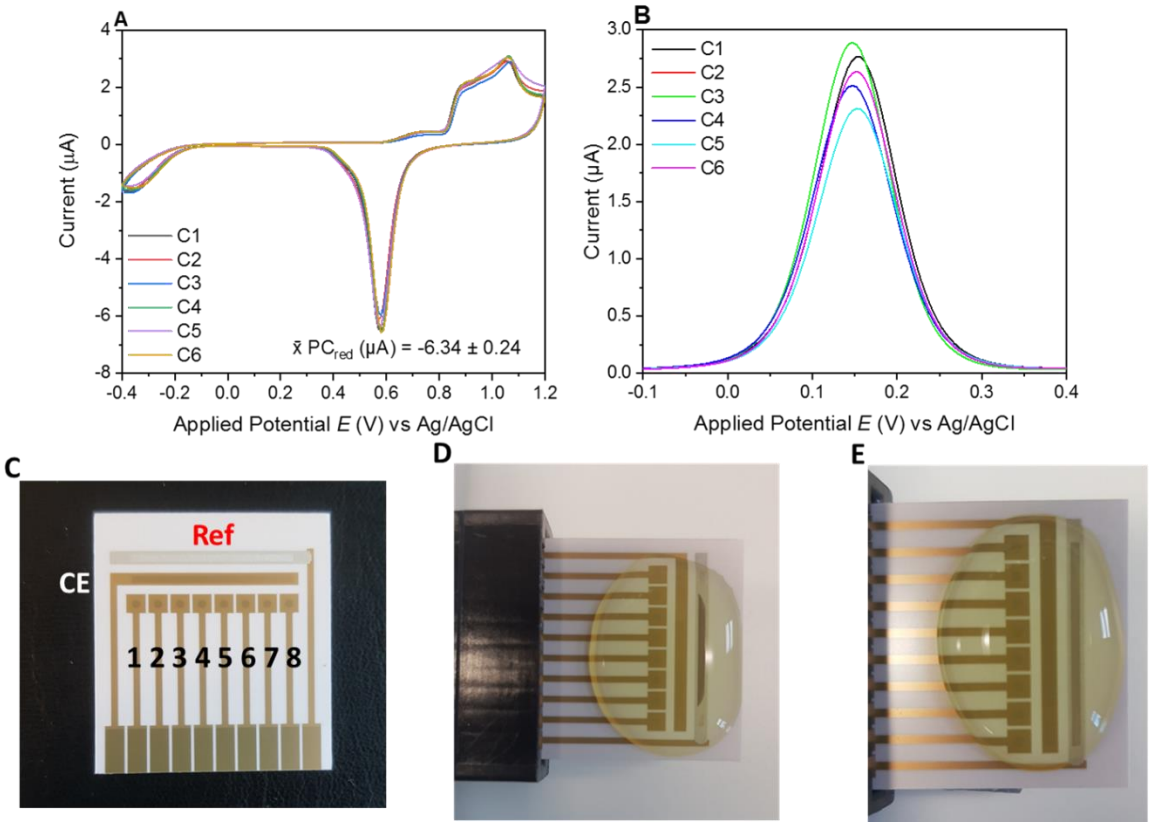

Figure 4.14 Electrochemical Cleaning of Flex Medical Array.(**A**) CV Data from scan 20 for 6x Flex devices, with the mean trace of all electrodes per device shown. (**B**) DPV data from 6x Flex devices, with the mean trace of all electrodes per device shown. (**C**) Image of Flex device detailed to map the position of each working electrode, reference and counter electrode. (**D**) Darkening of the central region of the reference electrode in the presence of faradaic redox buffer. (**E**) Entire reference electrode darkened in faradaic redox buffer. Data is presented in (**A**) and (**B**) as a line graph, this purely to aid presentation of multiple traces. Quantitative analysis is derived from the real data measured data points only.

CV data from the electrochemical cleaning of six different devices is presented in (**A**), with the mean signal recorded for all 8 working electrodes presented for each device. The mean reductive peak current after 20 scans for each of the traces is given as -6.34 + 0.24 μA. stability in the reductive peak current is achieved by ~ 15 scans for all of the working electrodes. This is indicative of a consistent cleaning across devices, and therefore consistency in the area of working electrodes. After which, each device was subject to DPV interrogation to establish a baseline characterisation of the cleaned surfaces prior to any functionalisation. Each trace in (**B**) describes the mean DPV signal of all working electrodes per device, with the varying magnitude of each peak providing a visual indication to discrepancies in signal transduction across devices. However, when the peak current of each working electrode (n = 36) across all devices are pooled, we see the true variation is low with a mean peak current of 2.58 ± 0.2 μA. An image of the device is given in (**C**), with the 8 working electrodes positioned as an array, with a neighbouring parallel gold counter electrode, and parallel reference electrode composed of a silver/silver chloride paste. This image is taken prior to any electrochemical treatment. Moving on to (**D**), this device has been subject to a single DPV measurement across a potential window as shown in (**B**), and then incubated in overnight at 37^0C in a SAM forming solution (1 μM OXA pDNA + 10 μM MCP; in 50 μM TCEP – TM Buffer (pH 8). Note, the darkening of a large region of the reference electrode. In (**E**) a separate device has been subject to the same conditions as the above, however the entire reference electrode has darkened. This is a common observation; with ~ 60% of all devices showing some degree of damage to the reference either after functionalisation, or a given number of subsequent measurements (most commonly less than 3). Interestingly, growth of the darkened region appears to be accelerated by repeat measurement. This phenomenon has also been observed for cleaned electrodes stored in 1× PBS at room temperature within 15 minutes. This is suggestive of activity from a species within the functionalisation / buffer solutions upon the reference material, though the specific mechanism is not yet confirmed. This may be a function of variety in the manufacture or composition of the silver chloride paste forming the on chip reference, though further investigation is required. Commonly, the damage of the reference material leads to a significant spike in applied potential by the potentiostat. In these cases, the gold working electrode is often stripped from the underlying substrate. As such, this prevents the current three electrode on chip design from being applicable for further experimentation.

To circumvent this issue, attempts were made to incorporate an external reference into this system, however this was technically challenging given the requirement to operate with small volumes on chip. Designs for a 3D printed well that could be adhered on to the chip to help accommodate an external reference were explored, though these prototypes are still in development and not shown here. A simpler method to bypass issues with the on chip reference was to explore the feasibility of running a 2-electrode cell measurement, with a combined Counter/Reference. Electrochemical cleaning data for such an approach is given Figure 4.15.

The cyclic voltammogram provided in (**A**) shows data from the 20th scan of the cleaning measurements. Stability is observed in the cathodic peak by the 15th scan for all working electrodes. The mean reductive peak current is 25.52 ± 0.79 µA. The DPV plot provided in (**B**) characterises each working electrode in faradaic buffer, with a mean peak current of 2.48 ± 0.09 µA. This is consistent with mean peak currents following CV cleaning with the use of the on chip reference. Note, the potential at which a peak current associated with the $Fe(CN)_6^{(-3/-4)}$ redox couple has shifted to ~ 0V. An accompanying Nyquist plot in (**C**) also highlights a good degree of conformity across all working electrodes with a small, distinct semi-circle region with a mean R_{CT}

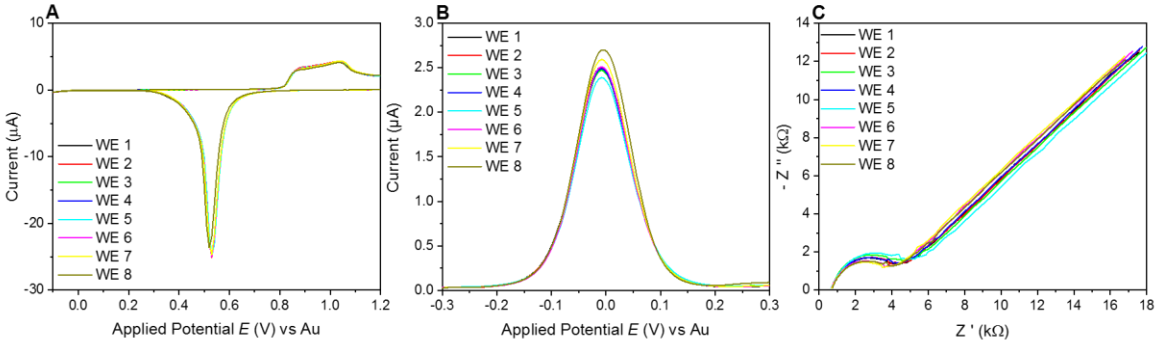

Figure 4.15 Characterisation of Flex Device with combined Au CE/Ref. (**A**) Cyclic voltammogram from final cleaning scan. Faradaic interrogations of device after common CE/Ref CV cleaning, with DPV (**B**), and EIS (**C**). Measurement Buffer 1 used for faradaic measurements.

of 3529.9 ± 386.72 Ω across the device. This initially suggests the feasibility of using an two electrode cell (WE/CE) for the electrochemical cleaning of the flex devices, while exploring methods to improve the on chip reference or successfully incorporate an external reference to the system. Thereafter, these devices were functionalised with a mixed SAM as follows, 1 µM OXA pDNA + 10 µM MCP with 50 µM TCEP (in TM Buffer pH 8). The SAM was allowed to form overnight (18 hours) at 37 ^{0}C, in accordance with PGE functionalisation protocols used throughout this chapter. The electrochemical data following DPV interrogation is presented below in Figure 4.16.

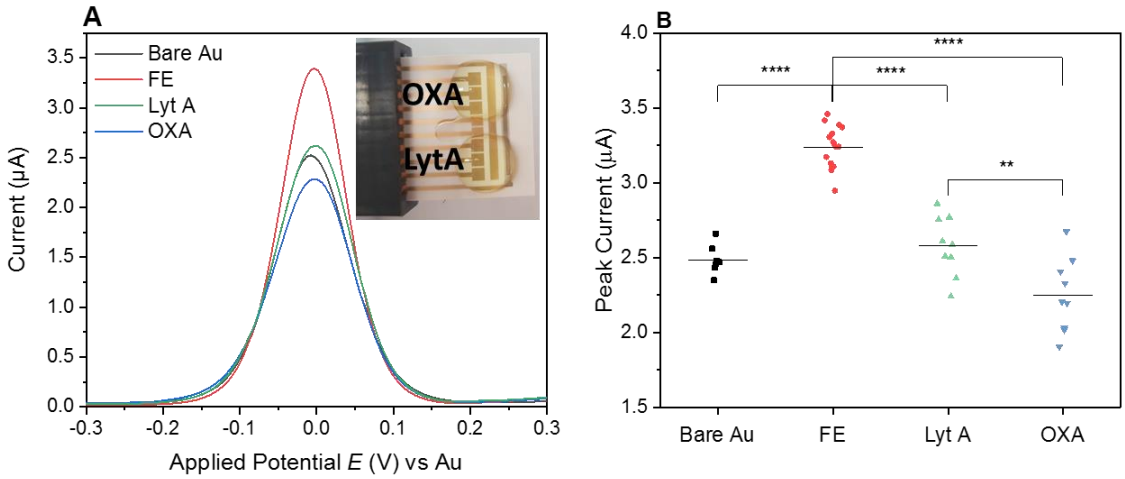

Figure 4.16 Assessment of Flex electrode functionalisation and response to complementary and non-complementary targets. (**A**) DPV trace for each stage in the experimental protocol. *Inset*: Flex device with WE 4+5 masked by varnish to prevent solution containing either target. (**B**) Peak current plotted for each condition, with three repeats for each condition, therefore *n* = 9 WE for Bare Au, *n* = 16 for FE, and *n* = 9 for Lyt A and OXA incubations.

The immobilisation of an organic film on planar gold has been well evidenced to induce a significant decline in the electron transfer rate of a solution based redox mediator. Consequently, a reduction in voltammetric peak amplitude is expected. In Figure 4.16 (**A**), the magnitude of the peak in the voltammogram increases in the voltammogram (red trace). This is unexpected, and may be indicative of the functionalisation protocol effecting the electroactive area of the device. This is reflected in (**B**) where a highly significant increase in peak current is recorded following overnight functionalisation. Thereafter, incubation with 1 µM of either the non-complementary Lyt A target, or the complementary 115nt OXA fragment. Both of which are sufficient to induce a significant decline in mean peak current, though there is a significant difference in the magnitude of the decline between the positive and the negative. An investigation was launched to determine the cause of functionalisation appearing to enhance system conductivity. This is documented below in Figure 4.17, where a Flex device has been functionalised with a 10 µM MCP SAM for 18 hours at 37 ^{0}C.

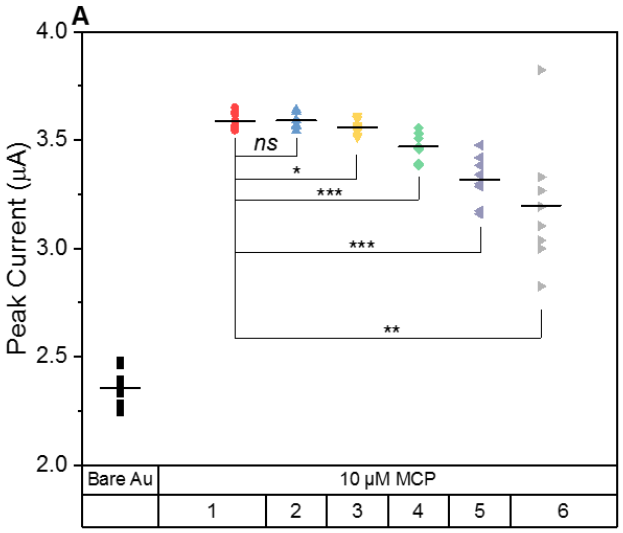

Figure 4.17 Device cleaning by thiol attack. Peak current following DPV interrogation, with Bare Au data gathered following CV cleaning, and then repeat DPV measurements after SAM formation. (*n* = 8 WE (single Flex device)).

The data spread of peak current is tightly clustered around the mean for the post-CV clean condition, indicative of a high degree of surface consistency. However, the growth in peak current is again dramatic following SAM formation. This is currently hypothesised to be a function of thiol attack upon a yet unknown species that is present on the surface of the device. The insulating agent used to prevent cross talk between each electrode, and mask off the track regions has not yet been shared by the manufacturer. It is possible that this molecular coating is been displaced by the thiolated alkane and increasing the electroactive area of each channel. Thereafter, a decline in peak current follows with successive voltammetric repeats. This is an observation previously recorded in the literature for repeat EIS measurements,[58] and also suggested to be a function of cyanide attack on gold leading to an etching of the surface from the ferro/ferri cyanide redox couple.[284,285]

Unfortunately, time constraints limited the ability to further characterise, and improve on the cleaning methods these substrates require. However, this multi-electrode array design does hold significant upside in the ability to dramatically increase experimental throughput, and minimise required sample volumes. Colleagues within the research group have continued with these investigations, and recent data (not included here) documents the ability to generate reliably clean surfaces with an O_2 plasma methodology. This is an interesting development as a

proposed thiol attack on a ubiquitous electrode coating may be responsible for the apparent "cleaning" response to MCP incubation (Figure 4.17). Again, the coating has not yet been shared by the manufacturer, however there is evidence in the literature to support O_2 plasma being sufficient to strip photo sensitive polymers such as SU-8 from devices.[286] It is possible that such a coating using for electrode insulating may be prevalent on gold surfaces from the manufacturing process, which the plasma step can successfully remove.

4.4 Conclusions

In this Chapter, experimental evidence has provided for three key findings. Firstly, the introduction of a new cleaning step in the PGE preparation phase (O_2 plasma), and a buffer system change (TM Buffer) allow for effective electrode functionalisation with a conventional linear ssDNA probe. These devices were capable of detecting a lengthy nucleic acid target, despite a substantial overhang following hybridisation to the immobilised probe. These new cleaning and buffering conditions were carried forward to examine three tetrahedral biosensing designs. Firstly, TDN were successfully assembled, and confirmed by PAGE. Thereafter TDN were incorporated into mixed SAMs via thiol modifications, and electrochemically interrogated by both voltammetric and EIS measurements. In response to complementary targets, these sensor designs were shown to be efficient in detecting low nM concentrations, and offer a small but encouraging enhancement in sensitivity compared to conventional linear probe e-DNA biosensors.

Next, TDN were assembled with Ferrocene labels, tagged to the top single stranded pendant extension from the nanostructure. Once immobilised, experiments were launched to assess the feasibility of employing a faradaic label for signal transduction. Evidence was presented to show the successful immobilisation of these nanostructures in a mixed SAM by the recording of peak currents attributable to Ferrocene oxidation. However, consistency and stability of this sensing approach was challenging and prevented further meaningful investigations.

A third and final TDN sensing strategy was then explored. In this novel method, TDN were designed as signal amplifiers in a sandwich assay; where the presence of a target oligonucleotide would serve to tether the nanostructure to a pDNA functionalised electrode.

While sensing performance metrics of limit of detection and effective working range could not be established for this system, a valuable proof of concept has been established for this sensing principle with significant signal change in response to target in a proportion of trials. This was further confirmed by the ability to discriminate between the complementary and non-complementary sequences.

Finally, this chapter documented the initial electrochemical characterisation of a custom device from an industrial partner. In these preliminary studies, issues of reference electrode stability and deterioration were observed, along with an apparent incidence of thiol attack on yet unknown species adsorbed on across all devices. These findings were passed on to colleagues in the research group who are currently investigating further the feasibility of such devices for e-DNA biosensor applications.

Chapter 5

Signal Amplification in Electrochemical DNA Biosensors Using Target-Capturing DNA Origami Tiles

ABSTRACT:

Electrochemical DNA biosensors are feasible tools for disease monitoring, with their ability to translate hybridisation events between a desired nucleic acid target and a functionalized transducer, into recordable electrical signals. Such an approach provides a powerful method of sample analysis, with a strong potential to generate a rapid time to result in response to low analyte concentrations. Here we report a novel strategy for the amplification of electrochemical signals associated with DNA hybridisation, by harnessing the programmability of the DNA origami method to construct a sandwich assay to boost charge transfer resistance (R_{CT}) associated with target detection. This allowed for an improvement in sensor limit of detection by two-orders of magnitude compared to a conventional label-free e-DNA biosensor design and linearity for target concentrations between 10 pM – 1 nM without the requirement for probe labeling, or enzymatic support. Additionally, this sensor design proved capable of achieving a high degree of strand selectivity in a challenging DNA-rich environment. This novel approach serves as a practical method for addressing strict sensitivity requirements necessary for a low cost PoC device.

5.1 Introduction

Central to the efficacy of e-DNA biosensors is the inherent strict base pair binding of DNA, allowing for highly efficient hybridization between complementary sequences. With the immobilization of single-stranded probe oligonucleotides into a self-assembled monolayer, a transducer surface can be functionalized to capture targets with high selectivity. In previous chapters, experimental data has been provided to document the performance of conventional linear and hairpin probes, tetrahedron probes, and a novel method of tetrahedron signal amplification.

Structural DNA based nanotechnology[139,287] and especially the DNA origami technique,[148,189,192] offers almost unrivalled spatial control over target molecules of interest. In DNA origami, a long single-stranded DNA scaffold is self-assembled into a user-defined shape upon mixing and annealing with short synthetic staple strands. The structures can then be further modified with customizable binding sites, coatings or other components as desired.[192] This facilitates easy assembly of even complex nanoscale shapes for all manners of purposes, such as the templating of other materials for e.g. materials science[288] and nanoelectronics,[289] controlled and targeted drug delivery,[156,290] nanorobotics,[291,292] and sensing[293] to name a few. The key capabilities of DNA origami lie in their modular nature and the addressability of each individual nucleobase in their structures, which enable accurate and reliable sub-nanometre positioning of functional elements like target molecules,[294] proteins[295] or optically active particles.[211,296] These qualities make DNA origami a versatile and promising pathway also for enhancing various measurement[297–299] and biosensing tools.[293,300,301]

The current applications of DNA origami in biosensing primarily focus on the optimization of capture element positioning for the electrochemical detection of simple nucleic acids,[119] large synthetic mesoscale targets,[302] or the voltage driven, single molecule capture of proteins in a nanopore.[236] Recently, also electrically actuated DNA origami nanolevers[303,304] and zippers[299] have been coming increasingly into view. Such structures have lately also been investigated in terms of their environment- and structure-dependent behaviour.[305,306] In addition to being able to actuate the DNA origami levers with electrical inputs for various uses,

the levers themselves can also conversely modulate the electrical properties of the surfaces they are bound to, enabling their use as electrochemical sensing elements.

Following this line of thought, this chapter reports on a novel approach for DNA detection limit amplification, with programmable DNA origami tiles. The pegboard-like DNA origami serves as a simple and modular platform for the target dependent tethering of the tile to a functionalized polycrystalline gold electrode (Figure 5.1). In the context of an origami tile, rational design is critical in aiding in the development of a systematic framework for determining the optimal number and positioning of possible tethering sites. This optimisation holds the promise of enhancing the efficiency and precision of DNA origami structures, especially when utilised in a sandwich assay like sensing application. The positioning of tethering sites assumes a critical role in achieving highly effective surface blocking, which may help to limit none specific interactions from fouling agents in a sample, and critically drive electrochemical signal quenching via steric hindrance and charge based repulsion of a redox mediator. Rationality in DNA origami tile design enables a means of tailoring a nanostructure architecture to specific functionalities, optimising the arrangement and number of tethering sites for sandwich assay designs, and unlocking the full potential of DNA origami based electrochemical sensing.

Incorporating these nanostructure assemblies to a conventional faradaic, label-free electrochemical biosensor methodology, it is possible to achieve significant improvements in detection capabilities, and shift the linear working range of a sensor from the low nM to low pM range, with a high strand degree of selectivity. Importantly, the translation of such a sensing design to low cost, disposable thin-film gold electrodes, positions this novel technology with a route to mass manufacturability and broad applicability. Additionally, with an optimisation of tile design established, modification of the capture arm sequences is highly programmable for a host of nucleic acid targets. An outline for this novel approach is provided overleaf in Figure 5.1, detailing the engineered nanostructures, principles of the electrochemical assay, and example EIS responses.

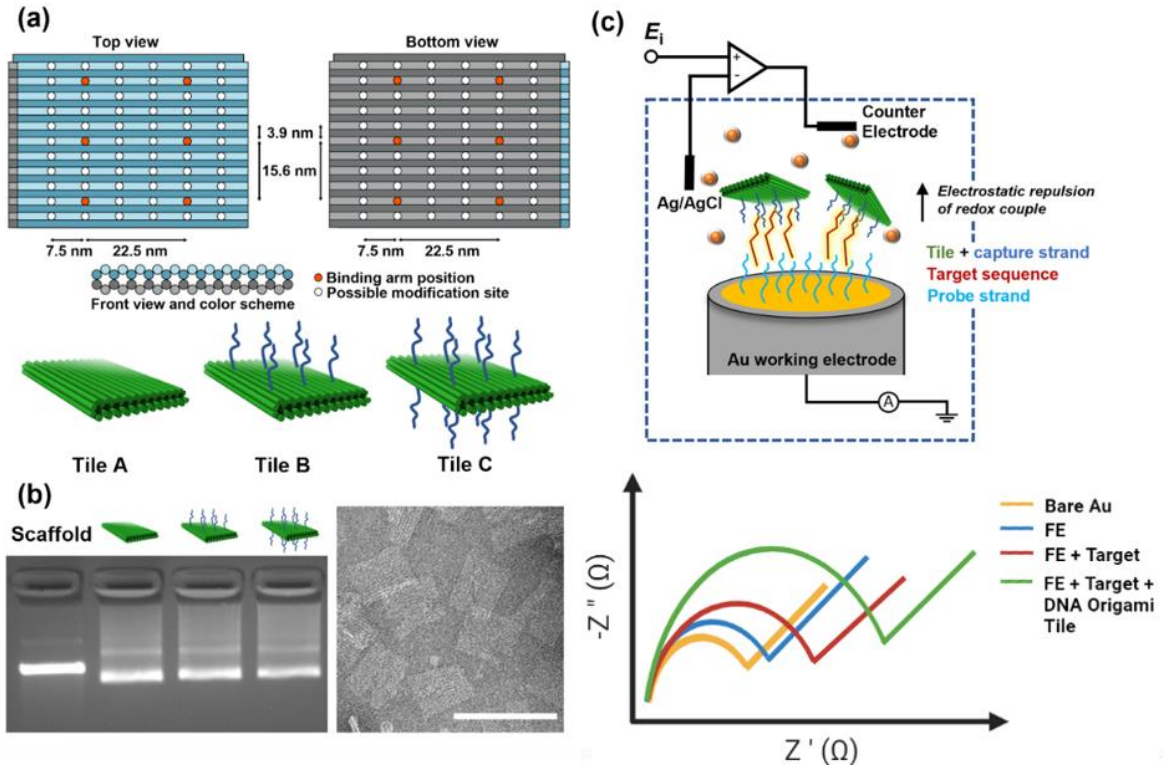

Figure 5.1 Design and characterization of the DNA origami tiles and their use in signal amplification in biosensors. (**a**) Pegboard-like DNA origami tile design showing possible binding arm positions (white circles) and the selected locations for capture strand modifications (red circles). Schematic view of the three different tiles: Tile A, B, and C with 0, 6, and 12 capture strands (deep blue), respectively. (**b**) Left: Agarose gel electrophoresis analysis for the folded DNA origami tiles shown in (**a**). The bands show a minor shift corresponding to the number of added capture strands. Right: Transmission electron microscopy (TEM) image of the DNA origami design. The scale bar is 100 nm. (**c**) The hypothesis of the signal amplification in the biosensor through the implementation of DNA origami tiles. Top panel: DNA origami (green) with capture strands (deep blue) bind to the target strands (red) and the formed complex further attaches to the ssDNA-probe- (light blue) functionalized gold electrode thus modulating the distribution of the redox species. Bottom panel: Schematic electrochemical impedance spectroscopy (EIS) responses. EIS can be used to monitor the drastic increase in the charge transfer resistance (R_{CT}) as the target-capturing DNA origami tile is present.

5.2 Materials and Methods

DNA Origami Tile Design and Assembly

5.2.1 Materials

All staple strands constituting the used DNA origami tiles were purchased from Integrated DNA Technologies and the employed M13mp18 scaffold strand was obtained from Tilibit Nanosystems. 50× stock TAE (Tris/acetic acid/ethylenediaminetetraacetic acid (EDTA)) buffer was purchased from Thermo Fisher Scientific (Finland) and molecular grade agarose from Meridian Bioscience (Ohio, US). All other chemicals required in the DNA origami assembly, purification and characterization were sourced from Merck/Sigma-Aldrich (Finland). Milli-Q deionized water was used in all procedures. DNA origami annealing was carried out in a Biometra T-Gradient thermocycler. Agarose gel electrophoresis was performed using a BioRad Mini-Sub Cell GT System with a BioRad PowerPac Basic power supply and imaged with a Bio-Rad ChemiDoc MP Imaging System. Concentrations were measured with a BioTek Eon Microplate UV/Vis spectrophotometer and a Take3 micro-volume plate. Transmission electron microscopy (TEM) sample grids (FCF400-CU) were sourced from Electron Microscopy Sciences, treated with a NanoClean 1070, Fischione Instruments plasma cleaner and imaged using a FEI Tecnai 12 TEM.

5.2.2 Design, Assembly, and Purification

The DNA origami tile was designed using caDNAno,[307] and it is based on a previously published two-layered honeycomb-lattice DNA origami pegboard.[308] The plate-like design features 66 evenly spaced modification sites with 3.9 nm × 7.5 nm separations on both sides in identical positions (in total 132 binding sites). For this study, 0, 6, or 12 sites were used for creating extended capture strands. In other words, we used three versions of the tile design with either 0 (Tile A), 6 (Tile B, strands on one side), or 12 capture strands (Tile C, 6 strands per each side). The designs are detailed in Figure 1(**a**).

The DNA origami tiles were assembled by first mixing a ~10× molar excess of synthetic staple strands with a circular 7,249-nt long M13mp18 scaffold strand in 2.5× folding buffer (FOB: TAE buffer supplemented with $MgCl_2$ and NaCl). The resulting solution contained 20 nM of scaffold and ~200 nM of each staple strand in 1× FOB (1× TAE (40 mM Tris, 19 mM acetic acid, 1

mM EDTA) with 20 nM $MgCl_2$ and 5 nM NaCl, pH ~8.5). To create the different tile versions, individual core staples at the modification sites were replaced by staples with capture strand extensions added to their 3' ends (5'–ttttttTTGTCTTCGTACCGAGCTTTCATCGAATTTTTA–3', where ''tttttt'' denotes a poly-T_6 spacer sequence). A list of all replaced staples is given in the Supplementary Information, Table S2. The mixtures were then heated to 90 °C and slowly annealed according to the following thermal ramp: Cooling from 90 °C to 70 °C at -1.5 °C/min, from 70 °C to 60 °C at -0.75 °C/min, and from 60 °C to 27 °C at -0.05 °C/min.

After annealing, the now folded DNA origami were purified using polyethylene glycol (PEG) precipitation.[309] Here, the unpurified origami were diluted to ~5 nM concentration with 1× FOB and mixed 1:1 with the PEG precipitation buffer (1× TAE, 15% (w/v) PEG 8000, 505 mM NaCl). The mixture was then centrifuged at 14,000× *g* for 30 min at room temperature. After centrifugation, the supernatant was removed by pipetting and the remaining DNA origami pellet was dissolved in its original volume of 1× FOB. The solution was then incubated overnight at room temperature to resuspend the DNA origami tiles. Finally, the concentrations of the purified DNA origami solutions were determined with an UV/Vis spectrophotometer.

5.2.3 Agarose Gel Electrophoresis (AGE)

Agarose gel electrophoresis was used to verify the integrity of the DNA origami tiles (Figure 1(**b**)). A 2% (w/v) agarose gel was prepared in 1× TAE with a 11 mM $MgCl_2$ concentration and a 0.46 µg/mL ethidium bromide staining. 10 µL aliquots were prepared from each of the investigated DNA origami samples by diluting them to a uniform 15 nM concentration with 1× FOB. Then, 2 µL of 6× gel loading solution was added to each aliquot and the samples were loaded into the gel. Similarly prepared 15 nM M13mp18 scaffold was used as the reference band. The gel was run for 45 min at 90 V in an ice bath with 1× TAE containing 11 mM of $MgCl_2$ as the running buffer. A Bio-Rad ChemiDoc MP Imaging System was used to image the gel under ultraviolet light.

5.2.4 Transmission Electron Microscopy (TEM)

The fabricated DNA origami tiles were also imaged with TEM (Figure 1(**b**)), based on a sample preparation protocol by Castro *et al.*[310] A 3 µL droplet of ~20 nM origami solution was deposited on an O_2 plasma cleaned (20 s flash) formvar carbon-coated copper TEM grid and incubated for 1 min. After incubation, the droplet was drained with a piece of filter paper and

sequentially negatively stained with 2% (w/v) uranyl formate that contained 25 mM of NaOH. The grid was first immersed in a smaller 5 µL uranyl formate droplet, immediately drained with filter paper and then immersed in a larger 20 µL droplet before incubating for 45 s. After incubation, the grid was once more blotted with filter paper and left to completely dry in ambient conditions for at least 30 min before imaging with TEM. For imaging, a 120 kV acceleration voltage was used. See the Supplementary Information Figures S1-S3 for additional TEM images of all used DNA origami tile variants.

Sensor Construction and Electrochemistry

5.2.5 Materials

All electrochemical measurements were undertaken using an Autolab PGSTAT128N potentiostat with the additional FRA32M electrochemical impedance spectroscopy module, by scripts written in the Nova 2.1 software package (Metrohm Autolab). Polycrystalline gold electrodes (PGEs) of a 2 mm diameter were purchased from IJ Cambria Scientific Ltd (Llanelli, UK). An external platinum counter electrode (Metrohm, Runcorn, UK) and Ag/AgCl 3M KCl reference electrode (Cole-Parmer, UK) complete the electrochemical cell. Oligonucleotides for sensor construction were sourced from Sigma Aldrich (Dorset, UK)

Chemical	Abbreviation	Supplier
De-ionised Water (resistivity ≥ 18 MΩcm)	Di	Sigma Aldrich (Dorset, UK)
Ethanol	EtOH	Sigma Aldrich (Dorset, UK)
Hydrogen Peroxide	H_2O_2	Sigma Aldrich (Dorset, UK)
Sulphuric Acid	H_2SO_4	Sigma Aldrich (Dorset, UK)
Potassium Chloride	KCl	Sigma Aldrich (Dorset, UK)
Potassium Ferricyanide	$K_3[Fe(CN)_6]$	Sigma Aldrich (Dorset, UK)
Potassium Ferrocyanide	$K_4[Fe(CN)_6]$	Sigma Aldrich (Dorset, UK)
Tris(hydroxymethyl)aminomethane	Tris Base	Sigma Aldrich (Dorset, UK)
Hydrochloric Acid	HCl	Sigma Aldrich (Dorset, UK)
Magnesium Chloride Hexahydrate	$MgCl_2 \cdot 6H_2O$	Sigma Aldrich (Dorset, UK)
Phosphate Buffered Saline Tablets	PBS	Sigma Aldrich (Dorset, UK)
10× TBE	-	Invitrogen

Table 5.1 Chemicals used in this study.

5.2.6 Buffers

De-ionised water was used as the solvent for making all aqueous solutions in this study. Details are given below in table 4.2.

Buffer	Composition
Piranha Solution	18 M H_2SO_4 + 30 % H_2O_2 at a 3:1 (v/v) ratio
TM Buffer (pH 8)	1× Tris-HCl (1M) + 50 mM $MgCl_2{\cdot}6H_2O$
TM Buffer (pH 8) + TCEP	50 µM TCEP in 10 × Tris-HCl (10 mM) + 50 mM $MgCl_2{\cdot}6H_2O$
Redox Buffer	2 mM Potassium Ferricyanide / Potassium Ferrocyanide in 1× PBS
Rinse Buffer	1× PBS

Table 5.2 Buffers used in this study.

5.2.8 Electrochemical Methods

Cleaning CV 1	Measurement Script 1	Measurement Script 2
For the stripping of contaminants from PGE	*Performance characterisation*	*Determining surface coverage*
Cyclic Voltammetry **Potential Window:** -0.1 V to 1.6 V **Scan Rate:** 0.1 V/s **N^{O} of scans:** 10	**DPV** **Potential Window:** -0.1 V to 0.5 V **Step:** 0.005 V **SWV** **Potential Window:** -0.1 V to 0.5 V **Step:** 0.005 V **Frequency (Hz):** 25 **OCP Determination** **Duration:** 20 seconds **EIS** **Applied Potential:** 0 V vs OCP **Frequency Range (Hz):** 10k – 0.1 **N^{O} of Frequencies / decade:** 10	**Chrono Colometry (**Δt > 1 ms) **Apply Potential:** 0 V ***Record Signal:*** **Duration:** 1 s **Interval Time:** 0.0025 s **Apply Potential:** 0.15 V ***Record Signal:*** **Duration:** 1 s **Interval Time:** 0.0025 s ***Apply Potential:*** *-0.35 V* ***Record Signal:*** **Duration:** 2 s **Interval Time:** 0.0025 s

Table 5.3 Electrochemical Methods

5.2.9 Oligonucleotides

TM Buffer (pH 8) + TCEP was used for the dilution of thiolated oligonucleotides. TM buffer (pH 8) was employed for the dilution of oligonucleotides with no thiol modifications. Specific sequences are provided in Supplementary Information Table S1

5.2.10 Electrode Preparation and Electrochemical Measurement

Appropriate cleaning is required to achieve conformity in PGE surfaces, and the removal of immobilized organics and contaminants. Mechanical polishing was first undertaken to produce a near mirror finish via a series of decreasing alumina slurry diameters from 1 µm to 0.03 µm, on microcloths of varying roughness, with sonication in isopropanol (IPA) for 2 min between each polishing step. Polishing occurred in a figure of eight motion for a duration of two min per electrode. Stripping of organics was attained by immersion of the gold surfaces in hot piranha (H_2SO_4 and H_2O_2 3:1 (v/v)) for 15 min. Finally, electrochemical cleaning was undertaken by repeated cyclic voltammetry in 0.1 M H_2SO_4 at 0.1 V/s, with a potential window of –0.1 to 1.6 V until a stable reduction peak was observed in the voltammogram (10–15 scans). It was necessary to confirm the effectiveness of the cleaning protocol with subsequent electrochemical interrogation of each PGE by Faradaic methods.

Measurement Script 1 was used to determine if key analytical tools of Peak Current (A) from DPV and R_{CT} (Ω) from EIS, lie within a consistent range for PGE immersed in the redox buffer. Details of the measurement script are provided in Table 5.3. PGE that report mean signals for any one of the above that exist out with 1.5 IQR, were discounted and not carried forward for further experimental work. Electrochemical circuit fitting of Nyquist Data from EIS measurements is required to extract analytical parameters of solution resistance (R_s), charge transfer resistance (R_{CT}), and capacitance (C). The simplified Randles circuit was chosen for circuit fitting of electrochemical data. Square Wave Voltammetry (SWV) interrogation of the sensor design was also explored, given its potential for enhancing signal gain reported in literature. However, SWV performance is a direct function of measurement frequency, and pulse amplitude. Both of which require close refinement for specific probe architectures, monolayer packing densities, and the electron transfer rates of the redox reporter.[101] Such a study of electrochemical parameters required to facilitate a sensing enhancement by SWV is yet to be undertaken, and current recorded data shows no meaningful improvement against DPV interrogation. For simplicity, SWV analysis has not been reported here.

5.2.11 Electrode Functionalization

After cleaning, electrodes were immersed in ethanol for 3 min, rinsed in Di-H_2O, and then dried under a steady Argon stream. A mixed SAM of pDNA and MCP was formed by overnight incubation (18 h) at 37 °C, with electrodes immersed in a solution of 1 µM probe : 10 µM MCP, in excess 50 µM TCEP (Tris (2-carboxyethyl)phosphine hydrochloride). The primary solvent throughout was TM buffer at pH 8 (10 mM Tris-HCl + 50 mM $MgCl_2 \cdot 6H_2O$). Following this step, electrodes are named as functionalized Electrodes (FE). With the completion of the functionalization protocol, all electrodes were rinsed in a gentle flow of Di water for 10 seconds to remove non-specifically adsorbed oligonucleotides from the sensor surface. FE were then dried under a steady stream of argon.

It was necessary to assess the performance of the functionalization protocols. FE were subject to electrochemical interrogation in the redox buffer, following Measurement Script 1. Again, any data point existing out with 1.5 IQR was noted as evidence of abnormal functionalization and this electrode was discounted from further study.

5.2.12 Target Detection

The detection method of this approach is centered around the capture of a DNA origami tile/target complex from solution by an immobilized probe on the electrode surface. As such, it was first necessary to incubate a solution of both Tile A, B, or C and target to allow this complex to form. In this study, the tile was held at a fixed concentration (dependent upon particular experimental aim) against a varying target concentration. This complex was allowed to form by a 30 min incubation at 37 °C. After which, FE were incubated directly in this solution for a further 30 min at 37 °C. Following all Target incubations, electrodes were rinsed in 1× PBS (phosphate-buffered saline) for 10 s, and gently dried under a steady stream of argon gas. They were then immersed in a redox buffer for the electrochemical characterization of sensing performance using Measurement Script 1.

5.3 Electrode Functionalization and Detection of Free Target

Prior to assessing the enhancement of sensing performance by a DNA origami Tile, it was then necessary to characterize the functionalization of gold electrode surfaces. In this study, polycrystalline gold electrodes were selected because of the ability to clean in piranha solution (to remove organic contaminants) and to regenerate these surfaces with high repeatability using standard electrode polishing techniques. In order to assess the immobilization behaviour of the DNA probe as part of a mixed SAM, an experiment was carried out where both differential pulse voltammetry (DPV), and electrochemical impedance spectroscopy (EIS) at open circuit potential were performed in potassium ferri/ferrocyanide solutions. Potassium ferri/ferrocyanide ($Fe(CN)_6^{(-3/-4)}$), is a commonly employed redox couple for the measurement of DNA immobilization on electrode surfaces. The ferri and ferrocyanide species possess trivalent and quadrivalent anions, meaning that interaction with immobilized DNA (a polyanion) is governed by electrostatic repulsion at an electrode surface**.** Figure 2 (**a**) details the functionalization process with comparisons drawn between the immobilized ssDNA-probe as part of mixed pDNA/MCP SAM, and a pristine electrode surface. Thereafter, Figures 2 (**b** + **c**) report on the capability of functionalized electrodes to monitor the hybridization of free targets without amplification by an origami tile complex.

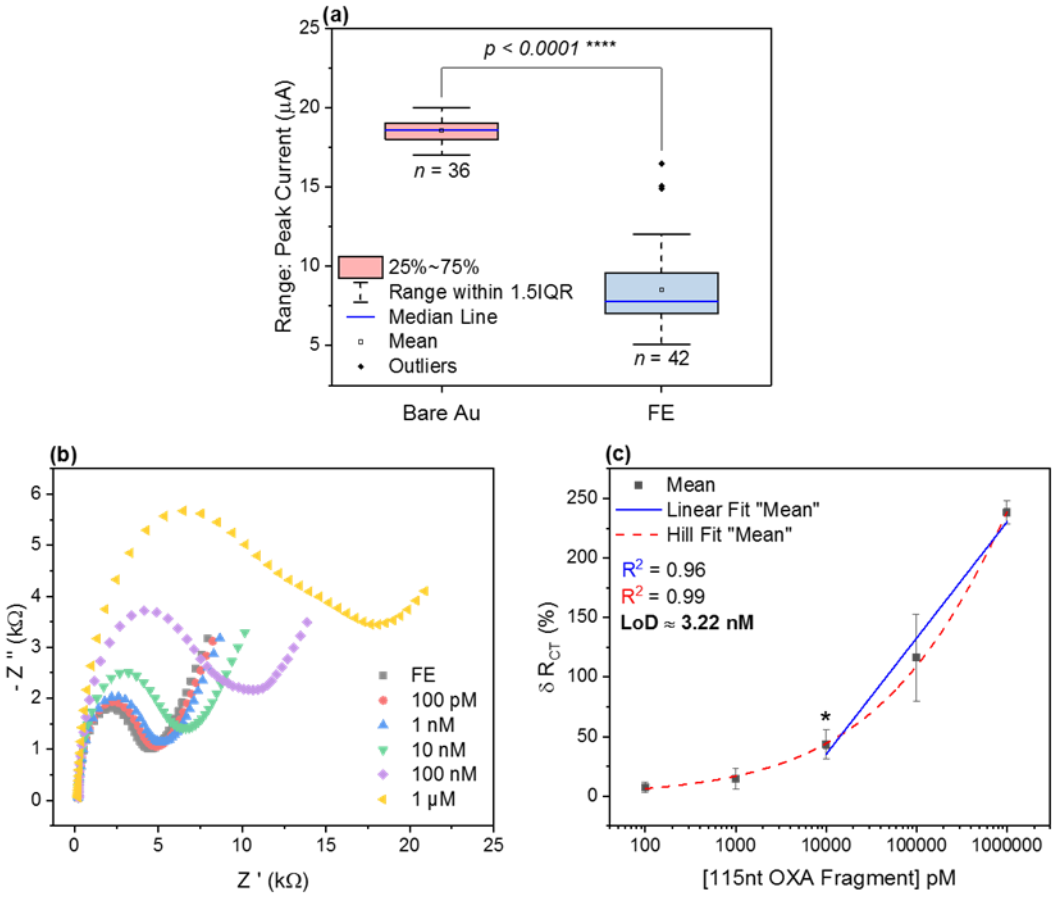

Figure 5.2 Electrochemical characterization of SAM assembly, and sensing performance without DNA origami tile amplification. (**a**) Comparison of mean peak current (µA) for cleaned PGE (bare Au) and functionalized electrodes (FE). (**b**) Mean EIS signal response to varying concentrations of complementary target (115-nt OXA Fragment). (**c**) Mean percentage change in R_{CT} plotted against a varying concentration of the complementary target. *n* = 4 PGE for both (**b**) and (**c**).

Figure 5.2 (**a**) highlights the reproducibility of both the cleaning and functionalization methodologies for PGE. Mean peak currents from a high sample size of PGE exist with a high degree of significance between them, representative of the SAM forming process. Probe surface densities have been estimated for the functionalization protocol by chronocoulometric methods.[70,71] Adoption of these methods produces a surface coverage of 4.62 ± 2.28 ×10^{12} molecules/cm^2. This is in good accordance with the literature where strong hybridization activity is measured electrochemically[71] and by surface plasmon resonance (SPR) for probe coverages in this range.[72]

In Figure 2 (**b**) averaged EIS signal traces in response to varying target concentrations are displayed. Incubation with increasing concentration contributes to a growth in the semi-circle region dominating the medium to high frequency range. Figure 2 (**c**) Provides mean percentage change of R_{CT} derived from the EIS traces, plotted against increasing target concentration. Experimental data is well fitted by a standard Hill equation for specific binding, with a strong coefficient of correlation at 0.99. The Hill equation employed is as follows:

$$Y = V_{max} \frac{x^n}{k^n + x^n} \qquad \text{Equation 5.1}$$

Where V_{max} is maximum binding obtained, x is the concentration of the target, k is the dissociation coefficient and n is the Hill slope describing cooperativity. The first significant mean percentage change in R_{CT} is reported following incubation with 10 nM of target (p = 0.012) which serves as the lower limit of the linear working range of the sensor. Note the upper limit of the working range for this sensor design is not yet clear, as no saturation point has been achieved. This linear range is shown here by the blue trace, with a correlation coefficient of 0.96.

The limit of detection can then be estimated by the following equation:

$$LoD = \frac{3\sigma}{slope} \qquad \text{Equation 5.2}$$

Where σ is the standard deviation of the blank (FE condition) and $slope$ the hill slope from the fitting function.[26] This generates an indicative LoD for this conventional pDNA biosensor design at 3.22 nM.

5.4 Determining an Optimal Origami Tile Design for Signal Amplification

Three origami tile structures were assembled to test the hypothesis of DNA nanostructures inducing the amplification of electrochemical signal change associated with target detection. Direct comparisons were drawn of δ Peak Current (μA) and R_{CT} (Ω) of functionalized electrodes following incubation with DNA origami tile (Tile A, B or C) at a fixed concentration of 1 nM and complementary target (OXA 115-nt Fragment) at 1 nM. EIS is a sensitive and label-free method for probing interfacial parameters, obtaining kinetic information and monitoring mass transport limited processes at modified electrode surfaces. In this technique, a small AC potential signal is applied at the working electrode and the resulting current response is measured. This is performed over a range of frequencies and allows parameters such as the solution resistance (R_S), the double layer capacitance (C_{dl}) and the charge transfer resistance (R_{CT}) to be extracted. It therefore serves as an effective tool for the assessment of this sensing approach.

In Figure 3 the ability of various tile designs to hybridize with the complementary target at a matched concentration is reported. The subsequent capture of the resultant complexes by the immobilized probe sequences on the electrode allows for direct comparison of a pre-target / post-target condition. The sensor design incorporating Tile (A), without capture arms, elicits no significant change in either i_{PC} or R_{CT}. At a target concentration of 1 nM, the underlying probe is not at a sufficient concentration for its hybridisation to the immobilized probe to be detected by current electrochemical methods without subsequent amplification. It cannot be confirmed at this stage if the Tile (A) and target have a method of interaction that is not yet understood. It may be possible to confirm if this is the case with a repeat of this experiment at a significantly higher concentration at 1 μM. Should there be no non-specific interactions of target and Tile (A) the expected electrochemical data would be in accordance with that gathered for 1 μM of Figure 2 (**b**).

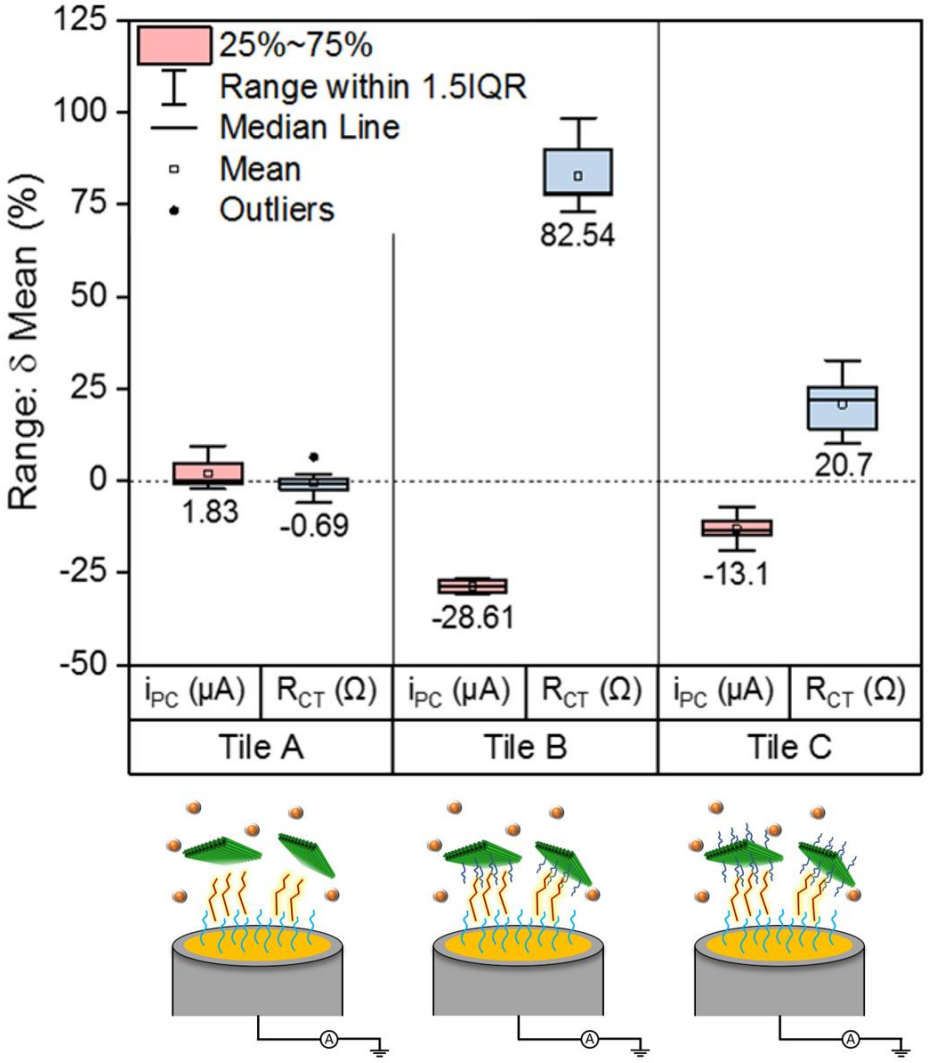

Figure 5.3 Selection of an appropriate tile design. Mean percentage change of peak current (i_{PC}) and R_{CT} is provided following incubation of Tile A, B or C at 1 nM with complementary target at 1 nM. n = 4 PGE with duplicate measurement per condition.

Tile B reports highly significant signal changes for both i_{PC} and R_{CT}. This supports the theory of large origami structures contributing to dramatic manipulation of the interfacial properties for functionalized electrodes via direct tethering through its complementary target present in solution. The impact of amplification by an origami tile is clear when contrasting the

mean signal change of a conventional DNA biosensor design to a complementary target, against that of our novel sensor design.

Tile C matches the level of significance in signal change for that of Tile B, however the magnitude of change is lesser. This suggests that the larger number of target capture arms may boost the number of target sequences occupying both planes of the tile. However, this does not directly aid in the subsequent arrest of this complex by the immobilized probe. As such, Tile B was chosen for further interrogation. Signal change, and level of significance, for each tile design are reported in Table 5.1.

	No Tile	**+ Tile A**	**+ Tile B**	**+ Tile C**
DPV - δ% Peak Current (μA)	-8.8 ± 0.06	-0.69 ± 3.45 *ns*	-28.61 ± 1.61 *p ≤ 0.0001*	-13.09 ± 0.04 *p ≤ 0.0001*
EIS - δ% R_{CT} (Ω)	14.52 ± 0.09	1.83 ± 4.05 *ns*	82.54 ± 9.61 *p ≤ 0.0001*	20.70 ± 0.08 *p = 0.0002*

Table 5.4 Tabulated electrochemical data for various DNA origami tile designs. Mean % change is provided for FE following incubation with a complementary target : tile complex of matched concentrations.

5.5 Electrochemical Performance of a DNA Origami Tile-Enhanced Biosensor

With an appropriate design confirmed, it was next necessary to assess the performance of our approach by investigating its response to complementary targets. The decline in redox events in the cell can be associated with the accumulation of local negative charge densities forming through the successful tethering of the large origami tile to the immobilized probe, by the connecting complementary 115-nt OXA fragment. The net effect of which is the electrostatic repulsion of the redox couple from the functionalized electrode, inhibition of redox mediation, and subsequent growth in R_{CT} (Figure 5 (**a**)).

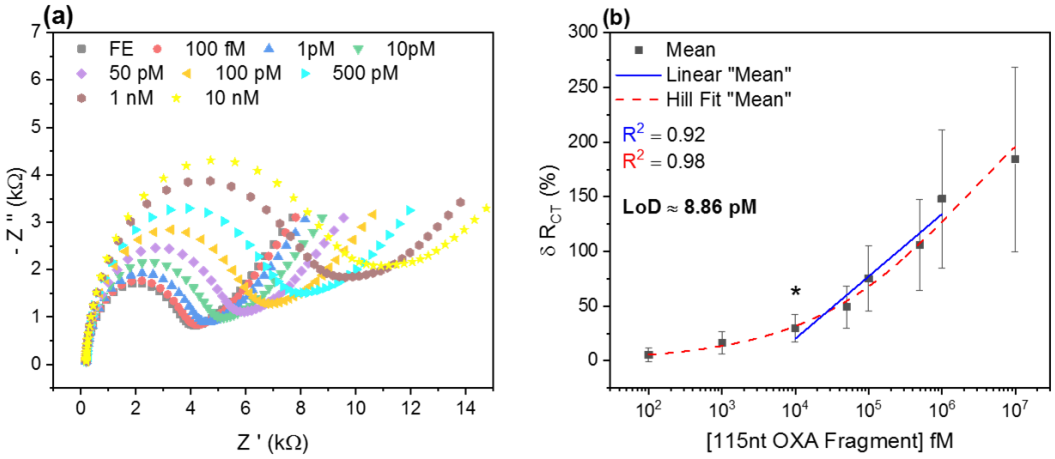

Figure 5.3 Electrochemical sensor performance with DNA origami tile amplification. (**a**) Nyquist plot of averaged EIS measurements in response to varying concentrations of complementary target (115-nt OXA Fragment) and Tile B at a fixed concentration of 50 pM. (**b**) Mean R_{CT} plotted against a varying concentration of the complementary target. (n = 4 PGE).

In this experiment, much of the data falls in a sigmoidal curve, which can again be well fitted by the Hill equation (Equation 5.1). This is evidenced in Figure 4 (**b**) with a strong correlation coefficient of 0.99. While there are many descriptions of how LoD is determined and quantified in the literature, a general description would be the minimum concentration of analyte that will induce an instrumental signal change (in this case R_{CT}) that is significant against the pre-target, or blank condition. By using Equation 5.2 we can derive an estimated Limit of Detection at 8.86 pM. This is supported by t-test analysis of experimental data, with significance in mean signal change first noted following incubation with 10 pM of target. This provides strong evidence to substantiate the theory of a DNA origami tile serving as an electrochemical signal amplifier. This apparatus has a linear working range between 10 pM and 1 nM, spanning two orders of magnitude. While the lower limit of the working range is three orders of magnitude lower than a conventional pDNA biosensor design, the working range is tighter. We theorize this to be a function of the size of the tile. As such, the electrode surface is quickly saturated, as low target concentrations are sufficient to effectively cross-link these structures to the immobilized probe and induce dramatic interfacial properties.

Inter-device variability in the FE condition is high, though this is a common observation in SAM formation.[311,312] The notion of low probe DNA coverage contributing to uniform monolayers is perhaps an oversimplification. This is increasingly apparent with reporting of

heterogeneous SAM formation,[73,74] and clustering of tightly spaced probes at < 10 nm in distance.[76] Despite this, target hybridisation efficiencies are still high, and even suggested unexpectedly to be supported by regions of dense probe clustering.[76] Emerging methods for controlling the distance of neighbouring immobilized probes, and the incidence of clustering on gold electrodes through electrodeposition is prevalent in the literature.[62,77,78,80] However, as no method of controlling the specific confirmation of the probe spacing has been employed here, the particular degree of uniformity in probe spacing cannot be confirmed. This would be expected to produce a degree of variability in the electrochemical characterisation of the functionalized electrode condition. Equally, a contribution to mean peak current / R_{CT} variation in the FE condition may occur from other electrochemical parameters, including real working electrode areas, and cell positioning. This was previously highlighted in Figure 2 (**a**), where the box plot reported a large variation in peak current following functionalization across a large sample size (n = 42). However, collating mean percentage change in R_{CT} produces consistency in trend for each electrode and allows for quantitative estimations of sensor LoD and working range. Therefore, we can conclude a sensitivity enhancement of complementary target detection, supported by our DNA origami tile amplification method (Table 5.2).

Conventional pDNA design	**DNA origami amplification**
Working Range:	Working Range:
10 nM – 1 µM+	**10 pM – 1 nM**
LoD:	LoD:
3.22 nM	**8.86 pM**

Table 5.5 Tabulated electrochemical performance metrics for a conventional pDNA biosensor design and our DNA origami tile amplification strategy.

5.6 Confirming the Mechanism of Electrochemical Response with a Non-Complementary Target

With known issues of sensor drift, directly associated with time dependent alkanethiol SAM reorganization, or degradation of the bioelectric interface through electrochemical interrogation,[61,58–60] it was necessary to consider if such factors may be influencing the electrochemical responses observed in Figure 4. To do so, an experiment was carried out, incorporating a non-complementary target of 115-nt in length, designed to have neither a recognition site for the immobilized probe or solution-based tile. In Figures 5 (**a** + **b**), mean peak current is reported in response to incubation with increasing concentrations of the non-complementary target, and a fixed concentration of Tile B.

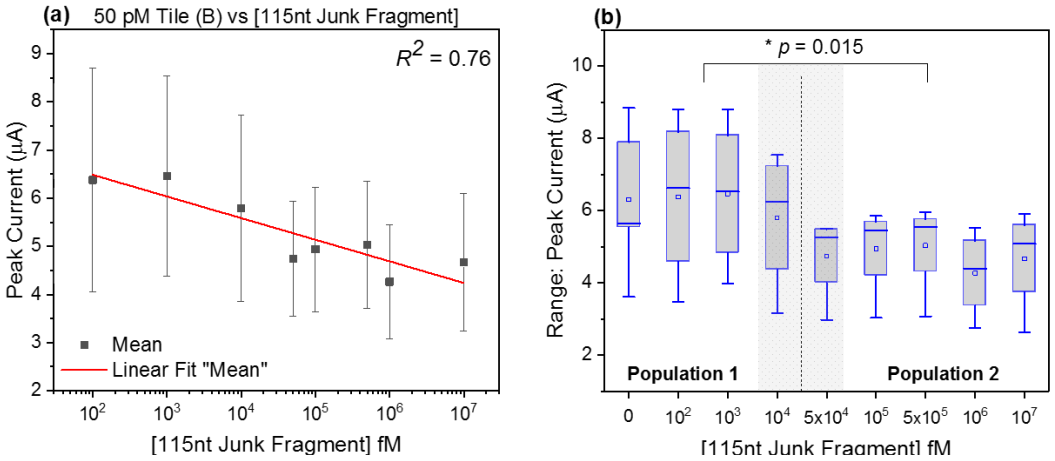

Figure 5.4 Electrochemical response to a non-complementary target. (**a**) Mean peak current response to varying concentrations of non-complementary target (115-nt Junk Fragment) and Tile (B) at a fixed concentration of 50 pM. (**b**) Box plot of DPV mean peak current plotted against a varying concentration of non-complementary target. Dash line denotes the division of the data set into two distinct populations. Gray shaded region corresponds to an estimated threshold of non-specific interactions contributing to electrochemical signal change. *n* = 4 PGE.

The scatter plot in Figure 5 (**a**) allows for the fitting of the experimental data to assess whether a linear region is present that could be attributed to concentration dependent non-specific DNA interactions, or the reorganization effects reported by Piper *et al*.[58] Fitting of the data is poor with a coefficient correlation of 0.78 across the experimental range, and indicative of no sporadic layer organization that contributes solely to significant decline in peak current. This is better reflected in Figure 5 (**b**), where peak current data for each condition is provided as a box plot. This allows for a determination of two significantly distinct populations within the

data, denoted 1 and 2 in Figure 5 (**b**), and separated by the gray dashed line. We suggest two possible phenomena responsible for this deviation in mean peak current. Firstly, the non-complementary target has reached a concentration whereby non-specific interactions with the underlying SAM are sufficient to induce a significant step change in mean peak current. Secondly, Tile B has a weak affinity for the monolayer. Successive incubations of the functionalized transducer in 50 pM of Tile B results in changing interfacial properties of the bioelectric surface, with an inappropriate immobilization of the tile. However, the magnitude of signal change attributable to non-specific interactions is markedly lesser than that associated with DNA origami tile amplification reported in Figure 4 (**b**). To further confirm the benefit of this method of signal amplification by origami nanostructures, the system was interrogated in a complex media containing a high DNA load.

5.7 Specificity of the DNA Biosensor Design

To validate the hypothesized sensor mechanism of action, an experiment was undertaken subjecting functionalized electrodes to Tile B at a concentration of 50 pM, and either of two target sequences. The complementary sequence, 115-nt OXA fragment used throughout this study, and a randomly generated non-complementary sequence of 115-nt in length, with the latter serving as a control. Confirmation of the sensor mechanism is provided in Figure 6 overleaf.

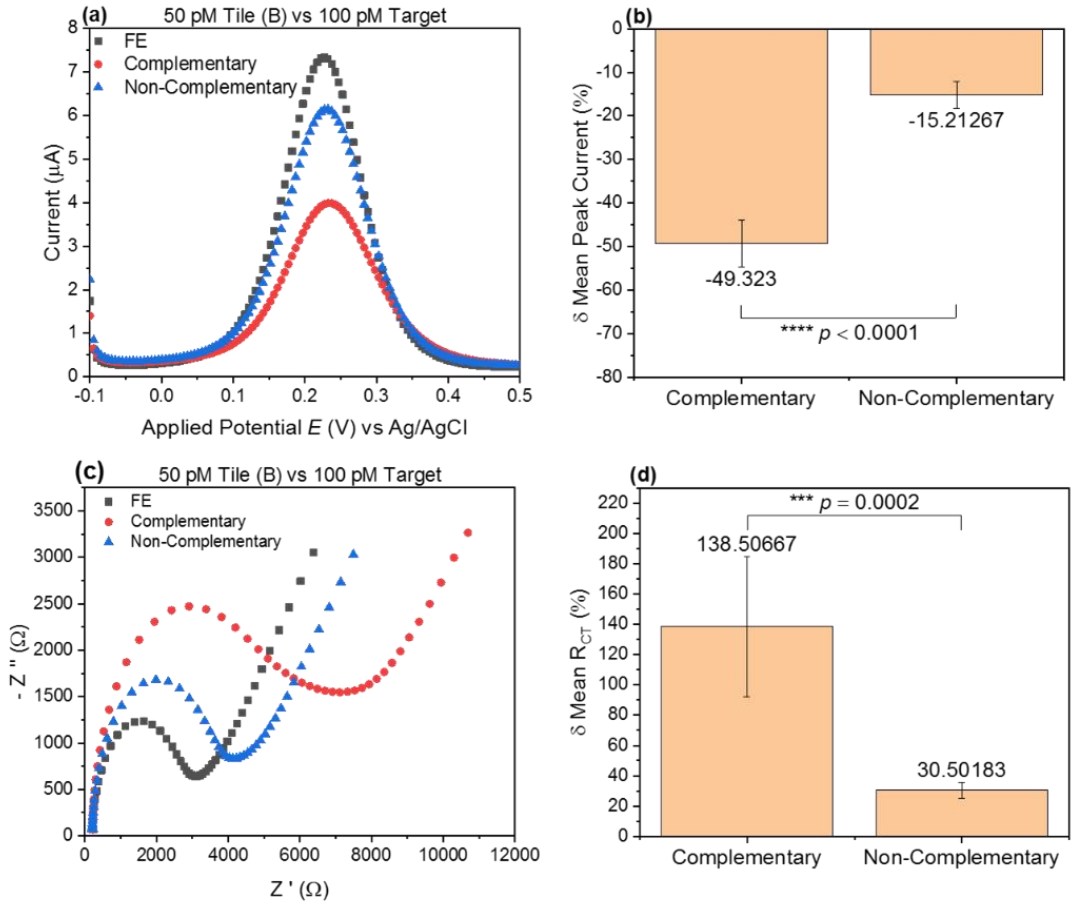

Figure 5.6 Electrochemical response of sensor design to complementary and non-complementary targets in a complex media. (**a**) Mean DPV signal response to 100 pM of complementary target (115-nt OXA Fragment) and 100 pM of non-complementary target against Tile B at a fixed concentration of 50 pM. (**b**) Mean percentage change for peak current following complementary and non-complementary target incubation. (**c**) Mean Nyquist plot response to 100 pM of complementary target (115-nt OXA Fragment) and 100 pM of non-complementary target against Tile B at a fixed concentration of 50 pM. (**d**) Mean percentage change for R_{CT} following complementary and non-complementary target incubation. *n* = 3 PGE with duplicate measurement.

Figure 6 (**a**) displays peak amplitude depression for both the complementary and non-complementary target incubations. However, the magnitude of peak reduction is significantly larger for the complementary target. This is documented in Figure 6 (**b**) with the respective percentage change of mean peak currents contrasted between both targets, with a high degree of significant difference noted (**** $p < 0.0001$). This is furthered by the data of impedimetric measurements presented in the bottom panel of Figure 6. The Nyquist plot of Figure 6 (**c**) shows the characteristic growth of the semicircle region associated with increasing impedance. Again this is common to both complementary and non-complementary targets, however the

magnitude of signal change is significantly greater for the complementary target. The specific mean percentage change of R_{CT} is given in Figure 6 (**d**) with the increase in charge transfer resistance significantly enhanced with a complementary target (*** p = 0.0002).

This is a particularly noteworthy result, given the large background content of DNA in solution, spiked to further challenge the sensor design. Constituent components of the sample solution include either the complementary or non-complementary targets at 100 pM, Tile B at 50 pM, and the necessary concentrations of all reagents required for the assembly of a commercially available DNA origami nanostructure provided by Tilibit Nanosystems. The details of the reaction mix from Tilibit Nanosystems are provided in Supplementary Information Table S3. With a high background DNA concentration, the impact of non-specifics was theorized to be significant. All incubation steps are undertaken at a temperature of 37 °C, and hybridisation of regions of scaffold and staples was expected to produce incomplete secondary structures. Consequently, the incidence of non-specific interactions between any such structure or inherent component, with any of the immobilized probe, target or tile, may contribute to the magnitude of signal change.

The electrochemical data given in Figure 6 would support this theory, with meaningful signal change associated with the non-complementary target experiment. However, the ability to discriminate with a high power of significance between complementary and non-complementary target experimentation corroborates previous data supporting signal amplification by a DNA origami Tile. The contribution of non-specific DNA interactions is commonly observed in biosensor literature, and there are multiple avenues to explore in minimizing their input Enhancing the stringency of washing stages to strip nucleotides adsorbed on exposed gold by ion-induced dipole binding,[55] or through hybridization with partial sequence complementarity. Introduction of microfluidic control may further the consistency of such washing stages, and provide a reduction in the manual processing step count, better tailoring the system to a PoC setting. Finally, the underlying SAM formed on the transducer surface can be re-investigated with considerations raised by Shaver et al; 2020, with modifications to the hydrophobicity of the constituent alkanethiols contributing to enhanced SAM stability,[61] or the charge characteristics of certain end group moieties.[65] Improvements in the underlying bioelectric properties may provide a greater magnitude in signal amplification possible through our novel approach, and advances the applicability of a SAM based biosensor for a PoC device.

5.8 Conclusions

This study successfully introduces a novel DNA origami nanostructure to aid in boosting the electrochemical signal gain associated with target hybridization. In harnessing the high programmability of the origami method, it has been possible to create a sandwich assay, where a desired target oligonucleotide serves to effectively cross-link the nanostructure to a functionalized electrode, and significantly modify surface interfacial properties. As such, simple-label free electrochemical methods allow for enhanced detection limits of two orders of magnitude, without the requirement for complex surface modifications, or enzymatic support. In addition, this sensor design proves effective in discriminating between complementary and non-complementary targets in a complex media, rich in nucleic acids confirming the power of its specificity. With the ever-declining cost of oligonucleotide synthesis, simplicity and elegance of origami design, we report these findings as a promising platform for signal amplification with a host of nucleic acid targets, and of direct relevance to tackling strict sensitivity requirements in PoC devices.

Chapter 6

Probing the Conformational States of a pH-Sensitive DNA Origami Zipper via Label-Free Electrochemical Methods

ABSTRACT:

DNA origami structures represent an exciting class of materials for use in a wide range of biotechnological applications. This study reports the design, production and characterisation of a DNA origami 'zipper' structure, which contains nine pH-responsive DNA locks. Each lock consists of two parts that are attached to the zipper's opposite arms; a DNA hairpin and a single-stranded DNA that are able to form a DNA triplex through Hoogsteen base pairing. The sequences of the locks were selected in a way that the zipper adopted a closed configuration at pH 6.5 and an open state at pH 8.0 (transition pKa 7.6). By adding thiol groups, it was possible to immobilise the zipper structure onto gold surfaces. The immobilisation process was characterised electrochemically to confirm successful adsorption of the zipper. The open and closed states were then probed electrochemically using differential pulse voltammetry and electrochemical impedance spectroscopy with both solution based redox agents and redox

active DNA intercalators. It was found that after immobilisation, the open or closed state of the zipper in different pH regimes could be determined by electrochemical interrogation. These findings pave the way for development of DNA origami-based pH sensing and other pH-responsive sensing and release strategies for zipper-functionalised gold surfaces.

6.1 Introduction

Throughout this thesis a particular focus has been given to the development and testing of e-DNA biosensors where a nucleic acid has been the target. As discussed previously, there is clinical need for the rapid detection of a range of nucleic acids, including DNA, RNA, miRNA etc. However, modern diagnostics may also tackle a host of distinct markers of disease or bacterial growth. One such physical condition that is of relevance may be local pH variation, often a trait associated with the tumor microenvironment,[226] bacterial growth and replication.[227]

Higher order DNA structures, such as DNA origami[148,189] have recently found a plethora of uses in various scientific areas[287,314] ranging from super-resolution imaging[155] to drug delivery.[156] Equally, these structures may provide a means of better managing packing densities, enhancing sensitivity by signal amplification, as well as introducing greater functionality to a sensor. Conformational switching is also possible in response to given environmental stimuli such as temperature gradients, strand displacement reactions, DNA-protein interactions, taking advantage of the photoactivated properties of the system, or more recently the local environmental pH.[225,232,292,315–317] Switchable DNA origami structures have been used for constructing DNA origami sensors with optical readout, such as plasmonics[318] and various fluorescence and surface-enhanced Raman scattering (SERS) -based methods.[319] To the author's knowledge, the application of structures derived from DNA origami for use in electrochemical biosensing has been limited to static DNA constructs.[233,302,320]

This chapter employs an unlabeled switchable/dynamic DNA origami zipper device (Figure 1), which we aim to observe via electrochemical methods of Differential Pulse Voltammetry (DPV) and Electrochemical Impedance Spectroscopy (EIS). This is of immediate interest to future electrochemical biosensing applications for numerous reasons. Firstly, the electrochemical driving of solution pH change by an applied potential through an electrode is well documented.[321] These structures are also readily modifiable to harbor recognition sites for

target oligonucleotides, capable of encapsulating or tethering a range of signaling molecules, or for the loading of a desired cargo molecule for a site-specific release.[232]

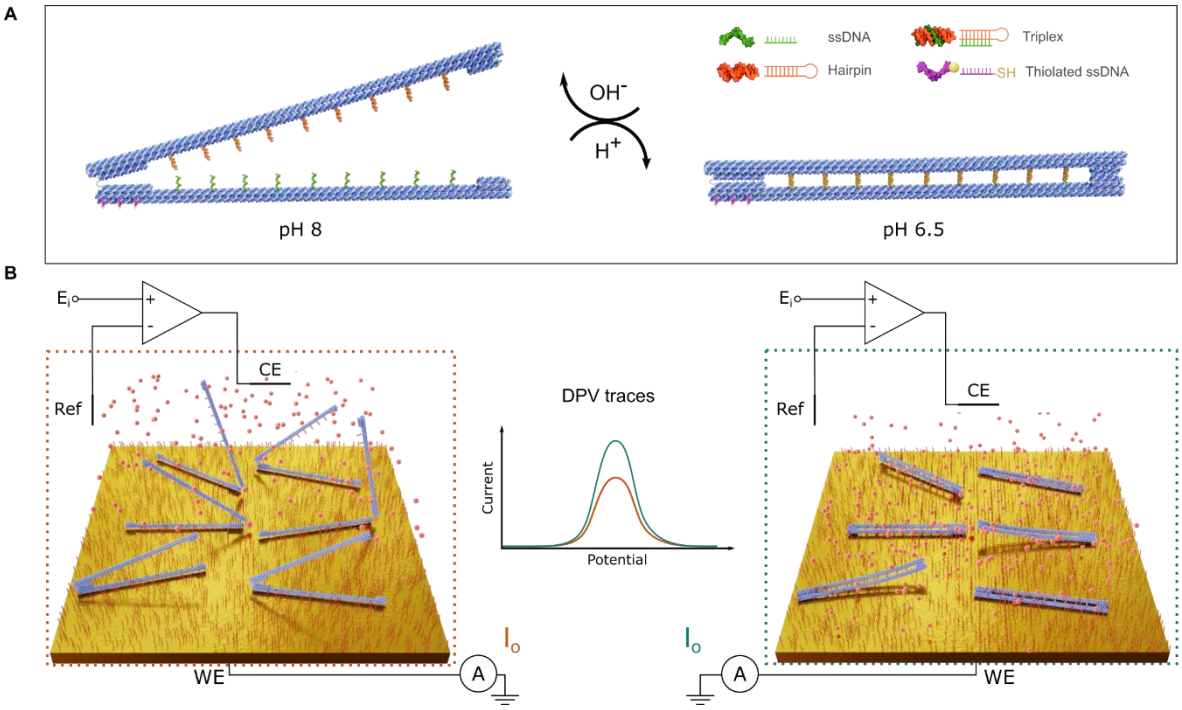

Figure 6.1 Schematics of the DNA origami zipper. (**A**) The conformational states of the zipper at pH 8 (left) and pH 6.5 (right). (**B**) The zippers are immobilized onto the gold electrode surface through thiol-modifications (purple strands in **A**). The opening and closing of the zipper modulate the average distance of the redox mediators (red spheres) from the electrode surface, thus resulting in a detectable current signal change in Differential Pulse Voltammetry (DPV) traces. WE and CE denote the Working Electrode and the Counter Electrode, respectively.

6.2 Materials and Methods

6.2.1. DNA Origami Zipper Design and Assembly

6.2.1.1 Materials

The 7560-nt single-stranded DNA scaffold for zipper assembly was purchased from Tilibit Nanosystems. The staple oligonucleotides, including the thiol-modified oligonucleotides for gold immobilization, were purchased from Integrated DNA Technologies. 50× TAE buffer was purchased from VWR Chemicals, the agarose from Thermo Fisher Scientific, and the gel loading dye and ethidium bromide from Sigma Aldrich. Deionized (DI) water of Milli-Q grade was used in all sample preparation and analysis steps.

6.2.1.2 Design, Assembly, and Purification

The zipper DNA origami structure was designed on a honeycomb lattice with the caDNAno software version 2.2.0.[313] The 3D solution structure and flexibility were predicted with the CanDo online software.[322,323] The sequences of the pH-responsive DNA triplexes (pH locks) were designed according to the reported dependency of the acid dissociation constant (pKa) on the percentage of TAT base triplets in the triplex sequence (%TAT).[230,232,315] The NUPACK online simulation tool[265] was used to ensure a correct secondary structure formation and a sufficient melting temperature of the DNA hairpins in the pH locks.

Folding reactions of the DNA zipper contained the circular 7560-nt scaffold strand at 20 nM concentration and a set of 216 staple oligonucleotides (see Tables S4 – S6 in the Supporting Information) in a 9.2× molar excess to the scaffold in 1× folding buffer (FOB; 1× TAE and 15 mM $MgCl_2$ at pH ~8.3). The structures were folded by heating the mixture to 90 °C and cooling to 27 °C with the following thermal annealing program in a G-Storm G1 thermal cycler: 1) Cooling from 90 °C to 70 °C at a rate of –0.2 °C/8 sec; 2) cooling from 70 °C to 60 °C at a rate of –0.1 °C/8 sec; and 3) cooling from 60 °C to 27 °C at a rate of –0.1 °C/2 min. The reactions were then cooled to 12 °C until the program was manually stopped. After folding, the structures were stored at 4 °C. The excess staple strands in the folding mixture were removed with polyethylene glycol (PEG) precipitation.[309] The folding mixture was diluted with a factor of 1:4 with 1× FOB and mixed at a 1:1 ratio with PEG precipitation buffer (1× TAE, 505 mM NaCl, 15% (w/v) PEG8000). The mixture

was centrifuged for 30 min at 14,000 g at room temperature (RT), the supernatant was discarded, and the pellet was resuspended in the original volume of 1× FOB by incubating at RT overnight.

The concentration of the DNA origami samples was estimated with the Beer-Lambert law and sample absorbance at 260 nm (A260 = ε260 × c × l). The molar extinction coefficient at 260 nm for the zippers was estimated as ε260 = 10.7 × 107 $M^{-1}cm^{-1}$,[324] according to the number of dsDNA (Nds) and ssDNA nucleotides (Nss) in the structures (Nds = 14,820 and Nss = 799 for both the active zippers and the open controls).

For studying the conformational state of the zippers in different pH media with AFM and AGE, the 1× FOB of PEG-purified zippers was exchanged for either 1× TAE buffer (pH 6.5 or pH 8.0) or 100 mM phosphate buffer (pH 6.5), each supplemented with 15 mM $MgCl_2$ and 5 mM NaCl. The buffer exchange was carried out with spin-filtration using Amicon Ultra 0.5 mL spin-filters with a 100 kDa molecular weight cutoff (Merck Millipore). The 1× FOB was first exchanged for DI water with 2 rounds of spin-filtration (6,000 g, 10 min, RT). The samples in DI water were then mixed in a 1:1 ratio with buffers prepared at a 2× concentration to yield the desired final buffer concentration, and incubated overnight at RT before analysis.

6.2.1.3 Atomic Force Microscopy (AFM)

The AFM characterization of zipper origami in 1× TAE buffer and phosphate buffer at pH 6.5 and pH 8.0 was carried out by a Dimension Icon AFM (Bruker). For sample preparation, the zipper samples were first diluted with corresponding buffers to 2–5 folds for obtaining optimal densities on the surface. Then 10 µL of diluted sample was drop-casted on a freshly-cleaved mica surface and incubated for 30 s followed by washing with 100 µL DI water 3 times and drying with N_2 gas flow. The images were captured in ScanAsyst Mode with ScanAsyst-Air probes at 1 Hz scanning speed with 512 × 512 resolution. Image analysis for obtaining statistics of the zipper opening angles was performed using the angle measurement tool in ImageJ2 version 1.51g.[325]

6.2.1.4 Agarose Gel Electrophoresis (AGE)

The electrophoretic mobility of the zippers after folding, PEG purification, and buffer exchange was characterized with AGE. Agarose gels containing 2% (w/v) agarose and 0.47 µg/mL ethidium bromide were prepared in a running buffer with 1× TAE and 11 mM $MgCl_2$ at pH ~8.3.

DNA samples were loaded on the gel in 1× loading dye. The gels were run at a constant voltage of 90 V for 45 minutes on an ice bath and imaged under UV light with either a BioRad ChemiDoc MP or a BioRad GelDoc XR+ imaging system.

6.2.2 Electrochemistry

6.2.2.1 Materials

Polycrystalline Gold Electrodes (PGEs) of a 2 mm diameter were purchased from IJ Cambria Scientific Ltd (Llanelli, UK). 3-Mercapto-1-propanol (MCP), and Methylene Blue hydrate were obtained from Sigma Aldrich (Dorset, UK). All other chemicals required, purchased from Acros Organics (Thermo Fisher Scientific Ltd) (Geel, Belgium).

Chemical	Abbreviation	Supplier
De-ionised Water (resistivity ≥ 18 MΩcm)	Di	Sigma Aldrich (Dorset, UK)
Ethanol	EtOH	Sigma Aldrich (Dorset, UK)
Hydrogen Peroxide	H_2O_2	Sigma Aldrich (Dorset, UK)
Sulphuric Acid	H_2SO_4	Sigma Aldrich (Dorset, UK)
Potassium Chloride	KCl	Sigma Aldrich (Dorset, UK)
Potassium Ferricyanide	$K_3[Fe(CN)_6]$	Sigma Aldrich (Dorset, UK)
Potassium Ferrocyanide	$K_4[Fe(CN)_6]$	Sigma Aldrich (Dorset, UK)
Tris(hydroxymethyl)aminomethane	Tris Base	Sigma Aldrich (Dorset, UK)
Hydrochloric Acid	HCl	Sigma Aldrich (Dorset, UK)
Sodium Hydroxide	NaOH	Sigma Aldrich (Dorset, UK)
Glacial Acetic Acid	AA	Sigma Aldrich (Dorset, UK)
EDTA disodium salt	EDTA	Sigma Aldrich (Dorset, UK)
Magnesium Chloride	$MgCl_2$	Sigma Aldrich (Dorset, UK)
Sodium Chloride	NaCl	Sigma Aldrich (Dorset, UK)
Phosphate Buffered Saline Tablets	PBS	Sigma Aldrich (Dorset, UK)

Table 6.1 Chemicals used in this study.

6.2.2.2 Buffer Preparation

Buffer	Composition
Piranha Solution	18 M H_2SO_4 + 30 % H_2O_2 at a 3:1 (v/v) ratio
Functionalisation Buffer	1× PBS
TM Buffer (pH 8) + TCEP	50 µM TCEP in 10 × Tris-HCl (10 mM) + 50 mM $MgCl_2 \cdot 6H_2O$
Redox Buffer	2 mM Potassium Ferricyanide / Potassium Ferrocyanide in 100 mM KCl
Rinse Buffer	1× PBS
Zipper Buffer 1	100 mM Phosphate/Tris Buffer with 15 mM $MgCl_2$ + 5 mM NaCl
Zipper Buffer 2	1× TAE Buffer with 15 mM $MgCl_2$ + 5 mM NaCl

Table 6.2 Buffers used in this study.

Electrochemical observations of DNA zipper confirmation requires repeat measurements, across a range of buffer pH previously shown to induce either a closed, or open state.[232] Two buffering systems across a pH range of 6.5 to 8, were employed in this work to determine the specific conditions required for successful immobilisation and confirmation measurements; Phosphate/Tris Buffer (Zipper Buffer 1), and 1× TAE Buffer (Zipper Buffer 2). Measurement buffers were produced at 0.2 pH intervals within the range, to electrochemically observe the switching dynamics of the zipper. Each pH buffer condition was spiked with 2 mM $Fe(CN)_6^{(-3/-4)}$ in 100 mM KCl^-, to give a working concentration of either 200 µM or 500 µM $Fe(CN)_6^{(-3/-4)}$.

6.2.2.3 Electrochemical Methods

Cleaning CV 1	**Measurement Script 1**
For the stripping of contaminants from PGE	*Performance characterisation*
<u>Cyclic Voltammetry</u> **Potential Window:** -0.1 V to 1.6 V **Scan Rate:** 0.1 V/s **N^{O} of scans:** 10	**<u>DPV</u>** **Potential Window:** -0.1 V to 0.5 V **Step:** 0.005 V **<u>SWV</u>** **Potential Window:** -0.1 V to 0.5 V **Step:** 0.005 V **Frequency (Hz):** 25 **<u>OCP Determination</u>** **Duration:** 20 seconds **<u>EIS</u>** **Applied Potential:** 0 V vs OCP **Frequency Range (Hz):** 10k – 0.1 **N^{O} of Frequencies / decade:** 10

Table 6.3 Electrochemical Methods

6.2.2.4 Electrode Polishing and Cleaning

Appropriate cleaning is required to achieve conformity in electrode surfaces, and the removal of immobilised organics and contaminants. Stripping of organics was attained by immersion of the gold surfaces in Piranha (H2SO4 and H2O2 3:1 (v/v)) for 20 minutes at RT. Surfaces were then mechanically polished to a near mirror finish via a series of decreasing alumina slurry diameters from 1 µm to 0.03 µm, on micro cloths of varying roughness, with sonication in IPA between each polishing step. Electrochemical cleaning was then undertaken by repeated cyclic voltammetry in 0.1 M H_2SO_4, until a stable reduction peak was observed in the voltammogram.

6.2.2.5 Electrode Functionalisation

After cleaning, electrodes were immersed in Ethanol for 3 minutes, rinsed in DI-H_2O, and then dried under a steady Argon stream. Electrodes were functionalised by overnight incubation (18 hours) at 37 °C, in a solution of DNA Origami at a concentration of 1 nM with backfilling agent MCP (3-mercapto-1-propanol), at a ratio of 10 times origami, all in the presence of an excess of the reducing agent TCEP (Tris(2-carboxyethyl)phosphine hydrochloride) (50 µM). For the immobilisation of a particular structural confirmation, appropriate pH conditions are essential. Therefore, electrode functionalisation is undertaken using a buffer of the necessary pH, as the solvent within which DNA origami and MCP are diluted. This ensures conformity in the layers produced, and provides necessary confidence in the starting confirmation of the structures prior to any measurements.

Following this step, electrodes are named as Functionalised Electrodes (FE). This co-immobilisation protocol of introducing DNA structure, and backfilling agent, to the electrode at the same time, has been previously identified as a simple and reliable method of establishing functionalised electrodes.

6.2.2.6 Sample Characterisation

Following overnight incubation, an initial determination of FE layer characterisation was undertaken. FE were allowed to incubate in the relevant buffer containing a spiked volume of redox mediator for a minimum of 15 minutes prior to initial measurement. This duration was chosen to help prevent signal drift due to fluid mechanical effects on the monolayers, associated with the introduction of new buffers. If electrodes were ever subject to a buffer switch, this 15

minute incubation was deemed necessary to negate the most severe incidence of signal drift. This incubation period is also sufficient to allow migration of Ferri/Ferrocyanide ions into the layer. During buffer switching, electrodes were rinsed in the deionised water for 10 seconds.

6.2.2.6. Electrochemical Measurements

Electrochemical measurements were undertaken in a conventional three-electrode cell (Gold Working PGE, Platinum Counter, and Saturated Ag/$AgCl^-$ Reference). An Autolab PGSTAT302N potentiostat (Metrohm-Autolab, Utrecht, Netherlands), was employed to run all measurements. An electrochemical script was written to characterise surfaces via Differential Pulse Voltammetry (DPV) (Potential Window –0.1 V to 1.6 V, Step 5 mV), Square Wave Voltammetry (SWV) (Potential Window –0.1 V to 1.6 V, Frequency 50 Hz, Step 5 mV) and Electrochemical Impedance Spectroscopy (EIS). The EIS response was measured at a frequency range of 10 kHz to 0.1 Hz, and the associated spectra was fitted to a simplified Randles Circuits (Supporting Information Figure S6); with the x^2 value determining the goodness of fit.

6.3 Results and Discussion

6.3.1 Characterisation of the DNA zipper structure

For pH sensing, the modular DNA zipper (Figure 1) was functionalized with 9 copies of pH locks. The active, pH-sensitive zippers were designed with 9 copies of 18-nt long Hoogsteen-type DNA triplexes with a %TAT = 66.7 for an approximate pKa of 7.6 (Idili et al. 2014, Kuzyk et al. 2017).[230,315] For the open controls, the ssDNA counterparts of the triplexes were substituted with scrambled DNA sequences that cannot take part in triplex formation (the sequences for the active zippers and the control zippers are presented in Supporting Information Figure S4). According to an AGE analysis, both types of zippers were folded successfully and they could be efficiently purified from excess staples with PEG precipitation. They also remain intact in pH 6.5 and pH 8.0 TAE buffers and in the pH 6.5 phosphate buffer (Supporting Information Figure S5).

The pH functionality of the DNA zippers was first confirmed with AFM imaging after incubating the samples overnight either in a pH 6.5 or in a pH 8.0 TAE buffer supplemented with 15 mM $MgCl_2$ and 5 mM NaCl. At pH 6.5, the pH-responsive zippers were predominantly in a

tightly closed conformation (Figure 6.2**A**). Based on an image analysis of the opening angles of the immobilized zippers, ~74% of the pH-responsive zippers at pH 6.5 displayed a vertex angle of 0°–10° corresponding to a closed configuration. At pH 8.0, the active zippers were in an open configuration and a wide distribution of vertex angles was observed (Figure 6.2**B**). The appearance of the active zippers in the open state was similar to the open controls at both pH 6.5 and pH 8.0. The result shows that the buffer pH induces a significant conformational change and a closing of the active zippers specifically due to the triplex formation, while the open controls stay in the open configuration at both pH values. Furthermore, only ~2% of the active zippers at pH 8.0 and open controls at pH 6.5 were fully closed, showing that the closed conformation is highly unfavourable unless stabilized by a triplex formation.

In addition to zippers with a closed configuration, the active zipper sample incubated at pH 6.5 was observed to contain some amount of agglomerated structures (Supporting Information Figure S6). The low pH did not induce agglomeration of the open controls (Supporting Information Figure S7). This shows that the aggregation takes place in solution when the zippers are able to form contacts with each other through formation of DNA triplexes between individual structures. The agglomerates disassemble fast after the solution pH is increased, as indicated by an AGE analysis where no aggregation of the pH 6.5 TAE samples is

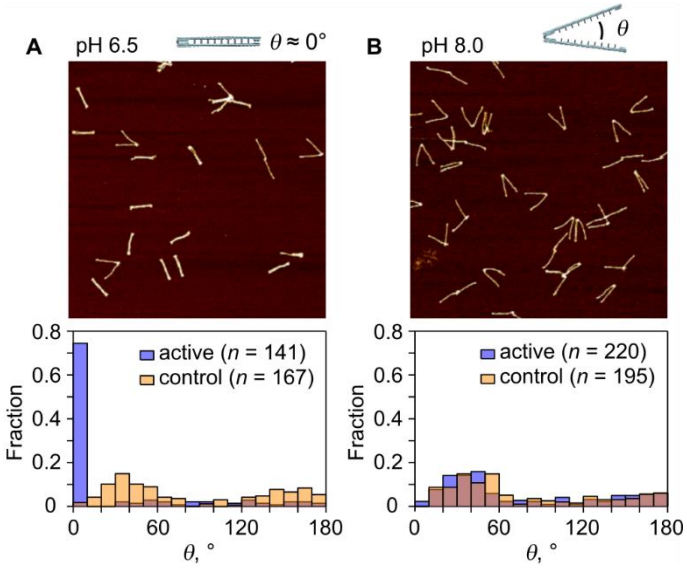

Figure 6.2 AFM analysis of the zipper conformation in TAE buffers. (A) AFM image of the active zippers at pH 6.5 (top panel) and the distribution of vertex angles (θ) measured for both the active zippers and the open controls. n denotes the number of individual structures analyzed for each sample type. (B) Active zippers at pH 8.0 (top) and statistics of the vertex angles of active and control zippers. Size of the AFM images is 2 × 2 μm^2. Larger area AFM images and images of the open control zippers are presented in the Supporting Information Figures S3–S4.

observed on a pH 8.3 gel (Supporting Information Figure S5). The functionality of the active zippers in pH 6.5 phosphate buffer containing 15 mM $MgCl_2$ and 5 mM NaCl was also studied. Closed and structurally intact zippers were seen in the AFM imaging, but both AFM and AGE analysis suggested a larger extent of agglomeration than in pH 6.5 TAE (Supporting Information Figures S5 and S8).

6.3.2 Electrode functionalisation

Having designed and produced the thiolated DNA zipper structure, it was then necessary to characterise its resultant immobilisation characteristics on gold electrode surfaces. In this study, polycrystalline gold electrodes were selected because of the ability to clean in piranha solution (to remove organic contaminants) and to regenerate these surfaces with high repeatability using standard electrode polishing techniques. In order to assess the immobilisation behaviour of the DNA zipper an experiment was carried out where both differential pulse voltammetry (DPV), and electrochemical impedance spectroscopy (EIS) at open circuit potential were performed in potassium ferri/ferrocyanide solutions in order to assess comparative surface functionalisation. Potassium ferri/ferrocyanide ($Fe(CN)_6^{(-3/-4)}$), is a commonly employed redox couple for the measurement of DNA immobilisation on electrode surfaces. The ferri and ferrocyanide species possess trivalent and quadrivalent anions meaning that interaction with immobilised DNA (a polyanion) is governed by electrostatic repulsion at an electrode surface. Comparisons of surface characteristics are drawn between the immobilised zipper, an immobilised DNA hairpin structure, an immobilised single stranded DNA probe and a pristine electrode surface. EIS is a sensitive and label-free method for probing interfacial parameters, obtaining kinetic information and monitoring mass transport limited processes at modified electrode surfaces. In this technique, a small AC potential signal is applied at the working electrode and the resulting current response is measured. This is performed over a range of frequencies and allows parameters such as the solution resistance (R_S), the double layer capacitance (C_{DL}) and the charge transfer resistance (R_{CT}) to be extracted. Figure 6.3, shows the EIS results from electrode functionalisation experiments by contrasting the zipper's behaviour with the immobilisation characteristics of a linear ssDNA probe (20 bp) and a ssDNA hairpin structure (91 bp).

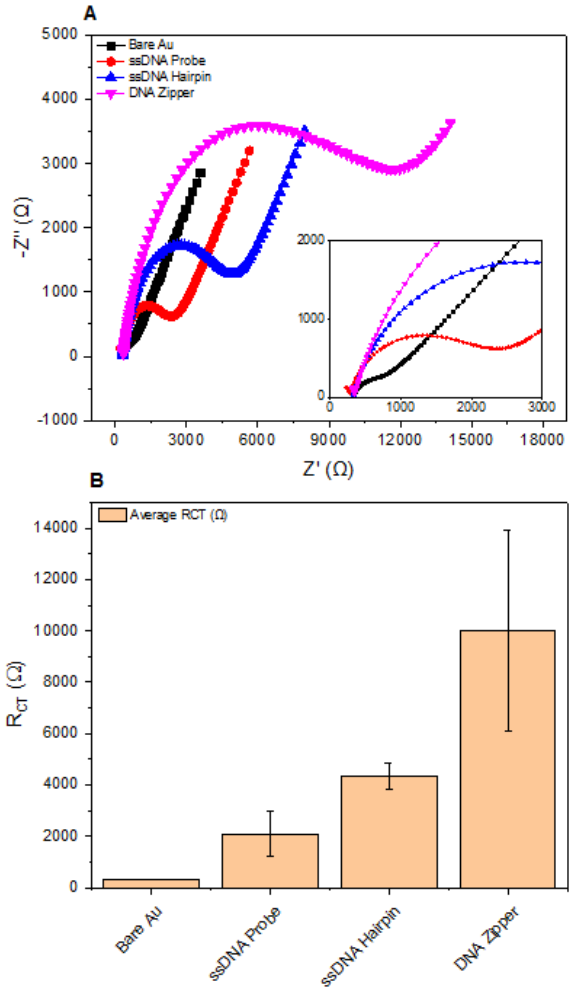

Figure 6.3 Electrochemical assessment of zipper immobilisation on Au PGE (**A**) Averaged Nyquist plots (*inset: Nyquist responses at the high frequency range)*, (**B**) Comparison of averaged R_{CT} (Ω) for bare gold, and various DNA SAMs.

Figure 6.3(**A**) shows typical Nyquist plots and a good representation of the impact of the zippers large size (~4.7 MDa) following surface functionalisation, by comparison with simple DNA films (hairpin and liner probe) associated with common biosensor designs. It can be seen in (**A**) that despite the concentration of zipper being 10 nM in comparison to the 1 µM concentrations of ssDNA Probe, and ssDNA Hairpin immobilisation solutions; the value of charge transfer resistance semi-circle increased by ~130% compared to that of the ssDNA hairpin. Here, measurement of the zipper was undertaken in 2 mM $Fe(CN)_6^{(-3/-4)}$ in 100mM KCl^- buffer, which is in keeping with a common electrochemical buffer principle employed in DNA biosensing work.

Note, the pH of the measurement buffer at this point has not yet been established, and specific structural confirmation is not clear. Compared to the ssDNA probe and ssDNA hairpin structure, variation of zipper states may account for the high variation associated with zipper R_{CT} values displayed in Figure 6.3 (**B**) which is a bar chart with error bars summarising impedimetric responses of the different modified electrodes surfaces. Having successfully confirmed zipper immobilisation by EIS, it was necessary to determine the minimum concentration of redox mediator, $Fe(CN)_6^{(-3/-4)}$, required to allow effective signal transduction through the DNA zipper containing film on the electrode surface. Previous studies have noted potential drawbacks to the use of higher concentrations of Ferri/Ferrocyanide with gold substrates, primarily from cyanide ion damage to the gold surface and resultant signal drift.[90,91] A $Fe(CN)_6^{(-3/-4)}$ buffer at 500 µM was sufficient to resolve consistent DPV traces in the µA range, with oxidation peaks occurring at ~200 mV (see Supporting Information Figure S10).

6.3.3 Investigating pH induced conformational switching of the DNA Zipper

In order to determine the validity of the idea that a change in the electrochemical signal could be associated with the pH driven opening of the zipper, a control structure was introduced into this study. The control structure had no pH locks within the flexible arms of the zipper, and as such, the molecule could not adopt a closed conformation. Alongside comparative measurements between the active, pH responsive zipper, and the control structure, the importance of the buffer system and its background contribution to signal changes was investigated. Comparisons were drawn between the ability of each buffer to resolve structural confirmation. Phosphate/Tris and TAE buffer systems were chosen for their appropriate buffering capabilities across the pH range under investigation.

Figure 6.4 shows the results from a series of experiments designed to understand changes in the electrochemical signal for two pH values, in different buffer systems by contrasting the responses of active and control zippers.

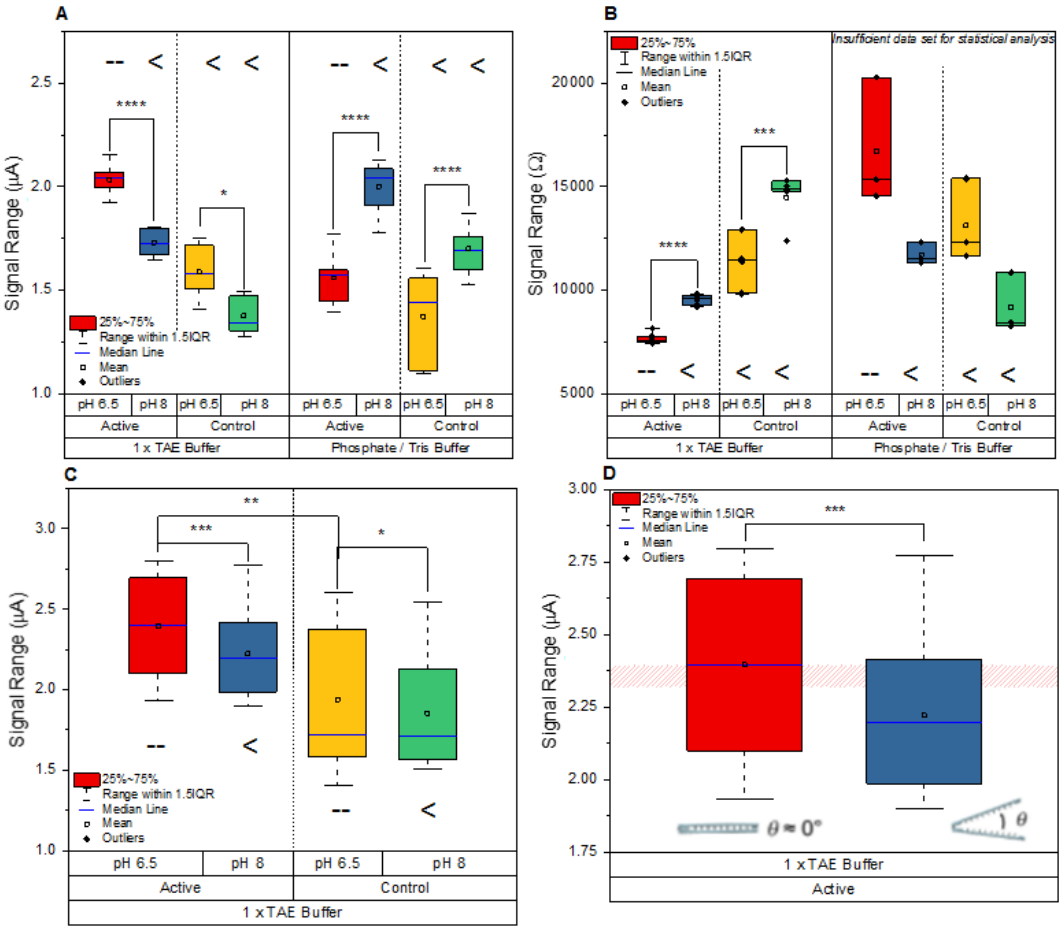

Figure 6.4 Peak current data of active pH responsive zipper and control open zipper following immobilisation on Au PGE in a closed starting confirmation. (**A**) Box plot of peak currents (µA), (**B**) Box plot of charge transfer resistance (R_{CT}) (Ω). (**C**) Peak current data (µA) of 1× TAE buffer measurements, and subtraction of signal change associated with electrochemical behaviour for each pH state. (**D**) Peak current data (µA) of 1× TAE buffer measurements, for active zipper (red bar = pH 6.5, blue bar = pH 8). Pink band represents threshold signal change required to exceed the contribution from a yet unknown parameter, which is present in the control panel of (**C**). (Levels of significance given at, *ns p › 0.05, * p ⩽ 0.05, ** p ⩽ 0.01, *** p ⩽ 0.001., **** p ⩽ 0.0001).* (**A**) and (**C** + **D**) *n* = 4 and *n* = 12 PGE respectively; with triplicate measurement per condition. (**B**) *n* = 4 PGE for 1× TAE system, 3 PGE for Phosphate / Tris Buffer System - single measurements for EIS.

In Figure 6.4(**A**), the switching of pH contributes to a highly significant increase in observed DPV peak current for both active, pH responsive zippers, and control zipper modified electrodes, when supported by a Phosphate/Tris buffer system ($p < 0.0001$ for both). AFM / PAGE data (Supporting Information Figure S5) supports the evidence provided here of the Phosphate/Tris buffer system being sub-optimal, with reduced substrate coverage and yield. We hypothesise that signal change is a combination of two factors. Firstly, poor film formation on

the electrode surface and its subsequent reorganisation; and secondly, the altered electrochemical behaviour exhibited by $Fe(CN)_6^{(-3/-4)}$ when the electrodes were exchanged between phosphate and tris buffer solutions. By employing a 1× TAE system, which appears preferential in the origami synthesis process, it is easier to resolve peak current variation associated with the opening of the zipper structure ($p < 0.0001$, and $p = 0.0236$ for active and control respectively). While this is an improvement, the signal change in our active system cannot yet be conclusively attributed to a switching event alone.

Mean charge transfer resistance as presented in Figure 6.4(**B**), for both the active and control zipper structures in the 1× TAE system, was subject to highly significant increases in signal following a pH change, with $p < 0.0001$, and $p = 0.0003$ respectively between the open and closed states. Sensitivity of this measurement technique may play some role in this, with the incidence and severity of layer reorganisation, or nanoscale pin hole effects, being substantially amplified. Despite this, an order of magnitude exists between the significance of active and control responses, further hinting at a contribution from opening zippers on the electrode surface.

In its closed confirmation, the phosphate rich backbone of the DNA zipper means the structure bears a high negative charge density and strong electrostatic barrier, localised around the closed zipper structures. The relative surface coverage of the zippers is low, and we hypothesise that the backfilling agent MCP, at a concentration 10 times that of the zipper, predominates across large areas of the surface; thus leading to a surface with distinct regions of discrete negative charge. Previous works have noted that mixed films of 1 µM ssDNA and Mercapto-Hexanol (MCH) at a 1:1000 ratio, can harbour 1012–1013 DNA strands per cm^2.[326,327] With a low concentration, the impedance of the layer is predominantly a function of the large size, and significant negative charge density. Ultimately, further work is required to determine the true surface coverage of the zipper, and chronocoulometry approaches like those developed by Steel et al; 1998,[70] may provide a quantitative assessment.

The use of trivalent and quadrivalent anions of the ferri and ferrocyanide species enable probing of the changes to the electrostatic repulsion from the polyanionic DNA zipper structures in their open and closed configurations. Remembering that the zippers appear to be present on the surface as discrete entities, we hypothesise in the closed conformation; this electrostatic repulsion of the redox mediator is limited to only the environment proximal to an immobilised

zipper. Upon opening, the flexible arms of the zipper separate from one another, and position themselves out into solution. The impact of this is a decrease in the density of charge around the zipper structures, but development of a more diffuse negatively charged barrier extending further out across the electrode surface and into solution. This in effect serves to produce a greater barrier to electron transfer between $Fe(CN)_6^{(-3/-4)}$ and the underlying gold substrate, which manifests as an increase in charge transfer resistance (Figure 6.4(**B**)) and decrease in DPV peak current (Figures 6.4(**A**) and 6.4(**C**)).

Supporting Information Figure S10 highlights the impact of buffer pH on basic electrochemical measurements with pristine unmodified gold electrodes. The DPV signal change associated with this pH switch in 1× TAE with 500 µM $Fe(CN)_6^{(-3/-4)}$ and 100 mM KCl^-; from 6.5 to 8, equates to a decrease of approximately 227 nA or 7.03% in peak current. It is therefore necessary to account for this phenomenon through subtraction of the artefact from our experimental data set, which is presented in Figure 6.4(**C**). This yields an overall reduction in the level of significance, for signal decreases associated with both the active and control zipper ($p = 0.0004$ and $p = 0.0487$ respectively). We can therefore hypothesise that there is a yet unexplained phenomenon contributing to redox currents in both active and control experiments. However, it cannot be the sole cause of signal changes associated with the active zipper. Comparison between the data sets of active and control structures at pH 6.5, yields a highly significant difference in mean peak current (µA), indicating that the active zipper is in fact being immobilised in a closed confirmation, prior to opening with the introduction of an alkaline buffer. Finally, a threshold signal change has been determined in Figure 6.4(**D**), with the pink band representing the % change (–3.27%) of mean peak current (µA) observed in the control panel. Here, our measured signal change in the active zipper exists outside this band, with a peak current reduction of 7.05%, or 173.6 nA. We have now accounted for two contributing factors influencing peak current. Firstly the known impact pH has on the electrochemical behaviour of our redox couple $Fe(CN)_6^{(-3/-4)}$, and secondly, the influence of an additional parameter that is well observed, but yet to be conclusively defined.

AFM images presented in Supporting Information Figure S6, highlights the incidence of structure agglomeration unique to zippers in their closed confirmation. It is possible that the protocol for immobilisation of DNA zippers presented in this paper yield islands of agglomerated structures on the electrode. Signal change associated with the switching of buffer pH from acidic to alkaline, may have to a contribution from the opening of the zipper leading to a breakup of

these clusters, and a film reorganisation. Work is currently ongoing to determine the incidence of agglomeration in our system, and the contribution breakup of these masses may provide to the overall signal change.

In totality, the results presented in Figure 6.4 clearly demonstrate that once baseline effects and measurement artefacts were removed, it was possible to probe the conformational states of the zipper structure in different pH regimes using label-free electrochemical methods. The interrogation of the control zipper side by side with the active structure gives great confidence that the conformation can be switched over the two-pH values and this can be resolved through EIS and DPV measurements. These experiments show that the electrochemical signal can be representative of zipper confirmation opening up several sensing applications including pH probing.

6.3.4 Methylene Blue Intercalation

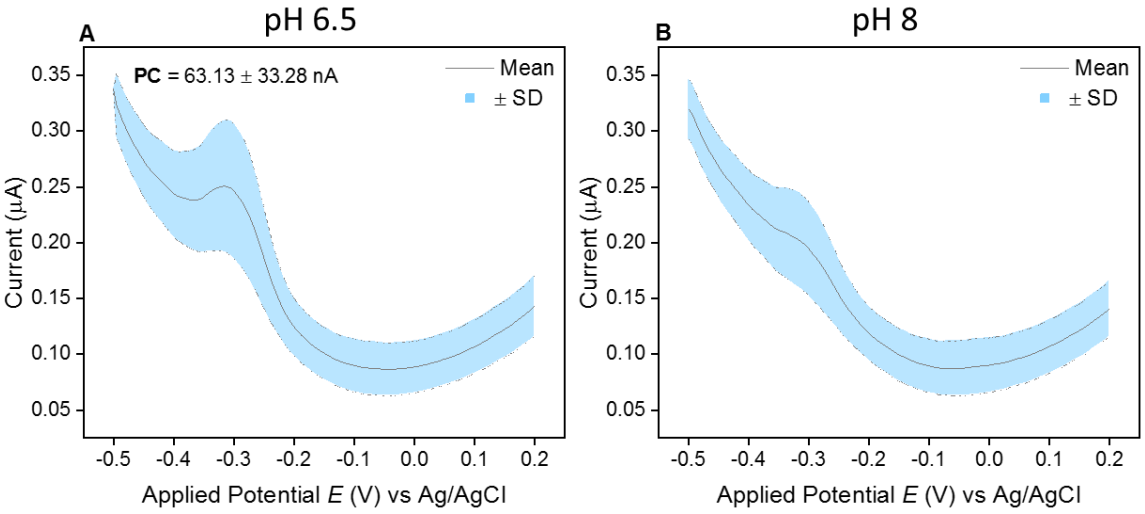

Figure 6.5 Assessment of Methylene Blue intercalation by DPV interrogation. Standard functionalisation protocol modified to allow for the incorporation of a working concentration of Methylene Blue at 20 µM in the functionalisation solution. Measurements undertaken in Zipper Buffer 2, at pH 6.5 or pH 8. *n* = 8 PGE.

Throughout this thesis, evidence in literature has been provided for methods of attenuating electrochemical signals by inducing conformational changes to a probe architecture. This is achieved by a deviation to structural confirmation physically diminishing the access of a

tagged redox reporter to mediate electron transfer with an underlying electrode. Ferrocene tags have been employed in this work to explore the feasibility of the above in a number of DNA sensor designs, to complement data gathered using standard $Fe(CN)_6^{(-3)}$ based redox buffers. This may have been applicable here, with end tethering of Ferrocene at opposing pH latches perhaps helping to electrochemically report the dynamic switching of zipper confirmation. Time constraints and high costs associated with custom Ferrocene tagged oligonucleotides unfortunately hindered the ability of launching such a study. However, there are strong studies in the literature exploring the use of methylene blue (MB) as a redox label for ratiometric biosensing designs.[98,99] Importantly, methylene blue can be incorporated without the requirement for it to be covalently tethered to an oligonucleotide.[328] This aromatic intercalator is well documented to undergo a $2e^-/1H^+$ reduction in aqueous systems to leucomethylene blue (LMB) and serve as a reversible redox couple centred with a reduction potential at ~ -300 mV vs Ag/AgCl.[329] The mechanism of interaction between dsDNA and MB is subject to salt condition based binding models. This is of importance for DNA origami applications as high salt concentrations are typical for driving the origami method. For example at a $MgCl_2$ concentration of 10 mM (15 mM used for Zipper analysis) MB experiences a transition to nonintercalative binding.[330,331] Detailed analysis of DNA origami loading with MB was undertaken by Kollmann and colleagues in 2018, with salt conditions akin to those in this study yielding a minor groove binding of MB. Importantly the specific origami superstructure plays a key role in mediating the binding efficiency of MB, with flexible constructs prone to reduced MB binding efficiencies with transient over/under wound DNA topologies.[332] This is of importance to the zipper structure as the hinge region is highly flexible which may account for electrochemical data reported in Figure 6.5. Here, the functionalisation solution has been modified to allow incorporation of MB at a concentration of 20 µM (all other constituent concentrations unchanged). The voltammograms of (**A**) and (**B**) are gathered following incubations at either extreme of the pH window to allow for a closed or open zipper confirmation. In (**A**) a small and variable peak at ~ -300 mV with a mean peak current of 63.13 ± 33.28 nA can be attributed to the reduction of bound MB within the zipper. Incubation at a pH of 8 is sufficient to quench all recordable peaks attributable to MB reduction as shown in (**B**). There are two possible explanations to what is the primary contributing factor to this data set. Firstly, the failure of the Hoogsteen triplex pH latches with an alkaline pH buffer incubation allows the flexible hinge regions to open the structure. In such a case, flexibility and transient over/under wound topologies may therefore limit the binding

efficiency of MB to the structure and therefore minimise the resultant electrochemical signal. However, the magnitude of such a contribution to signal quenching is not yet clear, as free MB should remain electroactive in solution. Secondly, MB loses affinity for DNA and dissociates with its reduction to leucomethylene blue. It is possible to reoxidise the LMB to MB by the introduction of freely diffusing $Fe(CN)_6^{(-3)}$ to the system, allowing for strengthened intercalation and further voltammetric measurements.[333] As the electrode is charged at negative potentials, the electrostatic repulsion of $Fe(CN)_6^{(-3)}$ prevents its reduction from contributing to electrochemical signal read-out. This may be a useful experiment to undertake in providing some evidence to whether the MB is lost from the structure through conformational change in the zipper, or if signal quenching is purely a function of finite MB reduction.

6.3.5 Live electrochemical monitoring of DNA Zipper confirmation

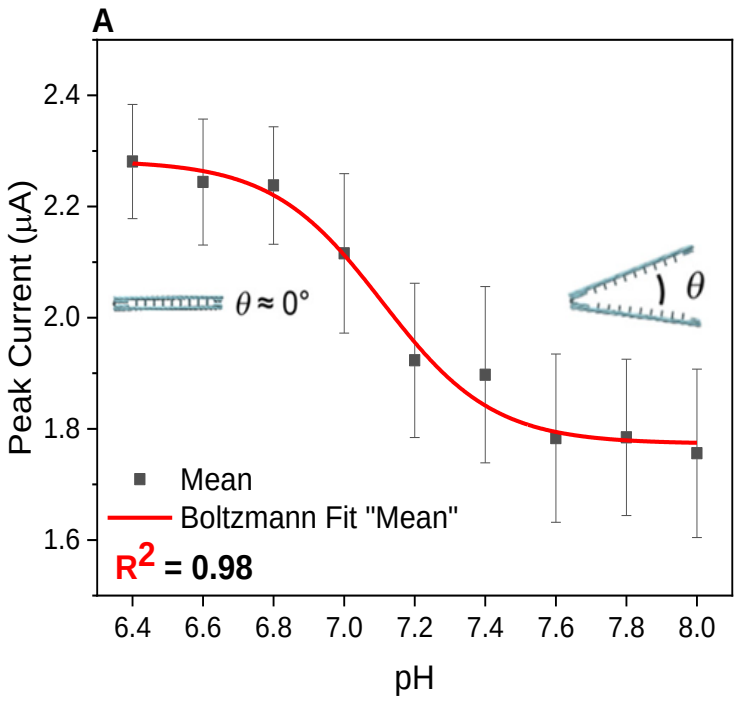

Figure 6.6 Live electrochemical monitoring of DNA Zipper confirmation by repeat DPV measurements at each buffer pH point. Measurements facilitated by spiking $Fe(CN)_6^{(-3/-4)}$ to Zipper Buffer 2 to give a concentration of 500 µM. *n* = 4 PGE.

A central aim of this study was to attempt to monitor the specific confirmation of the immobilised zippers as the buffer pH shift across an acidic to alkaline range. To do so, a series of buffers were prepared at 0.2 intervals of pH from 6.4 – 8, with a duplicate DPV measurement recorded for each FE per pH point. The resultant mean peak current is provided in Figure 6.6 (**A**), with a Boltzmann Function (below) providing an appropriate fit of the data with and $R^2 = 0.98$.

$$y = \frac{A_1 - A_2}{1 + e^{(x-x_0)/dx}} + A_2 \qquad \text{Equation 6.1}$$

This allows for a determination of a series of analytical parameters, including the maximum (A_1) and minimum (A_2) responses (μA), and a 50% threshold value (x_0), analogous to the EC50 of a dose response curve, and in this case representative of the pH point where 50% of the immobilised zippers are in an open confirmation. Again, it is necessary to state the "open" term is indicative of an opening angle > 0^0. x_0 is quantified to be at a pH of 7.1 ± 0.04. This is a promising data set in highlighting the ability to electrochemically monitor the switching dynamics of a reconfigurable nanostructure, and mirrors findings by Ijas and colleagues in 2019. In their work a DNA nanocapsule was labelled to enable Förster resonance energy transfer (FRET) measurements. Their structure design is similar in to the zipper construct with pH sensitive Hoogsteen Triplexes governing the incidence of open or closed confirmations. Each opposing halve of the nanocapsule was labelled with a donor or acceptor FRET pair to establish an observable acceptor emission and a high FRET efficiency when in a closed confirmation. Incremental shifts in solution buffer pH was accompanied by a reduction in FRET efficiency. This could be effectively modelled by a Hill Function, with a p*K*a of 7.27 ± 0.02, at point at which the authors report 50% of the structures to be in an open confirmation. The value reported by Ijas et al, is in higher than that observed here (~ 0.1 pH point greater), and is in good accordance with that predicted by the T-A·T base count comprising the pH latches.[232] However, these FRET measurements were undertaken with solution-based origami. Surface immobilisation of nanostructures can influence the conformational properties of nanostructures, where non-specific interactions can be significant. The inclusion of MCP as co-immobilised species in the functionalisation protocol should minimise the impact of such effects though it is important to consider such contributions. Such surface constraints on origami confirmation have been explored recently in a novel study by Cao et al, where an investigation was launched to attempt

to seed origami assemblies through thiolated probes immobilised on single crystal gold surfaces. While the zipper structures are successfully assembled with a high yield (see Figure 6.2) prior to immobilisation, the works by Cao and colleagues show that weak surface interactions are capable of hindering the folding mechanics of the origami method.[234] It is yet unclear the degree that surface interactions may have on the specific opening and closing mechanisms of the zipper construct. Additionally,

The feasibility of undertaking such a measurement under constant flow was considered, with electrochemical sampling occurring without the requirement of FE to have manual rinsing/buffer exchange stages. Unfortunately, the investment in time and resources required to develop a custom flow cell, and the necessary instrumentation to manage buffer exchange proved too challenging for the limited time remaining for this project. Building further methods of control may help to minimise the potential impacts of manual handling and rinsing that may contribute to variation in recorded signal. A key experiment often undertaken in DNA biosensor design is to establish an optimum surface coverage, or density of probes, for yielding effective target capture and signal generation. One could consider an analogous study necessary here in this work. If an electrochemical response is gathered via the conformational switching of a DNA nanostructure, a detailed investigation may be required for optimising zipper coverage in order to boost signal change. This is also of importance for understanding how immobilisation is influencing pKa, given the observed change in its value when comparing immobilised origami versus solution based nanostructures. Immobilisation is well documented to be responsible for changing pKa in literature, and the changing dielectrics of a bioelectric interface and nanostructure surface coverage may contribute to this significantly.

6.4. Conclusions

This study introduces a pH responsive thiolated DNA zipper capable of adopting closed and open configurations at pH 6.5 and 8.0 respectively. By immobilising the structure onto gold electrode surfaces and removing background artefacts arising from altering the buffer conditions, it was possible to reliably discriminate between the closed and open configurations of the zipper in two different pH regimes (6.5 and 8.0) using simple label-free electrochemical measurements. These findings provide a platform for future developments, which include

addition of secondary functions to these structures, including biorecognition elements for sensing applications, release of relevant cargo molecules upon opening or direct sensing of pH in complex media such as blood.

Chapter 7

Conclusions & Future Work

In 2017, Dr Nadrian Seeman and Dr Hanadi Sleiman published a comprehensive review in to the advent of DNA Nanotechnology, and its emergent applications in a myriad of scientific fields. Within which the authors introduced DNA in its well-understood role as a molecular library of genetic information, before illuminating its appropriateness and power to serve as a unique tool in the development of functional materials. The high level of programmability, and unrivalled specificity and predictability of its interactions, enables the design of higher order DNA constructs that can self-assemble in to intricate, and functional assemblies.[139]

Researchers have harnessed the predictability of Watson-Crick base pairing laws to power the development of electrochemical biosensor design since the 1990s, however this was premised upon the ability of such specificity to provide the mechanism of target detection through hybridisation. It was not until 2010, where works reported by Pei et al; first considered the use of DNA nanostructures to progress the field out from two dimensions, and in to the three-dimensional domain.[131] In the decade since, a brief search of the literature, featuring the key words of “Biosensing” and “DNA Nanotechnology” will provide an ever-increasing number of returns. However, a central question often overlooked is to what level the incorporation of structural nanotechnology provides a meaningful advance in the development of viable low cost, PoC ready devices.

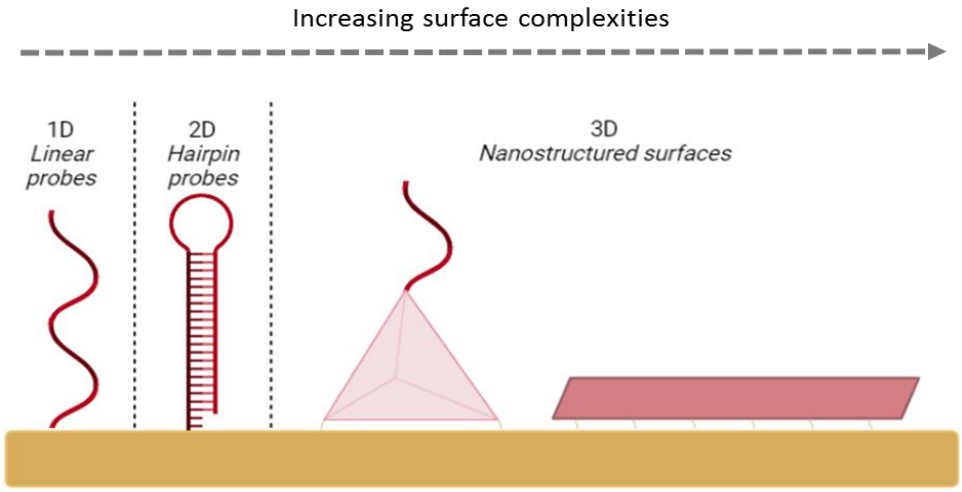

Figure 7.1 A roadmap for the development of DNA nanostructured devices for biosensing applications

The group led by Dr Damion Corrigan in the Department of Biomedical Engineering at the University of Strathclyde has a key research focus on low cost PoC diagnostics. It is within this space, that with the support of Dr Corrigan, and in fruitful collaboration with colleagues from Aalto University, and Ludwig-Maximilians University, the question posed above has been explored within this thesis. In order to do so, one must first begin with a conventional, "simple", approach for sensor design, before advancing on to more intricate assemblies. The figure above outlines the work presented within the experimental chapters of this thesis, as probe architecture is inspired by DNA nanotechnology.

1D linear probes often are allowed to form the recognition elements of e-DNA biosensors as part of a broader self-assembled monolayer.[28,34,35,36,38,40] This "simple" construct offers a number of benefits to a potential device. Namely, such self-assembled monolayers are resource-light, low cost, and can be easily engineered to detect a specific nucleic acid of interest. It is in this space that the first experiments of this thesis are undertaken. In Chapter 3, commercially available polycrystalline gold macro electrodes were successfully shown to be prepared and cleaned via a mechanical polishing stage, with decreasing alumina powder grit sizes (0.3, 0.1 and 0.05 mm), a piranha immersion, and subsequent cyclic voltammetric scans. An estimation of electrode cleanliness is made by an observation of peak current stability from the reduction of gold oxide. This is further supported by the magnitude of key analytical parameters derived from faradaic interrogations of the cleaned electrodes, with R_{CT} and DPV and SWV peak currents assessed for an acceptable nominal value. Thereafter immobilisation

protocols were explored for a linear ssDNA probe as part of mixed monolayer, and preliminary findings for sensitivity using such probe architectures were detailed. It was found that the linear probe as part of a 1:10 mixed SAM (probe:MCP) was capable of detecting complementary targets to a lower limit of 836 pM by faradaic EIS interrogation, with a possible working range extending from 1 nM to yet unrecorded upper boundary. This sets a baseline for sensor performance that one may hypothesise to further by the incorporation of higher order DNA structures within a design. However, this ratio of a 1:10 mixed SAM is based upon a series of studies showing this to be a useful mixing ratio.[34,35,36] There is not a current extensive study truly exploring the potential importance of alkanethiol to probe ratios, and is worthy of further study. Extending probe architectures to a 2D construct was investigated by first designing probe sequences that would adopt a hairpin confirmation. The hairpin probes were immobilised in probe concentrations equal to those of the linear probes, and again estimations of sensing capabilities were drawn by the analysis of complementary target assay data. Here complementary target detection could be estimated to a lower limit of 2.71 nM though no linear working range of the sensing apparatus could be determined. The specificity of each probe design was then interrogated with the hairpin confirmation exhibiting a higher degree of sequence stringency for target mismatch.

Ferrocene labelled linear and hairpin probes were then interrogated to discern if a redox active moiety facilitates a signal-off sensing approach. For the linear probe, establishing a reliable voltammetric peak that could be attributed to Ferrocene oxidation was challenging. Its observation was noted in only one of six functionalised devices. However, the hairpin probe confirmation was capable of producing redox signal in over 80 % of functionalised devices, though inter-device variation is high. This was attributed to the specific confirmation position the Ferrocene tag at an appropriate distance to the underlying electrode and thus facilitating electron transfer events. Following incubation with complementary target, the hairpin probe confirmation recorded a significant reduction in mean DPV current (p = 0.047). Given the challenges in establishing reliable baseline electrochemical behaviour for either probe confirmation, an alternative avenue of amplifying sensor performance was explored.

Translation of both systems to a microelectrode platform was investigated as numerous literature reports note the performance gain associated with decreasing electrode systems. Microelectrodes were sourced from Micrux Technologies, and cleaning steps established to generate cyclic voltammograms displaying characteristic “wave-like” responses bounded by

oxidative and reductive limiting currents. A 70-second immersion time in room temperature piranha was sufficient to reliably produce the required clean conditions. DPV interrogation proved sufficient to enhance sensing performance of a hairpin probe architecture with a highly significant reduction in mean DPV peak current (p = 0.0007) noted following complementary target incubation. This maintained a high degree of target sequence stringency, with no significance noted in mean signal change following incubation with a either a single or triple base pair mismatched target. Within Chapter 3 experimental data is presented to detail that label-free measurements built upon the hairpin probe offer improvements in specificity, though not sensitivity. However, in migrating the sensor design from the macro to microelectrode scale, the benefit is apparent in improved sensitivity in accordance with literature findings.[125,126] There are clear areas for optimising this system. Firstly, a determination of coverages for both the linear and hairpin confirmations may provide a meaningful insight to the approximate number of probes immobilised on the surface. This is vital in better determining the necessary SAM conditions for each of the probe confirmations. While Ferrocene was chosen initially as the redox tag for labelled probes, increasing evidence in the literature supports the use of Methylene Blue as a more appropriate redox mediator.[86,92,328] A comprehensive study contrasting tagged species may offer insights to whether labelled probes have an intrinsic value in sensor design, and guide any future work labelling more complex probe geometries. The electrode platform may also be reconsidered. For example, interdigitated microelectrode arrays provide a means of increasing throughput, and commercially available devices could be immediately interrogated.[127] Equally should one be ambitious it would be appropriate to consider the engineering necessary for device development. While the electrochemical findings reported in Chapter 3 are preliminary and ultimately require a large expansion in the data set, investigating sources of automation to minimise errors in SAM construction would undoubtedly improve the quality of recorded data. Be that through having flow cells to control washing or target incubation steps, which currently involve manual handling stages and exposure of sensor surfaces to environmental particulates.

In Chapter 4, numerous experiments were reported for the application of DNA tetrahedrons in e-DNA biosensing designs. This Chapter was divided into three subchapters, with differing sensing strategies. Firstly, in Chapter 4 an investigation was launched to assess a new PGE cleaning and preparation methodology including an O2 plasma stage. This was shown to produce highly reproducible surfaces and minimise the required number of subsequent CV

scans, improving decreasing preparation time and increasing throughput. Changes were also made to both SAM forming buffer conditions, and the target oligonucleotide. TM Buffer is necessary for the appropriate assembly and stability of tetrahedral nanostructures,[176] and was therefore necessary during immobilisation stages. The target oligonucleotide was exchanged for a lengthy 115nt fragment, based on a sequence within an AMR plasma mimic, encoding the OXA-1 resistance gene. Therefore, a systematic investigation was required for how both buffering conditions and target length may influence e-DNA biosensor design. The linear OXA probe was immobilised in a 1:10 ratio with MCP in TM buffer (pH 8). This was then interrogated by chronocoulometric methods to discern an estimation of probe coverage, which was in good accordance with literature entries for effective probe densities. Target incubation assays with the 115nt OXA Fragment produced effective sensing performance with an estimated LoD of 2.53 nM. This confirmed that the new buffering conditions were appropriate for further sensor designs.

TDNs were then assembled and immobilised through thiol modifications to three of the constituent oligonucleotides, in a mixed MCP SAM. Successful assembly was shown through PAGE analysis. Label-free electrochemical characterisation by voltammetric and EIS methods showed a slight enhancement in LoD at 1.98 nM, while maintaining sequence stringency against an equal length non-complementary target. Thereafter a second TDN sensing design was investigated, this time exploring signal transduction through a Ferrocene tagged ssDNA extension from the top vertice of an immobilised tetrahedron. Recording reliable electrochemical signals that can be attributed to Ferrocene oxidation proved challenging with a tetrahedron architecture. For a number of devices a linear trend of decreasing DPV peak current was noted with successive measurement repeats. This was indicative of a decrease in the number of Ferrocene tags present in the SAM with successive oxidation potentials applied to the system. It was concluded that potential benefits of redox labels incorporated within probe architectures offers a poor trade off when the cost of DNA modifications, and difficulty in established reliable baseline characteristics of sensors are considered.

A third and final TDN sensing design was explored in Chapter 4, investigating the feasibility of using tetrahedra as signal amplifiers in a sandwich assay design. Here, the complementary target serves to tether a solution-based tetrahedron to a functionalised electrode. The TDN was fixed at an assumed concentration of 500 nM. Only a matched concentration of 500 nM target : 500 nM TDN generated a highly significant electrochemical

signal change, with a mean percentage gain in R_{CT} of 246.3 %. Note this mean data was gathered from a single experiment. Subsequent repeats of the assay with a serial dilution of target yielded no significant difference in mean electrochemical signal for any of the chosen target concentration, or electrochemical method. However, there is some preliminary data to support the notion of TDNs being appropriate as signal amplifiers. Ultimately, the data set needs significant expansion to bolster this claim. Equally, there are simple procedural steps that may be included to optimise this sensing design. Firstly, purification is accepted practice in tetrahedral production. This is undertaken with filtered centrifugation and can be followed by a yield quantification by UV-spectrophotometry.[159,176] Within the project period these stages were not incorporated, though are a natural starting point for furthering this preliminary work. Additional gel electrophoresis work may also be undertaken to determine if the target : TDN complex is forming as hypothesised. Should hybridisation events not occur, a secondary band would be present in the lane. Finally, the specific geometry of the nanostructure may be considered. Numerous DNA polyhedra can be self-assembled, introducing variations in molecular weights and dimensions of the amplifier.

To conclude Chapter 4, an investigation was opened to a new multi-electrode device designed in accordance with Flex Medical Ltd (Stirling, Scotland). Cleaning protocols were assessed to prepare the devices for functionalisation, and preliminary electrochemical characterisation appeared promising. However, deterioration of the reference electrode prevented its use for further electrochemical interrogation. Thereafter, combining the counter and reference electrodes to produce a two-electrode cell allowed for the CV cleaning resulting in seemingly pristine surfaces, reflected by stable reduction peaks in the cleaning voltammograms, a low kΩ R_{CT}. Functionalisation protocols resulted in significant, and repeatable, decreases in peak current against the clean condition. This was theorised to be from thiol attack, with the thiolated species displacing unknown surface adsorbed species that the cleaning CV could not effectively strip. Following functionalisation with a conventional linear probe, incubation with target at 1 µM induced highly significant decreases in peak current. However, this was noted for both a complementary and non-complementary target. A more detailed investigation in to these surfaces is necessary, and has recently been carried out by colleagues within the group. Introduction of an O_2 plasma cleaning stage presented again strong electrochemical data to support clean pristine electrodes. Though again, MCP incubation at

concentrations < 1 mM appeared to further clean the surfaces. More work is currently ongoing in the group to better characterise this behaviour.

In Chapter 5, higher order nanostructures formed through the DNA origami method were reported. In close collaboration with colleagues at Aalto University, and Ludwig-Maximilians-University, a series of DNA origami tiles were designed and probed by electrochemical methods. Central to their designs was the incorporation of single stranded extensions with complementarity to the 115nt OXA fragment used throughout this thesis. This works builds on a hypothesis presented in Chapter 4 that nanostructures could serve as a signal amplifier in a sandwich assay. A six-capture arm pegboard-like structure was shown to be highly effective in capturing synthetic target oligonucleotides, with the resultant complex capable of hybridisation with a ss pDNA decorated electrode. A target dose response assay enabled an estimation of sensor design LoD at 8.86 pM with excellent linearity in a working range of 10 pM – 1 nM. This provided strong evidence to support the theory that high molecular weight, 3D DNA nanostructures are effective amplifiers of electrochemical signal change for e-DNA biosensors. Importantly, this structure was able to discriminate complementary and non-target sequences of equal length in challenging environments. This was assessed by introducing a DNA rich incubation buffer, containing a commercially available scaffold and staple mixture for pre-determined DNA origami assemblies. This highlights the power of this sensor design in functioning effectively within a complex media, a vital requirement of e-DNA biosensors. There are multiple avenues for further investigations in this technology. Firstly, the high programmability of the origami technique allows for further refinements to the pegboard tile. This could include the development of a series of structures with varying intervals between the capture arms extensions. The ability to manipulate the specific location of the capture arms may help optimise target hybridisation, and resultant complex capture efficiencies. Additionally the introduction of redox labels within the tiles may provide an additional method of monitoring target : tile complex capture by a functionalised electrode. Finally, an ambitious, though exciting future aim may be to explore the possibility of target dependant seeding of DNA origami at an electrode surface. The first reports of attempting to seed origami assembly at a functionalised surface was explored in literature in 2022,[234] and this may be a natural progression to the work shown here. If the origami design could be engineered to have dependency one or more target oligonucleotides serving as crucial staple sequences, one could envisage a system where a series of genomic fragments drive nanostructure assembly, and capture by a functionalised electrode.

In Chapter 6, a shift in sensing direction to environmental pH was explored. While this is a distinction from conventional e-DNA biosensing, a DNA nanostructure still forms the sensing apparatus. In this work, a DNA zipper was rationally designed to incorporate a series of extensions at either aspect of the flexible structure allowing Hoogsteen triplexes to induce a closed or open structural confirmation in response to environmental pH. The structure was successfully immobilised via its thiol-modified domains through EIS interrogation, with a significant increase in R_{CT} compared to linear and hairpin pDNA architectures. Conformational changes were then electrochemically monitored, and confirmed with the use of a control zipper structure without the necessary sequences to form these pH latches (permanently open confirmation). Thereafter, successful live electrochemical monitoring experiments were reported to produce estimations of a local pH point were 50% of immobilised structures were deemed in an open confirmation ($\theta > 0^0$), with close accordance to similar pH responsive nanostructures measured by FRET analysis in the literature. This was a novel finding for the field, with data presented in this thesis for electrochemical monitoring of a DNA origami structural confirmation being reported for the first time. Future work for this sensing approach should begin with determining estimations of zipper coverage in a mixed SAM by chronocoulometric methods, and establish an optimum number of immobilised pH sensors for maximising electrochemical signal change. Incorporation of colorimetric labelling to provide a secondary mechanism of confirmation status may also further validate the findings in this thesis. Finally, DNA origami allows for the successful immobilisation of molecular cargo within a nanostructure with relative ease.[232] Such a cargo could be electroactive, and drive an electrochemical signal output with its release upon opening, or be a particular therapeutic of interest. For example, the release of antimicrobials in response to local pH deviations with bacterial growth could be an ambitious application for these novel electrochemical pH sensors.

The undertaking of this pH has been a fruitful endeavour, both through experimental data that has been gathered and reported, but also in developing an understanding of key principles governing electrochemistry and DNA nanotechnology. I view this as an important interface in future PoC biosensor designs. This is hopefully apparent to the reader, particularly with key findings noted in Chapters 5 and 6. Both of these fields are powerful in advancing diagnostics, and their combinations is increasingly prevalent in the literature. Ultimately, this is an area of research I aim to continue to explore, and I believe much of the work presented in this thesis provide a solid basis for future investigations.

A natural continuation of this work would begin in further exploring the power of the DNA origami method in enhancing biosensor design. To date, this work has assessed simple constructs, with planar 2D origami tiles. However, this origami method allows for the construction of a vast array of geometries, and functionalities. It may therefore be apparent to the reader, that varying the geometries of an engineered nanostructure may induce a desired response to a biosensing apparatus. This could be a simple modification to the dimensions of the structure, or more advanced constructions of large lattices of linked structures. In the latter example, this system could be engineered to harness one more target oligonucleotides as both the tether of nanostructures to the underlying functionalised electrode, and the key sequence that drives the construction of a large network of joined nanostructures. In theory, such a design could produce a film capable of effectively coating a large electrode area, and dramatically influencing the impedance response of the system. In principle, a large lattice array of nanostructures would only require minimal modifications to the tile design presented in Chapter 5, and laboratory testing of this method could begin within a short time frame.

The central research question of this thesis was to explore how probe architecture, and specifically the introduction of DNA nanostructures may help advance e-DNA biosensor design. A key metric of sensor performance is often considered limit of detection, and working range. For clarity, the following schematic is provided to detail these metrics (where appropriate) in relation to each of probe architectures explored in this thesis.

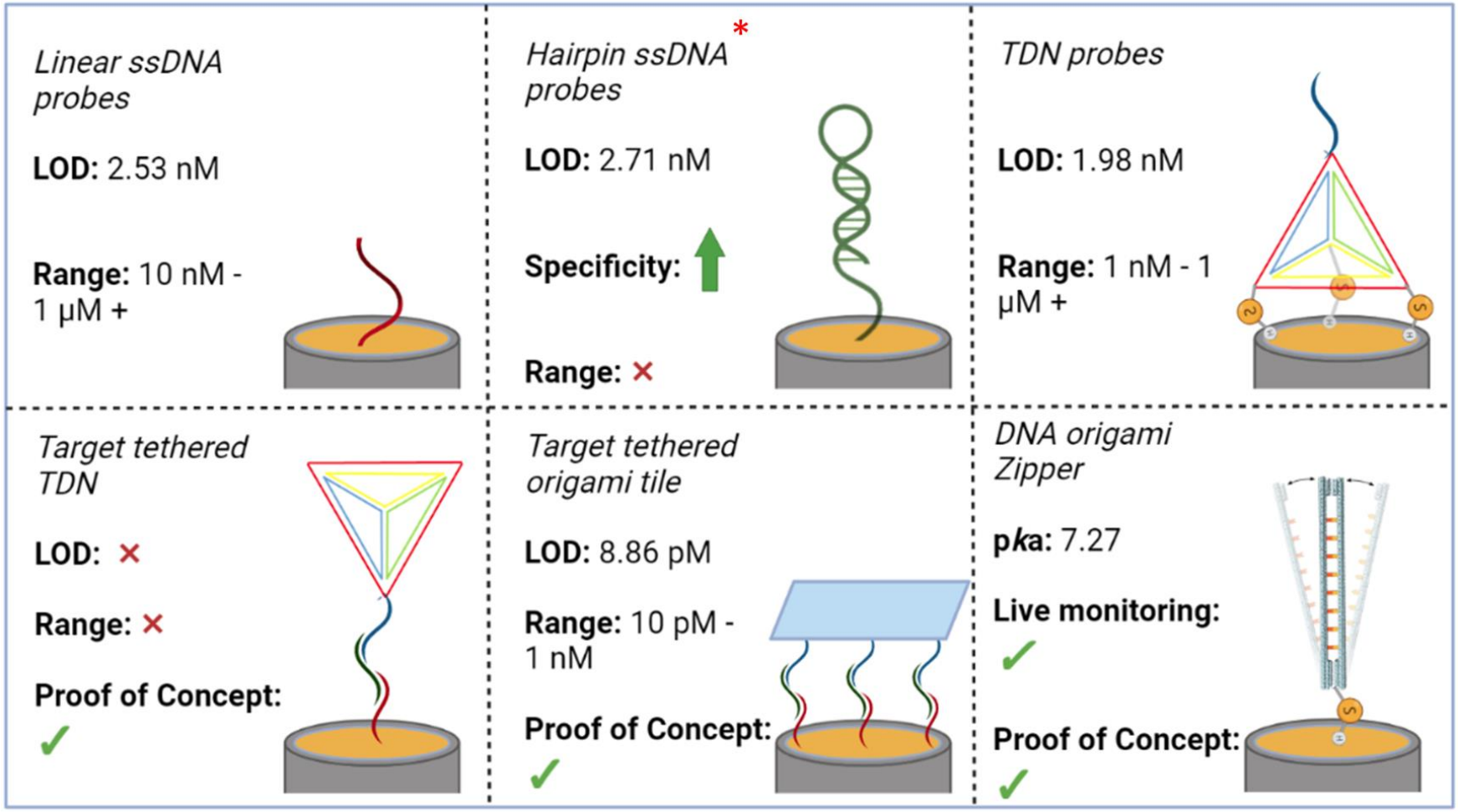

Figure 7.2 Overview of key experimental findings. Beginning from the simple linear ssDNA probes (top left), structural complexity of the probe was advanced to assess if sensor performance could be achieved. Hairpin probes (top centre) offered an improvement in target sequence stringency, with comparable LoD (* 20nt target). Immobilised TDNs (top right) offered a small but meaningful advance in detection limits. Proof of concept for using TDN as signal amplifiers (bottom left) was established. DNA origami tiles (bottom centre) were shown to be effective signal amplifiers with enhanced detection limits and strong specificity. pH responsive DNA Zippers (bottom right) were effectively immobilised and structural confirmation was successfully interrogated by electrochemical techniques.

Supplementary Information

List of supplementary figures and tables

(A) *Oligonucleotides used in this study and reaction mixtures for Tilibit nanostructures*

Table S1. Oligonucleotides used in sensor construction.

Table S2. Capture strands for tile assemblies.

Table S3. Reaction mixture for Tilibit Nanosystems assemblies.

Table S4. Staple strand sequences for folding the core zipper structure without pH lock extensions nor strands for immobilization.

Table S5. Extended staples for the hairpins and ssDNA counterparts of active and control zippers.

Table S6. Thiol-modified strands for arm 2.

(B) *TEM images for Chapter 5*

Figure S1. Tile A, capture strands on both sides

Figure S2. Tile B, capture strands on both sides

Figure S3. Tile C, capture strands on both sides

(C) *SI for Chapter 6*

Figure S4. The zipper structure and the sequences of the pH lock residues.

Figure S5. Agarose gel electrophoresis (AGE) analysis of the zippers after folding, purification, and buffer exchange.

Figure S6. Additional AFM images of the active zippers in TAE buffers.

Figure S7. AFM images of the control zippers in TAE buffers.

Figure S8. AFM images of the active zippers in pH 6.5 phosphate buffer.

Figure S9. Simplified Randles Circuit for the fitting of Electrochemical Impedance Spectroscopy data.

Figure S10. Impact of Redox Mediator $Fe(CN)_6^{(-3/-4)}$ concentration, pH on redox mediator performance.

(A) Oligonucleotides used in this study

Oligo	Sequence 5' – 3'
Single stranded probes	
OXA Probe v1	AACAGAAGCATGGCTCGAAA
OXA Probe – **Fc** v1	AACAGAAGCATGGCTCGAAA- Fc
OXA Probe v2	GGTGTTTTCTATGGCTGAGTTTTTAACTGGGAG
Hairpin v1	TCCAGCGTAACAGAAGCATGGCTCGAAAACGCTGTTACATTCCTAAGTCTGA AACATTACAGCTTGCTACACGAGAAGAGCCGCCATAGTA
Hairpin v2	TCCAGCGTAACAGAAGCATGGCTCGAAAACGCTGTTACATTCCTA
Hairpin – **Fc** v1	TCCAGCGTAACAGAAGCATGGCTCGAAAACGCTGTTACATTCCTAAGTCTGA AACATTACAGCTTGCTACACGAGAAGAGCCGCCATAGTA - Fc
Hairpin – **Fc** v2	TCCAGCGTAACAGAAGCATGGCTCGAAAACGCTGTTACATTCCTA-Fc
Tetrahedron Sequences	
Thiol – S1	**ThiolC6**-A**TTTATCACCCGCCATAGTAG**ACGTATCACCAGGCAGTTGAGACGAACATTC CTAAGTCTGAA
S1	A**TTTATCACCCGCCATAGTAG**ACGTATCACCAGGCAGTTGAGACGAACATTC CTAAGTCTGAA
Thiol – S2	**ThiolC6**-A**CATGCGAGGGTCCAATACCG**A***CGATTACAGCTTGCTACACG***ATTCAGACTT AGGAATGTTCG
S2	A**CATGCGAGGGTCCAATACCG**A***CGATTACAGCTTGCTACACG***ATTCAGACTT AGGAATGTTCG
Thiol – S3	**ThiolC6**-A**CTACTATGGCGGGTGATAAA**A***CGTGTAGCAAGCTGTAATCG***A*CGGGAAG AGCATGCCCATCC*
S3	A**CTACTATGGCGGGTGATAAA**A***CGTGTAGCAAGCTGTAATCG***A*CGGGAAG AGCATGCCCATCC*
S4	ATTTTTAAGCTACTTTCGAGCCATGCTTCTGTTGGTGTGGGGTTTTA**CGGTAT TGGACCCTCGCATG**ACTCAACTGCCTGGTGATACGA*GGATGGGCATGCTCTT CCCG*
S4 - **Fc**	ATTTTTAAGCTACTTTCGAGCCATGCTTCTGTTGGTGTGGGGTTTTA**CGGTAT TGGACCCTCGCATG**ACTCAACTGCCTGGTGATACGA*GGATGGGCATGCTCTT CCCG* - Fc
Targets	
OXA Std	TTTCGAGCCATGCTTCTGTT
OXA – Single Mismatch	TTTCGATCCATGCTTCTGTT
OXA – Triple Mismatch	TTTCGATCTATGCGTCTGTT

OXA 115nt Fragment	AACAGAAGCATGGCTCGAAAGTAGCTTAAAAATTTCACCAGAAGAACAAATT CAATTCCTGCGTAAAATTATTAATCACAATCTCCCAGTTAAAAACTCAGCCAT AGAAAACACC
115nt Junk Fragment	TATTACTTTTGCCTCAACGGCTCCTGCTTTCGCTGAAACCCAAGACAGGCAAC AGTAACCGCCTTTTGAAGGCGAGTCCTTCGTCTGTGACTAACTGTGCCAAATC GTCTTCCAA
Lyt A	TGTATCAAGCGTTTTCGGCA

Table S1 Oligonucleotides used in sensor construction. Sequences for origami constructs give in Table S2 - S6.

B	**AAAAGGGTAGATGGCTCAGGACAAGAGA**tttttt**TTGTCTTCGTACCGAGCTTTCATCGAATTTTTA** **TTAATTGTAACAGTTTTGACCATTTAAT**tttttt**TTGTCTTCGTACCGAGCTTTCATCGAATTTTTA** **TGCAGGTCCAGCTGTACAGGGGGCCAAC**tttttt**TTGTCTTCGTACCGAGCTTTCATCGAATTTTTA** **TTTCCTGTAATGAGCTGCCCGGAAATGG**tttttt**TTGTCTTCGTACCGAGCTTTCATCGAATTTTTA** **TTAAACAGCTTGCACCCTCAGGACGGAA**tttttt**TTGTCTTCGTACCGAGCTTTCATCGAATTTTTA** **GATTAGAGCGGATTCAAGAAAATCATAA**tttttt**TTGTCTTCGTACCGAGCTTTCATCGAATTTTTA**
C	**AAAAGGGTAGATGGCTCAGGACAAGAGA**tttttt**TTGTCTTCGTACCGAGCTTTCATCGAATTTTTA** **TTAATTGTAACAGTTTTGACCATTTAAT**tttttt**TTGTCTTCGTACCGAGCTTTCATCGAATTTTTA** **TGCAGGTCCAGCTGTACAGGGGGCCAAC**tttttt**TTGTCTTCGTACCGAGCTTTCATCGAATTTTTA** **TTTCCTGTAATGAGCTGCCCGGAAATGG**tttttt**TTGTCTTCGTACCGAGCTTTCATCGAATTTTTA** **TTAAACAGCTTGCACCCTCAGGACGGAA**tttttt**TTGTCTTCGTACCGAGCTTTCATCGAATTTTTA** **GATTAGAGCGGATTCAAGAAAATCATAA**tttttt**TTGTCTTCGTACCGAGCTTTCATCGAATTTTTA** **AGTAGCAGATTTAGTGATTCCTAGAATC**tttttt**TTGTCTTCGTACCGAGCTTTCATCGAATTTTTA** **AAAGCGAGCGCCGCGCGAAAGGGCCTCT**tttttt**TTGTCTTCGTACCGAGCTTTCATCGAATTTTTA** **AAAATACATCGTCAGGGAGTTCGGAATA**tttttt**TTGTCTTCGTACCGAGCTTTCATCGAATTTTTA** **TTTCTTTGCGCTCATGAGCTAGTGTTTT**tttttt**TTGTCTTCGTACCGAGCTTTCATCGAATTTTTA** **ATTGCTTCAAACATGCATCAAATTATAG**tttttt**TTGTCTTCGTACCGAGCTTTCATCGAATTTTTA** **GCGCATTCAAGAATTTTGCTAAGTAAAT**tttttt**TTGTCTTCGTACCGAGCTTTCATCGAATTTTTA**

Table S2 Capture strands for tile assemblies. The above extended strands are used to replace corresponding core staples in the DNA origami tile to create Tiles B and C. **Bold** denotes the core staple segment of the replacement strands and blue denotes the used capture sequence. ''tttttt'' is a poly-T_6 spacer. Sequences are given from 5' to 3'.

	Volume Added (µL)
10x Folding buffer	10
100 nM single-stranded scaffold DNA (type p7249)	6
200 mM $MgCl_2$	20
475 nM staple mixture (Cuboid with large aperture)	64

Table S3. Reaction mixture for Tilibit Nanosystems assemblies. Reaction mixtures were purchased from Tilibit Nanosystems in order to challenge the sensing apparatus. Scaffold: https://www.tilibit.com/products/folding-kit-basic-type-p7249-m13mp18, Cuboid with large aperture: https://www.tilibit.com/collections/prefabricated-structures/products/cuboid-with-large-aperture. This mixture was not heated, to allow for minimal secondary structure formation. The above mixture was spiked during incubation stages, to provide a high concentration of background DNA.

Arm 1		
Strand no.	**Sequence**	**Strand type**
[1]	GAGCTTGGTGTAGCAGTCTCTTATTTTG	core
[2]	CGAACGTCGGGCGCAGTAAGCCCTTAAATCAAGATCGGTATTGTCAGAT	core
[3]	TTCTGACATTCTGGAAATTGTTAGCAAACGTAGAGAATAAATTTCAT	core
[4]	TTAATGCGCGAAAGTTGAATGGCTATTAATATGGTTTTTG	core
[5]	CTAAAGGTAACCACTAAAGCCTTTATCC	core
[6]	GGCCCACCCTCAAGTTAACGG	core
[7]	GGCACAGACGACAAAATAAA	core
[8]	CCCAAATAAGTATTGTAACAG	core
[9]	GGTCGAGGTACCTATTGTTAATG	core
[10]	GGGCTGCGCGGAGCCCCTTTGG	core
[11]	GATTGTTCGCCTGATCGTAGGAATCATTTACCAACAAATAAA	core
[12]	ATTCCTGGCGAATTGTACCGCACTCATCTTACAAAAGGTTGA	core
[13]	GCGGAACAAACAAAGGCTGTCTTTCCTTGAAACGAGCCACCA	core
[14]	GAACGTTTCATTTGTCCCATCCTAATTTTTTACAGACCCTCA	core
[15]	ACTTTACATATATGTGTTTATCAACAATGGGAGAAGGAACCA	core
[16]	AGCCGTCTTAATTACGACGACAATAAACTGAGCGCCCCCTTA	core
[17]	TATCTAACTTAGATGAATATAAAGTACCAGCCCAAGTCAGAC	core
[18]	GGTCAGTAAATCATACATGTAATTTAGGATCTTACAGCACCG	core
[19]	CACCTTGGGTTGGGACAGTAGGGCTTAAAACAAAGATTAGCA	core
[20]	TGCCACGATCGCAATATGCGTTATACAAGGAATACTTGGGAA	core
[21]	GAACCCCTAAATTAAGGCGTTAAATAAAAATACCAAAGA	core
[22]	GCTTTTGCAAAAGAAATCCAAAAAAAAAGCGCC	core
[23]	CGCGTACTACAGACGAGCCTAATTTGCCAGGAGAACAAAAAT	core
[24]	CGAGCACGTTGACAGGATAAACAGCCATATAAACCAAATTCA	core
[25]	CCTCGTTAGCACCAGACCCAATCCAAATAAATCATTCAAAAG	core

[26]	AGCTAAACACAGAGCCTTTTTTGTTTAACGAATAATCCATCA	core
[27]	AAGGGATTTCACCCTCTGAAAATAGCAGCCACGAGCATACAT	core
[28]	GTACGCCAGAGCCGCCAGAGAATAACATAAAATAATAAATTA	core
[29]	TGTTTTTATCACCGGAGAAGCGCATTAGACAGATAAGCAGTA	core
[30]	CACCGAGTAAATCACCTTAACTGAACACCCACGCGCCTGAGT	core
[31]	CATCACGCATTGCCATAGTCAGAGGGTAATAACATGTGTAAA	core
[32]	TAGCAATACTCATAGCTAATATCAGAGAGAGTCCAGAATTTT	core
[33]	TAATAACATCGTTTTCCAAGAATTGAGTTAGACAAAAAAACA	core
[34]	TAGAAGAACCTTTAGCTAATAAGAGCAAGAAATAAGATAAGA	core
[35]	CCTTGCTGGTAGCGACAAATAGCAATAGCTCAGAGGCTAGTG	core
[36]	CAATATTACCGATAGCCGAAGCCCTTTTTAAACGCCAAGGTC	core
[37]	CAACAGGAAAAACGTCTAAGCAGATAGCCGTTGAGAATAACC	core
[38]	AAATACCTACATTACCTTACCAGAAGGAAAACGCTCATTATA	core
[39]	CAATCGTCTCAGCAAAAACGCAATAATAACATTCTTACTGAT	core
[40]	TTACATTGGGAGCCATCCAAAAGAACTGGCAGTATCAGACAA	core
[41]	TCACACGACAATTATCAGACTCCTTATTACATTACTATTTTCAA	core
[42]	TTAATGCCACAAACGCTAACGAGCGTCTATTTTCATTGCT	core
[43]	CGTTTTTTTCCAGATTGGCCTTGATATTGCCGCTATAATCCT	core
[44]	GGGTATTTATTTATGCCGCCGCCAGCATATAACGTTCATCAT	core
[45]	ACCAATCTCAAAAAAGAGCCACCACCCTGGAGGCCTCATTTT	core
[46]	CAAGAAAAAACAGGACCGCCTCCCTCAGAATCCTGTTTGCCC	core
[47]	ATGCAGATGAACAACTTTTCATAATCAAAAAGAGTGTATTAG	core
[48]	TAATTCTTAACCCAATCGGCATTTTCGGTTCTTTGAGATTAG	core
[49]	CGCGAGGTTTGAAGGTCATACATAAGTTAGAAGGA	core
[50]	AGCCAGTAACAATGAGAATCAAGTTTGCTCAAACTGGAAGGT	core
[51]	ATTTAACAGAAAAGACCAATGAAACCATCGCCAGCAATATCT	core
[52]	AAAGCCACCGAGGAATCACCAGTAGCACCATTTTGAAAGCAT	core
[53]	CCTGTTTATGATTAACCGTCACCGACTTCAGATTCGCAACAG	core

[54]	AATCATAGCAGTATATTCATTGGGAAGGGGGCGAC	core
[55]	GCTTATCTAGTTGCGAATTTAGCCTTGAAAGAGGC	core
[56]	CAAGCAACTACAATAGAATGGATAAACAATTCTGA	core
[57]	TTCAGAACAGAAAAAGGAGGGCGAGAGGGCGAT	core
[58]	GAATATAATCAAAACTGGCAAACGGGGAACCATCA	core
[59]	TTGAATACCATCAATACAGGG	core
[60]	TTTCAATTAGGAATTAGCTTT	core
[61]	AGAAAACAAAACATTAGATTA	core
[62]	CCTTTTTTATAAATCCAGAAG	core
[63]	GAATAACCTTTTAGAACTGTC	core
[64]	CCCTTAGAAAACTAATATTAG	core
[65]	CGCTGAGAAGAATTGAATCGG	core
[66]	TGAGAGACTCTCAATCCATTG	core
[67]	TAACTATATAAAATCTACGCT	core
[68]	AGAACGCGAACCGCCTACCAG	core
[69]	ATATATTGGTGAGGAAAAGGGACCTGAATACGT	core
[70]	CTTCTGAACCAGCAAGCTGATAGCCCTAAGAAACGATACA	core
[71]	GGCAGGTTGGTTGCGATGATGGCAATTCAAGTTACAGCAAGC	core
[72]	GAACCACAATCAGACCACCAGAAGGAGCCCTGAGCCAAGAAC	core
[73]	GAACCGCTAGACAGTTAAAAGTTTGAGTAATTAATTGTAGAA	core
[74]	GAGCCACAATCAGTTCGACAACTCGTATATGGAAATCCTGAA	core
[75]	TTAGCGTAATTAACAATACATTTGAGGATGCTTCTTCAGCTA	core
[76]	TGTAGCGCACTTGCTTAGGAGCACTAACTCCTTGAGGTAAAG	core
[77]	TAATCAGTAATATCTCAACAGTTGAAAGGAGTCAAATTTTCG	core
[78]	AGGCCGGAAACGCTTCAAATATCAAACCACCTTTTTCGCCAT	core
[79]	TTAGAGCGAAATGGCCAGCAGCAAATGAGTAAATGCCAGTAT	core
[80]	AAAGGTGCAGTAATCGGTCAGTATTAACGAAAACTGAAAAAG	core
[81]	CACCACACGGCCAACGAAGATAAAACAGATTAGTTAACACCGG	core

[82]	CACCCAGATCAGATAGTACCTTTTACATGGAA	core
[83]	TGAATCTACCGCGCAACAATAACGGATTTGGATTAGCCGCGC	core
[84]	GCCAAAAATATTTATAGAACCC	core
[85]	AACATGACAAGTTTCGATTTA	core
[86]	TTTCGGAGCCGTAACGGAACC	core
[87]	GGTCAGTCCGTTCCTAGGGCGTTATTTGCACGTAAGTTTAACCTAAGAA	core
[88]	TGCCCGTAAAGCGCGGTCACGTTAGAACCTACCATCAGTAACATAGAAG	core
[89]	CCCCCTGTCCTCATCACACCCTACTTCTGAATAATCGGGAGACCAATAG	core
[90]	TATTGGGAATAAGTTTATTACCAGC	core
[91]	tttttttttAATACCGAAC	core + poly-T
[92]	tttttttttAGAAAGCGATAAAGAAttttttttt	core + poly-T
[93]	tttttttttGTGATAAATTAATGGTttttttttt	core + poly-T
[94]	tttttttttTGCGTAGATT	core + poly-T
[95]	tttttttttCATATAAAAAACATCGttttttttt	core + poly-T
[96]	tttttttttCGGGAGGTCGTTTTAGttttttttt	core + poly-T
[97]	TAAAGGTGGCttttttttt	core + poly-T
[98]	tttttttttTACTGGTAATGGCTTTttttttttt	core + poly-T
[99]	TCACAATCAAttttttttt	core + poly-T
[100]	AAAAACACTGCCGCCACAGGCGGAttttttttttttttttTGAGACTTACGTGAAAGCCGG	core (staple connection to arm 2)
[101]	CGCGCAGAGATTATCATTTGA	core (modification site A)
[102]	AAGATGATGAAAGAAAGCGGG	core (modification site B)
[103]	TTAACAATTATTAATTGAACG	core (modification site C)
[104]	CATAAATCAAAACAATGAGGC	core (modification site D)
[105]	TCGTCGCTAAATAGATCGTTG	core (modification site E)
[106]	TAGCGATAGAATATCTCTGAG	core (modification site F)
[107]	AATTTATCATGGCAAACAGAA	core (modification site G)
[108]	TCCGGCTTACTGAACCCATGG	core (modification site H)

[109]	GCAAATCCACTGAGAGATTAT	core (modification site I)
Arm 2		
Strand no.	**Sequence**	**Strand type**
[110]	GCCACCAAACCCATGTCCACGTTGTTAA	core
[111]	GAACAGGGTTGATATAAGGGA	core
[112]	GCCACCCTACAACGATTGCCCAAAATAA	core
[113]	GAGGCAAAAGAATTACGTAAT	core
[114]	TTTTGCTAAGGGCGTCCTGTT	core
[115]	TAAGTGCAGAACGTAAATCGG	core
[116]	TAAACGGGAGTGACCGACAGTGCGGCCCTGCCAATTTACGCT	core
[117]	GCCACTAAATCTATGTCCCGCCAAAATATGTCAACCTCATCTAAAGTAC	core
[118]	ATTCATTCCAGGAGGTTCGGAATA	core
[119]	ATTATTACCTCAAATGTCAATCATATGTTTCATCAGTTTTTC	core
[120]	GGAAGAAAATCAAAAGCAAACAAGAGAACTCCGTGAACGCGC	core
[121]	TGCGATTCAAAGCGAGAGATCTACAAAGCACGTTGAGTCGGG	core
[122]	GAGATGGACTTCAATTCTAGCTGATAAAGTTTGAGGCTAACT	core
[123]	TGCCCTGGACCGGAGGCCGGAGACAGTCCTCCAGCCCGGAAG	core
[124]	CCAAATCTTAATTGTGCCTGAGTAATGTGGCAAAGTGTGAAA	core
[125]	CTTCATCTAGAGCTAAGGATAAAAATTTAGGGCGATACCGAG	core
[126]	ACAGATGTTAAATAGACCCTGTAATACTGAAAGGGACGTGGT	core
[127]	GGTCAATATATAACCCTCAGAGCATAAAAGGGTTTCTGACCT	core
[128]	CGCGACCTTTGACCCATACAGGCAAGGCCAAGCTTTGAATCG	core
[129]	AACGGAGTAGCTATCATCAATTCTACTAGGTTGTGCATCTGT	core
[130]	AAAACACTTATGAAATTCATGCGCACGAAGGTGGATTTT	core
[131]	CAGACAGCAGTGAGTCCTGTAGCCAGCTACCCCGGATTCATTGAA	core
[132]	TCGTAAACGAGTAATGCGTATTGGGCGCTCTAAAGGAACAAC	core

[133]	GCCTGAGATTGACCAGCTGCATTAATGATCTGTATGACGTTG	core
[134]	GGTAGCTATCGTAATGCGCTCACTGCCCGAGTGAGTACCTTA	core
[135]	ATGATATATCGGCCCCTGGGGTGCCTAAAATTTTTTGGGCTT	core
[136]	AAAAGGGCGCTTCTCAATTCCACACAACGGAGCCTTAAGGCT	core
[137]	TATTTTACAGGCTGCATGGTCATAGCTGGAATTTCTCATTAC	core
[138]	CTTTATTTTCGCTATAAAGACGGAGGATGACAACAGGCTGAC	core
[139]	ACCAAAAGCGATTATGAGTAAACAGGGCTGAGGCTAAAGAGG	core
[140]	ATTAAGCTTGTAAACATAAATCATTTCTACCCTCACGCAGAC	core
[141]	TTAAATTCATTTTTAGTTGCAGGTTCCGGGACTCC	core
[142]	AACATCCAGGGTGGTGGGCACGAATATAGGCTACACGAAATC	core
[143]	GAAGATTGCCATCATTCACCGCCTTATAGAGTCCA	core
[144]	TCAGAAACTGGCCTACGGGCACCCGAGATGTTGTT	core
[145]	TCCCCAGGTAGAGTTAGCGTAACGACAGG	core
[146]	CATAAAATCTATAGTAAATGAATTTATCG	core
[147]	GAAGTTAAGAACAACAGTTTCAGCGGCTT	core
[148]	AAAGTTTAATTGAATTGCGAATAATTGAG	core
[149]	ACCAACGAGAAAAAAGGCTCCAAAAATAC	core
[150]	ACCTAACGTAACTTGCTTTCGAGGTTTTC	core
[151]	GGCTAAGAGTAGTTGCGCCGACAATCCCC	core
[152]	TGTTAACGGTGATATATTCGGTCGCTTAA	core
[153]	TTCCCATAAGGTTTGCGGGATCGTCCCGA	core
[154]	TTAGTGCTCCAACGAGGGTAGCAACGGGG	core
[155]	ACATTTCATTGTGTGAGGCTT	core
[156]	GTGACATTAAATGTGAGACTAGCATGCTTTAAAC	core
[157]	GTTCAACCCGTCGGATTTCGATGACGAGAATGAC	core
[158]	GGGGAGACAGACGTCGTTAATAAAACGACAGAAAAACGGTAA	core
[159]	GCCGGAACAAACGGCGGAGTCTGGAATCAGGTCT	core
[160]	GCCGTAATGGGATAGGTGCTATCAATTATAGTCA	core

[161]	AAACCTGCAACTTTCTGGCTCATTATACCCTGACTGGTCATT	core
[162]	TCCGTGTAGATGGGCGCATTTTTGGATTGCATCA	core
[163]	CGTCCGTGCATCTGCCATTAATGCAGGAAGCCCG	core
[164]	CACATTAACTAAAGTCAACTTTAATCATGATTAAGCGGAGAG	core
[165]	TGAGGGACGACGACAGTTCAACCGATATCGCGTT	core
[166]	AAGTCAGGAAGATCGCAAAATCACTTCAAAGCGA	core
[167]	CATAAAGTCCAAAAACACCAGAACGAGTTTCGAGCCATCAAT	core
[168]	GAGCAGCTTTCCGGCACTGAGAAAAGCAAACTCC	core
[169]	TCAGGTGCCGGAAACCAGTAGGTAATTAGAGAGT	core
[170]	TTGTTATTTATCAGCAAAGCTGCTCATTGGTCAGGAAGATTC	core
[171]	CTGCGCCATTCGCCATTAATGCAACTCCTTTTGA	core
[172]	AATCGCAACTGTTGGGATTAGAACTTTTGCGGAT	core
[173]	CTCGAATACCGATAATCTTGACAAGAACAGGTCATCCTCATA	core
[174]	GGGTCGGTGCGGGCCTCTCAACGCTAATTGCTGA	core
[175]	CGATTACGCCAGCTGGCTTTGCGGTAGCTCAACA	core
[176]	GCTTGTTATAACCGTACAGACCAGGCGCAATGCTGGAGAAGC	core
[177]	GCTGGATGTGCTGCAAGACATTATTGCAACTAAA	core
[178]	TAAAGTTGGGTAACGCCGCTAAATGGAAGTTTCA	core
[179]	CCTGGTTGGCCGCTGAACCGAACTGACCGGTGTCTCGGTTGT	core
[180]	ACTTCCCAGTCACGACGAATAAAGAGTTGATTCC	core
[181]	TCAACGACGGCCAGTGCAAAGAATACGAGTAGAT	core
[182]	GCTGACGCATCGGATGTTACTTAGCCGGTCTGCGATAGCAAA	core
[183]	CCTTCTCAGGAGAAGCCAATAAATATTAGAT	core
[184]	AAGCAACTAAAGACTCATCGCCTGATAAGCAAATGTAGCATT	core
[185]	ATCAGCTGTAAACGCGACGATATAGCGAG	core
[186]	TCTAAGTATAGTAGGTCAATAACCTGTTATTTGTATTTACACT	core
[187]	TAGGAACGTATAAGTTTAGACTGGATAGTCAACTATACAAACTCA	core
[188]	TTCGCGTAGCCCCATACTGCGGAATCGTTGAG	core

[189]	AACGTCACAGTACCCCTCAGA	core
[190]	CGCCCTGGTAAAATTCATGAGGAAGTTTTGAGGACTCGTCGGATGTTCT	core
[191]	CGCTTCTCGAAGGCAACGAAA	core
[192]	CTATTAACGTCGAGCGCCACCCTCAGAAAGTTTCGCTGAGAGTAACCAA	core
[193]	ACAAAATCAAAAGAATAGACAGCTGCCTGTAGTAGGAAT	core
[194]	CCAGTTTTATAGCCTAGTACC	core
[195]	TGATGGTGCAAGCGGTACCGTAGGAATTACGAGGCTACCAGATTAAT	core
[196]	CAAAATCCCTGGCCTCACCAGATGCAGA	core
[197]	TTTTCACCCCTCATAAAGATT	core
[198]	tttttttCGCGAAACTTGACCCCttttttt	core + poly-T
[199]	tttttttCCAATAGGCCCTCATTttttttt	core + poly-T
[200]	ATTTTGTTAAttttttt	core + poly-T
[201]	tttttttGAGCTGAAACTTAAGTttttttt	core + poly-T
[202]	tttttttCCCTCGTTATAGTAAGttttttt	core + poly-T
[203]	CATTTGGGGCttttttt	core + poly-T
[204]	tttttttAGTGCTGAAT	core + poly-T
[205]	tttttttTTAAATTTCTGGTTTGttttttt	core + poly-T
[206]	ACCACATCGTCCAAAAAACAG	core (thiol)
[207]	CATCAGTCATAAATTTGATAA	core (thiol)
[208]	TACATAATAAAATGCAAATAT	core (thiol)
[209]	AGTTACTAACGTTTTGTCGTCTTTCGGCG	core (modification site A)
[210]	TTACCAGTCAGGGGATTTTGCTAAATCGT	core (modification site B)
[211]	AAAATGTGAATAATAGAAAGGAACAATTG	core (modification site C)
[212]	TTAAAGTAAATTCACGTTGAAAATCTGTA	core (modification site D)
[213]	AACACAGTGAATTAATTGTATCGGTCCGC	core (modification site E)
[214]	TAAGCGGATATTTAAACAGCTTGATTCGT	core (modification site F)
[215]	ATATATAGGCTACCATCGCCCACGCACCT	core (modification site G)
[216]	GTACAACTTTGTGCAGGGAGTTAAAGGTG	core (modification site H)

[217]	CAATAACGAGGGCAGCGAAAGACAGCATT	core (modification site I)

Table S4 Staple strand sequences for folding the core zipper structure without pH lock extensions nor strands for immobilization. For folding the active zippers or the open controls, the indicated strands for the modification sites A - I (green and orange; site A is located closest to the hinge of the zippers and site I furthest from the hinge) should be replaced with corresponding extended strands in Table S2. For immobilization, the indicated core strands (purple) are replaced with the thiol-modified stands in Table S3. Unpaired poly-T sequences (poly-T overhangs used for passivating the helix ends and poly-T spacer sequences in strand extensions) are written in lowercase letters.

Arm 1: DNA hairpins for both active and control zippers		
Strand no.	**Sequence**	**Strand type**
[101]	CGCGCAGAGATTATCATTTGAtttTTTCTTTCCTTCTTTTCCttttGGAAAAGAAGGAAAGAAA	core + 3' hairpin (modification site A)
[102]	AAGATGATGAAAGAAAGCGGGtttTTTCTTTCCTTCTTTTCCttttGGAAAAGAAGGAAAGAAA	core + 3' hairpin (modification site B)
[103]	TTAACAATTATTAATTGAACGtttTTTCTTTCCTTCTTTTCCttttGGAAAAGAAGGAAAGAAA	core + 3' hairpin (modification site C)
[104]	CATAAATCAAAACAATGAGGCtttTTTCTTTCCTTCTTTTCCttttGGAAAAGAAGGAAAGAAA	core + 3' hairpin (modification site D)
[105]	TCGTCGCTAAATAGATCGTTGtttTTTCTTTCCTTCTTTTCCttttGGAAAAGAAGGAAAGAAA	core + 3' hairpin (modification site E)
[106]	TAGCGATAGAATATCTCTGAGtttTTTCTTTCCTTCTTTTCCttttGGAAAAGAAGGAAAGAAA	core + 3' hairpin (modification site F)
[107]	AATTTATCATGGCAAACAGAAtttTTTCTTTCCTTCTTTTCCttttGGAAAAGAAGGAAAGAAA	core + 3' hairpin (modification site G)
[108]	TCCGGCTTACTGAACCCATGGtttTTTCTTTCCTTCTTTTCCttttGGAAAAGAAGGAAAGAAA	core + 3' hairpin (modification site H)
[109]	GCAAATCCACTGAGAGATTATtttTTTCTTTCCTTCTTTTCCttttGGAAAAGAAGGAAAGAAA	core + 3' hairpin (modification site I)
Arm 2: ssDNA extensions for active zippers		
Strand no.	**Sequence**	**Strand type**
[209]	AGTTACTAACGTTTTGTCGTCTTTCGGCGttttCCTTTTCTTCCTTTCTTT	core + pH lock extension (modification site A)
[210]	TTACCAGTCAGGGGATTTTGCTAAATCGTttttCCTTTTCTTCCTTTCTTT	core + pH lock extension (modification site B)

[211]	AAAATGTGAATAATAGAAAGGAACAATTGttttCCTTTTCTTCCTTTCTTT	core + pH lock extension (modification site C)
[212]	TTAAAGTAAATTCACGTTGAAAATCTGTAttttCCTTTTCTTCCTTTCTTT	core + pH lock extension (modification site D)
[213]	AACACAGTGAATTAATTGTATCGGTCCGCttttCCTTTTCTTCCTTTCTTT	core + pH lock extension (modification site E)
[214]	TAAGCGGATATTTAAACAGCTTGATTCGTttttCCTTTTCTTCCTTTCTTT	core + pH lock extension (modification site F)
[215]	ATATATAGGCTACCATCGCCCACGCACCTttttCCTTTTCTTCCTTTCTTT	core + pH lock extension (modification site G)
[216]	GTACAACTTTGTGCAGGGAGTTAAAGGTGttttCCTTTTCTTCCTTTCTTT	core + pH lock extension (modification site H)
[217]	CAATAACGAGGGCAGCGAAAGACAGCATTttttCCTTTTCTTCCTTTCTTT	core + pH lock extension (modification site I)
Arm 2: ssDNA extensions for control zippers		
Strand no.	**Sequence**	**Strand type**
[209]	AGTTACTAACGTTTTGTCGTCTTTCGGCGttAGAACGCCATAAGAGG	core + control extension (modification site A)
[210]	TTACCAGTCAGGGGATTTTGCTAAATCGTttAGAACGCCATAAGAGG	core + control extension (modification site B)
[211]	AAAATGTGAATAATAGAAAGGAACAATTGttAGAACGCCATAAGAGG	core + control extension (modification site C)
[212]	TTAAAGTAAATTCACGTTGAAAATCTGTAttAGAACGCCATAAGAGG	core + control extension (modification site D)
[213]	AACACAGTGAATTAATTGTATCGGTCCGCttAGAACGCCATAAGAGG	core + control extension (modification site E)
[214]	TAAGCGGATATTTAAACAGCTTGATTCGTttAGAACGCCATAAGAGG	core + control extension (modification site F)
[215]	ATATATAGGCTACCATCGCCCACGCACCTttAGAACGCCATAAGAGG	core + control extension (modification site G)
[216]	GTACAACTTTGTGCAGGGAGTTAAAGGTGttAGAACGCCATAAGAGG	core + control extension (modification site H)
[217]	CAATAACGAGGGCAGCGAAAGACAGCATTttAGAACGCCATAAGAGG	core + control extension (modification site I)

Table S5 Extended staples for the hairpins and ssDNA counterparts (Figure S1) of active and control zippers.

Arm 2		
Strand no.	**Sequence**	**Strand type**
[206]	/5ThioMC6-D/tttttACCACATCGTCCAAAAAACAG	thiol modification + core
[207]	/5ThioMC6-D/tttttCATCAGTCATAAATTTGATAA	thiol modification + core
[208]	/5ThioMC6-D/tttttTACATAATAAAATGCAAATAT	thiol modification + core

Table S6. Thiol-modified strands for arm 2.

(B) Supplementary TEM images for Chapter 5

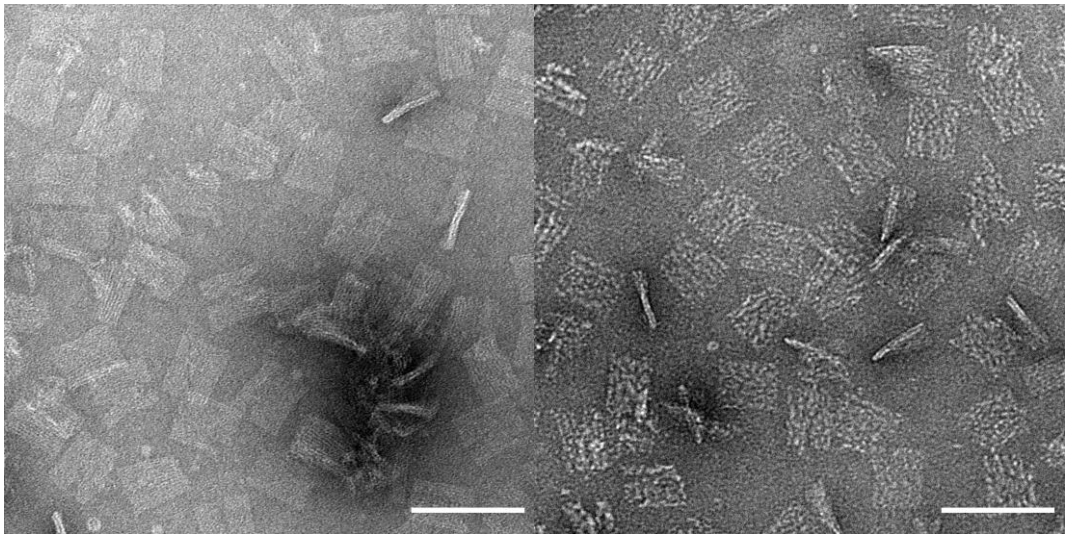

Figure S1. Tile A, no capture strands

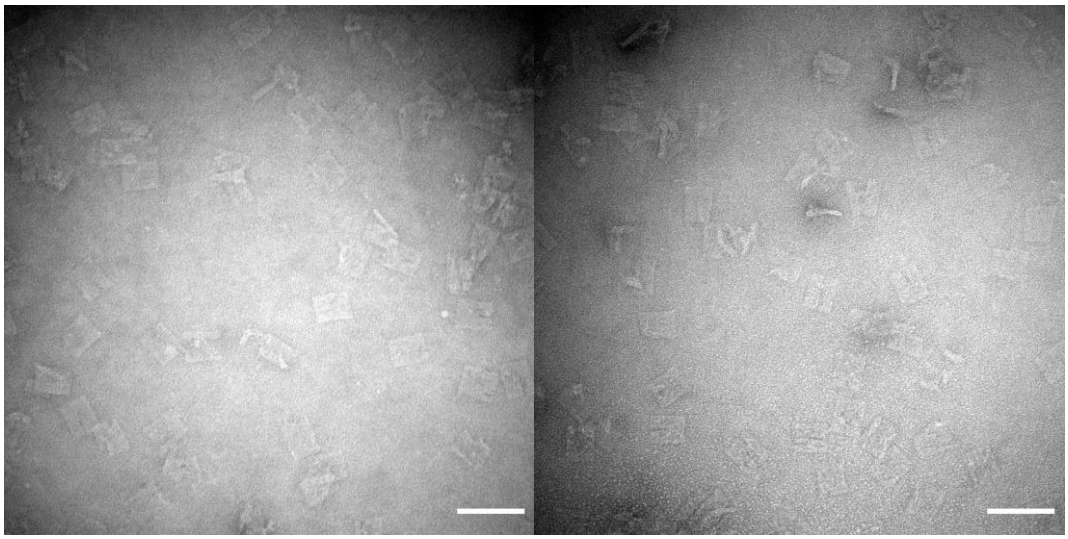

Figure S2. Tile B, capture strands on one side

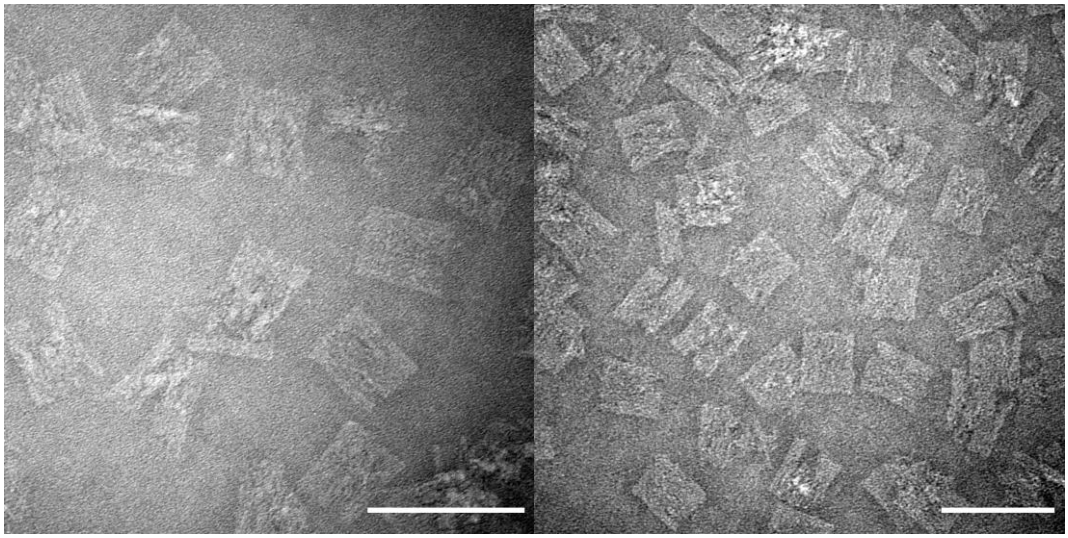

Figure S3. Tile C, capture strands on both sides

(C) SI for Chapter 6

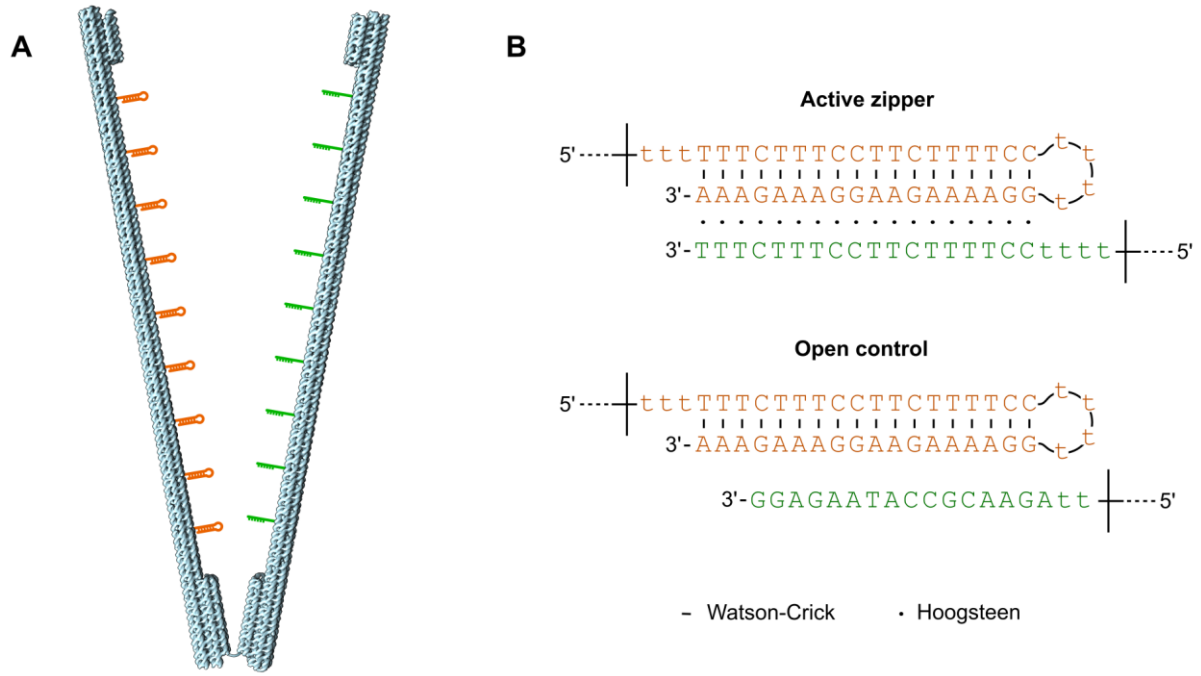

Figure S4. The zipper structure and the sequences of the pH lock residues. (**A**) Illustration of the DNA zipper structure, showing the location of the pH lock residues. (**B**) Sequences of the DNA hairpin- and ssDNA staple strand extensions in the active zippers (top panel) and in the open controls (bottom panel), with an illustration of the Watson-Crick and Hoogsteen hydrogen bonds.

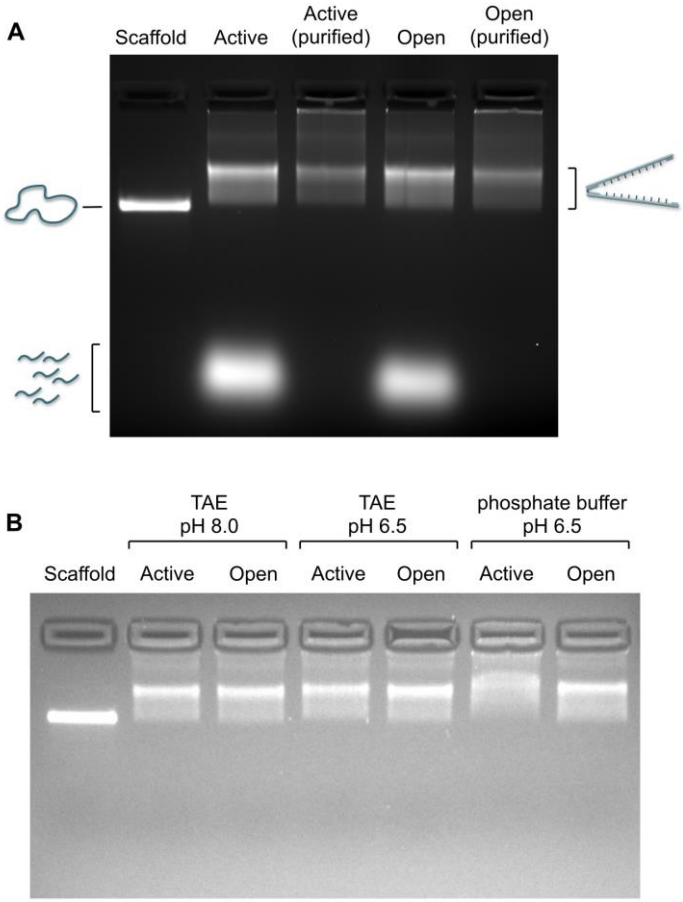

Figure S5. Agarose gel electrophoresis (AGE) analysis of the zippers after folding, purification, and buffer exchange. (**A**) Comparison of the electrophoretic mobility of the 7,560-nt DNA scaffold (lane 1), assembled zippers in the presence of excess staple strands (lanes 2 and 4), and PEG-purified zippers (lanes 3 and 5). (**B**) The electrophoretic mobility of the 7,560-nt scaffold (lane 1) and PEG-purified zippers that have been incubated in different buffer conditions before the gel run. The high pH of the gel (~8.3) can be expected to convert all structures into an open configuration and lead to a disassembly of aggregates. The slower migration of structures in pH 6.5 phosphate buffer may originate from the better buffering capacity of the phosphate buffer at pH 6.5 preventing pH-induced changes in the sample.

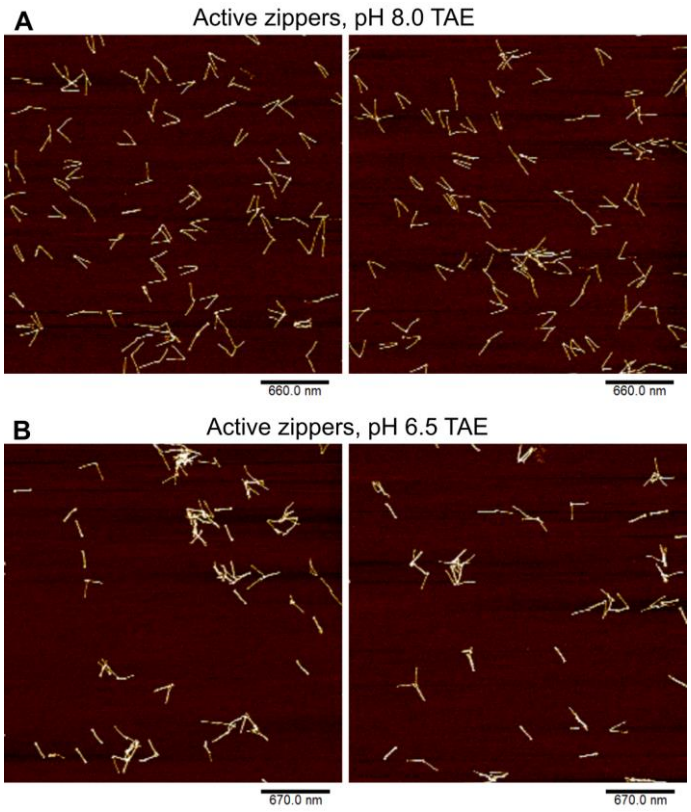

Figure S6. Additional AFM images of the active zippers in TAE buffers. (**A**) pH 8.0. (**B**) pH 6.5.

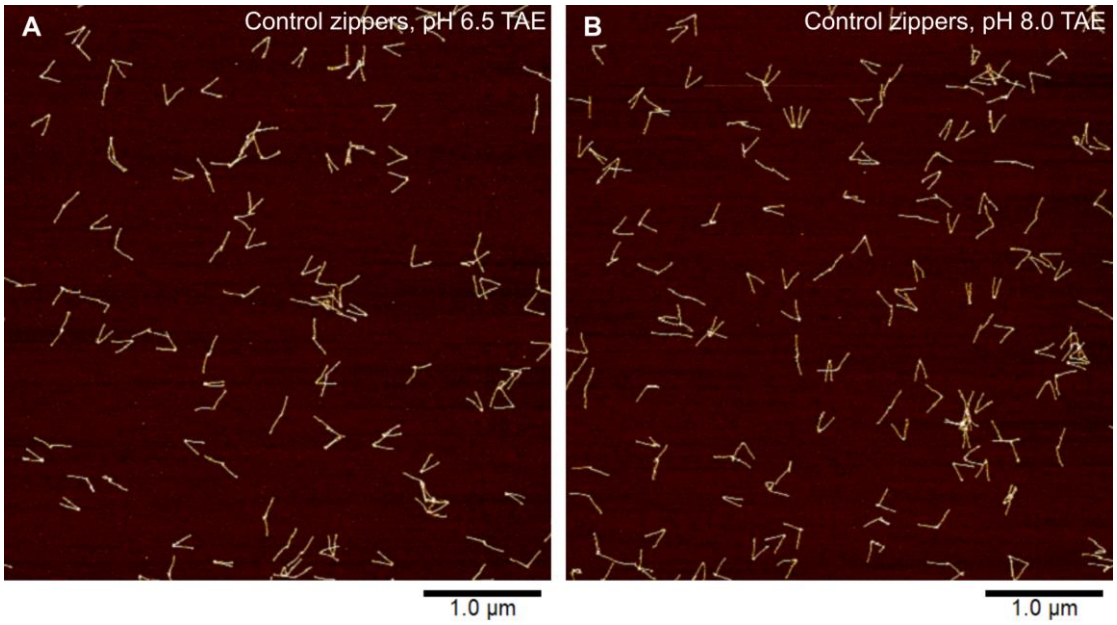

Figure S7. AFM images of the control zippers in TAE buffers. (**A**) pH 6.5. (**B**) pH 8.0.

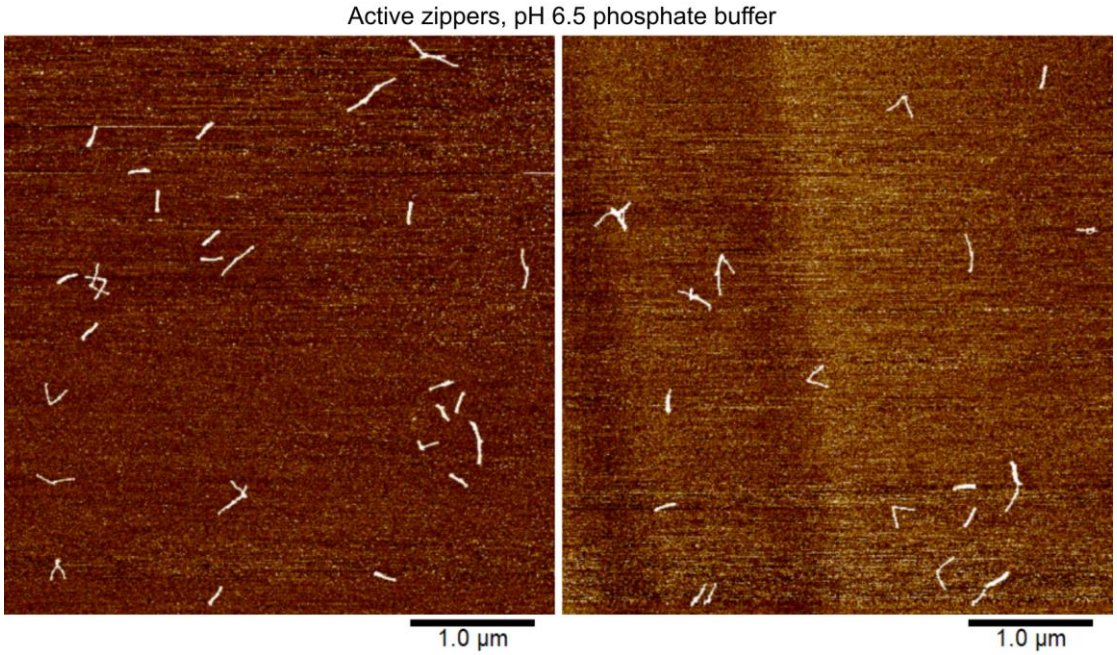

Figure S8. AFM images of the active zippers in pH 6.5 phosphate buffer.

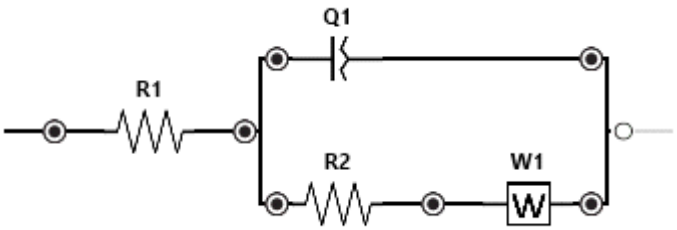

Figure S9. Simplified Randles Circuit for the fitting of Electrochemical Impedance Spectroscopy data, and subsequent determination of charge transfer resistance (Rct) (Ω). R1 is solution resistance, R2 is charge transfer resistance, Q1 is double-layer capacitance modelled by an imperfect capacitor, W1 is the impedance associated with bulk diffusion in solution (Warburg Element).

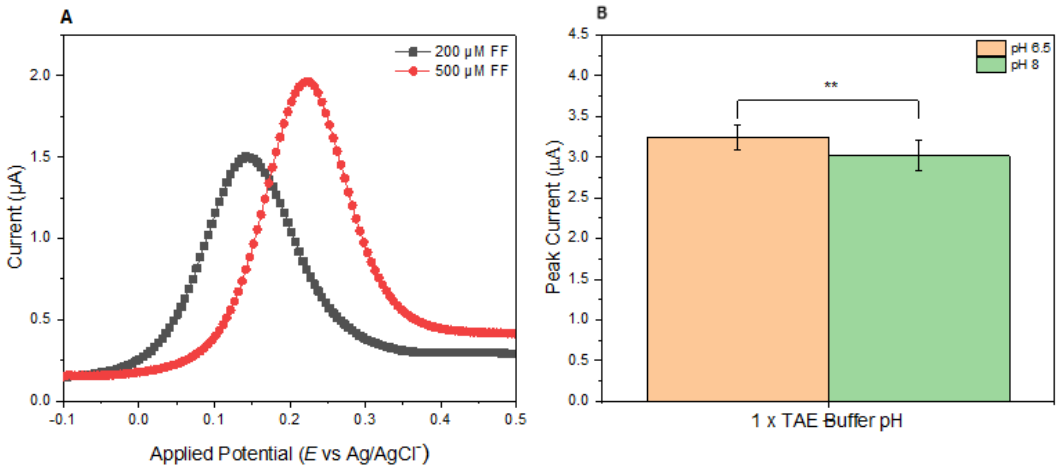

Figure S10. (**A**) Typical DPV traces for two concentrations of $Fe(CN)_6^{(-3/-4)}$. (**B**) Impact of Changing Buffer pH on the Basic Electrochemical Behaviour of FeCN. DPV peak current (µA) of FF at pH 6.5 and 8 on pristine gold electrodes. p = 0.0093, with a % reduction of 7.03, or 227.6 nA.

References

(1) Fair, R. J.; Tor, Y. Antibiotics and Bacterial Resistance in the 21st Century. *Perspect. Medicin. Chem.* **2014**, *6*, PMC.S14459. https://doi.org/10.4137/PMC.S14459.

(2) O'Neill, J. *TACKLING DRUG-RESISTANT INFECTIONS GLOBALLY: FINAL REPORT AND RECOMMENDATIONS*; 2016.

(3) Bennett, P. M. Plasmid Encoded Antibiotic Resistance: Acquisition and Transfer of Antibiotic Resistance Genes in Bacteria. *Br. J. Pharmacol.* **2008**, *153* (S1), S347–S357. https://doi.org/https://doi.org/10.1038/sj.bjp.0707607.

(4) Perry, J. A.; Wright, G. D. Forces Shaping the Antibiotic Resistome. *BioEssays* **2014**, *36* (12), 1179–1184. https://doi.org/https://doi.org/10.1002/bies.201400128.

(5) Prestinaci, F.; Pezzotti, P.; Pantosti, A. Antimicrobial Resistance: A Global Multifaceted Phenomenon. *Pathog. Glob. Health* **2015**, *109* (7), 309–318. https://doi.org/10.1179/2047773215Y.0000000030.

(6) Julian, D.; Dorothy, D. Origins and Evolution of Antibiotic Resistance. *Microbiol. Mol. Biol. Rev.* **2010**, *74* (3), 417–433. https://doi.org/10.1128/MMBR.00016-10.

(7) Murray, C. J. L.; Ikuta, K. S.; Sharara, F.; Swetschinski, L.; Robles Aguilar, G.; Gray, A.; Han, C.; Bisignano, C.; Rao, P.; Wool, E.; Johnson, S. C.; Browne, A. J.; Chipeta, M. G.; Fell, F.; Hackett, S.; Haines-Woodhouse, G.; Kashef Hamadani, B. H.; Kumaran, E. A. P.; McManigal, B.; Agarwal, R.; Akech, S.; Albertson, S.; Amuasi, J.; Andrews, J.; Aravkin, A.; Ashley, E.; Bailey, F.; Baker, S.; Basnyat, B.; Bekker, A.; Bender, R.; Bethou, A.; Bielicki, J.; Boonkasidecha, S.; Bukosia, J.; Carvalheiro, C.; Castañeda-Orjuela, C.; Chansamouth, V.; Chaurasia, S.; Chiurchiù, S.; Chowdhury, F.; Cook, A. J.; Cooper, B.; Cressey, T. R.; Criollo-Mora, E.; Cunningham, M.; Darboe, S.; Day, N. P. J.; De Luca, M.; Dokova, K.; Dramowski, A.; Dunachie, S. J.; Eckmanns, T.; Eibach, D.; Emami, A.; Feasey, N.; Fisher-Pearson, N.; Forrest, K.; Garrett, D.; Gastmeier, P.; Giref, A. Z.; Greer, R. C.; Gupta, V.; Haller, S.; Haselbeck, A.; Hay, S. I.; Holm, M.; Hopkins, S.; Iregbu, K. C.; Jacobs, J.; Jarovsky, D.; Javanmardi, F.; Khorana, M.; Kissoon, N.; Kobeissi, E.; Kostyanev, T.; Krapp, F.; Krumkamp, R.; Kumar, A.; Kyu, H. H.; Lim, C.; Limmathurotsakul, D.; Loftus, M. J.; Lunn, M.; Ma, J.; Mturi, N.; Munera-Huertas, T.; Musicha, P.; Mussi-Pinhata, M. M.; Nakamura, T.; Nanavati, R.; Nangia, S.; Newton, P.; Ngoun, C.; Novotney, A.; Nwakanma, D.; Obiero, C. W.; Olivas-Martinez, A.; Olliaro, P.; Ooko, E.; Ortiz-Brizuela, E.; Peleg, A. Y.; Perrone, C.; Plakkal, N.; Ponce-de-Leon, A.; Raad, M.; Ramdin, T.; Riddell, A.; Roberts, T.; Robotham, J. V.; Roca, A.; Rudd, K. E.; Russell, N.; Schnall, J.; Scott, J. A. G.; Shivamallappa, M.; Sifuentes-Osornio, J.; Steenkeste, N.; Stewardson, A. J.; Stoeva, T.; Tasak, N.; Thaiprakong, A.; Thwaites, G.; Turner, C.; Turner, P.; van Doorn, H. R.; Velaphi, S.; Vongpradith, A.; Vu, H.; Walsh, T.; Waner, S.; Wangrangsimakul, T.; Wozniak, T.; Zheng, P.; Sartorius, B.; Lopez, A. D.; Stergachis, A.; Moore, C.; Dolecek, C.; Naghavi, M. Global Burden of Bacterial Antimicrobial Resistance in 2019: A Systematic Analysis. *Lancet* **2022**, *399* (10325), 629–655. https://doi.org/10.1016/S0140-6736(21)02724-0.

(8) Pitout, J. D. D.; DeVinney, R. Escherichia Coli ST131: A Multidrug-Resistant Clone Primed for Global Domination [Version 1; Peer Review: 2 Approved]. *F1000Research* **2017**, *6* (195). https://doi.org/10.12688/f1000research.10609.1.

(9) Zhou, X. Y.; Bordon, F.; Sirot, D.; Kitzis, M. D.; Gutmann, L. Emergence of Clinical Isolates of Escherichia Coli Producing TEM-1 Derivatives or an OXA-1 Beta-Lactamase Conferring Resistance to Beta-Lactamase Inhibitors. *Antimicrob. Agents Chemother.* **1994**, *38* (5), 1085–1089. https://doi.org/10.1128/AAC.38.5.1085.

(10) Rice, L. B. Mechanisms of Resistance and Clinical Relevance of Resistance to β-Lactams, Glycopeptides, and Fluoroquinolones. *Mayo Clin. Proc.* **2012**, *87* (2), 198–208. https://doi.org/10.1016/j.mayocp.2011.12.003.

(11) Sugumar, M.; Kumar, K. M.; Manoharan, A.; Anbarasu, A.; Ramaiah, S. Detection of OXA-1 β-Lactamase Gene of Klebsiella Pneumoniae from Blood Stream Infections (BSI) by Conventional PCR and In-Silico Analysis to Understand the Mechanism of OXA Mediated Resistance. *PLoS One* **2014**, *9* (3), e91800-.

(12) Butterworth, A.; Pratibha, P.; Marx, A.; Corrigan, D. K. Electrochemical Detection of Oxacillin Resistance Using Direct-Labeling Solid-Phase Isothermal Amplification. *ACS Sensors* **2021**, *6* (10), 3773–3780. https://doi.org/10.1021/acssensors.1c01688.

(13) Butterworth, A.; Blues, E.; Williamson, P.; Cardona, M.; Gray, L.; Corrigan, D. K. SAM Composition and Electrode Roughness Affect Performance of a DNA Biosensor for Antibiotic Resistance. *Biosensors* **2019**, *9* (1), 22. https://doi.org/10.3390/bios9010022.

(14) WATSON, J. D.; CRICK, F. H. C. Molecular Structure of Nucleic Acids: A Structure for Deoxyribose Nucleic Acid. *Nature* **1953**, *171* (4356), 737–738. https://doi.org/10.1038/171737a0.

(15) Pray, L. Discovery of DNA Structure and Function: Watson and Crick.

(16) Drew, H. R.; Wing, R. M.; Takano, T.; Broka, C.; Tanaka, S.; Itakura, K.; Dickerson, R. E. Structure of a B-DNA Dodecamer: Conformation and Dynamics. *Proc. Natl. Acad. Sci.* **1981**, *78* (4), 2179–2183. https://doi.org/10.1073/pnas.78.4.2179.

(17) Bobo, F.; P, S. R.; F, M. A. K.; Kai, J.; Alex, T.; D, D. K.; Masayuki, T.; Per, L.; J, B. C.; Fredrik, W.; Bengt, N. Hydrophobic Catalysis and a Potential Biological Role of DNA Unstacking Induced by Environment Effects. *Proc. Natl. Acad. Sci.* **2019**, *116* (35), 17169–17174. https://doi.org/10.1073/pnas.1909122116.

(18) National Human Genome Research Institute. The Human Genome Project.

(19) Gautam, S. S.; Kc, R.; Leong, K. W.; Mac Aogáin, M.; O'Toole, R. F. A Step-by-Step Beginner's Protocol for Whole Genome Sequencing of Human Bacterial Pathogens. *J. Biol. methods* **2019**, *6* (1), e110–e110. https://doi.org/10.14440/jbm.2019.276.

(20) Jani, I. V; Peter, T. F. Nucleic Acid Point-of-Care Testing to Improve Diagnostic Preparedness. *Clin. Infect. Dis.* **2022**, ciac013. https://doi.org/10.1093/cid/ciac013.

(21) Xu, L.; Duan, J.; Chen, J.; Ding, S.; Cheng, W. Recent Advances in Rolling Circle Amplification-Based Biosensing Strategies-A Review. *Anal. Chim. Acta* **2021**, *1148*, 238187. https://doi.org/https://doi.org/10.1016/j.aca.2020.12.062.

(22) Wang, Y.; Li, H.; Wang, Y.; Zhang, L.; Xu, J.; Ye, C. Loop-Mediated Isothermal Amplification Label-Based Gold Nanoparticles Lateral Flow Biosensor for Detection of Enterococcus Faecalis and Staphylococcus Aureus. *Front. Microbiol.* **2017**, *8*.

(23) Miao, F.; Zhang, J.; Li, N.; Chen, T.; Wang, L.; Zhang, F.; Mi, L.; Zhang, J.; Wang, S.; Wang, Y.; Zhou, X.; Zhang, Y.; Li, M.; Zhang, S.; Hu, R. Rapid and Sensitive Recombinase Polymerase Amplification Combined With Lateral Flow Strip for Detecting African Swine Fever Virus. *Front. Microbiol.* **2019**, *10*.

(24) Herne, T. M.; Tarlov, M. J. Characterization of DNA Probes Immobilized on Gold Surfaces. *J. Am. Chem. Soc.* **1997**, *119* (38), 8916–8920. https://doi.org/10.1021/ja9719586.

(25) Han, K.; Liang, Z.; Zhou, N. Design Strategies for Aptamer-Based Biosensors. *Sensors (Basel).* **2010**, *10* (5), 4541–4557. https://doi.org/10.3390/s100504541.

(26) Jolly, P.; Rainbow, J.; Regoutz, A.; Estrela, P.; Moschou, D. A PNA-Based Lab-on-PCB Diagnostic Platform for Rapid and High Sensitivity DNA Quantification. *Biosens. Bioelectron.* **2019**, *123*, 244–250. https://doi.org/https://doi.org/10.1016/j.bios.2018.09.006.

(27) Levicky, R.; Koniges, U.; Tercero, N. Diagnostic Applications of Morpholinos and Label-Free Electrochemical Detection of Nucleic Acids. In *Morpholino Oligomers: Methods and Protocols*; Moulton, H. M., Moulton, J. D., Eds.; Springer New York: New York, NY, 2017; pp 181–190. https://doi.org/10.1007/978-1-4939-6817-6_15.

(28) Li, X.; Ye, M.; Zhang, W.; Tan, D.; Jaffrezic-Renault, N.; Yang, X.; Guo, Z. Liquid Biopsy of Circulating Tumor DNA and Biosensor Applications. *Biosens. Bioelectron.* **2019**, *126*, 596–607. https://doi.org/https://doi.org/10.1016/j.bios.2018.11.037.

(29) Henihan, G.; Schulze, H.; Corrigan, D. K.; Giraud, G.; Terry, J. G.; Hardie, A.; Campbell, C. J.; Walton, A. J.; Crain, J.; Pethig, R.; Templeton, K. E.; Mount, A. R.; Bachmann, T. T. Label- and Amplification-Free Electrochemical Detection of Bacterial Ribosomal RNA. *Biosens. Bioelectron.* **2016**, *81*, 487–494. https://doi.org/https://doi.org/10.1016/j.bios.2016.03.037.

(30) Thavarajah, W.; Verosloff, M. S.; Jung, J. K.; Alam, K. K.; Miller, J. D.; Jewett, M. C.; Young, S. L.; Lucks, J. B. A Primer on Emerging Field-Deployable Synthetic Biology Tools for Global Water Quality Monitoring. *npj Clean Water* **2020**, *3* (1), 18. https://doi.org/10.1038/s41545-020-0064-8.

(31) Magro, L.; Jacquelin, B.; Escadafal, C.; Garneret, P.; Kwasiborski, A.; Manuguerra, J.-C.; Monti, F.; Sakuntabhai, A.; Vanhomwegen, J.; Lafaye, P.; Tabeling, P. Paper-Based RNA Detection and Multiplexed Analysis for Ebola Virus Diagnostics. *Sci. Rep.* **2017**, *7* (1), 1347. https://doi.org/10.1038/s41598-017-00758-9.

(32) Batule, B. S.; Seok, Y.; Kim, M.-G. Paper-Based Nucleic Acid Testing System for Simple and Early Diagnosis of Mosquito-Borne RNA Viruses from Human Serum. *Biosens. Bioelectron.* **2020**, *151*, 111998. https://doi.org/https://doi.org/10.1016/j.bios.2019.111998.

(33) Kaur, N.; Toley, B. J. Paper-Based Nucleic Acid Amplification Tests for Point-of-Care Diagnostics. *Analyst* **2018**, *143* (10), 2213–2234. https://doi.org/10.1039/C7AN01943B.

(34) Butterworth, A.; Corrigan, D. K.; Ward, A. C. Electrochemical Detection of Oxacillin Resistance with SimpleStat: A Low Cost Integrated Potentiostat and Sensor Platform. *Anal. Methods* **2019**, *11* (14), 1958–1965. https://doi.org/10.1039/C9AY00383E.

(35) Corrigan, D. K.; Schulze, H.; Henihan, G.; Hardie, A.; Ciani, I.; Giraud, G.; Terry, J. G.; Walton, A. J.; Pethig, R.; Ghazal, P.; Crain, J.; Campbell, C. J.; Templeton, K. E.; Mount, A. R.; Bachmann, T. T. Development of a PCR-Free Electrochemical Point of Care Test for Clinical Detection of Methicillin Resistant Staphylococcus Aureus (MRSA). *Analyst* **2013**, *138* (22), 6997–7005. https://doi.org/10.1039/C3AN01319G.

(36) Butterworth, A.; Blues, E.; Williamson, P.; Cardona, M.; Gray, L.; Corrigan, D. K. SAM Composition and Electrode Roughness Affect Performance of a DNA Biosensor for Antibiotic Resistance. *Biosensors* **2019**, *9* (1). https://doi.org/10.3390/bios9010022.

(37) Cardoso, A. R.; Moreira, F. T. C.; Fernandes, R.; Sales, M. G. F. Novel and Simple Electrochemical Biosensor Monitoring Attomolar Levels of MiRNA-155 in Breast Cancer. *Biosens. Bioelectron.* **2016**, *80*, 621–630. https://doi.org/10.1016/j.bios.2016.02.035.

(38) Mousavisani, S. Z.; Raoof, J. B.; Ojani, R.; Bagheryan, Z. An Impedimetric Biosensor for DNA Damage Detection and Study of the Protective Effect of Deferoxamine against DNA Damage. *Bioelectrochemistry* **2018**, *122*, 142–148. https://doi.org/https://doi.org/10.1016/j.bioelechem.2018.03.012.

(39) Hu, F.; Zhang, W.; Meng, W.; Ma, Y.; Zhang, X.; Xu, Y.; Wang, P.; Gu, Y. Ferrocene-Labeled and Purification-Free Electrochemical Biosensor Based on Ligase Chain Reaction for Ultrasensitive Single Nucleotide Polymorphism Detection. *Anal. Chim. Acta* **2020**, *1109*, 9–18. https://doi.org/https://doi.org/10.1016/j.aca.2020.02.062.

(40) Lasserre, P.; Balansethupathy, B.; Vezza, V. J.; Butterworth, A.; Macdonald, A.; Blair, E. O.; McAteer, L.; Hannah, S.; Ward, A. C.; Hoskisson, P. A.; Longmuir, A.; Setford, S.; Farmer, E. C. W.; Murphy, M. E.; Flynn, H.; Corrigan, D. K. SARS-CoV-2 Aptasensors Based on Electrochemical Impedance Spectroscopy and Low-Cost Gold Electrode Substrates. *Anal. Chem.* **2022**, *94* (4), 2126–2133. https://doi.org/10.1021/acs.analchem.1c04456.

(41) Love, J. C.; Estroff, L. A.; Kriebel, J. K.; Nuzzo, R. G.; Whitesides, G. M. Self-Assembled Monolayers of Thiolates on Metals as a Form of Nanotechnology. *Chem. Rev.* **2005**, *105* (4), 1103–1170. https://doi.org/10.1021/cr0300789.

(42) Poirier, G. E.; Pylant, E. D. The Self-Assembly Mechanism of Alkanethiols on Au(111). *Science (80-.).* **1996**, *272* (5265), 1145–1148. https://doi.org/10.1126/science.272.5265.1145.

(43) Porter, M. D.; Bright, T. B.; Allara, D. L.; Chidsey, C. E. D. Spontaneously Organized Molecular Assemblies. 4. Structural Characterization of n-Alkyl Thiol Monolayers on Gold by Optical Ellipsometry, Infrared Spectroscopy, and Electrochemistry. *J. Am. Chem. Soc.* **1987**, *109* (12), 3559–3568. https://doi.org/10.1021/ja00246a011.

(44) Laibinis, P. E.; Whitesides, G. M.; Allara, D. L.; Tao, Y. T.; Parikh, A. N.; Nuzzo, R. G. Comparison of the Structures and Wetting Properties of Self-Assembled Monolayers of n-Alkanethiols on the Coinage Metal Surfaces, Copper, Silver, and Gold. *J. Am. Chem. Soc.* **1991**, *113* (19), 7152–7167. https://doi.org/10.1021/ja00019a011.

(45) Walczak, M. M.; Chung, C.; Stole, S. M.; Widrig, C. A.; Porter, M. D. Structure and Interfacial Properties of Spontaneously Adsorbed N-Alkanethiolate Monolayers on Evaporated Silver Surfaces. *J. Am. Chem. Soc.* **1991**, *113* (7), 2370–2378. https://doi.org/10.1021/ja00007a004.

(46) Li, Z.; Chang, S.-C.; Williams, R. S. Self-Assembly of Alkanethiol Molecules onto Platinum and Platinum Oxide Surfaces. *Langmuir* **2003**, *19* (17), 6744–6749. https://doi.org/10.1021/la034245b.

(47) Vericat, C.; Vela, M. E.; Benitez, G.; Carro, P.; Salvarezza, R. C. Self-Assembled Monolayers of Thiols and Dithiols on Gold: New Challenges for a Well-Known System. *Chem. Soc. Rev.* **2010**, *39* (5), 1805–1834. https://doi.org/10.1039/B907301A.

(48) Henderson, A. P.; Seetohul, L. N.; Dean, A. K.; Russell, P.; Pruneanu, S.; Ali, Z. A Novel Isotherm, Modeling Self-Assembled Monolayer Adsorption and Structural Changes. *Langmuir* **2009**, *25* (2), 931–938. https://doi.org/10.1021/la802677n.

(49) Kankate, L.; Turchanin, A.; Gölzhäuser, A. On the Release of Hydrogen from the S−H Groups in the Formation of Self-Assembled Monolayers of Thiols. *Langmuir* **2009**, *25* (18), 10435–10438. https://doi.org/10.1021/la902168u.

(50) Strong, L.; Whitesides, G. M. Structures of Self-Assembled Monolayer Films of Organosulfur Compounds Adsorbed on Gold Single Crystals: Electron Diffraction Studies. *Langmuir* **1988**, *4* (3), 546–558. https://doi.org/10.1021/la00081a009.

(51) Chidsey, C. E. D.; Loiacono, D. N. Chemical Functionality in Self-Assembled Monolayers: Structural and Electrochemical Properties. *Langmuir* **1990**, *6* (3), 682–691. https://doi.org/10.1021/la00093a026.

(52) Torrelles, X.; Vericat, C.; Vela, M. E.; Fonticelli, M. H.; Daza Millone, M. A.; Felici, R.; Lee, T.-L.; Zegenhagen, J.; Muñoz, G.; Martín-Gago, J. A.; Salvarezza, R. C. Two-Site Adsorption Model for the (√3 × √3)-R30° Dodecanethiolate Lattice on Au(111) Surfaces. *J. Phys. Chem. B* **2006**, *110* (11), 5586–5594. https://doi.org/10.1021/jp054879m.

(53) Inkpen, M. S.; Liu, Z.; Li, H.; Campos, L. M.; Neaton, J. B.; Venkataraman, L. Non-Chemisorbed Gold–Sulfur Binding Prevails in Self-Assembled Monolayers. *Nat. Chem.* **2019**, *11* (4), 351–358. https://doi.org/10.1038/s41557-019-0216-y.

(54) Bamdad, C. A DNA Self-Assembled Monolayer for the Specific Attachment of Unmodified Double- or Single-Stranded DNA. *Biophys. J.* **1998**, *75* (4), 1997–2003. https://doi.org/https://doi.org/10.1016/S0006-3495(98)77641-6.

(55) Sandström, P.; Boncheva, M.; Åkerman, B. Nonspecific and Thiol-Specific Binding of DNA to Gold Nanoparticles. *Langmuir* **2003**, *19* (18), 7537–7543. https://doi.org/10.1021/la034348u.

(56) Poirier, G. E. Coverage-Dependent Phases and Phase Stability of Decanethiol on Au(111). *Langmuir* **1999**, *15* (4), 1167–1175. https://doi.org/10.1021/la981374x.

(57) Häkkinen, H. The Gold–Sulfur Interface at the Nanoscale. *Nat. Chem.* **2012**, *4* (6), 443–455. https://doi.org/10.1038/nchem.1352.

(58) Piper, A.; Corrigan, D. K.; Mount, A. R. An Electrochemical Comparison of Thiolated Self-Assembled Monolayer (SAM) Formation and Stability in Solution on Macro- and

Nanoelectrodes. *Electrochem. Sci. Adv.* **2021**, *n/a* (n/a), e2100077. https://doi.org/https://doi.org/10.1002/elsa.202100077.

(59) Mani, G.; Johnson, D. M.; Marton, D.; Dougherty, V. L.; Feldman, M. D.; Patel, D.; Ayon, A. A.; Agrawal, C. M. Stability of Self-Assembled Monolayers on Titanium and Gold. *Langmuir* **2008**, *24* (13), 6774–6784. https://doi.org/10.1021/la8003646.

(60) Cristina, L. J.; Ruano, G.; Salvarezza, R.; Ferrón, J. Thermal Stability of Self-Assembled Monolayers of n-Hexanethiol on Au(111)-(1 × 1) and Au(001)-(1 × 1). *J. Phys. Chem. C* **2017**, *121* (50), 27894–27904. https://doi.org/10.1021/acs.jpcc.7b05883.

(61) Shaver, A.; Curtis, S. D.; Arroyo-Currás, N. Alkanethiol Monolayer End Groups Affect the Long-Term Operational Stability and Signaling of Electrochemical, Aptamer-Based Sensors in Biological Fluids. *ACS Appl. Mater. Interfaces* **2020**, *12* (9), 11214–11223. https://doi.org/10.1021/acsami.9b22385.

(62) Ma, T.; Martens, I.; Bizzotto, D. Thermal Stability of Thiolated DNA SAMs in Buffer: Revealing the Influence of Surface Crystallography and DNA Coverage via In Situ Combinatorial Surface Analysis. *Langmuir* **2020**, *36* (48), 14495–14506. https://doi.org/10.1021/acs.langmuir.0c01828.

(63) Srisombat, L.; Jamison, A. C.; Lee, T. R. Stability: A Key Issue for Self-Assembled Monolayers on Gold as Thin-Film Coatings and Nanoparticle Protectants. *Colloids Surfaces A Physicochem. Eng. Asp.* **2011**, *390* (1), 1–19. https://doi.org/https://doi.org/10.1016/j.colsurfa.2011.09.020.

(64) Fies, W. A.; Dugger, J. W.; Dick, J. E.; Wilder, L. M.; Browning, K. L.; Doucet, M.; Browning, J. F.; Webb, L. J. Direct Measurement of Water Permeation in Submerged Alkyl Thiol Self-Assembled Monolayers on Gold Surfaces Revealed by Neutron Reflectometry. *Langmuir* **2019**, *35* (16), 5647–5662. https://doi.org/10.1021/acs.langmuir.9b00541.

(65) Li, S.; Wang, Y.; Zhang, Z.; Wang, Y.; Li, H.; Xia, F. Exploring End-Group Effect of Alkanethiol Self-Assembled Monolayers on Electrochemical Aptamer-Based Sensors in Biological Fluids. *Anal. Chem.* **2021**, *93* (14), 5849–5855. https://doi.org/10.1021/acs.analchem.1c00085.

(66) Estrela, P.; Migliorato, P.; Takiguchi, H.; Fukushima, H.; Nebashi, S. Electrical Detection of Biomolecular Interactions with Metal–Insulator–Semiconductor Diodes. *Biosens. Bioelectron.* **2005**, *20* (8), 1580–1586. https://doi.org/https://doi.org/10.1016/j.bios.2004.08.010.

(67) Steichen, M.; Buess-Herman, C. Electrochemical Detection of the Immobilization and Hybridization of Unlabeled Linear and Hairpin DNA on Gold. *Electrochem. commun.* **2005**, *7* (4), 416–420. https://doi.org/https://doi.org/10.1016/j.elecom.2005.02.015.

(68) Boozer, C.; Chen, S.; Jiang, S. Controlling DNA Orientation on Mixed SsDNA/OEG SAMs. *Langmuir* **2006**, *22* (10), 4694–4698. https://doi.org/10.1021/la052908e.

(69) Doneux, T.; De Rache, A.; Triffaux, E.; Meunier, A.; Steichen, M.; Buess-Herman, C. Optimization of the Probe Coverage in DNA Biosensors by a One-Step Coadsorption Procedure. *ChemElectroChem* **2014**, *1* (1), 147–157. https://doi.org/https://doi.org/10.1002/celc.201300145.

(70) Steel, A. B.; Herne, T. M.; Tarlov, M. J. Electrochemical Quantitation of DNA Immobilized on Gold. *Anal. Chem.* **1998**, *70* (22), 4670–4677. https://doi.org/10.1021/ac980037q.

(71) Keighley, S. D.; Li, P.; Estrela, P.; Migliorato, P. Optimization of DNA Immobilization on Gold Electrodes for Label-Free Detection by Electrochemical Impedance Spectroscopy. *Biosens. Bioelectron.* **2008**, *23* (8), 1291–1297. https://doi.org/https://doi.org/10.1016/j.bios.2007.11.012.

(72) Macedo, L. J. A.; Miller, E. N.; Opdahl, A. Effect of Probe–Probe Distance on the Stability of DNA Hybrids on Surfaces. *Anal. Chem.* **2017**, *89* (3), 1757–1763. https://doi.org/10.1021/acs.analchem.6b04048.

(73) Josephs, E. A.; Ye, T. Nanoscale Spatial Distribution of Thiolated DNA on Model Nucleic Acid Sensor Surfaces. *ACS Nano* **2013**, *7* (4), 3653–3660. https://doi.org/10.1021/nn400659m.

(74) Bizzotto, D.; Burgess, I. J.; Doneux, T.; Sagara, T.; Yu, H.-Z. Beyond Simple Cartoons: Challenges in Characterizing Electrochemical Biosensor Interfaces. *ACS Sensors* **2018**, *3* (1), 5–12. https://doi.org/10.1021/acssensors.7b00840.

(75) Leung, K. K.; Gaxiola, A. D.; Yu, H.-Z.; Bizzotto, D. Tailoring the DNA SAM Surface Density on Different Surface Crystallographic Features Using Potential Assisted Thiol Exchange. *Electrochim. Acta* **2018**, *261*, 188–197. https://doi.org/https://doi.org/10.1016/j.electacta.2017.12.114.

(76) Gu, Q.; Nanney, W.; Cao, H. H.; Wang, H.; Ye, T. Single Molecule Profiling of Molecular Recognition at a Model Electrochemical Biosensor. *J. Am. Chem. Soc.* **2018**, *140* (43), 14134–14143. https://doi.org/10.1021/jacs.8b07325.

(77) Leung, K. K.; Martens, I.; Yu, H.-Z.; Bizzotto, D. Measuring and Controlling the Local Environment of Surface-Bound DNA in Self-Assembled Monolayers on Gold When Prepared Using Potential-Assisted Deposition. *Langmuir* **2020**, *36* (24), 6837–6847. https://doi.org/10.1021/acs.langmuir.9b03970.

(78) Leung, K. K.; Yu, H.-Z.; Bizzotto, D. Electrodepositing DNA Self-Assembled Monolayers on Au: Detailing the Influence of Electrical Potential Perturbation and Surface Crystallography. *ACS Sensors* **2019**, *4* (2), 513–520. https://doi.org/10.1021/acssensors.8b01695.

(79) Jambrec, D.; Kayran, Y. U.; Schuhmann, W. Controlling DNA/Surface Interactions for Potential Pulse-Assisted Preparation of Multi-Probe DNA Microarrays. *Electroanalysis* **2019**, *31* (10), 1943–1951. https://doi.org/https://doi.org/10.1002/elan.201900233.

(80) Ma, T.; Bizzotto, D. Improved Thermal Stability and Homogeneity of Low Probe Density DNA SAMs Using Potential-Assisted Thiol-Exchange Assembly Methods. *Anal. Chem.* **2021**, *93* (48), 15973–15981. https://doi.org/10.1021/acs.analchem.1c03353.

(81) Ihara, T.; Maruo, Y.; Takenaka, S.; Takagi, M. Ferrocene-Oligonucleotide Conjugates for Electrochemical Probing of DNA. *Nucleic Acids Res.* **1996**, *24* (21), 4273–4280.

(82) Anne, A.; Bouchardon, A.; Moiroux, J. 3‘-Ferrocene-Labeled Oligonucleotide Chains End-Tethered to Gold Electrode Surfaces: Novel Model Systems for Exploring Flexibility of Short DNA Using Cyclic Voltammetry. *J. Am. Chem. Soc.* **2003**, *125* (5), 1112–1113.

https://doi.org/10.1021/ja028640k.

(83) Chatelain, G.; Brisset, H.; Chaix, C. A Thermodynamic Study of Ferrocene Modified Hairpin Oligonucleotides upon Duplex Formation: Applications to the Electrochemical Detection of DNA. *New J. Chem.* **2009**, *33* (5), 1139–1147. https://doi.org/10.1039/B817057F.

(84) Hüsken, N.; Gębala, M.; Schuhmann, W.; Metzler-Nolte, N. A Single-Electrode, Dual-Potential Ferrocene–PNA Biosensor for the Detection of DNA. *ChemBioChem* **2010**, *11* (12), 1754–1761. https://doi.org/https://doi.org/10.1002/cbic.200900748.

(85) Du, Y.; Lim, B. J.; Li, B.; Jiang, Y. S.; Sessler, J. L.; Ellington, A. D. Reagentless, Ratiometric Electrochemical DNA Sensors with Improved Robustness and Reproducibility. *Anal. Chem.* **2014**, *86* (15), 8010–8016. https://doi.org/10.1021/ac5025254.

(86) González-Fernández, E.; Avlonitis, N.; Murray, A. F.; Mount, A. R.; Bradley, M. Methylene Blue Not Ferrocene: Optimal Reporters for Electrochemical Detection of Protease Activity. *Biosens. Bioelectron.* **2016**, *84*, 82–88. https://doi.org/https://doi.org/10.1016/j.bios.2015.11.088.

(87) Luo, L.; Wang, L.; Zeng, L.; Wang, Y.; Weng, Y.; Liao, Y.; Chen, T.; Xia, Y.; Zhang, J.; Chen, J. A Ratiometric Electrochemical DNA Biosensor for Detection of Exosomal MicroRNA. *Talanta* **2020**, *207*, 120298. https://doi.org/https://doi.org/10.1016/j.talanta.2019.120298.

(88) Wang, Q.; Gao, F.; Ni, J.; Liao, X.; Zhang, X.; Lin, Z. Facile Construction of a Highly Sensitive DNA Biosensor by In-Situ Assembly of Electro-Active Tags on Hairpin-Structured Probe Fragment. *Sci. Rep.* **2016**, *6* (1), 22441. https://doi.org/10.1038/srep22441.

(89) Brown, K.; Jacquet, C.; Biscay, J.; Allan, P.; Dennany, L. Tale of Two Alkaloids: PH-Controlled Electrochemiluminescence for Differentiation of Structurally Similar Compounds. *Anal. Chem.* **2020**, *92* (2), 2216–2223. https://doi.org/10.1021/acs.analchem.9b04922.

(90) Lazar, J.; Schnelting, C.; Slavcheva, E.; Schnakenberg, U. Hampering of the Stability of Gold Electrodes by Ferri-/Ferrocyanide Redox Couple Electrolytes during Electrochemical Impedance Spectroscopy. *Anal. Chem.* **2016**, *88* (1), 682–687. https://doi.org/10.1021/acs.analchem.5b02367.

(91) Vogt, S.; Su, Q.; Gutiérrez-Sánchez, C.; Nöll, G. Critical View on Electrochemical Impedance Spectroscopy Using the Ferri/Ferrocyanide Redox Couple at Gold Electrodes. *Anal. Chem.* **2016**, *88* (8), 4383–4390. https://doi.org/10.1021/acs.analchem.5b04814.

(92) Jin, Y.; Yao, X.; Liu, Q.; Li, J. Hairpin DNA Probe Based Electrochemical Biosensor Using Methylene Blue as Hybridization Indicator. *Biosens. Bioelectron.* **2007**, *22* (6), 1126–1130. https://doi.org/https://doi.org/10.1016/j.bios.2006.04.011.

(93) Farjami, E.; Clima, L.; Gothelf, K.; Ferapontova, E. E. "Off−On" Electrochemical Hairpin-DNA-Based Genosensor for Cancer Diagnostics. *Anal. Chem.* **2011**, *83* (5), 1594–1602. https://doi.org/10.1021/ac1032929.

(94) Cui, H.-F.; Xu, T.-B.; Sun, Y.-L.; Zhou, A.-W.; Cui, Y.-H.; Liu, W.; Luong, J. H. T. Hairpin DNA as a Biobarcode Modified on Gold Nanoparticles for Electrochemical DNA Detection. *Anal. Chem.* **2015**, *87* (2), 1358–1365. https://doi.org/10.1021/ac504206n.

(95) Wang, Q.; Gao, F.; Ni, J.; Liao, X.; Zhang, X.; Lin, Z. Facile Construction of a Highly Sensitive DNA Biosensor by In-Situ Assembly of Electro-Active Tags on Hairpin-Structured Probe Fragment. *Sci. Rep.* **2016**, *6*, 22441.

(96) Lozano Untiveros, K.; da Silva, E. G.; de Abreu, F. C.; da Silva-Júnior, E. F.; de Araújo-Junior, J. X.; Mendoça de Aquino, T.; Armas, S. M.; de Moura, R. O.; Mendonça-Junior, F. J. B.; Serafim, V. L.; Chumbimuni-Torres, K. An Electrochemical Biosensor Based on Hairpin-DNA Modified Gold Electrode for Detection of DNA Damage by a Hybrid Cancer Drug Intercalation. *Biosens. Bioelectron.* **2019**, *133*, 160–168. https://doi.org/https://doi.org/10.1016/j.bios.2019.02.071.

(97) Grégoire, B.; Sanjay, T.; Albert, L.; Russell, K. F. Thermodynamic Basis of the Enhanced Specificity of Structured DNA Probes. *Proc. Natl. Acad. Sci.* **1999**, *96* (11), 6171–6176. https://doi.org/10.1073/pnas.96.11.6171.

(98) Xiong, E.; Li, Z.; Zhang, X.; Zhou, J.; Yan, X.; Liu, Y.; Chen, J. Triple-Helix Molecular Switch Electrochemical Ratiometric Biosensor for Ultrasensitive Detection of Nucleic Acids. *Anal. Chem.* **2017**, *89* (17), 8830–8835. https://doi.org/10.1021/acs.analchem.7b01251.

(99) Ma, R.-N.; Wang, L.-L.; Wang, H.-F.; Jia, L.-P.; Zhang, W.; Shang, L.; Xue, Q.-W.; Jia, W.-L.; Liu, Q.-Y.; Wang, H.-S. Highly Sensitive Ratiometric Electrochemical DNA Biosensor Based on Homogeneous Exonuclease III-Assisted Target Recycling Amplification and One-Step Triggered Dual-Signal Output. *Sensors Actuators B Chem.* **2018**, *269*, 173–179. https://doi.org/https://doi.org/10.1016/j.snb.2018.04.143.

(100) Kang, D.; Zuo, X.; Yang, R.; Xia, F.; Plaxco, K. W.; White, R. J. Comparing the Properties of Electrochemical-Based DNA Sensors Employing Different Redox Tags. *Anal. Chem.* **2009**, *81* (21), 9109–9113. https://doi.org/10.1021/ac901811n.

(101) Dauphin-Ducharme, P.; Plaxco, K. W. Maximizing the Signal Gain of Electrochemical-DNA Sensors. *Anal. Chem.* **2016**, *88* (23), 11654–11662. https://doi.org/10.1021/acs.analchem.6b03227.

(102) Downs, A. M.; Gerson, J.; Ploense, K. L.; Plaxco, K. W.; Dauphin-Ducharme, P. Subsecond-Resolved Molecular Measurements Using Electrochemical Phase Interrogation of Aptamer-Based Sensors. *Anal. Chem.* **2020**, *92* (20), 14063–14068. https://doi.org/10.1021/acs.analchem.0c03109.

(103) Miranda-Castro, R.; de-los-Santos-Álvarez, P.; Lobo-Castañón, M. J.; Miranda-Ordieres, A. J. Hairpin-DNA Probe for Enzyme-Amplified Electrochemical Detection of Legionella Pneumophila. *Anal. Chem.* **2007**, *79* (11), 4050–4055. https://doi.org/10.1021/ac062260q.

(104) Liu, G.; Wan, Y.; Gau, V.; Zhang, J.; Wang, L.; Song, S.; Fan, C. An Enzyme-Based E-DNA Sensor for Sequence-Specific Detection of Femtomolar DNA Targets. *J. Am. Chem. Soc.* **2008**, *130* (21), 6820–6825. https://doi.org/10.1021/ja800554t.

(105) Hong, G.; Liu, Y.; Chen, W.; Weng, S.; Liu, Q.; Liu, A.; Zheng, D.; Lin, X. A Sandwich-Type DNA Electrochemical Biosensor for Hairpin-Stem-Loop Structure Based on Multistep

Temperature-Controlling Method. *Int. J. Nanomedicine* **2012**, *7*, 4953–4960. https://doi.org/10.2147/IJN.S35177.

(106) Hsieh, K.; Xiao, Y.; Tom Soh, H. Electrochemical DNA Detection via Exonuclease and Target-Catalyzed Transformation of Surface-Bound Probes. *Langmuir* **2010**, *26* (12), 10392–10396. https://doi.org/10.1021/la100227s.

(107) Liu, Z.; Zhang, W.; Zhu, S.; Zhang, L.; Hu, L.; Parveen, S.; Xu, G. Ultrasensitive Signal-on DNA Biosensor Based on Nicking Endonuclease Assisted Electrochemistry Signal Amplification. *Biosens. Bioelectron.* **2011**, *29* (1), 215–218. https://doi.org/https://doi.org/10.1016/j.bios.2011.07.076.

(108) Wang, K.; Lei, Y.; Zhong, G.-X.; Zheng, Y.-J.; Sun, Z.-L.; Peng, H.-P.; Chen, W.; Liu, A.-L.; Chen, Y.-Z.; Lin, X.-H. Dual-Probe Electrochemical DNA Biosensor Based on the "Y" Junction Structure and Restriction Endonuclease Assisted Cyclic Enzymatic Amplification for Detection of Double-Strand DNA of PML/RARα Related Fusion Gene. *Biosens. Bioelectron.* **2015**, *71*, 463–469. https://doi.org/https://doi.org/10.1016/j.bios.2015.04.071.

(109) Chen, Z.; Liu, X.; Liu, D.; Li, F.; Wang, L.; Liu, S. Ultrasensitive Electrochemical DNA Biosensor Fabrication by Coupling an Integral Multifunctional Zirconia-Reduced Graphene Oxide-Thionine Nanocomposite and Exonuclease I-Assisted Cleavage. *Front. Chem.* **2020**, *8*. https://doi.org/10.3389/fchem.2020.00521.

(110) Zhou, H.; Duan, S.; Huang, J.; He, F. An Ultrasensitive Electrochemical Biosensor for Pseudomonas Aeruginosa Assay Based on a Rolling Circle Amplification-Assisted Multipedal DNA Walker. *Chem. Commun.* **2020**, *56* (46), 6273–6276. https://doi.org/10.1039/D0CC01619E.

(111) Qing, M.; Chen, S. L.; Sun, Z.; Fan, Y.; Luo, H. Q.; Li, N. B. Universal and Programmable Rolling Circle Amplification-CRISPR/Cas12a-Mediated Immobilization-Free Electrochemical Biosensor. *Anal. Chem.* **2021**, *93* (20), 7499–7507. https://doi.org/10.1021/acs.analchem.1c00805.

(112) Sun, W.; Qin, P.; Gao, H.; Li, G.; Jiao, K. Electrochemical DNA Biosensor Based on Chitosan/Nano-V2O5/MWCNTs Composite Film Modified Carbon Ionic Liquid Electrode and Its Application to the LAMP Product of Yersinia Enterocolitica Gene Sequence. *Biosens. Bioelectron.* **2010**, *25* (6), 1264–1270. https://doi.org/https://doi.org/10.1016/j.bios.2009.10.011.

(113) Liew, P. S.; Lertanantawong, B.; Lee, S. Y.; Manickam, R.; Lee, Y. H.; Surareungchai, W. Electrochemical Genosensor Assay Using Lyophilized Gold Nanoparticles/Latex Microsphere Label for Detection of Vibrio Cholerae. *Talanta* **2015**, *139*, 167–173. https://doi.org/https://doi.org/10.1016/j.talanta.2015.02.054.

(114) del Río, J. S.; Lobato, I. M.; Mayboroda, O.; Katakis, I.; O'Sullivan, C. K. Enhanced Solid-Phase Recombinase Polymerase Amplification and Electrochemical Detection. *Anal. Bioanal. Chem.* **2017**, *409* (12), 3261–3269. https://doi.org/10.1007/s00216-017-0269-y.

(115) Sánchez-Salcedo, R.; Miranda-Castro, R.; de los Santos-Álvarez, N.; Lobo-Castañón, M. J. On-Gold Recombinase Polymerase Primer Elongation for Electrochemical Detection of Bacterial Genome: Mechanism Insights and Influencing Factors. *ChemElectroChem*

2019, *6* (3), 793–800. https://doi.org/https://doi.org/10.1002/celc.201801208.

(116) Liu, J.; Zhang, Y.; Xie, H.; Zhao, L.; Zheng, L.; Ye, H. Applications of Catalytic Hairpin Assembly Reaction in Biosensing. *Small* **2019**, *15* (42), 1902989. https://doi.org/https://doi.org/10.1002/smll.201902989.

(117) Gao, Q.; Zhang, W.; Guo, Y.; Qi, H.; Zhang, C. Highly Sensitive Impedimetric Sensing of DNA Hybridization Based on the Target DNA-Induced Displacement of Gold Nanoparticles Attached to SsDNA Probe. *Electrochem. commun.* **2011**, *13* (4), 335–337. https://doi.org/https://doi.org/10.1016/j.elecom.2011.01.018.

(118) Yang, Y.; Li, C.; Yin, L.; Liu, M.; Wang, Z.; Shu, Y.; Li, G. Enhanced Charge Transfer by Gold Nanoparticle at DNA Modified Electrode and Its Application to Label-Free DNA Detection. *ACS Appl. Mater. Interfaces* **2014**, *6* (10), 7579–7584. https://doi.org/10.1021/am500912m.

(119) Han, S.; Liu, W.; Zheng, M.; Wang, R. Label-Free and Ultrasensitive Electrochemical DNA Biosensor Based on Urchinlike Carbon Nanotube-Gold Nanoparticle Nanoclusters. *Anal. Chem.* **2020**, *92* (7), 4780–4787. https://doi.org/10.1021/acs.analchem.9b03520.

(120) Andoy, N. M.; Filipiak, M. S.; Vetter, D.; Gutiérrez-Sanz, Ó.; Tarasov, A. Graphene-Based Electronic Immunosensor with Femtomolar Detection Limit in Whole Serum. *Adv. Mater. Technol.* **2018**, *3* (12), 1800186. https://doi.org/https://doi.org/10.1002/admt.201800186.

(121) Hwang, M. T.; Heiranian, M.; Kim, Y.; You, S.; Leem, J.; Taqieddin, A.; Faramarzi, V.; Jing, Y.; Park, I.; van der Zande, A. M.; Nam, S.; Aluru, N. R.; Bashir, R. Ultrasensitive Detection of Nucleic Acids Using Deformed Graphene Channel Field Effect Biosensors. *Nat. Commun.* **2020**, *11* (1), 1543. https://doi.org/10.1038/s41467-020-15330-9.

(122) Hauke, A.; Kumar, L. S. S.; Kim, M. Y.; Pegan, J.; Khine, M.; Li, H.; Plaxco, K. W.; Heikenfeld, J. Superwetting and Aptamer Functionalized Shrink-Induced High Surface Area Electrochemical Sensors. *Biosens. Bioelectron.* **2017**, *94*, 438–442. https://doi.org/https://doi.org/10.1016/j.bios.2017.03.024.

(123) Li, S.; Lin, L.; Chang, X.; Si, Z.; Plaxco, K. W.; Khine, M.; Li, H.; Xia, F. A Wrinkled Structure of Gold Film Greatly Improves the Signaling of Electrochemical Aptamer-Based Biosensors. *RSC Adv.* **2021**, *11* (2), 671–677. https://doi.org/10.1039/D0RA09174J.

(124) Movilli, J.; Kolkman, R. W.; Rozzi, A.; Corradini, R.; Segerink, L. I.; Huskens, J. Increasing the Sensitivity of Electrochemical DNA Detection by a Micropillar-Structured Biosensing Surface. *Langmuir* **2020**, *36* (16), 4272–4279. https://doi.org/10.1021/acs.langmuir.0c00144.

(125) Quan Li, P.; Piper, A.; Schmueser, I.; Mount, A. R.; Corrigan, D. K. Impedimetric Measurement of DNA–DNA Hybridisation Using Microelectrodes with Different Radii for Detection of Methicillin Resistant Staphylococcus Aureus (MRSA). *Analyst* **2017**, *142* (11), 1946–1952. https://doi.org/10.1039/C7AN00436B.

(126) Blair, E. O.; Hannah, S.; Vezza, V.; Avcı, H.; Kocagoz, T.; Hoskisson, P. A.; Güzel, F. D.; Corrigan, D. K. Biologically Modified Microelectrode Sensors Provide Enhanced Sensitivity for Detection of Nucleic Acid Sequences from Mycobacterium Tuberculosis. *Sensors and Actuators Reports* **2020**, *2* (1), 100008.

https://doi.org/https://doi.org/10.1016/j.snr.2020.100008.

(127) Zhurauski, P.; Arya, S. K.; Jolly, P.; Tiede, C.; Tomlinson, D. C.; Ko Ferrigno, P.; Estrela, P. Sensitive and Selective Affimer-Functionalised Interdigitated Electrode-Based Capacitive Biosensor for Her4 Protein Tumour Biomarker Detection. *Biosens. Bioelectron.* **2018**, *108*, 1–8. https://doi.org/https://doi.org/10.1016/j.bios.2018.02.041.

(128) Madhanagopal, B. R.; Zhang, S.; Demirel, E.; Wady, H.; Chandrasekaran, A. R. DNA Nanocarriers: Programmed to Deliver. *Trends Biochem. Sci.* **2018**, *43* (12), 997–1013. https://doi.org/https://doi.org/10.1016/j.tibs.2018.09.010.

(129) Xia, Z.; Wang, P.; Liu, X.; Liu, T.; Yan, Y.; Yan, J.; Zhong, J.; Sun, G.; He, D. Tumor-Penetrating Peptide-Modified DNA Tetrahedron for Targeting Drug Delivery. *Biochemistry* **2016**, *55* (9), 1326–1331. https://doi.org/10.1021/acs.biochem.5b01181.

(130) Setyawati, M. I.; Kutty, R. V.; Leong, D. T. DNA Nanostructures Carrying Stoichiometrically Definable Antibodies. *Small* **2016**, *12* (40), 5601–5611. https://doi.org/https://doi.org/10.1002/smll.201601669.

(131) Pei, H.; Lu, N.; Wen, Y.; Song, S.; Liu, Y.; Yan, H.; Fan, C. A DNA Nanostructure-Based Biomolecular Probe Carrier Platform for Electrochemical Biosensing. *Adv. Mater.* **2010**, *22* (42), 4754–4758. https://doi.org/10.1002/adma.201002767.

(132) Li, S.; Tian, T.; Zhang, T.; Cai, X.; Lin, Y. Advances in Biological Applications of Self-Assembled DNA Tetrahedral Nanostructures. *Mater. Today* **2018**. https://doi.org/10.1016/J.MATTOD.2018.08.002.

(133) Wu, N.; Chen, F.; Zhao, Y.; Yu, X.; Wei, J.; Zhao, Y. Functional and Biomimetic DNA Nanostructures on Lipid Membranes. *Langmuir* **2018**, *34* (49), 14721–14730. https://doi.org/10.1021/acs.langmuir.8b01818.

(134) Shen, H.; Wang, Y.; Wang, J.; Li, Z.; Yuan, Q. Emerging Biomimetic Applications of DNA Nanotechnology. *ACS Appl. Mater. Interfaces* **2019**, *11* (15), 13859–13873. https://doi.org/10.1021/acsami.8b06175.

(135) Sethi, S.; Sugiyama, H.; Endo, M. Biomimetic DNA Nanotechnology to Understand and Control Cellular Responses. *ChemBioChem* **2022**, *23* (6), e202100446. https://doi.org/https://doi.org/10.1002/cbic.202100446.

(136) Rangnekar, A.; LaBean, T. H. Building DNA Nanostructures for Molecular Computation, Templated Assembly, and Biological Applications. *Acc. Chem. Res.* **2014**, *47* (6), 1778–1788. https://doi.org/10.1021/ar500023b.

(137) Zhang, C.; Zhao, Y.; Xu, X.; Xu, R.; Li, H.; Teng, X.; Du, Y.; Miao, Y.; Lin, H.; Han, D. Cancer Diagnosis with DNA Molecular Computation. *Nat. Nanotechnol.* **2020**, *15* (8), 709–715. https://doi.org/10.1038/s41565-020-0699-0.

(138) Seeman, N. C. Structural DNA Nanotechnology: An Overview. *Methods Mol. Biol.* **2005**, *303*, 143–166. https://doi.org/10.1385/1-59259-901-X:143.

(139) Seeman, N. C.; Sleiman, H. F. DNA Nanotechnology. *Nat. Rev. Mater.* **2017**, *3* (1), 17068. https://doi.org/10.1038/natrevmats.2017.68.

(140) Cohen, S. N.; Chang, A. C. Y.; Boyer, H. W.; Helling, R. B. Construction of Biologically Functional Bacterial Plasmids In Vitro. *Proc. Natl. Acad. Sci. U. S. A.* **1973**, *70* (11), 3240–3244.

(141) Matos, J.; West, S. C. Holliday Junction Resolution: Regulation in Space and Time. *DNA Repair (Amst).* **2014**, *19*, 176–181. https://doi.org/https://doi.org/10.1016/j.dnarep.2014.03.013.

(142) Seeman, N. C. Nucleic Acid Junctions and Lattices. *J. Theor. Biol.* **1982**, *99* (2), 237–247. https://doi.org/https://doi.org/10.1016/0022-5193(82)90002-9.

(143) Wang, Y.; Mueller, J. E.; Kemper, B.; Seeman, N. C. Assembly and Characterization of Five-Arm and Six-Arm DNA Branched Junctions. *Biochemistry* **1991**, *30* (23), 5667–5674. https://doi.org/10.1021/bi00237a005.

(144) Kadrmas, J. L.; Ravin, A. J.; Leontis, N. B. Relative Stabilities of DNA Three-Way, Four-Way and Five-Way Junctions (Multi-Helix Junction Loops): Unpaired Nucleotides Can Be Stabilizing or Destabilizing. *Nucleic Acids Res.* **1995**, *23* (12), 2212–2222.

(145) Chen, J.; Seeman, N. C. Synthesis from DNA of a Molecule with the Connectivity of a Cube. *Nature* **1991**, *350* (6319), 631–633. https://doi.org/10.1038/350631a0.

(146) Chen, J.; Seeman, N. C. The Electrophoretic Properties of a DNA Cube and Its Substructure Catenanes. *Electrophoresis* **1991**, *12* (9), 607–611. https://doi.org/https://doi.org/10.1002/elps.1150120902.

(147) Zhang, Y.; Seeman, N. C. Construction of a DNA-Truncated Octahedron. *J. Am. Chem. Soc.* **1994**, *116* (5), 1661–1669. https://doi.org/10.1021/ja00084a006.

(148) Rothemund, P. W. K. Folding DNA to Create Nanoscale Shapes and Patterns. *Nature* **2006**, *440*, 297.

(149) Shih, W. M.; Quispe, J. D.; Joyce, G. F. A 1.7-Kilobase Single-Stranded DNA That Folds into a Nanoscale Octahedron. *Nature* **2004**, *427* (6975), 618–621.

(150) Goodman, R. P.; Schaap, I. A. T.; Tardin, C. F.; Erben, C. M.; Berry, R. M.; Schmidt, C. F.; Turberfield, A. J. Rapid Chiral Assembly of Rigid DNA Building Blocks for Molecular Nanofabrication. *Science (80-.).* **2005**, *310* (5754), 1661.

(151) Aldaye, F. A.; Sleiman, H. F. Modular Access to Structurally Switchable 3D Discrete DNA Assemblies. *J. Am. Chem. Soc.* **2007**, *129* (44), 13376–13377. https://doi.org/10.1021/ja075966q.

(152) He, Y.; Ye, T.; Su, M.; Zhang, C.; Ribbe, A. E.; Jiang, W.; Mao, C. Hierarchical Self-Assembly of DNA into Symmetric Supramolecular Polyhedra. *Nature* **2008**, *452* (7184), 198–201. https://doi.org/10.1038/nature06597.

(153) He, Y.; Chen, Y.; Liu, H.; Ribbe, A. E.; Mao, C. Self-Assembly of Hexagonal DNA Two-Dimensional (2D) Arrays. *J. Am. Chem. Soc.* **2005**, *127* (35), 12202–12203. https://doi.org/10.1021/ja0541938.

(154) He, Y.; Mao, C. Balancing Flexibility and Stress in DNA Nanostructures. *Chem. Commun.* **2006**, No. 9, 968–969. https://doi.org/10.1039/B513962G.

(155) Scheckenbach, M.; Bauer, J.; Zähringer, J.; Selbach, F.; Tinnefeld, P. DNA Origami

Nanorulers and Emerging Reference Structures. *APL Mater.* **2020**, *8* (11). https://doi.org/10.1063/5.0022885.

(156) Keller, A.; Linko, V. Challenges and Perspectives of DNA Nanostructures in Biomedicine. *Angew. Chemie Int. Ed.* **2020**, *59* (37), 15818–15833. https://doi.org/https://doi.org/10.1002/anie.201916390.

(157) Diggans, J.; Leproust, E. Next Steps for Access to Safe, Secure DNA Synthesis. *Front. Bioeng. Biotechnol.* **2019**, *7*.

(158) Goodman, R. P.; Schaap, I. A. T.; Tardin, C. F.; Erben, C. M.; Berry, R. M.; Schmidt, C. F.; Turberfield, A. J. Rapid Chiral Assembly of Rigid DNA Building Blocks for Molecular Nanofabrication. *Science (80-.).* **2005**, *310* (5754), 1661–1665. https://doi.org/10.1126/science.1120367.

(159) Goodman, R. P.; Berry, R. M.; Turberfield, A. J. The Single-Step Synthesis of a DNA Tetrahedron. *Chem. Commun.* **2004**, No. 12, 1372–1373. https://doi.org/10.1039/B402293A.

(160) Keum, J.-W.; Bermudez, H. Enhanced Resistance of DNAnanostructures to Enzymatic Digestion. *Chem. Commun.* **2009**, No. 45, 7036–7038. https://doi.org/10.1039/B917661F.

(161) Halford, S. E.; Marko, J. F. How Do Site-specific DNA-binding Proteins Find Their Targets? *Nucleic Acids Res.* **2004**, *32* (10), 3040–3052. https://doi.org/10.1093/nar/gkh624.

(162) Hogan, M. E.; Roberson, M. W.; Austin, R. H. DNA Flexibility Variation May Dominate DNase I Cleavage. *Proc. Natl. Acad. Sci.* **1989**, *86* (23), 9273. https://doi.org/10.1073/pnas.86.23.9273.

(163) Brukner, I.; Sánchez, R.; Suck, D.; Pongor, S. Sequence-Dependent Bending Propensity of DNA as Revealed by DNase I: Parameters for Trinucleotides. *EMBO J.* **1995**, *14* (8), 1812–1818. https://doi.org/https://doi.org/10.1002/j.1460-2075.1995.tb07169.x.

(164) Pingoud, A.; Jeltsch, A. Structure and Function of Type II Restriction Endonucleases. *Nucleic Acids Res.* **2001**, *29* (18), 3705–3727. https://doi.org/10.1093/nar/29.18.3705.

(165) Rivetti, C.; Guthold, M.; Bustamante, C. Scanning Force Microscopy of DNA Deposited onto Mica: EquilibrationversusKinetic Trapping Studied by Statistical Polymer Chain Analysis. *J. Mol. Biol.* **1996**, *264* (5), 919–932. https://doi.org/https://doi.org/10.1006/jmbi.1996.0687.

(166) Manning, G. S. The Persistence Length of DNA Is Reached from the Persistence Length of Its Null Isomer through an Internal Electrostatic Stretching Force. *Biophys. J.* **2006**, *91* (10), 3607–3616. https://doi.org/10.1529/biophysj.106.089029.

(167) Mantelli, S.; Muller, P.; Harlepp, S.; Maaloum, M. Conformational Analysis and Estimation of the Persistence Length of DNA Using Atomic Force Microscopy in Solution. *Soft Matter* **2011**, *7* (7), 3412–3416. https://doi.org/10.1039/C0SM01160F.

(168) Roth, E.; Glick Azaria, A.; Girshevitz, O.; Bitler, A.; Garini, Y. Measuring the Conformation and Persistence Length of Single-Stranded DNA Using a DNA Origami Structure. *Nano Lett.* **2018**, *18* (11), 6703–6709. https://doi.org/10.1021/acs.nanolett.8b02093.

(169) Walsh, A. S.; Yin, H.; Erben, C. M.; Wood, M. J. A.; Turberfield, A. J. DNA Cage Delivery to Mammalian Cells. *ACS Nano* **2011**, *5* (7), 5427–5432. https://doi.org/10.1021/nn2005574.

(170) Li, J.; Pei, H.; Zhu, B.; Liang, L.; Wei, M.; He, Y.; Chen, N.; Li, D.; Huang, Q.; Fan, C. Self-Assembled Multivalent DNA Nanostructures for Noninvasive Intracellular Delivery of Immunostimulatory CpG Oligonucleotides. *ACS Nano* **2011**, *5* (11), 8783–8789. https://doi.org/10.1021/nn202774x.

(171) Kim, K.-R.; Kim, D.-R.; Lee, T.; Yhee, J. Y.; Kim, B.-S.; Kwon, I. C.; Ahn, D.-R. Drug Delivery by a Self-Assembled DNA Tetrahedron for Overcoming Drug Resistance in Breast Cancer Cells. *Chem. Commun.* **2013**, *49* (20), 2010–2012. https://doi.org/10.1039/C3CC38693G.

(172) Lee, H.; Lytton-Jean, A. K. R.; Chen, Y.; Love, K. T.; Park, A. I.; Karagiannis, E. D.; Sehgal, A.; Querbes, W.; Zurenko, C. S.; Jayaraman, M.; Peng, C. G.; Charisse, K.; Borodovsky, A.; Manoharan, M.; Donahoe, J. S.; Truelove, J.; Nahrendorf, M.; Langer, R.; Anderson, D. G. Molecularly Self-Assembled Nucleic Acid Nanoparticles for Targeted in Vivo SiRNA Delivery. *Nat. Nanotechnol.* **2012**, *7* (6), 389–393. https://doi.org/10.1038/nnano.2012.73.

(173) Kim, K.-R.; Bang, D.; Ahn, D.-R. Nano-Formulation of a Photosensitizer Using a DNA Tetrahedron and Its Potential for in Vivo Photodynamic Therapy. *Biomater. Sci.* **2016**, *4* (4), 605–609. https://doi.org/10.1039/C5BM00467E.

(174) Chen, N.; Qin, S.; Yang, X.; Wang, Q.; Huang, J.; Wang, K. "Sense-and-Treat" DNA Nanodevice for Synergetic Destruction of Circulating Tumor Cells. *ACS Appl. Mater. Interfaces* **2016**, *8* (40), 26552–26558. https://doi.org/10.1021/acsami.6b08695.

(175) Xue, H.; Ding, F.; Zhang, J.; Guo, Y.; Gao, X.; Feng, J.; Zhu, X.; Zhang, C. DNA Tetrahedron-Based Nanogels for SiRNA Delivery and Gene Silencing. *Chem. Commun.* **2019**, *55* (29), 4222–4225. https://doi.org/10.1039/C9CC00175A.

(176) Zhang, T.; Tian, T.; Zhou, R.; Li, S.; Ma, W.; Zhang, Y.; Liu, N.; Shi, S.; Li, Q.; Xie, X.; Ge, Y.; Liu, M.; Zhang, Q.; Lin, S.; Cai, X.; Lin, Y. Design, Fabrication and Applications of Tetrahedral DNA Nanostructure-Based Multifunctional Complexes in Drug Delivery and Biomedical Treatment. *Nat. Protoc.* **2020**, *15* (8), 2728–2757. https://doi.org/10.1038/s41596-020-0355-z.

(177) Pei, H.; Lu, N.; Wen, Y.; Song, S.; Liu, Y.; Yan, H.; Fan, C. A DNA Nanostructure-Based Biomolecular Probe Carrier Platform for Electrochemical Biosensing. *Adv. Mater.* **2010**, *22* (42), 4754–4758. https://doi.org/10.1002/adma.201002767.

(178) Wen, Y.; Pei, H.; Wan, Y.; Su, Y.; Huang, Q.; Song, S.; Fan, C. DNA Nanostructure-Decorated Surfaces for Enhanced Aptamer-Target Binding and Electrochemical Cocaine Sensors. *Anal. Chem.* **2011**, *83* (19), 7418–7423. https://doi.org/10.1021/ac201491p.

(179) Wang, S.; Zhang, L.; Wan, S.; Cansiz, S.; Cui, C.; Liu, Y.; Cai, R.; Hong, C.; Teng, I.-T.; Shi, M.; Wu, Y.; Dong, Y.; Tan, W. Aptasensor with Expanded Nucleotide Using DNA Nanotetrahedra for Electrochemical Detection of Cancerous Exosomes. *ACS Nano* **2017**, *11* (4), 3943–3949. https://doi.org/10.1021/acsnano.7b00373.

(180) Ge, Z.; Lin, M.; Wang, P.; Pei, H.; Yan, J.; Shi, J.; Huang, Q.; He, D.; Fan, C.; Zuo, X.

Hybridization Chain Reaction Amplification of MicroRNA Detection with a Tetrahedral DNA Nanostructure-Based Electrochemical Biosensor. *Anal. Chem.* **2014**, *86* (4), 2124–2130. https://doi.org/10.1021/ac4037262.

(181) Chen, X.; Huang, J.; Zhang, S.; Mo, F.; Su, S.; Li, Y.; Fang, L.; Deng, J.; Huang, H.; Luo, Z.; Zheng, J. Electrochemical Biosensor for DNA Methylation Detection through Hybridization Chain-Amplified Reaction Coupled with a Tetrahedral DNA Nanostructure. *ACS Appl. Mater. Interfaces* **2019**, *11* (4), 3745–3752. https://doi.org/10.1021/acsami.8b20144.

(182) Lu, J.; Wang, J.; Hu, X.; Gyimah, E.; Yakubu, S.; Wang, K.; Wu, X.; Zhang, Z. Electrochemical Biosensor Based on Tetrahedral DNA Nanostructures and G-Quadruplex–Hemin Conformation for the Ultrasensitive Detection of MicroRNA-21 in Serum. *Anal. Chem.* **2019**, *91* (11), 7353–7359. https://doi.org/10.1021/acs.analchem.9b01133.

(183) Zeng, D.; Wang, Z.; Meng, Z.; Wang, P.; San, L.; Wang, W.; Aldalbahi, A.; Li, L.; Shen, J.; Mi, X. DNA Tetrahedral Nanostructure-Based Electrochemical MiRNA Biosensor for Simultaneous Detection of Multiple MiRNAs in Pancreatic Carcinoma. *ACS Appl. Mater. Interfaces* **2017**, *9* (28), 24118–24125. https://doi.org/10.1021/acsami.7b05981.

(184) Liu, S.; Su, W.; Li, Z.; Ding, X. Electrochemical Detection of Lung Cancer Specific MicroRNAs Using 3D DNA Origami Nanostructures. *Biosens. Bioelectron.* **2015**, *71*, 57–61. https://doi.org/10.1016/J.BIOS.2015.04.006.

(185) Wang, X.; Niu, S.; Wei, M.; Liu, S.; Liu, R.; Shi, C.; Ma, C. Ultrasensitive Electrochemical DNA Biosensor Based on a Tetrahedral Structure and Proximity-Dependent Surface Hybridization. *Analyst* **2020**, *145* (1), 150–156. https://doi.org/10.1039/C9AN01897B.

(186) Zeng, D.; Zhang, H.; Zhu, D.; Li, J.; San, L.; Wang, Z.; Wang, C.; Wang, Y.; Wang, L.; Zuo, X.; Mi, X. A Novel Ultrasensitive Electrochemical DNA Sensor Based on Double Tetrahedral Nanostructures. *Biosens. Bioelectron.* **2015**, *71*, 434–438. https://doi.org/10.1016/J.BIOS.2015.04.065.

(187) Seeman, N. C. Nucleic Acid Junctions and Lattices. *J. Theor. Biol.* **1982**, *99* (2), 237–247. https://doi.org/http://dx.doi.org/10.1016/0022-5193(82)90002-9.

(188) Rothemund, P. W. K. Folding DNA to Create Nanoscale Shapes and Patterns. *Nature* **2006**, *440* (7082). https://doi.org/10.1038/nature04586.

(189) Douglas, S. M.; Dietz, H.; Liedl, T.; Högberg, B.; Graf, F.; Shih, W. M. Self-Assembly of DNA into Nanoscale Three-Dimensional Shapes. *Nature* **2009**, *459* (7245), 414–418. https://doi.org/10.1038/nature08016.

(190) Douglas, S. M.; Marblestone, A. H.; Teerapittayanon, S.; Vazquez, A.; Church, G. M.; Shih, W. M. Rapid Prototyping of 3D DNA-Origami Shapes with CaDNAno. *Nucleic Acids Res.* **2009**, *37* (15), 5001–5006. https://doi.org/10.1093/nar/gkp436.

(191) Majikes, J.; Liddle, J. DNA Origami Design: A How-To Tutorial. Journal of Research (NIST JRES), National Institute of Standards and Technology, Gaithersburg, MD 2021. https://doi.org/https://doi.org/10.6028/jres.126.001.

(192) Dey, S.; Fan, C.; Gothelf, K. V; Li, J.; Lin, C.; Liu, L.; Liu, N.; Nijenhuis, M. A. D.; Saccà, B.;

Simmel, F. C.; Yan, H.; Zhan, P. DNA Origami. *Nat. Rev. Methods Prim.* **2021**, *1* (1), 13. https://doi.org/10.1038/s43586-020-00009-8.

(193) Linko, V.; Nummelin, S.; Aarnos, L.; Tapio, K.; Toppari, J. J.; Kostiainen, M. A. DNA-Based Enzyme Reactors and Systems. *Nanomaterials* . 2016. https://doi.org/10.3390/nano6080139.

(194) Gothelf, K. V. Chemical Modifications and Reactions in DNA Nanostructures. *MRS Bull.* **2017**, *42* (12), 897–903. https://doi.org/DOI: 10.1557/mrs.2017.276.

(195) Grossi, G.; Jaekel, A.; Andersen, E. S.; Saccà, B. Enzyme-Functionalized DNA Nanostructures as Tools for Organizing and Controlling Enzymatic Reactions. *MRS Bull.* **2017**, *42* (12), 920–924. https://doi.org/DOI: 10.1557/mrs.2017.269.

(196) Kuzyk, A.; Schreiber, R.; Fan, Z.; Pardatscher, G.; Roller, E.-M.; Högele, A.; Simmel, F. C.; Govorov, A. O.; Liedl, T. DNA-Based Self-Assembly of Chiral Plasmonic Nanostructures with Tailored Optical Response. *Nature* **2012**, *483* (7389), 311–314. https://doi.org/10.1038/nature10889.

(197) Boxuan, S.; Veikko, L.; Kosti, T.; Siim, P.; Tibebe, L.; Ashwin, G.; V, G. K.; A, K. M.; Jussi, T. J. Plasmonic Nanostructures through DNA-Assisted Lithography. *Sci. Adv.* **2022**, *4* (2), eaap8978. https://doi.org/10.1126/sciadv.aap8978.

(198) Graugnard, E.; Hughes, W. L.; Jungmann, R.; Kostiainen, M. A.; Linko, V. Nanometrology and Super-Resolution Imaging with DNA. *MRS Bull.* **2017**, *42* (12), 951–959. https://doi.org/DOI: 10.1557/mrs.2017.274.

(199) Andersen, E. S.; Dong, M.; Nielsen, M. M.; Jahn, K.; Subramani, R.; Mamdouh, W.; Golas, M. M.; Sander, B.; Stark, H.; Oliveira, C. L. P.; Pedersen, J. S.; Birkedal, V.; Besenbacher, F.; Gothelf, K. V; Kjems, J. Self-Assembly of a Nanoscale DNA Box with a Controllable Lid. *Nature* **2009**, *459* (7243), 73–76. https://doi.org/10.1038/nature07971.

(200) Tomaru, T.; Suzuki, Y.; Kawamata, I.; Nomura, S. M.; Murata, S. Stepping Operation of a Rotary DNA Origami Device. *Chem. Commun.* **2017**, *53* (55), 7716–7719. https://doi.org/10.1039/C7CC03214E.

(201) Choi, Y.; Choi, H.; Lee, A. C.; Lee, H.; Kwon, S. A Reconfigurable DNA Accordion Rack. *Angew. Chemie Int. Ed.* **2018**, *57* (11), 2811–2815. https://doi.org/https://doi.org/10.1002/anie.201709362.

(202) Kuzuya, A.; Sakai, Y.; Yamazaki, T.; Xu, Y.; Komiyama, M. Nanomechanical DNA Origami "single-Molecule Beacons" Directly Imaged by Atomic Force Microscopy. *Nat. Commun.* **2011**, *2* (1), 449. https://doi.org/10.1038/ncomms1452.

(203) Derr, N. D.; Goodman, B. S.; Jungmann, R.; Leschziner, A. E.; Shih, W. M.; Reck-Peterson, S. L. Tug-of-War in Motor Protein Ensembles Revealed with a Programmable DNA Origami Scaffold. *Science (80-.).* **2012**, *338* (6107), 662–665. https://doi.org/10.1126/science.1226734.

(204) Chen, H.; Zhang, H.; Pan, J.; Cha, T.-G.; Li, S.; Andréasson, J.; Choi, J. H. Dynamic and Progressive Control of DNA Origami Conformation by Modulating DNA Helicity with Chemical Adducts. *ACS Nano* **2016**, *10* (5), 4989–4996.

https://doi.org/10.1021/acsnano.6b01339.

(205) Yang, Y.; Endo, M.; Hidaka, K.; Sugiyama, H. Photo-Controllable DNA Origami Nanostructures Assembling into Predesigned Multiorientational Patterns. *J. Am. Chem. Soc.* **2012**, *134* (51), 20645–20653. https://doi.org/10.1021/ja307785r.

(206) Kohman, R. E.; Han, X. Light Sensitization of DNA Nanostructures via Incorporation of Photo-Cleavable Spacers. *Chem. Commun.* **2015**, *51* (26), 5747–5750. https://doi.org/10.1039/C5CC00082C.

(207) Jiang, Q.; Liu, Q.; Shi, Y.; Wang, Z.-G.; Zhan, P.; Liu, J.; Liu, C.; Wang, H.; Shi, X.; Zhang, L.; Sun, J.; Ding, B.; Liu, M. Stimulus-Responsive Plasmonic Chiral Signals of Gold Nanorods Organized on DNA Origami. *Nano Lett.* **2017**, *17* (11), 7125–7130. https://doi.org/10.1021/acs.nanolett.7b03946.

(208) Turek, V. A.; Chikkaraddy, R.; Cormier, S.; Stockham, B.; Ding, T.; Keyser, U. F.; Baumberg, J. J. Thermo-Responsive Actuation of a DNA Origami Flexor. *Adv. Funct. Mater.* **2018**, *28* (25), 1706410. https://doi.org/https://doi.org/10.1002/adfm.201706410.

(209) Enzo, K.; Jonathan, L.; Sushi, M.; Florian, R.; C, L. D.; C, S. F. A Self-Assembled Nanoscale Robotic Arm Controlled by Electric Fields. *Science (80-.).* **2018**, *359* (6373), 296–301. https://doi.org/10.1126/science.aao4284.

(210) Krajczewski, J.; Kołątaj, K.; Kudelski, A. Plasmonic Nanoparticles in Chemical Analysis. *RSC Adv.* **2017**, *7* (28), 17559–17576. https://doi.org/10.1039/C7RA01034F.

(211) Shen, B.; Kostiainen, M. A.; Linko, V. DNA Origami Nanophotonics and Plasmonics at Interfaces. *Langmuir* **2018**, *34* (49), 14911–14920. https://doi.org/10.1021/acs.langmuir.8b01843.

(212) Dass, M.; Gür, F. N.; Kołątaj, K.; Urban, M. J.; Liedl, T. DNA Origami-Enabled Plasmonic Sensing. *J. Phys. Chem. C* **2021**, *125* (11), 5969–5981. https://doi.org/10.1021/acs.jpcc.0c11238.

(213) Shaw, A.; Lundin, V.; Petrova, E.; Fördős, F.; Benson, E.; Al-Amin, A.; Herland, A.; Blokzijl, A.; Högberg, B.; Teixeira, A. I. Spatial Control of Membrane Receptor Function Using Ligand Nanocalipers. *Nat. Methods* **2014**, *11* (8), 841–846. https://doi.org/10.1038/nmeth.3025.

(214) Iwaki, M.; Wickham, S. F.; Ikezaki, K.; Yanagida, T.; Shih, W. M. A Programmable DNA Origami Nanospring That Reveals Force-Induced Adjacent Binding of Myosin VI Heads. *Nat. Commun.* **2016**, *7* (1), 13715. https://doi.org/10.1038/ncomms13715.

(215) Grossi, G.; Dalgaard Ebbesen Jepsen, M.; Kjems, J.; Andersen, E. S. Control of Enzyme Reactions by a Reconfigurable DNA Nanovault. *Nat. Commun.* **2017**, *8* (1), 992. https://doi.org/10.1038/s41467-017-01072-8.

(216) Huang, D.; Patel, K.; Perez-Garrido, S.; Marshall, J. F.; Palma, M. DNA Origami Nanoarrays for Multivalent Investigations of Cancer Cell Spreading with Nanoscale Spatial Resolution and Single-Molecule Control. *ACS Nano* **2019**, *13* (1), 728–736. https://doi.org/10.1021/acsnano.8b08010.

(217) Aksel, T.; Yu, Z.; Cheng, Y.; Douglas, S. M. Molecular Goniometers for Single-Particle

Cryo-Electron Microscopy of DNA-Binding Proteins. *Nat. Biotechnol.* **2021**, *39* (3), 378–386. https://doi.org/10.1038/s41587-020-0716-8.

(218) Douglas, S. M.; Bachelet, I.; Church, G. M. A Logic-Gated Nanorobot for Targeted Transport of Molecular Payloads. *Science (80-.).* **2012**, *335* (6070), 831.

(219) Zhang, Q.; Jiang, Q.; Li, N.; Dai, L.; Liu, Q.; Song, L.; Wang, J.; Li, Y.; Tian, J.; Ding, B.; Du, Y. DNA Origami as an In Vivo Drug Delivery Vehicle for Cancer Therapy. *ACS Nano* **2014**, *8* (7), 6633–6643. https://doi.org/10.1021/nn502058j.

(220) Perrault, S. D.; Shih, W. M. Virus-Inspired Membrane Encapsulation of DNA Nanostructures To Achieve In Vivo Stability. *ACS Nano* **2014**, *8* (5), 5132–5140. https://doi.org/10.1021/nn5011914.

(221) Li, S.; Jiang, Q.; Liu, S.; Zhang, Y.; Tian, Y.; Song, C.; Wang, J.; Zou, Y.; Anderson, G. J.; Han, J.-Y.; Chang, Y.; Liu, Y.; Zhang, C.; Chen, L.; Zhou, G.; Nie, G.; Yan, H.; Ding, B.; Zhao, Y. A DNA Nanorobot Functions as a Cancer Therapeutic in Response to a Molecular Trigger in Vivo. *Nat. Biotechnol.* **2018**, *36*, 258.

(222) Chi, Q.; Yang, Z.; Xu, K.; Wang, C.; Liang, H. DNA Nanostructure as an Efficient Drug Delivery Platform for Immunotherapy. *Front. Pharmacol.* **2020**, *10*.

(223) Weiden, J.; Bastings, M. M. C. DNA Origami Nanostructures for Controlled Therapeutic Drug Delivery. *Curr. Opin. Colloid Interface Sci.* **2021**, *52*, 101411. https://doi.org/https://doi.org/10.1016/j.cocis.2020.101411.

(224) Mela, I.; Vallejo-Ramirez, P. P.; Makarchuk, S.; Christie, G.; Bailey, D.; Henderson, R. M.; Sugiyama, H.; Endo, M.; Kaminski, C. F. DNA Nanostructures for Targeted Antimicrobial Delivery. *Angew. Chemie Int. Ed.* **2020**, *59* (31), 12698-127021 I. Mela, P. P. Vallejo-Ramirez, S. Ma. https://doi.org/https://doi.org/10.1002/anie.202002740.

(225) Ijäs, H.; Nummelin, S.; Shen, B.; Kostiainen, M. A.; Linko, V. Dynamic DNA Origami Devices: From Strand-Displacement Reactions to External-Stimuli Responsive Systems. *Int. J. Mol. Sci.* **2018**, *19* (7), 2114. https://doi.org/10.3390/ijms19072114.

(226) Justus, C.; Dong, L.; Yang, L. Acidic Tumor Microenvironment and PH-Sensing G Protein-Coupled Receptors. *Front. Physiol.* **2013**, *4*.

(227) Olivia, G.; Ashley, S.; Ashraf, Z.; Jehangir, C.; M, I. B.; Daaniyah, B.; Santiago, C.-M.; Jeremy, M.; Paul, O.; Aaron, J.; H, N. I.; Jonathan, D.; David, S.; Stefano, P.; Nathalie, B.; R, L. B. Persister Escherichia Coli Cells Have a Lower Intracellular PH than Susceptible Cells but Maintain Their PH in Response to Antibiotic Treatment. *MBio* **2022**, *12* (4), e00909-21. https://doi.org/10.1128/mBio.00909-21.

(228) Hoogsteen, K. The Crystal and Molecular Structure of a Hydrogen-Bonded Complex between 1-Methylthymine and 9-Methyladenine. *Acta Crystallogr.* **1963**, *16* (9), 907–916. https://doi.org/10.1107/S0365110X63002437.

(229) Takahashi, S.; Sugimoto, N. Watson–Crick versus Hoogsteen Base Pairs: Chemical Strategy to Encode and Express Genetic Information in Life. *Acc. Chem. Res.* **2021**, *54* (9), 2110–2120. https://doi.org/10.1021/acs.accounts.0c00734.

(230) Idili, A.; Vallée-Bélisle, A.; Ricci, F. Programmable PH-Triggered DNA Nanoswitches. *J. Am. Chem. Soc.* **2014**, *136* (16), 5836–5839. https://doi.org/10.1021/ja500619w.

(231) Chandrasekaran, A. R.; Rusling, D. A. Triplex-Forming Oligonucleotides: A Third Strand for DNA Nanotechnology. *Nucleic Acids Res.* **2018**, *46* (3), 1021–1037. https://doi.org/10.1093/nar/gkx1230.

(232) Ijäs, H.; Hakaste, I.; Shen, B.; Kostiainen, M. A.; Linko, V. Reconfigurable DNA Origami Nanocapsule for PH-Controlled Encapsulation and Display of Cargo. *ACS Nano* **2019**, *13* (5), 5959–5967. https://doi.org/10.1021/acsnano.9b01857.

(233) Han, S.; Liu, W.; Yang, S.; Wang, R. Facile and Label-Free Electrochemical Biosensors for MicroRNA Detection Based on DNA Origami Nanostructures. *ACS Omega* **2019**, *4* (6), 11025–11031. https://doi.org/10.1021/acsomega.9b01166.

(234) Gu, Q.; Zhang, Y.; Cao, H. H.; Ye, S.; Ye, T. Transfer of Thiolated DNA Staples from DNA Origami Nanostructures to Self-Assembled Monolayer-Passivated Gold Surfaces: Implications for Interfacial Molecular Recognition. *ACS Appl. Nano Mater.* **2021**, *4* (8), 8429–8436. https://doi.org/10.1021/acsanm.1c01685.

(235) Wang, Y.; Wang, D.; Mirkin, M. V. Resistive-Pulse and Rectification Sensing with Glass and Carbon Nanopipettes. *Proc. R. Soc. A Math. Phys. Eng. Sci.* **2017**, *473* (2199), 20160931. https://doi.org/10.1098/rspa.2016.0931.

(236) Raveendran, M.; Lee, A. J.; Sharma, R.; Wälti, C.; Actis, P. Rational Design of DNA Nanostructures for Single Molecule Biosensing. *Nat. Commun.* **2020**, *11* (1), 4384. https://doi.org/10.1038/s41467-020-18132-1.

(237) Pilon, L.; Wang, H.; d'Entremont, A. Recent Advances in Continuum Modeling of Interfacial and Transport Phenomena in Electric Double Layer Capacitors. *J. Electrochem. Soc.* **2015**, *162* (5), A5158–A5178. https://doi.org/10.1149/2.0211505jes.

(238) Allen J. Bard, L. R. F. *Electrochemical Methods: Fundamentals and Applications, 2nd Edition*; Wiley, 2001.

(239) Pensa, E.; Vericat, C.; Grumelli, D.; Salvarezza, R. C.; Park, S. H.; Longo, G. S.; Szleifer, I.; Méndez De Leo, L. P. New Insight into the Electrochemical Desorption of Alkanethiol SAMs on Gold. *Phys. Chem. Chem. Phys.* **2012**, *14* (35), 12355–12367. https://doi.org/10.1039/c2cp41291h.

(240) Hoogvliet, J. C.; Dijksma, M.; Kamp, B.; van Bennekom, W. P. Electrochemical Pretreatment of Polycrystalline Gold Electrodes To Produce a Reproducible Surface Roughness for Self-Assembly: A Study in Phosphate Buffer PH 7.4. *Anal. Chem.* **2000**, *72* (9), 2016–2021. https://doi.org/10.1021/ac991215y.

(241) B, A. H.; G, N. R. C.; Bert, J.; A, van H. P.; M, B. P. W.; M, de L. D.; Bert, de B. Electron Tunneling through Alkanedithiol Self-Assembled Monolayers in Large-Area Molecular Junctions. *Proc. Natl. Acad. Sci.* **2007**, *104* (27), 11161–11166. https://doi.org/10.1073/pnas.0701472104.

(242) Sharma, R.; Deacon, S. E.; Nowak, D.; George, S. E.; Szymonik, M. P.; Tang, A. A. S.; Tomlinson, D. C.; Davies, A. G.; McPherson, M. J.; Wälti, C. Label-Free Electrochemical Impedance Biosensor to Detect Human Interleukin-8 in Serum with Sub-Pg/Ml Sensitivity. *Biosens. Bioelectron.* **2016**, *80*, 607–613. https://doi.org/https://doi.org/10.1016/j.bios.2016.02.028.

(243) Elgrishi, N.; Rountree, K. J.; McCarthy, B. D.; Rountree, E. S.; Eisenhart, T. T.; Dempsey, J. L. A Practical Beginner's Guide to Cyclic Voltammetry. *J. Chem. Educ.* **2018**, *95* (2), 197–206. https://doi.org/10.1021/acs.jchemed.7b00361.

(244) Wang, S.; Zhang, J.; Gharbi, O.; Vivier, V.; Gao, M.; Orazem, M. E. Electrochemical Impedance Spectroscopy. *Nat. Rev. Methods Prim.* **2021**, *1* (1), 41. https://doi.org/10.1038/s43586-021-00039-w.

(245) Zoltowski, P. On the Electrical Capacitance of Interfaces Exhibiting Constant Phase Element Behaviour. *J. Electroanal. Chem.* **1998**, *443* (1), 149–154. https://doi.org/https://doi.org/10.1016/S0022-0728(97)00490-7.

(246) Forster, R. J. Microelectrodes: New Dimensions in Electrochemistry. *Chem. Soc. Rev.* **1994**, *23* (4), 289–297. https://doi.org/10.1039/CS9942300289.

(247) Corrigan, D. K.; Blair, E. O.; Terry, J. G.; Walton, A. J.; Mount, A. R. Enhanced Electroanalysis in Lithium Potassium Eutectic (LKE) Using Microfabricated Square Microelectrodes. *Anal. Chem.* **2014**, *86* (22), 11342–11348. https://doi.org/10.1021/ac5030842.

(248) Corrigan, D. K.; Elliott, J. P.; Blair, E. O.; Reeves, S. J.; Schmüser, I.; Walton, A. J.; Mount, A. R. Advances in Electroanalysis, Sensing and Monitoring in Molten Salts. *Faraday Discuss.* **2016**, *190* (0), 351–366. https://doi.org/10.1039/C6FD00002A.

(249) Corrigan, D. K.; Vezza, V.; Schulze, H.; Bachmann, T. T.; Mount, A. R.; Walton, A. J.; Terry, J. G. A Microelectrode Array with Reproducible Performance Shows Loss of Consistency Following Functionalization with a Self-Assembled 6-Mercapto-1-Hexanol Layer. *Sensors (Basel).* **2018**, *18* (6), 1891. https://doi.org/10.3390/s18061891.

(250) Ma, J.; Chai, W.; Lu, J.; Tian, T.; Wu, S.; Yang, Y.; Yang, J.; Li, C.; Li, G. Coating a DNA Self-Assembled Monolayer with a Metal Organic Framework-Based Exoskeleton for Improved Sensing Performance. *Analyst* **2019**, *144* (11), 3539–3545. https://doi.org/10.1039/C9AN00084D.

(251) Xu, X.; Makaraviciute, A.; Kumar, S.; Wen, C.; Sjödin, M.; Abdurakhmanov, E.; Danielson, U. H.; Nyholm, L.; Zhang, Z. Structural Changes of Mercaptohexanol Self-Assembled Monolayers on Gold and Their Influence on Impedimetric Aptamer Sensors. *Anal. Chem.* **2019**, *91* (22), 14697–14704. https://doi.org/10.1021/acs.analchem.9b03946.

(252) Flynn, N. T.; Tran, T. N. T.; Cima, M. J.; Langer, R. Long-Term Stability of Self-Assembled Monolayers in Biological Media. *Langmuir* **2003**, *19* (26), 10909–10915. https://doi.org/10.1021/la035331e.

(253) Peterson, A. W.; Heaton, R. J.; Georgiadis, R. M. The Effect of Surface Probe Density on DNA Hybridization. *Nucleic Acids Res.* **2001**, *29* (24), 5163–5168. https://doi.org/10.1093/nar/29.24.5163.

(254) Arinaga, K.; Rant, U.; Knežević, J.; Pringsheim, E.; Tornow, M.; Fujita, S.; Abstreiter, G.; Yokoyama, N. Controlling the Surface Density of DNA on Gold by Electrically Induced Desorption. *Biosens. Bioelectron.* **2007**, *23* (3), 326–331. https://doi.org/https://doi.org/10.1016/j.bios.2007.04.012.

(255) Kang, D.; Zuo, X.; Yang, R.; Xia, F.; Plaxco, K. W.; White, R. J. Comparing the Properties of

Electrochemical-Based DNA Sensors Employing Different Redox Tags. *Anal. Chem.* **2009**, *81* (21), 9109–9113. https://doi.org/10.1021/ac901811n.

(256) Li, H.; Arroyo-Currás, N.; Kang, D.; Ricci, F.; Plaxco, K. W. Dual-Reporter Drift Correction To Enhance the Performance of Electrochemical Aptamer-Based Sensors in Whole Blood. *J. Am. Chem. Soc.* **2016**, *138* (49), 15809–15812. https://doi.org/10.1021/jacs.6b08671.

(257) Hassan, R. A.; Heng, L. Y.; Tan, L. L. Novel DNA Biosensor for Direct Determination of Carrageenan. *Sci. Rep.* **2019**, *9* (1), 6379. https://doi.org/10.1038/s41598-019-42757-y.

(258) Fischer, L. M.; Tenje, M.; Heiskanen, A. R.; Masuda, N.; Castillo, J.; Bentien, A.; Émneus, J.; Jakobsen, M. H.; Boisen, A. Gold Cleaning Methods for Electrochemical Detection Applications. *Microelectron. Eng.* **2009**, *86* (4), 1282–1285. https://doi.org/http://dx.doi.org/10.1016/j.mee.2008.11.045.

(259) Electrochemical_methods_2ed_2001_-_Bard_Faulkner.

(260) Lavín, Á.; Vicente, J. de; Holgado, M.; Laguna, M. F.; Casquel, R.; Santamaría, B.; Maigler, M. V.; Hernández, A. L.; Ramírez, Y. On the Determination of Uncertainty and Limit of Detection in Label-Free Biosensors. *Sensors (Basel).* **2018**, *18* (7), 2038. https://doi.org/10.3390/s18072038.

(261) Miller, J.; Miller, J. C. *Statistics and Chemometrics for Analytical Chemistry*, 6th ed.; Pearson Education, 2010.

(262) Alexis, V.-B.; Francesco, R.; W, P. K. Thermodynamic Basis for the Optimization of Binding-Induced Biomolecular Switches and Structure-Switching Biosensors. *Proc. Natl. Acad. Sci.* **2009**, *106* (33), 13802–13807. https://doi.org/10.1073/pnas.0904005106.

(263) Zanut, A.; Rossetti, M.; Marcaccio, M.; Ricci, F.; Paolucci, F.; Porchetta, A.; Valenti, G. DNA-Based Nanoswitches: Insights into Electrochemiluminescence Signal Enhancement. *Anal. Chem.* **2021**, *93* (30), 10397–10402. https://doi.org/10.1021/acs.analchem.1c01683.

(264) Fan, C.; Plaxco, K. W.; Heeger, A. J. Electrochemical Interrogation of Conformational Changes as a Reagentless Method for the Sequence-Specific Detection of DNA. *Proc. Natl. Acad. Sci.* **2003**, *100* (16), 9134. https://doi.org/10.1073/pnas.1633515100.

(265) Zadeh, J. N.; Steenberg, C. D.; Bois, J. S.; Wolfe, B. R.; Pierce, M. B.; Khan, A. R.; Dirks, R. M.; Pierce, N. A. NUPACK: Analysis and Design of Nucleic Acid Systems. *J. Comput. Chem.* **2011**, *32* (1). https://doi.org/10.1002/jcc.21596.

(266) Sykes, K. S.; Oliveira, L. F. L.; Stan, G.; White, R. J. Electrochemical Studies of Cation Condensation-Induced Collapse of Surface-Bound DNA. *Langmuir* **2019**, *35* (40), 12962–12970. https://doi.org/10.1021/acs.langmuir.9b02299.

(267) Ricci, F.; Lai, R. Y.; Plaxco, K. W. Linear, Redox Modified DNA Probes as Electrochemical DNA Sensors. *Chem. Commun.* **2007**, No. 36, 3768–3770. https://doi.org/10.1039/B708882E.

(268) Sosna, M.; Denuault, G.; Pascal, R. W.; Prien, R. D.; Mowlem, M. Development of a Reliable Microelectrode Dissolved Oxygen Sensor. *Sensors Actuators B Chem.* **2007**, *123* (1), 344–351. https://doi.org/https://doi.org/10.1016/j.snb.2006.08.033.

(269) Sheffer, M.; Vivier, V.; Mandler, D. Self-Assembled Monolayers on Au Microelectrodes. *Electrochem. commun.* **2007**, *9* (12), 2827–2832. https://doi.org/https://doi.org/10.1016/j.elecom.2007.10.008.

(270) Miodek, A.; Regan, E. M.; Bhalla, N.; Hopkins, N. A. E.; Goodchild, S. A.; Estrela, P. Optimisation and Characterisation of Anti-Fouling Ternary SAM Layers for Impedance-Based Aptasensors. *Sensors (Basel).* **2015**, *15* (10), 25015–25032. https://doi.org/10.3390/s151025015.

(271) Hintsche, R.; Paeschke, M.; Wollenberger, U.; Schnakenberg, U.; Wagner, B.; Lisec, T. Microelectrode Arrays and Application to Biosensing Devices. *Biosens. Bioelectron.* **1994**, *9* (9), 697–705. https://doi.org/https://doi.org/10.1016/0956-5663(94)80068-5.

(272) Raiber, K.; Terfort, A.; Benndorf, C.; Krings, N.; Strehblow, H.-H. Removal of Self-Assembled Monolayers of Alkanethiolates on Gold by Plasma Cleaning. *Surf. Sci.* **2005**, *595* (1), 56–63. https://doi.org/https://doi.org/10.1016/j.susc.2005.07.038.

(273) Widdascheck, F.; Kothe, M.; Hauke, A. A.; Witte, G. The Effect of Oxygen Plasma Treatment of Gold Electrodes on the Molecular Orientation of CuPc Films. *Appl. Surf. Sci.* **2020**, *507*, 145039. https://doi.org/https://doi.org/10.1016/j.apsusc.2019.145039.

(274) Yeager, E.; Bockris, J. M.; Conway, B. E.; Saranapani, S. *Comprehensive Treatise of Electrochemistry: Vol. 9, Electrodiscs: Experimental Techniques*; 1984; Vol. 9.

(275) Corrigan, D. K.; Schulze, H.; McDermott, R. A.; Schmüser, I.; Henihan, G.; Henry, J. B.; Bachmann, T. T.; Mount, A. R. Improving Electrochemical Biosensor Performance by Understanding the Influence of Target DNA Length on Assay Sensitivity. *J. Electroanal. Chem.* **2014**, *732*, 25–29. https://doi.org/https://doi.org/10.1016/j.jelechem.2014.08.026.

(276) Carter, M. L. J.; Rusling, D. A.; Gurr, S.; Brown, T.; Fox, K. R. Stability of the Different Arms of a DNA Tetrahedron and Its Interaction with a Minor Groove Ligand. *Biophys. Chem.* **2020**, *256*, 106270. https://doi.org/https://doi.org/10.1016/j.bpc.2019.106270.

(277) Lin, M.; Wang, J.; Zhou, G.; Wang, J.; Wu, N.; Lu, J.; Gao, J.; Chen, X.; Shi, J.; Zuo, X.; Fan, C. Programmable Engineering of a Biosensing Interface with Tetrahedral DNA Nanostructures for Ultrasensitive DNA Detection. *Angew. Chemie Int. Ed.* **2015**, *54* (7), 2151–2155. https://doi.org/https://doi.org/10.1002/anie.201410720.

(278) Xiao, Y.; Lubin, A. A.; Baker, B. R.; Plaxco, K. W.; Heeger, A. J. Single-Step Electronic Detection of Femtomolar DNA by Target-Induced Strand Displacement in an Electrode-Bound Duplex. *Proc. Natl. Acad. Sci.* **2006**, *103* (45), 16677. https://doi.org/10.1073/pnas.0607693103.

(279) Fabbrizzi, L. The Ferrocenium/Ferrocene Couple: A Versatile Redox Switch. *ChemTexts* **2020**, *6* (4), 22. https://doi.org/10.1007/s40828-020-00119-6.

(280) Ferapontova, E. E.; Domínguez, E. Direct Electrochemical Oxidation of DNA on Polycrystalline Gold Electrodes. *Electroanalysis* **2003**, *15* (7), 629–634. https://doi.org/https://doi.org/10.1002/elan.200390079.

(281) Chiorcea-Paquim, A.-M.; Oliveira-Brett, A. M. DNA Electrochemical Biosensors for In Situ Probing of Pharmaceutical Drug Oxidative DNA Damage. *Sensors (Basel).* **2021**, *21*

(4), 1125. https://doi.org/10.3390/s21041125.

(282) Gao, Y.; Wolf, L. K.; Georgiadis, R. M. Secondary Structure Effects on DNA Hybridization Kinetics: A Solution versus Surface Comparison. *Nucleic Acids Res.* **2006**, *34* (11), 3370–3377. https://doi.org/10.1093/nar/gkl422.

(283) Cederquist, K. B.; Keating, C. D. Hybridization Efficiency of Molecular Beacons Bound to Gold Nanowires: Effect of Surface Coverage and Target Length. *Langmuir* **2010**, *26* (23), 18273–18280. https://doi.org/10.1021/la1031703.

(284) Vogt, S.; Su, Q.; Gutiérrez-Sánchez, C.; Nöll, G. Critical View on Electrochemical Impedance Spectroscopy Using the Ferri/Ferrocyanide Redox Couple at Gold Electrodes. *Anal. Chem.* **2016**, *88* (8), 4383–4390. https://doi.org/10.1021/acs.analchem.5b04814.

(285) Lee, S.; Kim, W. J.; Chung, M. Enhanced Electrochemical Biosensing on Gold Electrodes with a Ferri/Ferrocyanide Redox Couple. *Analyst* **2021**, *146* (17), 5236–5244. https://doi.org/10.1039/D1AN00952D.

(286) Rasmussen, K. H.; Keller, S. S.; Jensen, F.; Jorgensen, A. M.; Hansen, O. SU-8 Etching in Inductively Coupled Oxygen Plasma. *Microelectron. Eng.* **2013**, *112* (Supplement C), 35–40. https://doi.org/https://doi.org/10.1016/j.mee.2013.05.011.

(287) Nummelin, S.; Kommeri, J.; Kostiainen, M. A.; Linko, V. Evolution of Structural DNA Nanotechnology. *Adv. Mater.* **2018**, *30* (24). https://doi.org/10.1002/adma.201703721.

(288) Heuer-Jungemann, A.; Linko, V. Engineering Inorganic Materials with DNA Nanostructures. *ACS Cent. Sci.* **2021**, *7* (12), 1969–1979. https://doi.org/10.1021/acscentsci.1c01272.

(289) Hui, L.; Bai, R.; Liu, H. DNA-Based Nanofabrication for Nanoelectronics. *Adv. Funct. Mater.* **2022**, *32* (16), 2112331. https://doi.org/https://doi.org/10.1002/adfm.202112331.

(290) Jiang, Q.; Liu, S.; Liu, J.; Wang, Z.-G.; Ding, B. Rationally Designed DNA-Origami Nanomaterials for Drug Delivery In Vivo. *Adv. Mater.* **2019**, *31* (45), 1804785. https://doi.org/https://doi.org/10.1002/adma.201804785.

(291) DeLuca, M.; Shi, Z.; Castro, C. E.; Arya, G. Dynamic DNA Nanotechnology: Toward Functional Nanoscale Devices. *Nanoscale Horizons* **2020**, *5* (2), 182–201. https://doi.org/10.1039/C9NH00529C.

(292) Nummelin, S.; Shen, B.; Piskunen, P.; Liu, Q.; Kostiainen, M. A.; Linko, V. Robotic DNA Nanostructures. *ACS Synth. Biol.* **2020**, *9* (8), 1923–1940. https://doi.org/10.1021/acssynbio.0c00235.

(293) Shen, L.; Wang, P.; Ke, Y. DNA Nanotechnology-Based Biosensors and Therapeutics. *Adv. Healthc. Mater.* **2021**, *10* (15), 2002205. https://doi.org/https://doi.org/10.1002/adhm.202002205.

(294) Voigt, N. V; Tørring, T.; Rotaru, A.; Jacobsen, M. F.; Ravnsbæk, J. B.; Subramani, R.; Mamdouh, W.; Kjems, J.; Mokhir, A.; Besenbacher, F.; Gothelf, K. V. Single-Molecule Chemical Reactions on DNA Origami. *Nat. Nanotechnol.* **2010**, *5* (3), 200–203. https://doi.org/10.1038/nnano.2010.5.

(295) Stephanopoulos, N. Hybrid Nanostructures from the Self-Assembly of Proteins and DNA. *Chem* **2020**, *6* (2), 364–405. https://doi.org/https://doi.org/10.1016/j.chempr.2020.01.012.

(296) Kuzyk, A.; Jungmann, R.; Acuna, G. P.; Liu, N. DNA Origami Route for Nanophotonics. *ACS Photonics* **2018**, *5* (4), 1151–1163. https://doi.org/10.1021/acsphotonics.7b01580.

(297) Castro, C. E.; Dietz, H.; Högberg, B. DNA Origami Devices for Molecular-Scale Precision Measurements. *MRS Bull.* **2017**, *42* (12), 925–929. https://doi.org/10.1557/mrs.2017.273.

(298) Shen, B.; Piskunen, P.; Nummelin, S.; Liu, Q.; Kostiainen, M. A.; Linko, V. Advanced DNA Nanopore Technologies. *ACS Appl. Bio Mater.* **2020**, *3* (9), 5606–5619. https://doi.org/10.1021/acsabm.0c00879.

(299) Raab, M.; Jusuk, I.; Molle, J.; Buhr, E.; Bodermann, B.; Bergmann, D.; Bosse, H.; Tinnefeld, P. Using DNA Origami Nanorulers as Traceable Distance Measurement Standards and Nanoscopic Benchmark Structures. *Sci. Rep.* **2018**, *8* (1), 1780. https://doi.org/10.1038/s41598-018-19905-x.

(300) Yonggang, K.; Stuart, L.; Yung, C.; Yan, L.; Hao, Y. Self-Assembled Water-Soluble Nucleic Acid Probe Tiles for Label-Free RNA Hybridization Assays. *Science (80-.).* **2008**, *319* (5860), 180–183. https://doi.org/10.1126/science.1150082.

(301) Koirala, D.; Shrestha, P.; Emura, T.; Hidaka, K.; Mandal, S.; Endo, M.; Sugiyama, H.; Mao, H. Single-Molecule Mechanochemical Sensing Using DNA Origami Nanostructures. *Angew. Chemie Int. Ed.* **2014**, *53* (31), 8137–8141. https://doi.org/https://doi.org/10.1002/anie.201404043.

(302) Arroyo-Currás, N.; Sadeia, M.; Ng, A. K.; Fyodorova, Y.; Williams, N.; Afif, T.; Huang, C.-M.; Ogden, N.; Andresen Eguiluz, R. C.; Su, H.-J.; Castro, C. E.; Plaxco, K. W.; Lukeman, P. S. An Electrochemical Biosensor Exploiting Binding-Induced Changes in Electron Transfer of Electrode-Attached DNA Origami to Detect Hundred Nanometer-Scale Targets. *Nanoscale* **2020**, *12* (26), 13907–13911. https://doi.org/10.1039/D0NR00952K.

(303) Kroener, F.; Heerwig, A.; Kaiser, W.; Mertig, M.; Rant, U. Electrical Actuation of a DNA Origami Nanolever on an Electrode. *J. Am. Chem. Soc.* **2017**, *139* (46), 16510–16513. https://doi.org/10.1021/jacs.7b10862.

(304) Kruse, M.; Möser, C.; Smith, D. M.; Müller-Landau, H.; Rant, U.; Hölzel, R.; Bier, F. F. Measuring Influenza A Virus and Peptide Interaction Using Electrically Controllable DNA Nanolevers. *Adv. Mater. Technol.* **2022**, *7* (5), 2101141. https://doi.org/https://doi.org/10.1002/admt.202101141.

(305) Kroener, F.; Traxler, L.; Heerwig, A.; Rant, U.; Mertig, M. Magnesium-Dependent Electrical Actuation and Stability of DNA Origami Rods. *ACS Appl. Mater. Interfaces* **2019**, *11* (2), 2295–2301. https://doi.org/10.1021/acsami.8b18611.

(306) Xin, Y.; Piskunen, P.; Suma, A.; Li, C.; Ijäs, H.; Ojasalo, S.; Seitz, I.; Kostiainen, M. A.; Grundmeier, G.; Linko, V.; Keller, A. Environment-Dependent Stability and Mechanical Properties of DNA Origami Six-Helix Bundles with Different Crossover Spacings. *Small* **2022**, *18* (18), 2107393. https://doi.org/https://doi.org/10.1002/smll.202107393.

(307) Marblestone, A. H.; Vazquez, A.; Church, G. M.; Douglas, S. M.; Teerapittayanon, S.; Shih, W. M. Rapid Prototyping of 3D DNA-Origami Shapes with CaDNAno. *Nucleic Acids Res.* **2009**, *37* (15), 5001–5006. https://doi.org/10.1093/nar/gkp436.

(308) Julin, S.; Nonappa; Shen, B.; Linko, V.; Kostiainen, M. A. DNA-Origami-Templated Growth of Multilamellar Lipid Assemblies. *Angew. Chemie Int. Ed.* **2021**, *60* (2), 827–833. https://doi.org/https://doi.org/10.1002/anie.202006044.

(309) Stahl, E.; Martin, T. G.; Praetorius, F.; Dietz, H. Facile and Scalable Preparation of Pure and Dense DNA Origami Solutions. *Angew. Chemie Int. Ed.* **2014**, *53* (47). https://doi.org/10.1002/anie.201405991.

(310) Castro, C. E.; Kilchherr, F.; Kim, D.-N.; Shiao, E. L.; Wauer, T.; Wortmann, P.; Bathe, M.; Dietz, H. A Primer to Scaffolded DNA Origami. *Nat. Methods* **2011**, *8*, 221.

(311) Ho, L. S. J.; Limson, J. L.; Fogel, R. Certain Methods of Electrode Pretreatment Create Misleading Responses in Impedimetric Aptamer Biosensors. *ACS Omega* **2019**, *4* (3), 5839–5847. https://doi.org/10.1021/acsomega.9b00075.

(312) Vogiazi, V.; de la Cruz, A.; Heineman, W. R.; White, R. J.; Dionysiou, D. D. Effects of Experimental Conditions on the Signaling Fidelity of Impedance-Based Nucleic Acid Sensors. *Anal. Chem.* **2021**, *93* (2), 812–819. https://doi.org/10.1021/acs.analchem.0c03269.

(313) Douglas, S. M.; Marblestone, A. H.; Teerapittayanon, S.; Vazquez, A.; Church, G. M.; Shih, W. M. Rapid Prototyping of 3D DNA-Origami Shapes with CaDNAno. *Nucleic Acids Res.* **2009**, *37* (15), 5001–5006. https://doi.org/10.1093/nar/gkp436.

(314) Hong, F.; Zhang, F.; Liu, Y.; Yan, H. DNA Origami: Scaffolds for Creating Higher Order Structures. *Chem. Rev.* **2017**, *117* (20), 12584–12640. https://doi.org/10.1021/acs.chemrev.6b00825.

(315) Kuzyk, A.; Urban, M. J.; Idili, A.; Ricci, F.; Liu, N. Selective Control of Reconfigurable Chiral Plasmonic Metamolecules. *Sci. Adv.* **2017**, *3* (4), e1602803–e1602803. https://doi.org/10.1126/sciadv.1602803.

(316) Daljit Singh, J. K.; Luu, M. T.; Abbas, A.; Wickham, S. F. J. Switchable DNA-Origami Nanostructures That Respond to Their Environment and Their Applications. *Biophys. Rev.* **2018**, *10* (5), 1283–1293. https://doi.org/10.1007/s12551-018-0462-z.

(317) Ryssy, J.; Natarajan, A. K.; Wang, J.; Lehtonen, A. J.; Nguyen, M.-K.; Klajn, R.; Kuzyk, A. Light-Responsive Dynamic DNA-Origami-Based Plasmonic Assemblies. *Angew. Chemie Int. Ed.* **2020**. https://doi.org/10.1002/anie.202014963.

(318) Funck, T.; Nicoli, F.; Kuzyk, A.; Liedl, T. Sensing Picomolar Concentrations of RNA Using Switchable Plasmonic Chirality. *Angew. Chemie Int. Ed.* **2018**, *57* (41), 13495–13498. https://doi.org/https://doi.org/10.1002/anie.201807029.

(319) Loretan, M.; Domljanovic, I.; Lakatos, M.; Rüegg, C.; Acuna, G. P. DNA Origami as Emerging Technology for the Engineering of Fluorescent and Plasmonic-Based Biosensors. *Mater. (Basel, Switzerland)* **2020**, *13* (9), 2185. https://doi.org/10.3390/ma13092185.

(320) Ge, Z.; Fu, J.; Liu, M.; Jiang, S.; Andreoni, A.; Zuo, X.; Liu, Y.; Yan, H.; Fan, C. Constructing

Submonolayer DNA Origami Scaffold on Gold Electrode for Wiring of Redox Enzymatic Cascade Pathways. *ACS Appl. Mater. Interfaces* **2019**, *11* (15), 13881–13887. https://doi.org/10.1021/acsami.8b12374.

(321) Frasconi, M.; Tel-Vered, R.; Elbaz, J.; Willner, I. Electrochemically Stimulated PH Changes: A Route To Control Chemical Reactivity. *J. Am. Chem. Soc.* **2010**, *132* (6), 2029–2036. https://doi.org/10.1021/ja9094796.

(322) Castro, C. E.; Kilchherr, F.; Kim, D.-N.; Shiao, E. L.; Wauer, T.; Wortmann, P.; Bathe, M.; Dietz, H. A Primer to Scaffolded DNA Origami. *Nat. Methods* **2011**, *8* (3), 221–229. https://doi.org/10.1038/nmeth.1570.

(323) Kim, D.-N.; Kilchherr, F.; Dietz, H.; Bathe, M. Quantitative Prediction of 3D Solution Shape and Flexibility of Nucleic Acid Nanostructures. *Nucleic Acids Res.* **2012**, *40* (7), 2862–2868. https://doi.org/10.1093/nar/gkr1173.

(324) Hung, A. M.; Micheel, C. M.; Bozano, L. D.; Osterbur, L. W.; Wallraff, G. M.; Cha, J. N. Large-Area Spatially Ordered Arrays of Gold Nanoparticles Directed by Lithographically Confined DNA Origami. *Nat. Nanotechnol.* **2010**, *5* (2), 121–126. https://doi.org/10.1038/nnano.2009.450.

(325) Rueden, C. T.; Schindelin, J.; Hiner, M. C.; DeZonia, B. E.; Walter, A. E.; Arena, E. T.; Eliceiri, K. W. ImageJ2: ImageJ for the next Generation of Scientific Image Data. *BMC Bioinformatics* **2017**, *18* (1). https://doi.org/10.1186/s12859-017-1934-z.

(326) Herne, T. M.; Tarlov, M. J. Characterization of DNA Probes Immobilized on Gold Surfaces. *J. Am. Chem. Soc.* **1997**, *119* (38), 8916–8920. https://doi.org/10.1021/ja9719586.

(327) Murphy, J. N.; Cheng, A. K. H.; Yu, H.-Z.; Bizzotto, D. On the Nature of DNA Self-Assembled Monolayers on Au: Measuring Surface Heterogeneity with Electrochemical in Situ Fluorescence Microscopy. *J. Am. Chem. Soc.* **2009**, *131* (11), 4042–4050. https://doi.org/10.1021/ja808696p.

(328) Pheeney, C. G.; Barton, J. K. DNA Electrochemistry with Tethered Methylene Blue. *Langmuir* **2012**, *28* (17), 7063–7070. https://doi.org/10.1021/la300566x.

(329) Dauphin-Ducharme, P.; Arroyo-Currás, N.; Plaxco, K. W. High-Precision Electrochemical Measurements of the Guanine-, Mismatch-, and Length-Dependence of Electron Transfer from Electrode-Bound DNA Are Consistent with a Contact-Mediated Mechanism. *J. Am. Chem. Soc.* **2019**, *141* (3), 1304–1311. https://doi.org/10.1021/jacs.8b11341.

(330) Tuite, E.; Norden, B. Sequence-Specific Interactions of Methylene Blue with Polynucleotides and DNA: A Spectroscopic Study. *J. Am. Chem. Soc.* **1994**, *116* (17), 7548–7556. https://doi.org/10.1021/ja00096a011.

(331) Zhang, L. Z.; Tang, G.-Q. The Binding Properties of Photosensitizer Methylene Blue to Herring Sperm DNA: A Spectroscopic Study. *J. Photochem. Photobiol. B Biol.* **2004**, *74* (2), 119–125. https://doi.org/https://doi.org/10.1016/j.jphotobiol.2004.03.005.

(332) Kollmann, F.; Ramakrishnan, S.; Shen, B.; Grundmeier, G.; Kostiainen, M. A.; Linko, V.; Keller, A. Superstructure-Dependent Loading of DNA Origami Nanostructures with a

Groove-Binding Drug. *ACS Omega* **2018**, *3* (8), 9441–9448. https://doi.org/10.1021/acsomega.8b00934.

(333) Gorodetsky, A. A.; Buzzeo, M. C.; Barton, J. K. DNA-Mediated Electrochemistry. *Bioconjug. Chem.* **2008**, *19* (12), 2285–2296. https://doi.org/10.1021/bc8003149.

(334) Rashid, J. I. A.; Yusof, N. A. The Strategies of DNA Immobilization and Hybridization Detection Mechanism in the Construction of Electrochemical DNA Sensor: A Review. *Sens. Bio-Sensing Res.* **2017**, *16*, 19–31. https://doi.org/https://doi.org/10.1016/j.sbsr.2017.09.001.

(335) Chagnes, A. Chapter 2 - Fundamentals in Electrochemistry and Hydrometallurgy. In *Lithium Process Chemistry*; Chagnes, A., Światowska, J., Eds.; Elsevier: Amsterdam, 2015; pp 41–80. https://doi.org/https://doi.org/10.1016/B978-0-12-801417-2.00002-5.

(336) Cobb, S. J.; Macpherson, J. V. Enhancing Square Wave Voltammetry Measurements via Electrochemical Analysis of the Non-Faradaic Potential Window. *Anal. Chem.* **2019**, *91* (12), 7935–7942. https://doi.org/10.1021/acs.analchem.9b01857.